Volume 69C
Number 4
Oct.–Dec. 1965

Engineering and Instrumentation

U.S. DEPARTMENT OF COMMERCE

SECTION C

JOURNAL OF RESEARCH

NATIONAL BUREAU OF STANDARDS

Journal of Research
of the
National Bureau of Standards

C. Engineering and Instrumentation

OCT.–DEC. • 1965

VOLUME • 69C

NUMBER • 4

Editor: Martin Greenspan

Associate Editors: G. F. Montgomery, R. V. Smith

Publication dates:
Feb. 15, May 15, Aug. 15, Nov. 15, 1965

JOURNAL OF RESEARCH

The National Bureau of Standards Journal of Research reports research and development in the fields of activity shown at right. Also included from time to time are survey articles on topics closely related to the Bureau's scientific and technical program.

The Journal is published in four separate sections as follows:

A. Physics and Chemistry

Contains papers of interest primarily to scientists working in these fields. Issued six times a year. Annual subscription: domestic, $4.00; foreign, $4.75. Single copy, 70¢.

B. Mathematics and Mathematical Physics

Presents studies and compilations designed mainly for the mathematician and the theoretical physicist. Issued quarterly. Annual subscription: domestic, $2.25; foreign, $2.75. Single copy, 75¢.

C. Engineering and Instrumentation

Reports research and development results of interest chiefly to the engineer and the applied scientist. Issued quarterly. Annual subscription: domestic, $2.25; foreign, $2.75. Single copy, 75¢.

D. Radio Science (formerly Radio Propagation)

Published in cooperation with U.S. National Committee of URSI. Presents papers in radio propagation, communications, and radio science generally. Issued monthly. Annual subscription: domestic, $9.00; foreign, $11.50. Single copy, $1.00.

U.S. DEPARTMENT OF COMMERCE
John T. Connor, Secretary
NATIONAL BUREAU OF STANDARDS
A. V. Astin, Director

The National Bureau of Standards is a principal focal point in the Federal Government for assuring maximum application of the physical and engineering sciences to the advancement of technology in industry and commerce. Its responsibilities include development and maintenance of the national standards of measurement, and the provisions of means for making measurements consistent with those standards; determination of physical constants and properties of materials; development of methods for testing materials, mechanisms, and structures, and making such tests as may be necessary, particularly for government agencies; cooperation in the establishment of standard practices for incorporation in codes and specifications; advisory service to government agencies on scientific and technical problems; invention and development of devices to serve special needs of the Government; assistance to industry, business, and consumers in the development and acceptance of commercial standards and simplified trade practice recommendations; administration of programs in cooperation with United States business groups and standards organizations for the development of international standards of practice; and maintenance of a clearinghouse for the collection and dissemination of scientific, technical, and engineering information.

Institute for Basic Standards. Applied Mathematics. Electricity. Metrology. Mechanics. Heat. Atomic Physics. Physical Chemistry. Laboratory Astrophysics.* Radiation Physics. Radio Standards Laboratory:* Radio Standards Physics; Radio Standards Engineering. Office of Standard Reference Data.

Institute for Materials Research. Analytical Chemistry. Polymers. Metallurgy. Inorganic Materials. Reactor Radiations. Cryogenics.* Materials Evaluation Laboratory. Office of Standard Reference Materials.

Institute for Applied Technology. Building Research. Information Technology. Performance Test Development. Electronic Instrumentation. Textile and Apparel Technology Center. Technical Analysis. Office of Weights and Measures. Office of Engineering Standards. Office of Invention and Innovation. Office of Technical Resources. Clearinghouse for Federal Scientific and Technical Information.**

Central Radio Propagation Laboratory.* Ionospheric Telecommunications. Tropospheric Telecommunications. Space Environment Forecasting. Aeronomy.

*Located at Boulder, Colo. 80301.
**Located at 5285 Port Royal Road, Springfield, Va. 22171.

Order all publications from the Superintendent of Documents
U.S. Government Printing Office, Washington, D.C., 20402.

Use of funds for printing this publication approved by the Director of the Bureau of the Budget (June 19, 1961).

JOURNAL OF RESEARCH of the National Bureau of Standards—C. Engineering and Instrumentation
Vol. 69C, No. 4, October–December 1965

Some Applications of the Wave Front Shearing Interferometer

James B. Saunders

(May 27, 1965)

This paper gives the results of several applications of the wave front shearing prism interferometer. The instrument is very compact and easy to apply. It is applied to the testing of chromatic aberration of simple and compound lenses; and to the testing of wave forms that characterize the monochromatic aberrations (spherical, coma, and astigmatism). Results are shown for several different type lenses. This interferometer is equally applicable to the testing of small lenses and large telescope objectives.

Key Words: Interferometer, testing of lenses, lens aberrations, aberrations, prism interferometer, chromatic aberration of lenses.

Previous applications of lens testing interferometers have been limited because of the difficulties associated with their use. The Twyman lens testing interferometer, for instance, requires several precision elements that have apertures equal to or exceeding that of the lens to be tested. The curvature of the convex reference mirror should match the back focus of the lens to a reasonable approximation, thus necessitating the use of a different reference mirror for lenses of different focal lengths. The relatively large separation of the elements invites vibrations and is vulnerable to temperature and atmospheric disturbances. Several modifications of the wave front shearing prism interferometer (abbreviated to WFSPI), that are small and relatively free from some of the above mentioned objections, have been described by Saunders [1].[1]

All the elements of the WFSPI are combined into one small compound prism. Since it operates at a point of convergence of the light beam (fig. 1) it can be very small. A small prism can be made so that imperfections in it are quite negligible. A prism 2.5 cm in length will accommodate any lens that provides a working distance (image point to back surface of lens) in excess of 1.7 cm if its aperture does not exceed this distance.

[1] Figures in brackets indicate the literature references at the end of this paper.

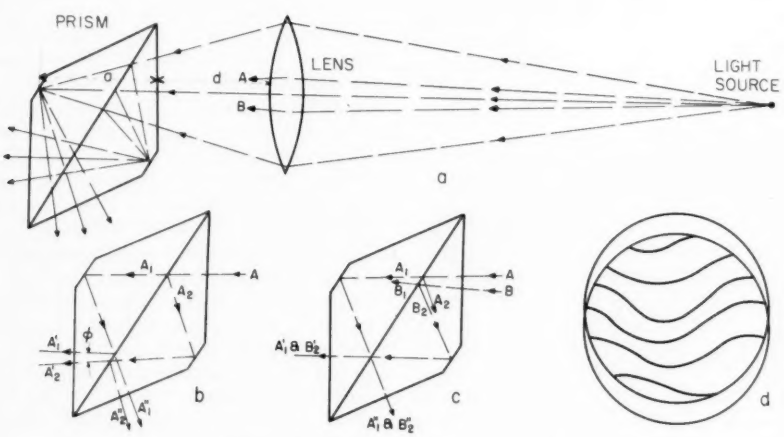

FIGURE 1. *Optics of the interferometer.*
Interference is obtained by the combination of one component, $A'_1(A''_1)$, of ray A with one component, $B'_2(B''_2)$, of ray B that leave the source in different directions.

The maximum separation of any two interfering beams is the lateral shear, S, which is usually a small fraction of the diameter of the lens being tested. Thus, the effects of temperature and atmospheric disturbances are easily suppressed.

Interference fringes may be obtained with white light. However, a narrow band interference filter is preferred for most work.

The WFSPI divides a wave front into two components, shears one component relative to the other, and recombines the two beams of light so as to produce interference in the overlapping area. Each ray that enters the prism is divided into four components, two emerging from one face and two from another, as shown in figure 1b. None of these four components are recombined and, therefore, do not interfere with each other. Interference is obtained by the combination of one component of each of two rays that leave the source in different directions (rays A and B) and are subsequently recombined by the prism, as shown in figure 1c. An observer's eye, receiving either pair of the recombined rays, sees interference fringes in whatever plane it is focused on. When the eye is focused on the lens, it sees fringes in the plane of the lens (fig. 1d).

A reference surface, such as is required in the Twyman interferometer, is not used since this interferometer yields results by comparing a wave front with an image of itself. The shape and width of the fringes are measures of the deviation of the original wave front from a sphere. A simple mathematical operation [2] has been described that permits a computation of the wave front from observations of a single fringe pattern.

The fringe configuration produced by a lens that is afflicted with chromatic aberration will change with change in the wavelength of the light source. Figure 2 shows a plot of image distance (focal length of the lens if the source is at infinity) versus wavelength for a single element lens that has a focal length of approximately 42 cm and an aperture of 9 cm. The slit of a prism monochromator was used, with a zirconium arc, as the light source. A small filament [3], mounted on a milling machine table and applied as described by Platzeck [4] and Gaviola, was also used to locate the focal positions. The photographs inserted in figure 2 represent the fringe configurations for the three indicated wavelengths.

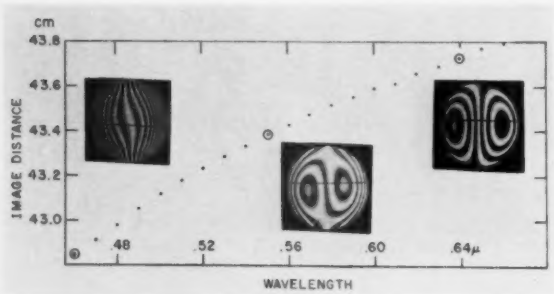

FIGURE 2. *Image distance versus wavelength.*
Plano-convex lens, focal length 42 cm, aperture 9 cm. The inserted photographs are the fringe patterns for the indicated wavelengths.

It can be shown by ray tracings that the image distance, q_ν, corresponding to any wavelength, λ_ν, is given by the formula

$$q_\nu = d + an_\nu^{-1} - \lambda_\nu N_\nu d/\phi b n_\nu,$$

where d is the distance from the lens to the prism (fig. 1a); a is the distance from the entrance face of the prism to the point where the principal ray suffers total internal reflection; n_ν is the refractive index of the prism; N_ν and b are, respectively, the number of fringes and distance between the two reference points, P_1'' and P_2' (fig. 3). The sign of N_ν is chosen so that it increases when d is increased. The angle ϕ is the relative deviation, inside the prism, of any two components of an original ray that emerges from the same face of the prism (such as rays A_1' and A_2' of fig. 1b). The difference in focal distance, Δq_{12}, for any two wavelengths, λ_1 and λ_2, is given by

$$\Delta q_{12} = a(n_1^{-1} - n_2^{-1}) - d(\lambda_1 N_1 n_1^{-1} - \lambda_2 N_2 n_2^{-1})/\phi b.$$

A change of one in the value of N corresponds to approximately 0.5 mm in the focal distance for the prism used while obtaining the data for figure 2. This prism produces a shear of 0.006 radians.

When the chromatic aberration is small, a prism of high sensitivity (large shear angle) should be used. Figure 4 is a plot of image distance versus wavelength for an air spaced doublet (focal length = 463 mm, aperture = 64 mm). The shear is approximately 0.047 radians. One fringe corresponds to approximately 0.1 mm shift in the image point. The photographs from which the data were obtained are shown in figure 5.

The shape of a wave front, produced by a lens, is representative of all monochromatic aberrations of the lens in whatever manner it is used when producing this wave form. The interferometer of figure 1a produces a set of interference fringes that is characteristic of the shape of the wave front. The photograph shown in figure 6 depicts fringes produced by an f/2 camera lens with the source located 20 m from the lens. The curve marked f/2 in figure 7 is a plot of the deviations of the corresponding wave front from a best fitting reference sphere. It is apparent that if the between-the-lens diaphragm had been adjusted to an f/3 system the fringe pattern would have been reduced in area to that of the overlapping area of the two inserted circles in figure 6. When this reduced fringe pattern is analyzed by the method described in reference 2, the computed deviations from a best fitting sphere are found to be represented by curve f/3 in figure 7.

Since the curve that represents the deviation of the wave front from a best fitting sphere also represents the image forming characteristics of the lens, it is suggested that the quality of any lens may be represented by a relatively simple number. The manner of

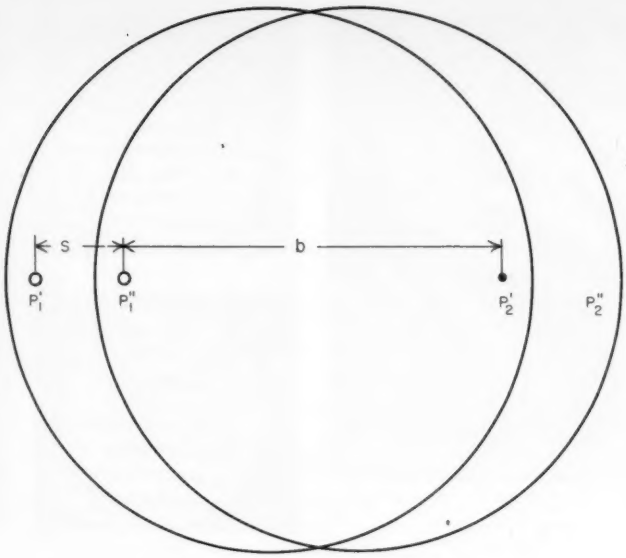

FIGURE 3. *Reference points P_1'' and P_2' are used for measuring change in focus.*

Points P_1' and P_1'' (P_2' and P_2'') are the two sheared images of a reference point $P_1(P_2)$. The separation of reference points P_1 and P_2 equals $(S + b)$, where S is the lateral shear of the beam in the plane of the lens. The reference points may be marked on the surface of the lens.

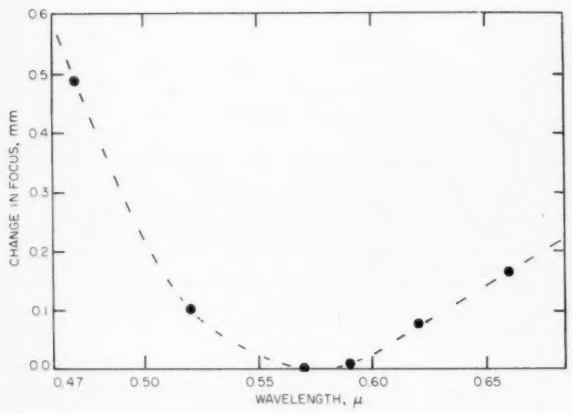

FIGURE 4. *Image distance versus wavelength for a 2-element achromatic lens.*

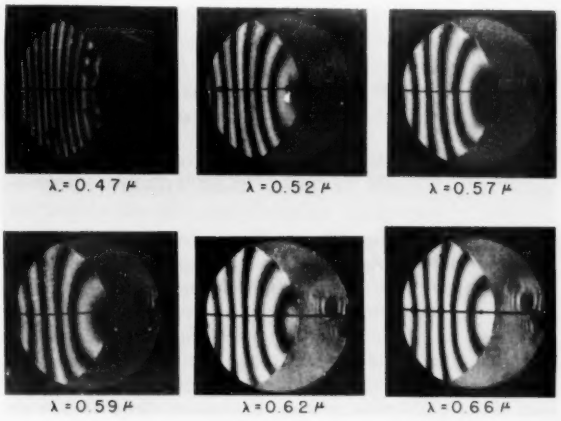

FIGURE 5. *Photograph of interference fringes for different wavelengths.*

selecting this number may be best decided later, but it appears that the weighted arithmetical mean deviation of the wave front from a statistically chosen best fitting sphere might represent the image forming characteristics of the lens. This number would vary with the position of the object, relative to the lens and its axis; however, so does the quality of the image. The weights should be chosen so as to give equal weight per unit area over the whole lens. The chosen number should also include other factors, such as aperture for instance, and might therefore be a compound number.

The weighted mean deviations of wave fronts are readily obtained from the corresponding fringe patterns produced by this interferometer. The weighted arithmetical mean deviation for curve f/2 in figure 7 is 2.1λ and for f/3 it is 0.1λ. The relative magnitude of these two numbers is believed to represent, to a close approximation, the corresponding relative image forming qualities.

FIGURE 6. *Interference fringes in a f/2 camera lens.*
The inserted circles represent the edge of an iris diaphragm when adjusted to transmit an f/3 beam of light.

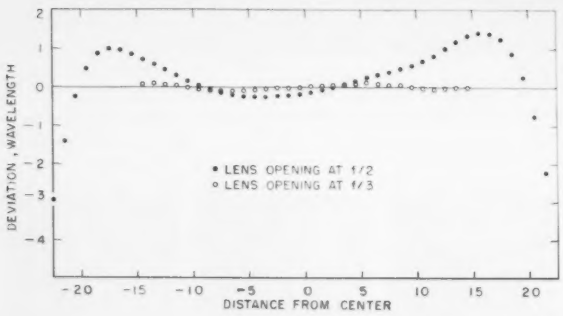

FIGURE 7. *Deviations of the wave front, produced by an f/2 lens when wide open and at f/3, from best fitting reference spheres.*

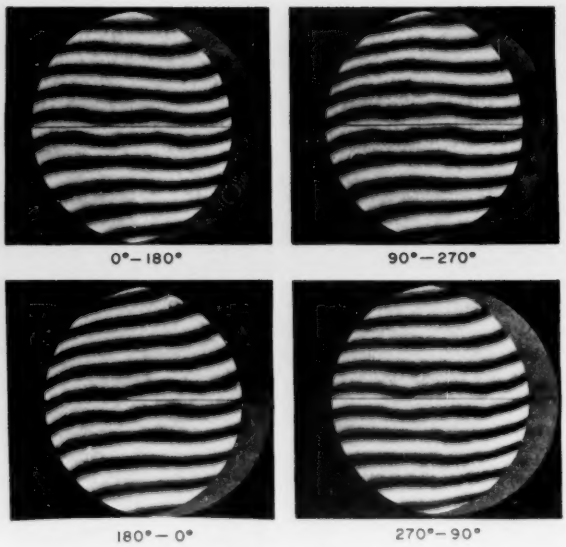

FIGURE 8. *Interference fringes of a lens when sheared in opposite directions along two axes that are normal to each other.*

The photographs of figure 8 are the fringes produced by an aerial camera lens of 8-in. aperture and 50-in. focal length that was designed and made at NBS. This lens has four air-spaced elements, and was designed to be used with another element—a concave lens near the focus—as an image flattener. The directions of shear are indicated for each photograph. Only four of the eight photographs that were made are shown here. Figure 9 shows the eight curves, representing the deviations from best fitting spheres along the indicated diameters. The eight equally spaced directions are indicated in the drawing. The abscissas of each of the four pairs of curves in figure 9 represent the same direction along the indicated diameter. The difference in wave front shape, for the several diameters, clearly indicates assymmetry in the wave front.

An astronomical objective may be tested in the laboratory by autocollimation if a sufficiently large optical flat is available. If such a flat is not available, it may be tested in the manner illustrated in figure 1a, by placing a small source at a considerable distance from the lens. Figure 10 shows the photographs of the fringes and figure 11 shows the corre-

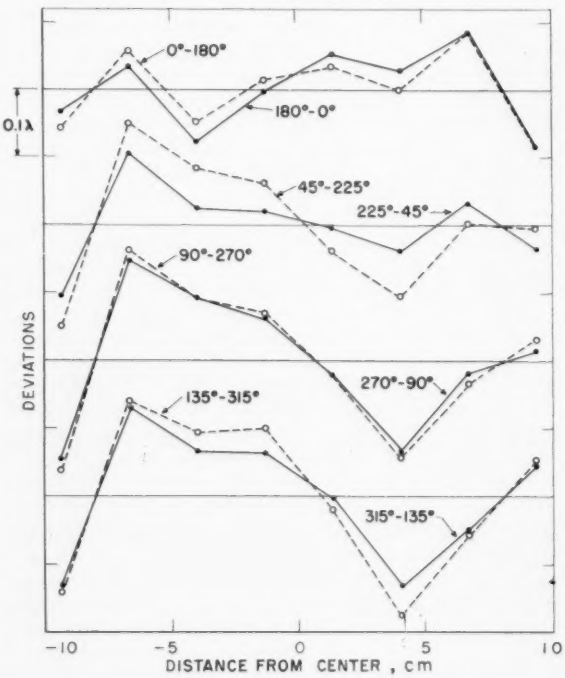

FIGURE 9. *Curves representing deviations of wave fronts from close fitting spheres.*
The direction of shear, relative to the initial position of the lens, was increased 45° between successive exposures for making the corresponding photographs.

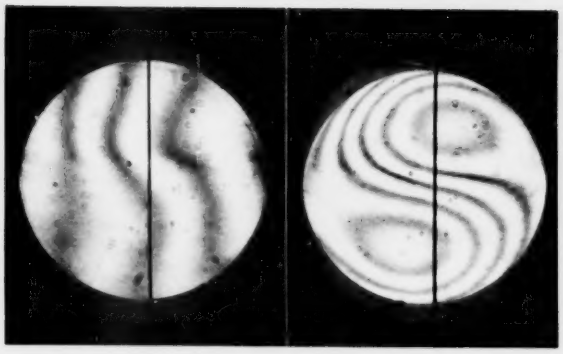

FIGURE 10. *Fringes produced by a lens when used properly, a, and when the axis is reversed, b.*
Aperture equals 12 in.; focal length equals 15 ft.; air spaced, two element objective.

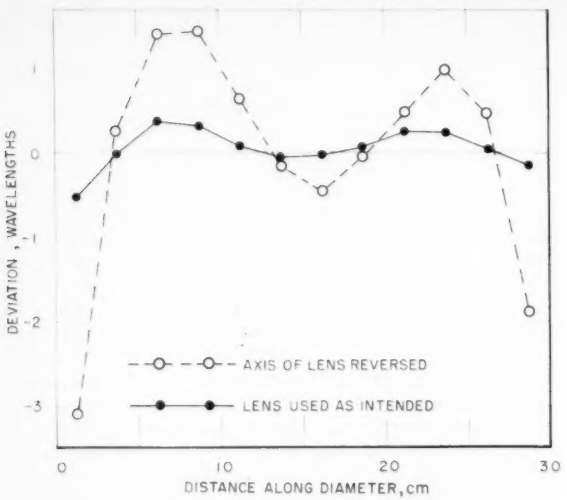

FIGURE 11. *Deviations of wave front versus distance along one diameter of an astronomical refractor.*
The two curves represent data computed from the two photographs of figure 10.

sponding deviation curves for a 12-in. aperture, 15-ft focal length refractor, when it is used as intended and when the axis is reversed.

Figure 12 shows interference fringes produced by the 32-in. aperture, 40-ft focal length reflecting telescope at the University of Virginia at Charlottesville, Va. The 12-sec exposure used for this photograph practically elimates the atmospheric effect by recording the average position of the fringes. The photograph is too recent to have permitted inclusion of the data analysis in this report.

FIGURE 12. *First photograph of interference fringes produced by a star for testing an astronomical reflector.*
Aperture 32 in.; focal length equal 40 ft., Cassigrainian type telescope.

Test made with this interferometer show that it is as easy to assemble as a Foucault knife edge test. It gives quantitative results that are as accurate as other interferometer tests. The fringe pattern is practically independent of vibrations of the instrument. Technical personnel are not required for its use. It is relatively easy to make, the cost of material for it is negligible, and it is easy to reduce the effects of temperature gradients and atmospheric turbidity to negligible effects, and it is easy to reduce the effects of temperature gradients and atmospheric turbidity to negligible significance. Because of the simplicity of its operation, size, ruggedness and stability, this interferometer readily lends itself to combination with electronics for automatic testing for lenses.

References

[1] Saunders, J. B., Wave front shearing prism interferometer, J. Res. NBS **68C** (Engr. and Instr.) No. 3, 155 (July-Sept. 1964).
[2] Saunders, J. B., Measurement of wave fronts without a reference standard, J. Res. NBS **66B** (Math. and Math. Phys.) No. 1, 29 (Jan.-Mar. 1962).
[3] Saunders, J. B., An improved optical test for spherical aberration, J. Opt. Soc. Am. **44**, 664 (1954).
[4] R. Platzeck and E. Gaviola, J. Opt. Soc. Am. **29**, 487 (1939).

(Paper 69C4–204)

JOURNAL OF RESEARCH of the National Bureau of Standards—C. Engineering and Instrumentation
Vol. 69C, No. 4, October–December 1965

Precision Method for Evaluating Primary Aberrations of Lenses With a Twyman Interferometer

James B. Saunders

(May 21, 1965)

A simplified procedure for separate evaluation of the three primary aberrations of lenses with the Twyman lens testing interferometer is described. Each of the aberration coefficients is found to be a function of observations at only four points on the lens. Equations are given for the optimum choice of reference points that give best results. These equations are applied to data previously reported in the literature. The results indicate that this procedure is sufficiently precise to reveal high order aberrations in a lens that was assumed to be practically free from such aberrations.

Key Words: Interferometer, lens testing, Twyman interferometer.

1. Introduction

The formula for optical path difference in the Twyman lens testing interferometer, used by Professor Kingslake, contains seven parameters. It would seem that data from seven reference points would be necessary for evaluating any one of the parameters. By judiciously choosing the location of the reference points each of the primary monochromatic aberrations may be evaluated from data taken at only four points. It will be shown that the results obtained from four points, with a given lens, are of the same order of accuracy as those previously obtained, by least squares, from 44 points. This represents a very large reduction in computations.

Each of the primary monochromatic aberrations is separately evaluated. The results indicate that the sensitivity of the Twyman interferometer is sufficient, not only to measure the aberration coefficients accurately, but also to measure changes in these aberrations with changes in the aperture of the lens.

The discovery that four properly chosen points are adequate for evaluation of each aberration coefficient with the Twyman interferometer was the result of an anologous discovery that two points are adequate for the same measurements with the Kösters prism interferometer.

2. Fundamental Equations

The terminology previously used by Kingslake [1] will be used in this paper. The data which he obtained with a simple lens [2] will be used for demonstration of the procedures described here. This lens was assumed to be practically free from higher order aberrations over the aperture used for obtaining results.

[1] R. Kingslake, The interferometer patterns due to the primary aberrations, Trans. Opt. Soc. **27**, 94 (1925–6).
[2] R. Kingslake, The analysis of an interferogram, Trans. Opt. Soc. **28**, 1 (1926–7).

The formula for optical path difference is

$$A(x^2+y^2)^2+By(x^2+y^2)+C(x^2+3y^2)+D(x^2+y^2)+Ey+Fx+G=p \quad (1)$$

where A, B, and C represent, respectively, coefficients of spherical aberration, coma, and astigmatism. These coefficients are related to the aberration constants, a_1, a_2, and a_3, by the equations,

$$\left.\begin{aligned} 4A=a_1&=\frac{\text{Longitudinal (primary) spherical aberration}}{s^2f^2}\\ fB/h=a_2&=\frac{\text{coma}}{s^2h}\\ 2f^2C/h^2=a_3&=\frac{\text{distance between focal lines}}{2h^2}\end{aligned}\right\} \quad (2)$$

where s is half the aperture of the lens, h is the image distance from the optic axis and f is the distance from the image to the back surface of the lens. The xy-rectangular coordinate system, used in eq (1), is chosen so that the xy-plane is in the principal plane of the lens—with the y-axis in the meridional plane. The origin is on the optic axis of the lens. The coefficients, D, E, F, and G relate to adjustments of the interferometer. The order of interference is G, at the origin (on the axis of the lens), and is p at any point (x, y).

Figure 1 shows a photograph of the interferogram used by Kingslake in footnote 2. This interferogram contains the effects of any and all aberrations that are associated with this lens when it is used in the manner described. If this interferogram should contain higher order aberrations, eq (1) could not represent the fringes. The parameters, A, B, and C would be found to vary with the aperture of the lens; whereas,

FIGURE 1. *Interference fringes of a simple ophthalmic lens as seen in a Twyman lens testing interferometer.*

The inscribed circle represents the "useful aperture of the lens." This area was previously assumed to be practically free from higher order aberrations. The (+) and (−) signs, about the margin, represent regions of positive and negative orders of interference.

if the lens is free from higher order aberrations these parameters would be independent of lens aperture and, therefore, also independent of the location of the chosen reference points.

The family of curves in figure 2 represents the interferogram of a lens that is absolutely free from higher order aberrations. These curves (fringes) are computed from eq (1) and represent the area inside the circle in figure 1. The values for the parameters are those obtained by Kingslake (see footnote 2). Each curve corresponds to an integral order of interference (integral value for p).

3. Choice of Reference Points

Data from a family of at least four reference points are required to obtain a unique value for each of the aberration coefficients, A, B, and C in eq (1). The relative distribution of these points (fig. 3) can be so chosen that when the observed data (values for x, y, and p) at four points are substituted for their counterparts in eq (1), the resultant four equations will permit the elimination of all parameters except the one desired. There are many different arrangements of these four reference points that will permit solutions of the aberration parameters. Preliminary study showed that, in each case, one such arrangement of points could be found that yields optimum accuracy. Therefore, only one arrangement of points will be given here for evaluating each of the three aberration parameters. These arrangements are those which give optimum accuracy.

FIGURE 2. *Graphical representation of computed fringes inside the circle of figure 1.*

These curves were computed from the optical path difference formula (eq (1)) for a lens that contains only primary aberrations.

4. Astigmatism

If we draw a circle of radius r, with its center at the origin, in figure 3, it will intersect the coordinate axes at $(r, 0)$ $(0, r)$, $(-r, 0)$, and $(0, -r)$. If we choose these four points in the interferogram of figure 1, we may evaluate the parameter C from data observed at these points.

The observed data are the orders of interference, p, and the coordinates, x and y, at the four reference points. The data, labeled (x_1, y_1, p_1), (x_2, y_2, p_2), (x_3, y_3, p_3), and (x_4, y_4, p_4), may be considered as the coordinates in a three dimension rectangular coordinate system. We get optimum accuracy when the following relationships exist between the x and y coordinates:

$$x_1 = y_2 = -x_3 = -y_4 = r,$$

$$y_1 = x_2 = y_3 = x_4 = 0.$$

On substituting these values in eq (1), successively for the four points, we obtain the following four equations:

$$\left.\begin{aligned} r^4A \quad &+ r^2C + r^2D \quad + rF + G = p_1 \\ r^4A + r^3B + 3r^2C + r^2D + rE \quad &+ G = p_2 \\ r^4A \quad &+ r^2C + r^2D \quad - rF + G = p_3 \\ r^4A - r^3B + 3r^2C + r^2D - rE \quad &+ G = p_4 \end{aligned}\right\}. \tag{3}$$

If we add the first equation in 3 to the third and the second to the fourth, we obtain,

$$\left.\begin{aligned} 2Ar^4 + 2Cr^2 + 2Dr^2 + 2G &= p_1 + p_3 \\ 2Ar^4 + 6Cr^2 + 2Dr^2 + 2G &= p_2 + p_4 \end{aligned}\right\}. \tag{4}$$

By subtracting the first member equation of 4 from the second member we obtain

$$4Cr^2 = p_2 + p_4 - p_1 - p_3. \tag{5}$$

Values for x and y, along the two axes, are given by Kingslake for integral values of p. These values are represented graphically in figure 4. The values for the p's in table 1 are interpolated from figure 4. When the p's, that correspond to any chosen value for r, are substituted in eq (5) we obtain corresponding values for C. These values are given in column 6, table 1. The probable error in C is given in column 7 as ΔC, and is based on the assumption that the probable error in a single observation is the same as that obtained by Kingslake. The probable error, ΔP, of a single observation was found to be 0.013λ. Values for C are plotted in figure 5 as ordinates for corresponding values of r as abscissas. The magnitude of the probable error, ΔC, is represented by the length of arrows attached to the corresponding points. Obviously, the most precise value for C is obtained by using large values for r.

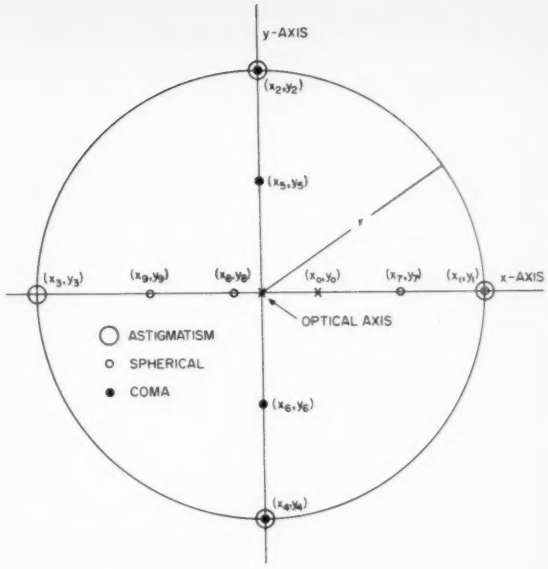

FIGURE 3. *The distribution of reference points for most precise evaluation of primary aberrations.*

The four larger circles, on the axes, are for astigmatism; the four smaller circles, on the x-axis, are for spherical aberration; and the four solid disks, on the y-axis, are for coma.

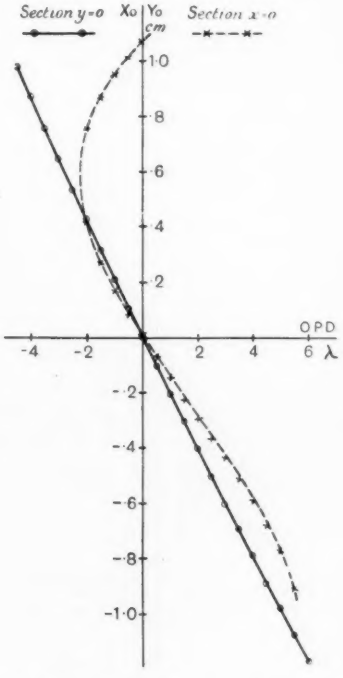

FIGURE 4. *Cross sections of the wave front along the* x *and* y*-axes.*

TABLE 1. *Value for astigmatism, C, and probable error, ΔC, (in wavelength) for different lens apertures (in millimeters)*

Radius vector	Orders of interference				Coefficient of astigmatism	
r	p_1	p_2	p_3	p_4	C	ΔC
1	−0.48	−0.63	0.48	0.68	1.250	0.650
2	−.96	−1.17	.96	1.32	0.938	.163
3	−1.43	−1.61	1.46	2.04	1.111	.072
4	−1.89	−1.97	1.97	2.74	1.078	.041
5	−2.35	−2.20	2.47	3.41	1.090	.026
6	−2.80	−2.28	2.98	4.04	1.097	.018
7	−3.25	−2.15	3.52	4.60	1.112	.013
8	−3.70	−1.82	4.06	5.08	1.133	.010
9	−4.15	−1.32	4.58	5.45	1.142	.008
10	−4.61	−0.53	5.13	5.74	1.173	.007
11	−5.13	+.38	5.66	5.86	1.200	.005

Since the fringes in figure 2 are precisely represented by eq (1), the values of the corresponding parameters should be independent of the choice of reference points. The value for C (labeled C_k in fig. 5) obtained from any family of four reference points in figure 2 will be the same as that found by Kingslake because this value was used for computing these curves. The corresponding probable error in C_k (i.e., ΔC_k) given by Kingslake is also indicated in figure 5 to illustrate the relative probable error for results obtained from four favorably chosen reference points and from 44 reference points treated statistically by the Method of Least Squares. Since the coefficient, C, varies with r (i.e., from one family of reference points to another) eq (1) obviously does not apply to the fringe pattern of figure 1. The lens that produced this set of fringes is obviously afflicted with higher order aberrations.

5. Coma

Coma cannot be evaluated from a family of reference points that are all equally distant from the origin, as is the case for astigmatism. However, if we choose a family of four points on the y-axis (fig. 3) made up of two pairs such that the two points of each pair are equally distant from the origin but of opposite sign, then we can obtain an equation for B as a function of the coordinates of these four points. If the ordinates of the inner pair of points are one half the value of those for the outer points and the outer points are near the margin of the lens the resultant value for B will be the most precise value obtainable from any family of four points. The marginal point should be far enough from the margin to permit an accurate evaluation of the corresponding order of interference.

The observed x, y, p-coordinates for the four points are (x_2, y_2, p_2), (x_5, y_5, p_5), (x_6, y_6, p_6), and (x_4, y_4, p_4), where

$$\left.\begin{aligned} x_2 = x_5 = x_6 = x_4 = 0 \\ y_2 = 2y_5 = -2y_6 = -y_4 = r \end{aligned}\right\}.$$

We may substitute the coordinates for each of these four points into eq (1) and obtain four equations, from which we may obtain the following formula for B:

$$3r^3B = 2(p_2 - p_4 + 2p_6 - 2p_5).$$

If we compute values for B that correspond to different values of r (i.e., for different apertures of the lens) we obtain the results shown in figure 6. The

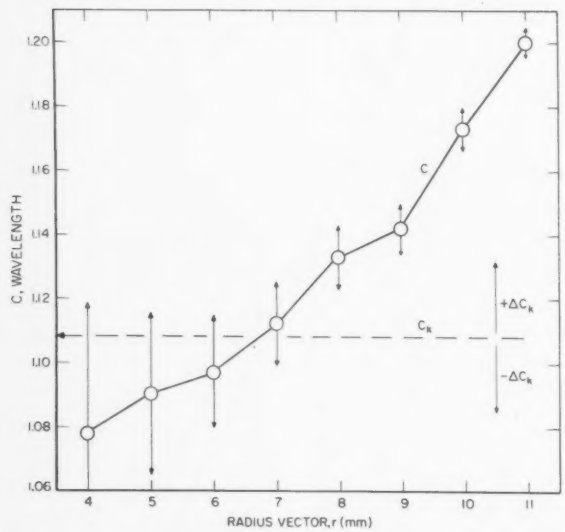

FIGURE 5. *Values of the coefficient of astigmatism, C, versus semi-aperture, r, of the lens.*

The vertical arrows represent computed probable errors in C. The horizontal dashed line represents the value for C obtained from figure 2 and given in footnote 2.

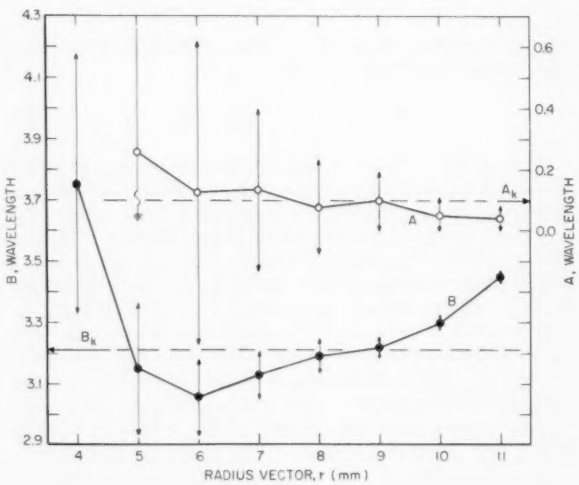

Figure 6. *Values of the coefficients of coma, B (on the left) and spherical aberration, A (on the right) versus the semiaperture, r, of the lens.*

The vertical arrows represent computed probable errors. The horizontal, dashed lines represent values obtained from figure 2 and given in footnote 2.

probable error, ΔB, of B (based on the same assumptions used for obtaining ΔC, above) is indicated by the vertical arrows attached to the corresponding points. The value of B, computed from figure 2, (indicated as B_K in fig. 5), is constant for all families of reference points. This value for B_K is the same as that given by Kingslake for the same lens.

6. Spherical Aberration

Spherical aberration cannot be evaluated from a family of reference points that are equally distant from the origin, as is the case for astigmatism; nor can it be evaluated from a family of four points on the y-axis, as is the case for coma. However, if we choose a family of four points on the x-axis, made up of two pairs such that the two points of each pair are equally distant from some convenient point, x_0 (see fig. 3) but in opposite directions from x_0, then we can obtain an equation for A as a function of the coordinates of these four points alone. Also, if the distance from x_0 to each of the inner pair of points (x_7 and x_8) are one-half the value of those for the outer points (x_1 and x_9), and the outermost point, x_1, is near the margin of the lens, the resultant value for A will be the most precise value obtainable from any such family of points.

The x, y, p-coordinates of the four points are (x_1, y_1, p_1), (x_7, y_7, p_7), (x_8, y_8, p_8), and (x_9, y_9, p_9), where

$$\left.\begin{aligned} &x_1=(8/5)x_7=4x_0=-8x_8=-2x_9=r,\\ &y_1=y_7=y_0=y_8=y_9=0 \end{aligned}\right\}.$$

This family of points has the same relationship to x_0 as the family of points in eq (5) has to the origin (optic axis).

On successively substituting the coordinates of these four points into eq (1) we obtain four equations from which we may obtain the following formula for A:

$$81Ar^4=128[p_1-p_9+2(p_8-p_7)].$$

Values for A, computed for different values of r (i.e., for different apertures) are shown in figure 6, together with the corresponding probable errors, ΔA. The value for A, computed from figure 2 (indicated as A_K in fig. 6), is constant for all values of r. The value A_K is that given by Kingslake for the same lens.

7. Conclusions

The method for obtaining the coefficients of primary, monochromatic aberrations, described here, requires a very small amount of calculations. A 10-in. slide rule is adequate for most work.

The coefficients of all three of the aberrations are found to vary with the aperture of the lens. This indicated that the method is sufficiently precise to evaluate even higher orders of aberrations provided the necessary formula for optical path difference is available.

(Paper 69C4–205)

JOURNAL OF RESEARCH of the National Bureau of Standards—C. Engineering and Instrumentation
Vol. 69C, No. 4, October–December 1965

Comparators for Voltage Transformer Calibrations at NBS

Wilbur C. Sze

(July 28, 1965)

An inductive comparator is described for measuring ratio-correction-factor and phase-angle error of voltage transformers by comparison with reference transformers. The simple circuit utilizes a resistance-capacitance network and an inductive voltage divider. The relative magnitude of the ratio-correction-factors is obtained from the dial readings of the inductive voltage divider, and the phase angle between the voltage phasors is equal to $\pm\omega CR$. The accuracy of these measurements at 60 and 400 hertz is within 2 parts-per-million for ratio and within 10 microradians for phase angle at the limits of the phase-angle range of ± 38 milliradians. Only a few ranges of reference transformers are required since fractional ratios from 1/1 to 1/4 may be measured as readily as ratios near unity, without diminution in accuracy. A general discussion of a resistive comparator, which has been in continuous operation at NBS since 1939, is included.

Key Words: Voltage divider, inductive voltage divider, resistive voltage divider, voltage transformer calibration, ratio-correction-factor, phase-angle errors, voltage transformer comparator, voltage-transformer-test-set, comparator, test-set, calibration.

1. Introduction

The method most widely used by public utilities and standardizing laboratories to determine the ratio and phase angle of voltage transformers is by comparison with calibrated reference transformers. However, it is a relative rather than an absolute method, in that the accuracy of the results obtained depends upon the knowledge of accuracy of the reference transformers [1].[1]

At the NBS laboratories, a group of reference transformers is available by means of which test transformers having any ratio from 1:1 to 2000:1 can be calibrated. The accurate initial establishment of the voltage ratio and phase angle for these reference transformers has been discussed elsewhere and will not be repeated here [2, 3].

The purposes of this paper are (1) to describe the resistive comparator which has been in continuous operation since 1939; (2) to describe a new inductive comparator; and (3) to analyze various factors affecting the accuracy with which measurements can be made.

2. Resistive Comparator

This comparator was designed and constructed at NBS by F. K. Harris and has been in continuous operation since 1939, except for a very brief period during which new switches were installed to replace the worn out original ones [4, 5].

The schematic circuit of this comparator is shown in figure 1.[2] The in-phase voltage balance condition is achieved by adjusting the tap of the resistive divider, and the quadrature voltage, by varying the mutual inductor, M.

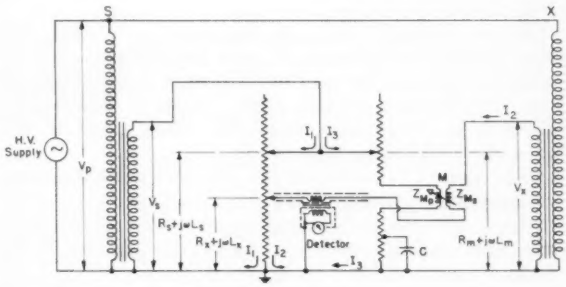

FIGURE 1.

2.1. Description of Components

The R_s and R_m circuits are supplied from the secondary of transformer S. Each can be varied from 2000 to 4000 Ω in increments of 100 Ω. The exact values are determined by the ratios of the test and reference transformers. The 100-Ω and 1000-Ω unit resistors of R_s are of woven wire and mounted on ceramic forms. Thus the residual, L_s, of R_s is reduced to a minimum [6]. The R_m circuit, nominally equal to R_s, include the primary circuit of M which has a d-c resistance of 200 Ω. The capacitor, C, shunting the lower portion of the resistance, serves to compensate for the self-inductance introduced by M [5]. Multiple taps are brought out from R_m to supply the shield potential of corresponding sections of R_s and of the detector circuit [7]. The shielding is shown in figure 4.

As shown in figure 2, the portion of the R_s circuit between 1800 and 2000 Ω carries a continuously adjustable tap, R_x, which is connected through the detector circuit and M to the secondary of the test transformer.

[1] Figures in brackets indicate the literature references at the end of this paper.

[2] Simplified by not showing the shielding arrangements around each segment of R_s.

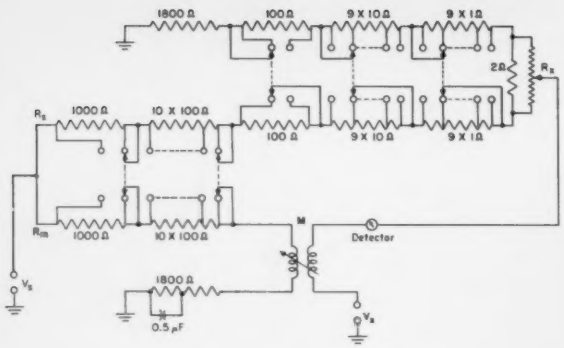

FIGURE 2.

FIGURE 3.

The mutual inductor used in this circuit consists of a 10×20 mH per section unit (± 200 mH maximum) and a continuously adjustable inductometer (± 25 mH maximum) [8, 9].

Both the R_s/R_x ratio of the resistive divider and the mutual inductance, M, are periodically redetermined to insure that maximum accuracy is maintained for transformer testing. The residual reactances, L_s and L_x, were also accurately determined at the time the comparator was built.

The design is such that the resistors must dissipate considerable power. Therefore, the entire resistive divider, R_s and R_m, is immersed in oil to minimize the effect of temperature coefficient on the R_s/R_x ratio.

The detector circuit consists of a doubly shielded impedance-matching transformer (1000–4000 turns) and a wave-analyzer used as a tuned null detector.

2.2. Comparator Desk

Figure 3 shows the general layout of the desk. The resistive divider is located to the right with the R_s adjustment dials in the back and the R_x dials in front. The step mutual inductor and the inductometer are located in the left portion of the desk. The detector is in the rear right. Since this comparator is adaptable for calibrating voltage-transformer-test-sets, the panel shown at the lower left side of the desk is for arranging the connections for calibrating either transformers or test-sets. Figure 4 shows the internal wiring of the resistive divider and the individual shields around units of R_s.

2.3. Theoretical Relations

The equations for obtaining the ratio-correction-factor and phase-angle error are developed as follows. By definition, the voltage ratio of a transformer is the ratio of the primary terminal voltage to the secondary terminal voltage so that

$$\frac{|V_{\text{Pri}}|}{|V_{\text{Sec}}|} = N' = Nf$$

where N' is the actual voltage ratio, N the nominal ratio, and f the ratio-correction-factor. If θ represents the angle between the primary and reversed secondary voltage phasors, then

$$V_s = \frac{|V_p|}{N'_s} (\cos \theta_s + j \sin \theta_s)$$

and [3]

$$V_x = \frac{|V_p|}{N'_x} (\cos \theta_x + j \sin \theta_x)$$

By inspection of figure 1, the following mesh current equations are obtained

$$V_s = I_1 Z_s + I_2 Z_x$$

$$V_x = I_1 Z_x + I_2 (Z_x + Z_{Ms}) + I_3 j\omega M$$

$$V_s = I_2 j\omega M + I_3 Z_m$$

[3] Subscripts s and x denote that the symbols refer to the reference or test transformers, respectively.

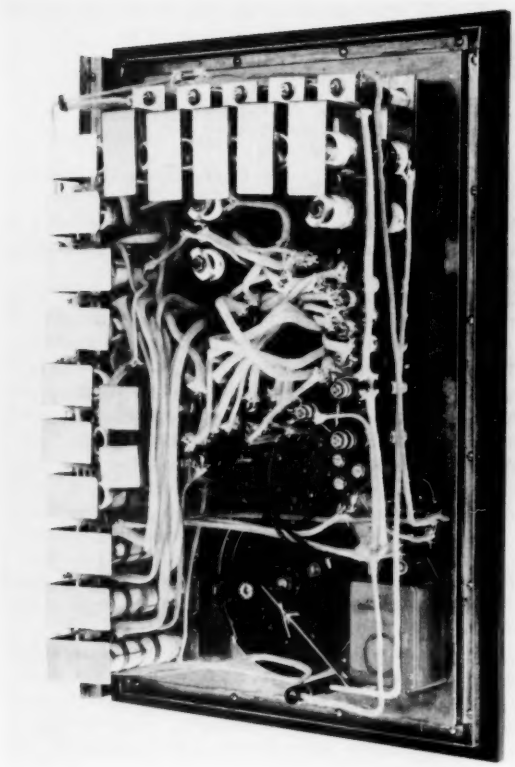

FIGURE 4.

$I_2=0$ when a null is indicated on the detector, then

$$V_s=I_1Z_s=I_3Z_m$$

and

$$V_x=V_s\left(\frac{Z_x}{Z_s}+\frac{j\omega M}{Z_m}\right)$$

Since $Z_m=R_m$ by the addition of C, and $R_m=R_s$ nominally, the balance equation becomes

$$\frac{(\cos\theta_x+j\sin\theta_x)}{N_xf_x}=\frac{(\cos\theta_s+j\sin\theta_s)}{N_sf_s}\left\{\frac{R_x}{R_s}\left[1+j\omega\left(\frac{L_x}{R_x}-\frac{L_s}{R_s}+\frac{M}{R_x}\right)\right]\right\}$$

and on separation

$$f_x=\frac{N_sR_s}{N_xR_x}\left(\frac{f_s\cos\theta_x}{\cos\theta_s-\sin\theta_s\omega\left(\frac{L_x}{R_x}-\frac{L_s}{R_s}+\frac{M}{R_x}\right)}\right)$$

$$\approx\frac{N_sR_s}{N_xR_x}+(f_s-1)+\frac{1}{2}(\theta_s^2-\theta_x^2)$$

and [4]

$$\theta_x=\theta_s+\omega\left(\frac{L_x}{R_x}-\frac{L_s}{R_s}+\frac{M}{R_x}\right)\text{ radians}$$

As previously indicated, R_s and R_m circuits constitute a burden on the reference transformer. Therefore, f_s and θ_s are determined with these burdens.

The design of the divider is such that the balance conditions require

$$\frac{N_x'}{N_s'}=\frac{R_s}{R_x}\geq 1,$$

this requirement is met by using reference transformers whose voltage ratios have been adjusted to values 2 percent less than the integral values usually encountered as nominal ratios in instrument transformers.

The minimum resolution of this setup is such that the precision for ratio measurements is 2 ppm and for phase angle, 15 μrad at 25 and 60 Hz. However, susceptibility of the mutual inductor to the gradients of stray magnetic fields, large residuals and uncertainty in ratio calibration of the resistive divider limit the accuracy of these measurements to 10 ppm and 60 μrad, respectively. These errors increase rapidly with frequency. Therefore, this comparator is not suitable for accurate calibrations beyond 60 Hz.

3. Inductive Comparator

This comparator avoids a number of the objectionable features of the resistive comparator. The shielding is simple and is easily accomplished; the method is capable of extension to cover the audio-frequency range; the apparatus is less bulky and requires very little power for operation; the components are inherently more accurate and stable and readily available commercially; the ratio difference is indicated directly on the decade dials; and the set (except the detector) is self-contained in one portable case.

The schematic diagram of the circuit is shown in figure 5, which indicates the positions of resistor, R, and detector when the voltage phasor of the test transformer, X, leads that of the reference transformer, S. For lagging angles, the positions of R and detector are

[4] The (f_s-1) and θ_s for the NBS reference transformers are very small. Therefore, the approximations made are justifiable.

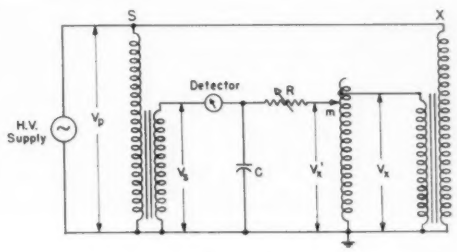

FIGURE 5.

simply interchanged. The in-phase voltage balance is obtained by adjusting the tap on the inductive voltage divider, and the quadrature voltage balance is obtained by adjusting either the resistor or the capacitor.

3.1. Theoretical Relations

As previously defined, the voltage ratio is

$$\frac{|V_{\text{Pri}}|}{|V_{\text{Sec}}|}=N'=Nf,$$

$$V_s=\frac{|V_p|}{N_s f_s}(\cos\theta_s+j\sin\theta_s),$$

and

$$V_x=\frac{|V_p|}{N_x f_x}(\cos\theta_x+j\sin\theta_x)=\frac{V'_x}{m},$$

m being the actual ratio of the inductive voltage divider. Corrections to the ratios and the phase angles of the inductive voltage divider used are insignificant and can be neglected. Then from figure 5,

$$\frac{V_s}{V'_x}=\frac{1-j\omega CR}{1+\omega^2C^2R^2}\approx 1-\omega^2C^2R^2-j\omega CR$$

The balance equation of the circuit becomes

$$\frac{N_x f_x(\cos\theta_s+j\sin\theta_s)}{mN_s f_s(\cos\theta_x+j\sin\theta_x)}=1-\omega^2C^2R^2-j\omega CR$$

and on separation and by neglecting second order terms

$$\theta_x=\frac{N_x f_x}{mN_s f_s}(\theta_s+\omega CR+\theta_s\omega^2C^2R^2)\approx\theta_s+\omega CR$$

radians, and

$$f_x=\frac{mN_s f_s}{N_x}\left(\frac{\cos\theta_x-\omega^2C^2R^2+\omega CR\sin\theta_x}{\cos\theta_s}\right)$$

$$\approx\frac{mN_s}{N_x}+(f_s-1)-\frac{1}{2}(\omega CR)^2$$

For relative lagging phase angle, with the detector and resistor, R, interchanged,

$$\theta_x\approx\theta_s-\omega CR \text{ radians, and}$$

$$f_x\approx\frac{mN_s}{N_x}+(f_s-1)+\frac{1}{2}(\omega CR)^2$$

3.2. Loading Effects

Since the input impedance of the inductive voltage divider at 60 Hz is in excess of 0.8 MΩ (nearly 1.00 power factor), the effect of loading of the f_x and θ_x of the test transformer can be expressed as

$$\left(\frac{\text{Equivalent Total Impedance Referred to Transformer Secondary}}{\text{(External Impedance)}}\right)$$

$$=(\text{Correction to } f_x \text{ and } \theta_x).$$

A transformer with an equivalent resistance of 1 Ω (which is easily measurable) will result in a correction of approximately 1 ppm [5].

The effect of loading by the quadrature balancing network on either the inductive voltage divider or the reference transformer is usually insignificant. At the limits of phase-angle range of ±37.8 mrad (130 min), the correction to ratio and phase angle of the inductive voltage divider is ~1 ppm and < 4 μrad, respectively; or, to the reference transformer, << 1 ppm and << 1 μrad.

3.3. Description of Components

All the components in this circuit are readily available commercially or accessible in most testing laboratories. In figure 5, R is a 0–10 kΩ, 10-turn, continuously adjustable resistor with small residual reactance. C is a 10 × 1 nF decade capacitor with a dissipation factor of < 0.0003. Both R and C were calibrated before and after assembly. The deviations from nominal values were found to be within 5 Ω and 5 pF, respectively.

The inductive voltage divider is a six-decade unit designed for optimum performance at 60 Hz.[5] For tests at higher frequencies (up to 1 kHz), it can easily be replaced by a unit of appropriate design, or by application of appropriate loading corrections to the ratio-correction-factor and phase angle. However, due to the simplicity of the circuitry and infrequent requests for calibrations at higher frequencies, a tem-

[5] Since maximum voltage on this divider is limited to 150 V at 60 Hz, it must be connected across the test transformer rather than the reference transformer whose secondary voltage may exceed this value in some instances.

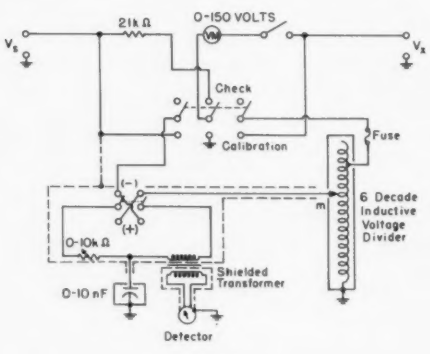

FIGURE 6.

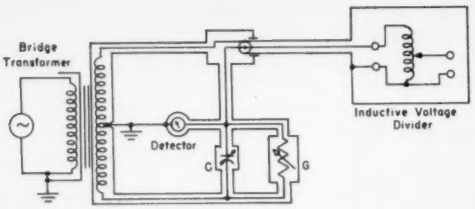

FIGURE 7.

porary setup is generally used at NBS. This consists of a high frequency divider, commercially available air capacitors, and an a-c decade resistor.

The input impedance of the inductive voltage divider was measured in a capacitive voltage divider setup; see figure 7 for circuit diagram [10]. The voltage-ratio corrections and phase-angle errors were obtained by a tracking method [11]. However, for a well designed inductive voltage divider, these corrections are usually < 0.2 ppm of input in ratio linearity deviation and < 8 μrad of input in phase deviation.

The detector circuit consists of a wave-analyzer used as a tuned null indicator and a specially constructed shielded transformer, shown in figure 6. This transformer is used to match impedances and to isolate the measuring circuit from the detector circuit electrostatically. It consists of a high permeability toroidal core, a 700-turn inner primary winding, two electrostatic shields, a 3500-turn outer secondary winding, and an overall Mu-metal case. The use of a toroid minimizes the magnetic pickup from stray fields in the laboratory.

The polarity checking voltmeter is a 0–150 V, 3-in. panel-type instrument of 3 percent accuracy. The 21 kΩ resistor matches its internal resistance. The voltmeter indicates the secondary voltage of the test transformer when the selector switch is in the "CALIBRATION" position.

Figures 8 and 9 show the exterior and interior of the comparator. The cylindrical shield shown in the interior view encloses the 10-kΩ resistor.

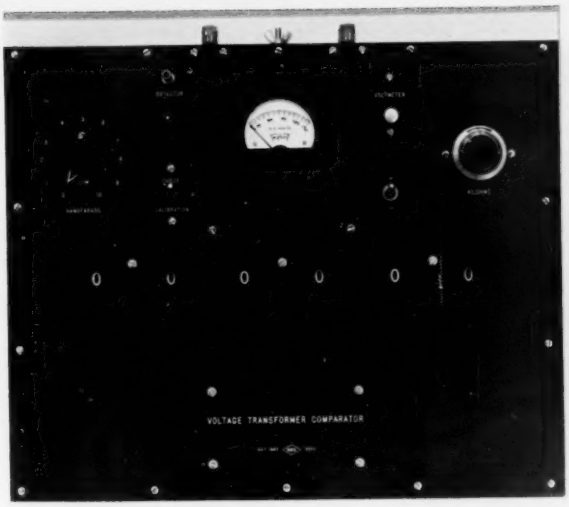

FIGURE 8.

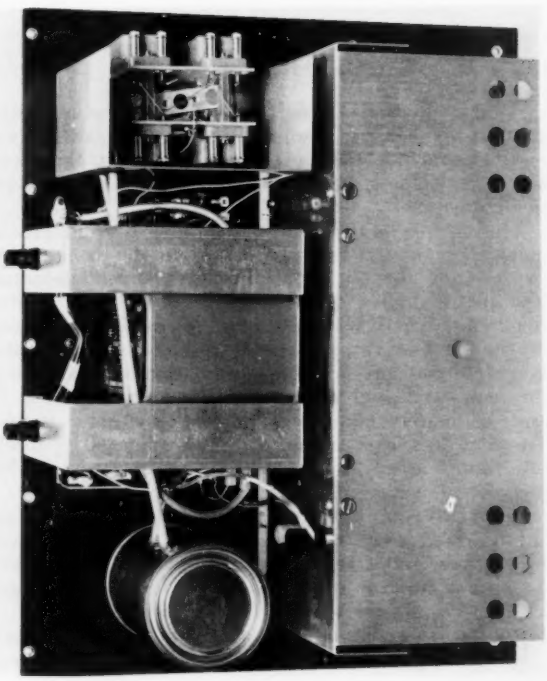

FIGURE 9.

3.4. Accuracy Determination

After the completion of the comparator, the calibration of each component was rechecked.

The accuracy of the completed comparator was verified by the following procedures: (1) connecting a single voltage source to both "V_s" and "V_x" terminals to obtain the zero corrections for C and R and the unity correction for dial settings of the inductive voltage divider; (2) calibrating several pairs of transformers of the same ratio to reference transformers of appropriate ratios, thus determining the relative ratio-correction-factors and phase-angle errors with several values of secondary burden for each pair of transform-

784-657 O-65-2

ers; (3) comparing each pair of these calibrated transformers to each other with the comparator alternately as reference and test units and with various combinations of previously used secondary burdens; and (4) connecting a single voltage source to "V_x" terminals and to the input of a calibrated inductive voltage divider, whose output is connected to "V_s" terminals in order to check the fractional ratio measurements.

3.5. Transformer Testing Procedure

A reference transformer is selected so that $N_s \geq N_x$. The selector switch is set to "CHECK" position; and the ratio, m, is set to equal N_x/N_s. The secondaries of the test and reference transformers are connected to "V_x" and "V_s" terminals respectively. With the transformers energized and the voltmeter switch depressed, the voltmeter indicates $(V_s - V_x)/2$ if the polarities of V_s and V_x are correctly connected to the comparator. [The polarity of V_x must be reversed if voltmeter indicates $(V_s + V_x)/2$.] The test proceeds with the selector switch turned to "CALIBRATION." V_x is now indicated on the voltmeter.

If $N_x > N_s$ by more than 10 percent, the test can still be made, but the reference transformer must be connected to "V_x" terminal and the test transformer to "V_s". At the balanced condition, the ratio, m, will indicate the reciprocal of the relative ratio-correction-factors, and the relative phase-angle switch will show the negative of the markings as shown in figures 6 and 8.

3.6. Consideration of Errors

An examination of errors requires a careful appraisal of all components of the measuring circuit as well as a justification of estimations, even though in this case one would expect most of the associated errors to be negligible.

The first to be considered are those possible errors concealed through approximation in developing the expressions for obtaining the ratio-correction-factor and phase-angle relations, where the effects of the residual of the 10-kΩ resistor and the dissipation factor of the decade capacitor are ignored. Approximate magnitudes of these errors can be obtained by adding the estimated equivalent residual reactance across R and estimated equivalent series resistance to C. These effects were found to be less than 0.5 ppm for ratio and 5 μrad for phase angle at the limits of the phase angle range (±38 mrad) at 60 Hz.

A second source of uncertainty is in the calibration of the inductive voltage dividers. However, past experience indicates that errors should not exceed 0.2 ppm of input in ratio linearity deviation and 2 μrad of input in phase deviation [12].

Errors caused by the leads, switch contacts, and imperfect shields are estimated to be < 0.5 ppm and < 2 μrad.

The last important uncertainty that should be considered is in obtaining the transformer secondary load corrections. Such errors are estimated to be 0.5 ppm and 3 μrad for each transformer.

Finally, one should add 3 times the standard deviations (0.3 ppm of ratio and 1 μrad) of the results obtained in repeated balances of the comparator to the combination of the systematic-error estimates.

Source of errors	Uncertainties to ratio-correction-factor		Uncertainties to phase angles	
	n	n^2	n	n^2
	ppm		μrad	
From assumptions made in equations	0.5	0.25	5	25
Calibration of the inductive voltage divider	.2	.04	2	4
Obtaining secondary load corrections (S)	.5	.25	3	9
Obtaining secondary load corrections (X)	.5	.25	3	9
Leads and contacts	.5	.25	2	4
Σn^2		1.04		51
$(\Sigma n^2)^{1/2}$	1.02		7.1	
3 × standard deviations	0.90		3.0	
Maximum error	1.9 ppm		10.1 μrad	

4. Conclusion

A high accuracy inductive comparator has been developed for measuring the relative voltage ratio and phase angle of voltage transformers and testing sets at power and audio frequencies. An overall accuracy of < 2 ppm in ratio measurements and < 10 μrad in phase angle at 60 and 400 Hz is achieved, with a slight reduction in the accuracy attainable at higher audio frequencies.

The simple circuit does not require any special equipment. Only a few ranges of reference transformers are required, since fractional ratios from 1/1 to 1/4 may be measured as readily as ratios near unity.

This inductive comparator could replace testing sets now in general use. It is compact and portable, has a broader useful frequency range, and exceeds the accuracy of many commercial sets presently available by one or two orders of magnitude.

The resistive comparator will continue to be used at NBS for calibration of voltage transformers at 25 Hz at which frequency the operating voltage is usually above the maximum operating voltage of the inductive comparator.

The author acknowledges the valuable help and advice received from Mr. F. L. Hermach, Chief, Electrical Instrument Section, NBS. Mr. R. J. Berry contributed skillfully in constructing the new comparator.

5. References

[1] F. B. Silsbee and F. M. Defandorf, A transformer method for measuring high alternating voltages and its comparison with an absolute electrometer, J. Res. NBS 20, 317–336 (1938) RP1079.

[2] W. K. Clothier and L. Medina, The absolute calibration of voltage transformers, Proc. Institution of Electrical Engineers, **104A**, 204–214 (1957).

[3] F. K. Harris, W. C. Sze, N. L. Kusters, O. Petersons, W. J. M. Moore, An international comparison of voltage transformer calibrations to 350 kV, IEEE Trans. on Communication & Electronics No. 70, pp. 13–19 (1964).

[4] Private communication from F. K. Harris, Chief, Absolute Electrical Measurements Section, NBS.

[5] F. K. Harris, Electrical Measurements (John Wiley and Sons, Inc., New York, N.Y.) pp. 410–411, 565–569 and 611–612 (1951).

[6] W. Duddell and T. Mather, Improvements in non-inductive resistance, British Patent No. 5171 (1901).

[7] F. B. Silsbee, A shielded resistor for voltage transformer testing, Bull. BS **20**, 489–514 (1926).

[8] Private communication from F. K. Harris and B. L. Dunfee, NBS.

[9] H. B. Brooks and A. B. Lewis, Improved continuously variable self and mutual inductor, J. Res. NBS **19**, 493 (1937) RP1040.

[10] M. C. McGregor, J. F. Hersh, R. D. Cutkosky, F. K. Harris and F. R. Kotter, New apparatus at NBS for absolute capacitance measurement, IRE Trans., Instr., **I-7**, 253–261 (1958).

[11] NBS Technical News Bulletin, **49**, 1 (1965).

[12] W. C. Sze, A. F. Dunn, and T. L. Zapf, An international comparison of inductive voltage divider calibrations at 400 and 1000 hertz, IEEE Trans. on Instr. and Meas. **IM-14**, No. 3, 124–131 (1965).

(Paper 69C4–206)

JOURNAL OF RESEARCH of the National Bureau of Standards—C. Engineering and Instrumentation
Vol. 69C, No. 4, October–December 1965

Voltage Dependence of Precision Air Capacitors

J. Q. Shields

(August 1, 1965)

Methods are presented for measuring both the relative and absolute voltage dependence of admittance standards. The practical circuits based on the methods are composed of precision bridges which are described in detail. Measurements with these circuits yield values for the proportional changes in admittance which result from specified changes in voltage. The results of measurements on selected capacitors are presented. Uncertainties are of the order of one part in 10^9.

A general instability in the voltage dependence of precision air capacitors was observed at the higher accuracy levels. Most of the instability is believed to be caused by changes in the electrode surfaces.

Key Words: Bridge, capacitor, coaxial choke, difference transformer, electrode surfaces, thin films, three-terminal, transformer, voltage coefficient, voltage dependence, voltage ratio.

1. Introduction

Several years ago a computable cross capacitor, based on a theorem by A. M. Thompson and D. G. Lampard [1],[1] was constructed at NBS [2]. The value of this capacitor is computable, in esu, within an estimated accuracy of 2 parts per million (ppm). A new cross capacitor of improved design is now being constructed. It is expected that this capacitor will be computable, in esu, within a few parts in 10^8 or better.

The expected increase in accuracy not only requires better bridges and capacitors, but also requires that many sources of error be reevaluated. One such source of error is the voltage dependence of precision air capacitors.

To meet our particular needs, the quantity chosen as a measure of voltage dependence is termed γ and is defined by the equation

$$Y_2 = Y_1(1+\gamma)$$

where Y_1 is the admittance of a given standard at voltage V_1, Y_2 is the admittance of the same standard at voltage V_2, and the condition $V_2 > V_1$ is imposed to restrict the meaning of γ. A given standard may have any number of values of γ, each with a specified voltage change. Since γ represents a proportional change in admittance ($\Delta Y/Y$), this measure of voltage dependence is in the preferred form for corrections to precision measurements.

In the past, most measurements of voltage dependence have been confined to a determination of the ratio, $(1+\gamma_a)/(1+\gamma_b)$, where γ_a and γ_b apply to different capacitors but have the same specified voltage change. One exception to the above is the work of N. L. Kusters and O. Petersons [3]. They developed a method for measuring the voltage dependence of an individual capacitor, provided the voltage dependence results only from electrode deflections.

The accuracy requirements described earlier resulted in the need for a method which would be independent of the mechanisms which cause voltage dependence. Such a method is described in section 2. The method yields values of γ corresponding to a change in voltage from V to $2V$, where V is a variable.

The practical circuits based on the method are described in sections 3 and 4. These circuits were used to measure values of γ for several capacitors corresponding to the following voltage changes: 12.5 to 25, 25 to 50, 50 to 100, and 100 to 200 V, rms, at 1592 Hz. Measurement uncertainties had to be kept small since the above values of γ are used to calculate other values of γ in different voltage ranges such as from zero to 200 V. The latter value is needed for the determination of the absolute unit of capacitance. Small uncertainties also provide the means for quickly detecting instabilities in the voltage dependence of capacitors. It was found that the voltage dependence of precision air capacitors was, in general, unstable at the accuracy level described. This subject is discussed in section 5.

2. Theory

One method for measuring the voltage ratio of a transformer is to connect admittance standards to the transformer so as to form a bridge as shown in figure 1 [4]. In general, if the transformer has a nominally $m:n$ ratio, then $m+n$ nominally equal admittances are used, and $m+n$ detector balances are required corresponding to a cyclic permutation of these admittances. In this sequence of balances each admittance appears with voltage E_1 m times, and with voltage E_2 n times. If $E_1 \neq E_2$, a ratio measurement error results since the admittance of a practical standard changes when the voltage applied to it

[1] Figures in brackets indicate the literature references at the end of this paper.

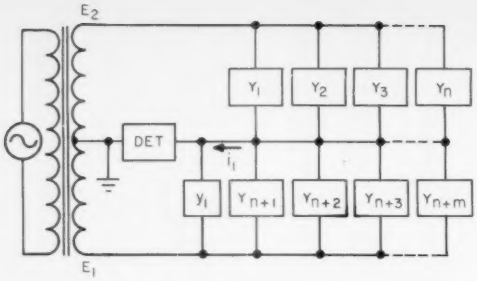

FIGURE 1. *Circuit for measuring the voltage ratio of a transformer* [4].

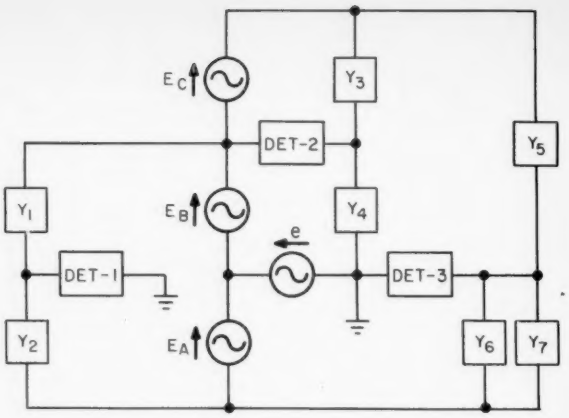

FIGURE 2. *Basic three-bridge-circuit.*

is changed. The difference between the measured ratio and the true ratio is related to the average change in admittance of the standards.

If the transformer ratio can be determined from a second set of measurements which is independent of voltage, the combination of the two sets of measurements will yield a value for the average change in admittance of the $m+n$ standards corresponding to a change in voltage from E_1 to E_2. The change in admittance of each standard can then be determined by measuring the relative changes between various pairs of standards.

The basis of this paper is a method of the type described above in which the second set of measurements consists of determining a group of 1:1 ratios which can be combined to determine the $m:n$ ratio of a transformer. For simplicity, a transformer having a 2:1 ratio was chosen so that only two 1:1 ratios need be determined.

It is assumed that taps are brought out from the secondary winding of a bridge transformer [5] so as to obtain three secondary voltages of approximately equal magnitude. These voltages are represented by E_A, E_B, and E_C in figure 2. The circuit shown in figure 2 consists of three bridges, each of which may be balanced, in turn, by the small, adjustable voltage e. For the case in which the circuit elements are closely matched, $e/E_A \equiv q \ll 1$, and only a low accuracy calibration of q is needed for high accuracy determinations of ratios such as E_B/E_A.

It is assumed that the changes in $Y_1, Y_2, Y_3 \ldots Y_7$ which result from changes in e can be neglected. Following from this, we may consider the voltages applied to Y_5, Y_6, and Y_7 to be either E_A or $2E_A$ and define the values of Y_5, Y_6, and Y_7 to be Y_5', Y_6', and Y_7' at voltage E_A, and $Y_5'(1+\gamma_5)$, $Y_6'(1+\gamma_6)$, and $Y_7'(1+\gamma_7)$ at voltage $2E_A$.

The balance equations for bridge 1 are

$$\frac{Y_1}{Y_2}=\frac{E_A-e_1}{E_B+e_1}=\frac{1-q_1}{1+\delta_B+q_1} \tag{1}$$

$$\frac{Y_2}{Y_1}=\frac{E_A-e_2}{E_B+e_2}=\frac{1-q_2}{1+\delta_B+q_2} \tag{2}$$

where $\dfrac{E_B}{E_A}\equiv 1+\delta_B$. Eliminating Y_1 and Y_2, we obtain

$$\delta_B=-(q_1+q_2). \tag{3}$$

The balance equations for bridge 2 are

$$\frac{Y_3}{Y_4}=\frac{E_B+e_3}{E_C}=\frac{1+\delta_B+q_3}{1+\delta_C} \tag{4}$$

$$\frac{Y_4}{Y_3}=\frac{E_B+e_4}{E_C}=\frac{1+\delta_B+q_4}{1+\delta_C} \tag{5}$$

where $\dfrac{E_C}{E_A}\equiv 1+\delta_C$. Eliminating Y_3 and Y_4, we obtain

$$\delta_C=\frac{q_3+q_4+2\delta_B}{2}+\epsilon_1 \tag{6}$$

where ϵ_1 is a small correction term consisting of second and higher order terms in q.

The balance equations for bridge 3 are

$$\frac{Y_5'(1+\gamma_5)}{Y_6'+Y_7'}=\frac{E_A-e_5}{E_B+E_C+e_5}=\frac{1-q_5}{2+\delta_B+\delta_C+q_5} \tag{7}$$

$$\frac{Y_6'(1+\gamma_6)}{Y_7'+Y_5'}=\frac{E_A-e_6}{E_B+E_C+e_6}=\frac{1-q_6}{2+\delta_B+\delta_C+q_6} \tag{8}$$

$$\frac{Y_7'(1+\gamma_7)}{Y_5'+Y_6'}=\frac{E_A-e_7}{E_B+E_C+e_7}=\frac{1-q_7}{2+\delta_B+\delta_C+q_7}. \tag{9}$$

Eliminating Y_5', Y_6', and Y_7', we obtain

$$\bar{\gamma}=-\frac{\delta_B+\delta_C+q_5+q_6+q_7}{2}+\epsilon_2. \tag{10}$$

where

$$\bar{\gamma}\equiv\frac{\gamma_5+\gamma_6+\gamma_7}{3} \tag{11}$$

and ϵ_2 is a small correction term consisting of second and higher order terms in q and γ.

Solving eqs (3), (6), and (10), we obtain

$$\bar{\gamma}=\frac{4q_1+4q_2-q_3-q_4-2q_5-2q_6-2q_7}{4}-\frac{\epsilon_1-2\epsilon_2}{2}. \quad (12)$$

In order to separate real and imaginary parts, let

$$\gamma \equiv \gamma' - j\gamma'' \quad (13)$$

and

$$q \equiv q' - jq'' \quad (14)$$

so that

$$\bar{\gamma}'=\frac{4q_1'+4q_2'-q_3'-q_4'-2q_5'-2q_6'-2q_7'}{4}-\frac{\epsilon_1'-2\epsilon_2'}{2} \quad (15)$$

and

$$\bar{\gamma}''=\frac{4q_1''+4q_2''-q_3''-q_4''-2q_5''-2q_6''-2q_7''}{4}-\frac{\epsilon_1''-2\epsilon_2''}{2} \quad (16)$$

For the capacitors and accuracies described in this paper, γ' is equal to the proportional change in capacitance ($\Delta C/C$), and γ'' is equal to the change in dissipation factor, corresponding to a specified increase in voltage.

The values of γ_5, γ_6, and γ_7 can be separated from the value of $\bar{\gamma}$ by measuring the differences, $\gamma_5-\gamma_6$, $\gamma_6-\gamma_7$, and $\gamma_7-\gamma_5$. Measurements of this type are described in section 4. Combining the differences, we obtain

$$\gamma_5=\bar{\gamma}+(\gamma_5-\gamma_6)/3-(\gamma_7-\gamma_5)/3 \quad (17)$$

$$\gamma_6=\bar{\gamma}+(\gamma_6-\gamma_7)/3-(\gamma_5-\gamma_6)/3 \quad (18)$$

$$\gamma_7=\bar{\gamma}+(\gamma_7-\gamma_5)/3-(\gamma_6-\gamma_7)/3. \quad (19)$$

3. Practical Three-Bridge-Circuit

The method described in the previous section was used to determine the voltage dependence of three 100 picofarad (pF) air capacitors, designated 100A, 100B, and 100C. This section describes the equipment and techniques used to determine the values of

$$\bar{\gamma}_{100} \equiv \frac{\gamma_{100A}+\gamma_{100B}+\gamma_{100C}}{3} \quad (20)$$

corresponding to the following voltage changes: 12.5 to 25, 25 to 50, 50 to 100, and 100 to 200 V, rms, at 1592 Hz.

If small capacitors are to be well defined, they must be shielded. The addition of shielding to the circuit of figure 2 is shown in figures 3a, 3b, and 3c. Each of the admittance standards represented in figures 3a, 3b, and 3c consists of a completely shielded three-terminal air capacitor connected to a pair of coaxial cables. The defining terminals of each standard are located at one of the detector junctions and at one of the coaxial connectors designated a, b, c . . . g.

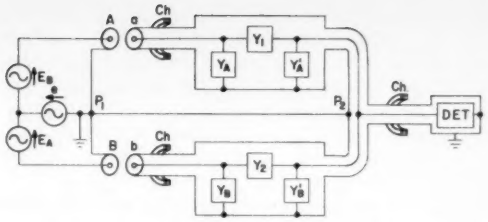

FIGURE 3a. *Bridge 1 of the practical three-bridge-circuit.*

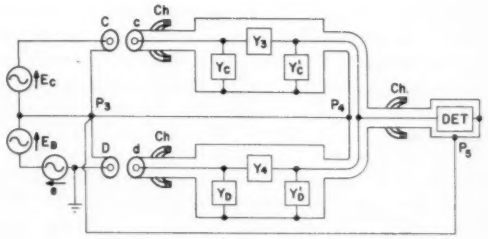

FIGURE 3b. *Bridge 2 of the practical three-bridge-circuit.*

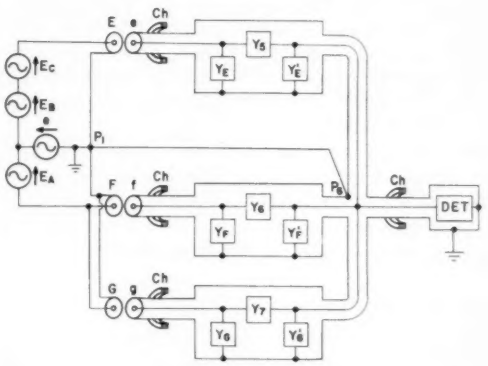

FIGURE 3c. *Bridge 3 of the practical three-bridge-circuit.*

The required circuits are obtained by joining connectors a, b, c . . . g to connectors, A, B, C . . . G in various configurations. When connector a is joined to connector A and b to B, the balance equation is given by equation (1), section 2. When a is joined to B and b to A, the balance equation is given by eq (2). Similarly, eqs (4) and (5) are applicable to figure 3b and eqs (7), (8), and (9) are applicable to figure 3c. For purposes of evaluating the effects of self and mutual impedances in the leads (not shown in the figures), it will initially be assumed that: (1) net cur-

rents through the "coaxial chokes" [6], designated Ch in the figures, are negligibly small, (2) the voltages at connector A are, to sufficient accuracy, independent of whether A is joined to a or to b, and similarly for the voltages at connectors B, C, D . . . G, (3) only negligible effects result from externally induced emfs and external loading, e.g., capacitance from the bridge shielding to its surroundings.

Subject to the above assumptions, the two values of e corresponding to the two balance conditions for bridge 1 yield a measure of the voltage ratio, V_A/V_B where V_A is the voltage between the inner and outer terminals of connector A with $e=0$ and V_B is the voltage between the inner and outer terminals of connector B with $e=0$. Similarly, a measure of the voltage ratios, V_C/V_D and V_E/V_F are obtained using bridges 2 and 3, respectively. The value of $\bar{y}_{100}$ is calculated from the measured values of V_A/V_B, V_C/V_D, and V_E/V_F. It is assumed that the relationship between voltages V_A, V_B, V_C . . . V_G is known. Ideally, the voltage drops in the leads which precede connectors A, B, C . . . G should be zero, but if the voltage drops are small, eq (12) is sufficiently accurate when the relationship between the voltages is as follows: $V_A=-V_D$, $V_B=V_F=V_G$, $V_E=V_A+V_C$. Since voltage ratios rather than voltages are measured, other satisfactory relationships between the voltages can be described, e.g., V_C and V_D can each be changed if V_C/V_D remains unchanged. Thus, the error in the measurement of $\bar{y}_{100}$ which results from voltage drops in the leads will be small if the impedances in the leads which join various terminals of connectors A, B, C . . . G are small or properly matched. These features are present in the junction box shown within broken lines in figure 4. Parallel lines represent copper strips separated by thin strips of insulation.

The error in the measurement of $\bar{y}_{100}$ resulting from lead impedances within the junction box and resulting from contact impedances between connectors A, B, C . . . G and connectors a, b, c . . . g was found to be approximately 1×10^{-9}. Most of this error was corrected for by changing the currents at the terminals of connectors a, b, c . . . g and observing the change in the measured value of $\bar{y}_{100}$. Since the current at the inner or outer terminal of connector a was nearly proportional to the internal load, Y_1+Y_A, and similarly for the currents at the terminals of b, c, d, . . . g, the following procedure was used: (1) Y_A, Y_B, Y_C . . . Y_G were adjusted so that each of the seven internal loads, Y_1+Y_A, Y_2+Y_B, Y_3+Y_C . . . Y_7+Y_G, were increased by a known factor, (2) the change in the measured value of $\bar{y}_{100}$ was used to calculate a third value of $\bar{y}_{100}$ corresponding to the internal loads being zero. The above procedure amounts to an extrapolation of the effect of internal loads to zero.

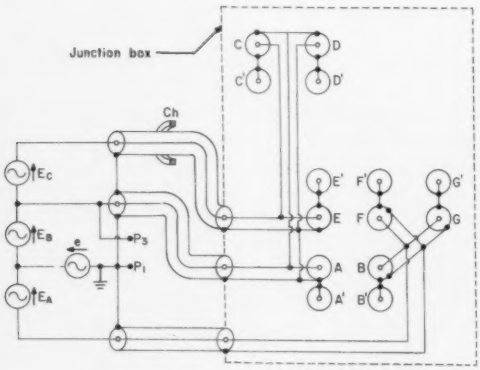

FIGURE 4. *Source of bridge voltages.*
Junction box (within broken lines) connected by coaxial cables to an "active direct-reading ratio set" [7].

The internal loads were measured by disconnecting A, B, C . . . G from a, b, c . . . g, shorting the detectors, and measuring the two-terminal admittances between the inner and outer terminals of connectors a, b, c . . . g. Since the lead impedances within the junction box were small, low accuracy measurements were sufficient for purposes of extrapolating the internal loads to zero. The larger equivalent lead impedances in that portion of the circuit which preceded the junction box (see fig. 4) required that more accurate measurements be made for purposes of adjusting Y_B, Y_D, Y_F, and Y_G so that $Y_1+Y_A=Y_2+Y_B$, $Y_3+Y_C=Y_4+Y_D$, and $Y_5+Y_E=Y_6+Y_F=Y_7+Y_G$. The accuracy of adjustment needed was determined by connecting additional loads between the inner and outer terminals of A, B, C . . . G, each in turn, and noting the changes in e required to rebalance the bridges. It was found that if the internal loads were adjusted within $\pm1\times10^{-9}$ mho, the voltages at connector A were, to sufficient accuracy, independent of whether A was joined to a or to b, and similarly for the voltages at B, C, D . . . G.

The coaxial chokes used consisted of a number of turns of the coaxial cable threaded through a high permeability core. The resulting impedance to net current in the cable was about 400 Ω at 1592 Hz. Since the impedance in the path, $P_1-A-a-P_2$, of figure 3a was about 0.1 Ω, net current through the coaxial choke was of the order of a few parts in 10^4 of the current in the inner or outer conductor of the cable [6]. The impedances in the paths, P_1-A-a and P_1-B-b, differed by less than 2 mΩ. The maximum internal load was about 3000 pF.

Thus far in the discussion the effects of externally induced emfs and external loading have been neglected. Although these effects were small in the practical circuit used, they were not negligible. Appropriate corrections were determined from additional measurements which consisted of recording the unbalance at the detectors when the admittance standards of each bridge, in turn, were joined to the shorting connectors, A', B', C', . . . G', (see fig. 4) while the other standards were joined to A, B, C, . . . G. Since the accuracy of the corrections depended on the size of the unbalance at each detector, it was desirable for the effects of externally induced emfs and external loads to be small. The techniques used to reduce these effects will be considered next.

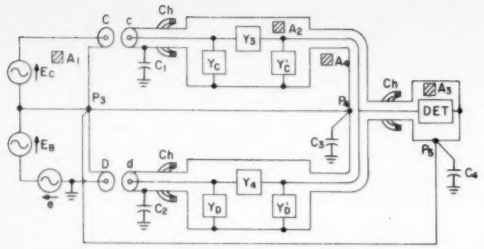

FIGURE 5. *Bridge 2 redrawn to illustrate external loads and sources of induced emf.*

Bridge 2 has been redrawn in figure 5 for purposes of illustrating the different types of induced emf's and external loads. Since the shielding of bridge 2 is not at ground potential, the largest external loads are associated with this bridge. External loads are represented by C_1, C_2, C_3, and C_4 in figure 5. Induced emfs are represented indirectly by showing areas in which a time-varying magnetic flux is assumed to exist. These areas are designated A_1, A_2, A_3, and A_4 in figure 5.

Most of the flux through A_1 existed in the region preceding the junction box and thus had no effect on the measured value of $\overline{Y}_{100}$. Flux through A_2 was reduced by using coaxial cables of sufficient length so that the three-terminal capacitor could be positioned at a distance from sources of appreciable magnetic field. Flux through A_3 was reduced by using coaxial cables and magnetic shielding in that portion of the detector circuit which precedes voltage amplification. The effects of flux through A_4 were reduced by the use of coaxial chokes, e.g., if the high permeability core positioned between connector c and P_4 were removed from the circuit, the current through Y_3 which results from flux through A_4 would be increased by a factor of a few thousand.

The effects of external loads were reduced by the use of coaxial chokes in conjunction with low-impedance leads which bypass the junction box (hereafter termed bypass leads). The lead connecting P_3 to P_4 and the lead connecting P_3 to P_5 are examples of bypass leads in figure 5. These leads, which have impedances of about 0.1 Ω, supply most of the current to C_3 and C_4. Thus, if coaxial chokes and bypass leads are properly positioned, voltage drops will be reduced in critical portions of the circuit such as the junction box leads and the cables of the admittance standards and detector circuit.

The effects of external loads were also reduced by the use of an electrostatic shield which is represented by a broken line in figure 6. This figure represents more closely the actual circuit used. The electrostatic shield, maintained at a potential of approximately E_B with respect to ground, encloses those circuit elements which would otherwise have a large capacitance to the grounded surroundings. Current to the shield is supplied by the bypass lead connected to P_3.

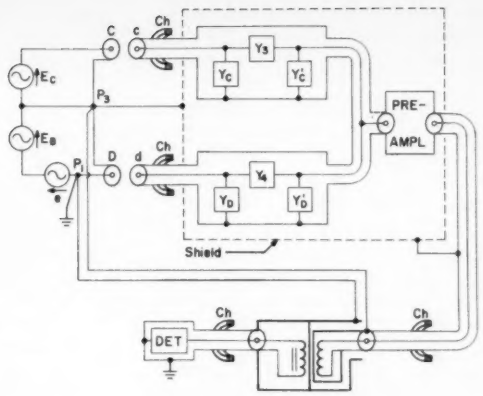

FIGURE 6. *Bridge 2 redrawn to show the difference transformer and additional shielding.*

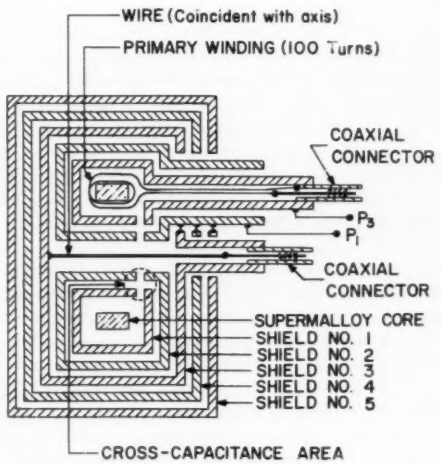

FIGURE 7. *Cross section through the axis of the difference transformer.*

The transformer shown in figure 6 is termed a difference transformer[2] and is used to change the potential of the detector cables with respect to ground from approximately E_B to zero. This was necessary in order that a phase-sensitive detector having a grounded power supply could be used. An adequate signal-to-noise ratio was maintained by using a battery-operated preamplifier having a voltage amplification of approximately 10^3 (see fig. 6). Coaxial chokes assured that the bypass leads in figure 6 supplied most of the current to the large capacitance which existed between the shielding of the difference transformer.

A cross-sectional view of the difference transformer is shown in figure 7. The secondary winding is a

[2] The basic ideas in the transformer are similar to those in a transformer built by A. M. Thompson and termed by him a difference transformer.

single turn consisting of shield No. 3 connected to a wire through the center of the core. With the exception of shield No. 4 which is mu-metal, all shielding is brass.

Most of the current resulting from the capacitance between shield No. 1 and shield No. 2 does not encircle the Supermalloy core. The current which does encircle the core, if not compensated, would induce a voltage in the detector winding. The two capacitances which result in core excitation are associated with the corners of the shield gaps. With reference to the cross-capacitance area shown in figure 7, the two capacitances are (1) from the upper left to the lower right, (2) from the upper right to the lower left. It can be seen that the two currents encircle the core in opposite senses, and hence their effects can be made to cancel by proper adjustment of the gap geometry. The gap was adjusted experimentally by observing the detector voltage with the transformer input open circuited and with the bypass leads connected.

As a result of the techniques described above, the unbalance at the detectors was small when the admittance standards of each bridge, in turn, were joined to the shorting connectors, A', B', C' . . . G', while the other standards were joined to A, B, C . . . G. Thus, accurate corrections were obtained for most of the effects of induced emf's and external loads. Those effects which were not accounted for in the corrections will be considered next.

Since currents were reduced when the standards were connected to the shorting terminals A', B', C', . . . G', induced emf's resulting from currents in that portion of the circuit shown in figure 4 were not entirely accounted for in the above corrections. The use of coaxial cables, parallel-strip leads, and magnetic shielding assured that the resulting errors were negligible. It is interesting to note that if the errors had not been negligible, they would have been accounted for in the extrapolation of the internal loads to zero. The effect of induced emf's resulting from currents within the standards was negligible since the phase of the induced emf's was shifted by 180° when the standards were permuted.

Magnetic fields in the vicinity of the junction box may induce emf's which are selective with respect to connectors A, B, C . . . G, thus causing errors in the measurement of $\overline{\gamma}_{100}$. Induced emf's of this type were kept small by using closely spaced copper strips in the construction of the junction box (see fig. 4). The following procedure was used to assure that the remaining errors were negligible: (1) A small probe was used to measure the magnetic field in the vicinity of the junction box, including the region where changes in geometry occur due to changes in the connections of the standards to the junction box, (2) the current in a loop of wire was adjusted so as to increase the measured field by a factor of approximately 100, (3) the changes in e required to rebalance the bridges were related to changes in $\overline{\gamma}_{100}$.

The external loads, C_1 and C_2 in figure 5, represent the capacitances between the grounded surroundings and those cables which are located between the coaxial chokes and connectors c and d. The circuit was designed so that C_1 and C_2 would be small and nearly equal. Measurements of C_1 and C_2 and of the lead impedances in the junction box indicated that the resulting error in the measurement of $\overline{\gamma}_{100}$ was small. This error is accounted for in item 1, table 1. Also accounted for in item 1, table 1 are errors resulting from capacitance between the copper strips of the junction box and errors resulting from imperfect balancing of the internal loads.

TABLE 1. *Uncertainties in the measurement of* $\overline{\gamma}_{100} \equiv \overline{\gamma}'_{100} - j\overline{\gamma}''_{100}$

Sources of error	Systematic errors in $\overline{\gamma}'_{100}$	Systematic errors in $\overline{\gamma}''_{100}$
	Parts in 10^{10}	Parts in 10^{10}
1. Loading	1	1
2. Contact impedances	.....	2
3. Detector zero	1	1
4. Calibration of q	2	1
5. Drift of admittances and transformer ratio	2	1
Sum	6	6

Standard deviation of $\overline{\gamma}'_{100}$ or $\overline{\gamma}''_{100}$ is 3×10^{-10}.

Table 1 lists only the significant errors which were not corrected for by extrapolating the internal loads to zero or by using the shorting terminals, A', B', C' . . . G', as described earlier. Item 2, table 1, accounts for small changes in the contact impedances between a, b, c . . . g and A, B, C, . . . G which were found to occur with continued use. Item 3, table 1, accounts for possible systematic errors which result from observer bias in determining the null balance condition.

Item 4, table 1, accounts for errors in the calibration of the instrument used to obtain E_A, E_B, E_C, and e. The essential features of the instrument, termed an "active direct-reading ratio set," are described in reference [7]. The adjustments of $q \equiv \frac{e}{E_A} \equiv q' - jq''$ were made by adjusting two sets of dials, one corresponding to changes in q' and the other to changes in q''. The maximum range of q' or q'' was ± 10 ppm with a minimum adjustment of 2×10^{-10}.

Item 5, table 1, accounts for errors which result from the admittances and transformer ratio having a nonconstant drift rate and from observer bias in timing the bridge balances which were made so as to obtain values of q in the following sequence: q_3, q_4, q_3; q_1, q_2, q_1; q_5, q_6, q_7, q_6, q_5; q_1, q_2, q_1; q_3, q_4, q_3. The above set of values could be obtained in about 12 minutes with $E_A = 100$ V, rms. The standard deviations of $\overline{\gamma}'_{100}$ and $\overline{\gamma}''_{100}$, obtained from one such set, were about 6×10^{-10}. Slightly larger standard deviations were obtained at lower voltages. A sufficient number of measurements was made so that the final values of $\overline{\gamma}'_{100}$ and $\overline{\gamma}''_{100}$ had standard deviations of about 3×10^{-10}.

4. Difference Measurements

The difference in voltage dependence between two standards whose admittances are approximately equal can be determined from ordinary bridge measurements, e.g., simple substitution combined with a change in bridge voltage. The particular circuit used for this type of difference measurement is described in section 4.1.

When the admittances of the two standards are radically different, additional measurements are required. These measurements are described in section 4.2.

4.1. Difference Measurements Involving Approximately Equal Admittances

The circuit shown in figure 3a is typical of the circuits used for difference measurements. The two general balance equations for this bridge have already been presented, namely eqs (1) and (2). For the case in which the voltage, E_A, has two specific values, E_{AL} and E_{AH}, four specific balance equations may be written:

$$\frac{Y_{1L}}{Y_{2L}}=\frac{E_{AL}-e_{1L}}{E_{BL}+e_{1L}}=\frac{1-q_{1L}}{1+\delta_{BL}+q_{1L}} \tag{21}$$

$$\frac{Y_{2L}}{Y_{1L}}=\frac{E_{AL}-e_{2L}}{E_{BL}+e_{2L}}=\frac{1-q_{2L}}{1+\delta_{BL}+q_{2L}} \tag{22}$$

$$\frac{Y_{1H}}{Y_{2H}}=\frac{E_{AH}-e_{1H}}{E_{BH}+e_{1H}}=\frac{1-q_{1H}}{1+\delta_{BH}+q_{1H}} \tag{23}$$

$$\frac{Y_{2H}}{Y_{1H}}=\frac{E_{AH}-e_{2H}}{E_{BH}+e_{2H}}=\frac{1-q_{2H}}{1+\delta_{BH}+q_{2H}}. \tag{24}$$

If

$$Y_{1H}\equiv Y_{1L}(1+\gamma_1) \tag{25}$$

and

$$Y_{2H}\equiv Y_{2L}(1+\gamma_2) \tag{26}$$

then

$$\gamma_1-\gamma_2=(q_{2H}-q_{2L})-(q_{1H}-q_{1L})+\epsilon_3 \tag{27}$$

where ϵ_3 is a small correction term consisting of second and higher order terms in q and γ.

The method described above was used to measure each of the following differences: $\gamma_{100A}-\gamma_{100B}$, $\gamma_{100B}-\gamma_{100C}$, $\gamma_{100C}-\gamma_{100A}$, $\gamma_{1000A}-\gamma_{1000B}$, $\gamma_{1000B}-\gamma_{1000C}$, and $\gamma_{1000C}-\gamma_{1000A}$, where the subscripts refer to three 100 pF air capacitors and three 1000 pF air capacitors designated 100A, 100B, 100C, and 1000A, 1000B, 1000C, respectively. Four values were obtained for each of the above differences corresponding to the following voltage changes: 12.5 to 25, 25 to 50, 50 to 100, and 100 to 200 V, rms, at 1592 Hz. The discussion of measurement uncertainties which follows is applicable to each of these values.

Since the differences, $q_{2H}-q_{2L}$ and $q_{1H}-q_{1L}$, were small and of opposite sign in eq (27), most errors of the type described in section 3 were negligible. The only exceptions were errors resulting from drift of the admittances and transformer ratio. These errors were partially reduced by the measuring sequence which follows: q_{1L}, q_{1H}, q_{1L}, q_{2L}, q_{2H}, q_{2L}. Rather than attempting to obtain a precise bridge balance at a specified time, each balance in the above sequence was made as quickly as possible. Nonuniform timing was almost inevitable since the detector sensitivity was better at high voltage. The resulting errors were kept small by injecting a small current to compensate the effect of capacitor drift. This was accomplished with an auxiliary circuit, termed a "drifter circuit."

If no adjustments of e are made, the relative changes in capacitance with time result in a time-variation in the amplitude of the current at the detector. The drifter circuit is used to inject a compensating current at the detector. The basic part of the circuit is a three-terminal, variable, air capacitor having a maximum capacitance of 10 pF. The adjusting shaft of the capacitor is connected to a constant-speed motor with speed reducer, thus providing a capacitance which varies linearly with time. Coaxial cables are used to connect the terminals of the capacitor to the detector junction and to an inductive voltage divider whose voltage is supplied by the "active direct-reading ratio-set" used to obtain E_A, E_B, and e.

The amplitude of the current injected at the detector has a first derivative with respect to time which can be adjusted by adjusting the inductive voltage divider and a second derivative which is zero. Since the drift rate of the admittance standards changed only slightly during the time needed for a set of detector balances, the use of the drifter circuit resulted in appreciable reductions in the time rate of change of e required to maintain a detector balance. In addition, the deviations from constant drift rate, which can result in systematic errors, were easily measured.

A sufficient number of measurements was made so that the standard deviation of each of the final values, $\gamma'_{100A}-\gamma'_{100B}$, $\gamma''_{100A}-\gamma''_{100B}$, $\gamma'_{1000A}-\gamma'_{1000B}$, etc., was 3×10^{-10} or less. A systematic error of 2×10^{-10} was assigned to each of the final values to account for incomplete compensation of the admittance and transformer ratio drift.

4.2. Difference Measurements Involving Radically Different Admittances

The circuit shown in figure 8 is used to measure the difference,

$$\overline{\gamma}_a-\overline{\gamma}_b\equiv\frac{\gamma_8+\gamma_9+\gamma_{10}}{3}-\frac{\gamma_5+\gamma_6+\gamma_7}{3}. \tag{28}$$

If connectors Q, R, and S are permuted cyclically with respect to connectors E, F, and G of the junction box (fig. 4), six different bridge balances can be made.

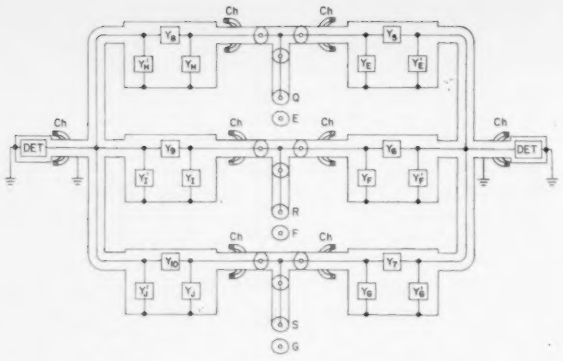

FIGURE 8. *Circuit used for difference measurements with* $Y_5 \approx Y_6 \approx Y_7 \neq Y_8 \approx Y_9 \approx Y_{10}$.

Three of the six balance equations have already been presented, eqs (7), (8), and (9). The other three equations are easily obtained by changing the subscripts of Y', γ, e, and q in eqs (7), (8), and (9). Solving the six equations, we obtain

$$\overline{\gamma}_a - \overline{\gamma}_b = \frac{q_5 + q_6 + q_7 - q_8 - q_9 - q_{10}}{2} + \epsilon_4 \qquad (29)$$

where ϵ_4 is a small correction term consisting of second and higher order terms in γ and q.

The method described above was used to measure the difference,

$$\overline{\gamma}_{1000} - \overline{\gamma}_{100} \equiv \frac{\gamma_{1000A} + \gamma_{1000B} + \gamma_{1000C}}{3} - \frac{\gamma_{100A} + \gamma_{100B} + \gamma_{100C}}{3} \qquad (30)$$

Four different values were obtained for the above difference, corresponding to the following changes in voltage: 12.5 to 25, 25 to 50, 50 to 100, and 100 to 200 V, rms, at 1592 Hz. The discussion of measurement uncertainties which follows is applicable to each of these values.

Corrections were obtained for the effects of induced emf's and external loads (see section 3) by joining connectors Q, R, and S to the shorting connectors, E', F', and G' (fig. 4). It was not necessary for the internal loads to be equal or to extrapolate the internal loads to zero. Errors resulting from admittance and transformer ratio drift were reduced by obtaining values of q in the following sequence: q_5, q_6, q_7, q_6, q_5, q_8, q_9, q_{10}, q_9, q_8, q_5, q_6, q_7, q_6, q_5. A sufficient number of measurements was made so that the standard deviation of each of the differences, $\overline{\gamma}'_{1000} - \overline{\gamma}'_{100}$ and $\overline{\gamma}''_{1000} - \overline{\gamma}''_{100}$, was reduced to about 5×10^{-10}. In addition, an allowance of 5×10^{-10} was assigned to each of the differences to account for systematic errors which may be described as similar to items 3, 4, and 5 in table 1.

5. Results

The values in tables 2, 3, and 4 were calculated from the results of measurements described in sections 3 and 4. Capacitors 100A, 100B, and 100C are of cylindrical construction, whereas capacitors 1000A, 1000B, and 1000C are of parallel-plate construction. Most of the voltage dependence of capacitors 1000A, 1000B, and 1000C is believed to be caused by electrode deflections [3]. Most of the voltage dependence of capacitors 100A, 100B, and 100C is believed to be associated with the electrode surfaces.

The values in table 4 were obtained either immediately after assembly of the capacitors, one month after assembly, or eight months after assembly. The values in table 2 were obtained eight months after assembly. A comparison indicates that the values of γ_{100A}, γ_{100B}, and γ_{100C} were probably smallest immediately after assembly. The changes in γ are believed to have been caused by structural changes on the surfaces of the brass electrodes or by the migration of thin films onto the electrode surfaces from regions of the capacitor which were difficult to clean. A consideration of typical dimensions leads to the conclusion that sizeable effects could result from thin films, e.g., the ratio of molecular diameters to typical electrode separations is considerably larger than the desired accuracy of a few parts in 10^9.

Measurements, similar to those in table 4 and with comparable accuracies, were also made on capacitors 1000A, 1000B, and 1000C. The largest change during the eight month period was 4×10^{-10}. Capacitors 1000A, 1000B, and 1000C had been in use for a number of years prior to the measurements described. The electrodes were gold plated. These capacitors and capacitors 100A, 100B, and 100C were evacuated with an oil sealed mechanical pump trapped with dry ice.

TABLE 2. *Voltage dependence of capacitors 100A, 100B, and 100C*

Values of γ' represent proportional changes in capacitance ($\Delta C/C$). Values of γ'' represent changes in dissipation factor. Standard deviation $= 3 \times 10^{-10}$. Systematic error $< 7 \times 10^{-10}$.

Change in voltage	γ'_{100A}	γ'_{100B}	γ'_{100C}
Volts (rms)	Parts in 10^9	Parts in 10^9	Parts in 10^9
100 to 200	+1.9	+8.0	+0.9
50 to 100	+.9	+2.9	+.6
25 to 50	+.3	+1.4	+.4
12.5 to 25	.0	+0.6	+.1
Change in voltage	γ''_{100A}	γ''_{100B}	γ''_{100C}
Volts (rms)	Parts in 10^9	Parts in 10^9	Parts in 10^9
100 to 200	+0.1	−0.4	0.0
50 to 100	.0	+.2	+.1
25 to 50	−.4	−.5	−.2
12.5 to 25	.0	−.2	−.3

TABLE 3. *Voltage dependence of capacitors 1000A, 1000B, and 1000C*

Standard deviation = 6×10^{-10}. Systematic error < 1.2×10^{-9}.

Change in voltage	γ'_{1000A}	γ'_{1000B}	γ'_{1000C}
Volts (rms)	Parts in 10^9	Parts in 10^9	Parts in 10^9
100 to 200	+70.8	+55.7	+84.5
50 to 100	+18.2	+14.9	+23.2
25 to 50	+5.0	+4.3	+6.7
12.5 to 25	+2.0	+1.2	+1.9
Change in voltage	γ''_{1000A}	γ''_{1000B}	γ''_{1000C}
Volts (rms)	Parts in 10^9	Parts in 10^9	Parts in 10^9
100 to 200	+0.1	+1.2	+2.3
50 to 100	.0	+1.1	+2.2
25 to 50	+.3	+1.1	+1.6
12.5 to 25	+.6	+0.3	+0.8

TABLE 4. *Instabilities in the voltage dependence of capacitors 100A, 100B, and 100C*

All values correspond to a change in voltage from 100 to 200 V, rms. Standard deviation = 2×10^{-10}. Systematic error < 2×10^{-10}.

Time	$\gamma'_{100A} - \gamma'_{100B}$	$\gamma'_{100B} - \gamma'_{100C}$	$\gamma'_{100C} - \gamma'_{100A}$
Months	Parts in 10^9	Parts in 10^9	Parts in 10^9
0	−0.5	+0.9	−0.4
1	−.6	+.8	−.2
8	−6.1	+7.1	−1.0
Time	$\gamma''_{100A} - \gamma''_{100B}$	$\gamma''_{100B} - \gamma''_{100C}$	$\gamma''_{100C} - \gamma''_{100A}$
Months	Parts in 10^9	Parts in 10^9	Parts in 10^9
0	−0.2	+0.4	−0.2
1	+.1	.0	−.1
8	+.5	−.4	−.1

The values of γ' in tables 2 and 3 can be used to determine the functions which relate capacitance to voltage. If we assume the function

$$C_V = C_0(1 + kV^m) \tag{31}$$

where C_V is the capacitance at voltage V and C_0 is the capacitance at zero voltage, then the values of γ' in each column of tables 2 and 3 will be in the ratio of $2^{3m}:2^{2m}:2^m:1$. Values of m were calculated from the measured values, γ_{100A}, γ_{100B}, γ_{1000A}, etc., and also from the measured differences, $\gamma_{100A} - \gamma_{100B}$, $\gamma_{1000A} - \gamma_{1000B}$, etc., which had smaller uncertainties of essentially different origin (see sec. 4.1). The results of the two types of calculations differed only slightly. The calculations yielded $m \approx 3/2$ for capacitors 100A, 100B, and 100C and $m \approx 2$ for capacitors 1000A, 1000B, and 1000C.

As a partial check on the overall measuring system, the value of $\bar{\gamma}_{1000} \equiv (\gamma_{1000A} + \gamma_{1000B} + \gamma_{1000C})/3$ from 100 to 200 V was determined by two methods: (1) Indirectly by measuring the difference, $\bar{\gamma}_{1000} - \bar{\gamma}_{100}$, as described in section 4.2, (2) directly by using capacitors 1000A, 1000B, and 1000C in bridge 3 of the three-bridge-circuit (sec. 3). The results differed by less than 3×10^{-10}.

Capacitors were chosen from more than two dozen capacitors on the basis of stability ascertained by difference measurements, similar to those described in section 4.1. The voltage dependence of capacitors 100A, 100B, 100C, 1000A, 1000B, and 1000C was found to be considerably more stable than that of the other capacitors. The measurements were limited to 100 pF capacitors and 1000 pF capacitors. The use of the drifter circuit (sec. 4.1) eliminated the need for special temperature control of the capacitors.

The earliest measurements involved three commercial 100 pF air capacitors of parallel plate design. The values obtained from difference measurements were observed to depend not only on time but also on the voltages which had previously been applied to the capacitors. In addition, a sudden, nonreversible change in capacitance of 14 ppm was observed in one of the capacitors when the applied voltage was increased beyond 50 V rms. The cause of the unusual behavior was found to be metallic whiskers on the tin-plated housing of the capacitor.

Difference measurements were also made on a set of ten 100 pF capacitors of cylindrical design. The construction of these capacitors is described in reference [2]. The values obtained from the difference measurements, corresponding to a change in voltage from 80 to 160 volts, were observed to change by as much as 3×10^{-8} over a period of a few days. Changes as large as 3×10^{-8} were also observed when the temperature of the capacitors was increased by approximately 10 °C.

A different phenomenon was observed when difference measurements were made on a set of three 100 pF capacitors of cylindrical design which were evacuated during measurement. The time rate of change of capacitance was found to be a function of voltage. The phenomenon is believed to be related to outgassing of the epoxy which was used to insulate and support the electrodes. Measurements of the time rate of change of capacitance as a function of voltage were made as follows: (1) The bridge was balanced and the drifter circuit was adjusted so as to obtain a steady bridge balance, (2) the detector was shorted, and the voltage applied to one capacitor was reduced to zero for 30 sec, (3) the original conditions were restored and the change in bridge balance was recorded. With 160 V originally applied to the capacitors, the changes in bridge balance were equivalent to proportional changes in capacitance of about 1×10^{-8}.

Difference measurements, corresponding to a change in voltage from 100 to 200 V, were made on three commercial 1000 pF capacitors of parallel plate construction. The changes in the values obtained from the difference measurements varied from a few parts in 10^9 to 2×10^{-8} over the period of one week.

The basic design of capacitors 100A, 100B, and 100C is shown to approximate scale in figure 9. Critical radii differ by approximately 3.2 mm. Line and detector electrodes are separated from the ground electrodes by four sets of three glass spacers. The force of the compressed springs is about 45 N.

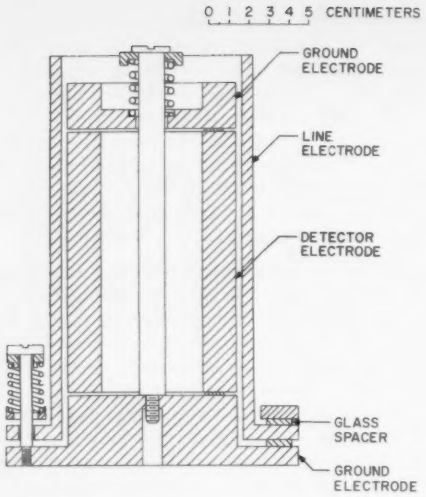

FIGURE 9. *Cross section through the axis of capacitor 100A, 100B, or 100C.*

It was found that after the capacitor was assembled and connected into a measuring circuit, very small radial displacements of the line electrode could be obtained by sharply tapping its base radially. This procedure was used to adjust the capacitance very close to a minimum, thus assuring that the radial components of the electrical forces were small. The design of the capacitor is such that it can easily be disassembled for cleaning or for experimental purposes. A grounded housing (not shown in the figure) is used to evacuate the capacitor.

6. Conclusion

The basic purpose of the present work has been to develop an accurate system for measuring both the relative and absolute voltage dependence of admittance standards. The causes of voltage dependence have been pursued only to the extent necessary to reduce instabilities. Additional measurements will be required to evaluate the instabilities which remain.

Since the mechanisms which cause instabilities in the voltage dependence of capacitors may also result in general instability, the present work has pointed out certain problem areas which should be considered in the construction of precision standards of capacitance. In addition, the present work has served as a proving ground for bridge measurements and voltage ratio measurements at the higher accuracy levels.

The author acknowledges the many suggestions of R. D. Cutkosky and the assistance rendered by D. N. Homan and Lai H. Lee in obtaining the numerical results of this paper.

7. References

[1] A. M. Thompson and D. G. Lampard, A new theorem in electrostatics and its application to calculable standards of capacitance, Nature **177**, 888 (1956).

[2] M. C. McGregor, et al., New apparatus at the National Bureau of Standards for absolute capacitance measurement, IRE Trans. Instru. **I-7**, December 1958.

[3] N. L. Kusters and O. Petersons, The voltage coefficients of precision capacitors, IEEE Trans. Communication and Electronics **82** (1963).

[4] R. D. Cutkosky and J. Q. Shields, The precision measurement of transformer ratios, IRE Trans. Instr., **I-9** (Sept. 1960).

[5] A. M. Thompson, The precise measurement of small capacitances, IRE Trans. Instr. **I-7** (Dec. 1958).

[6] A. M. Thompson, A C bridge methods for the measurement of three-terminal admittances, IEEE Trans. Instr. and Measurement (Dec. 1964).

[7] R. D. Cutkosky, Active and passive direct-reading ratio sets for the comparison of audio-frequency admittances, J. Res. NBS **68C** (Engr. and Instr.), No. 4 (Oct.-Dec. 1964).

(Paper 69D4-207)

JOURNAL OF RESEARCH of the National Bureau of Standards—C. Engineering and Instrumentation
Vol. 69C, No. 4, October–December 1965

Single-Crystal X-ray Diffraction at High Pressures

C. Weir, S. Block, and G. Piermarini

(July 23, 1965)

Construction and operation of a high-pressure single-crystal x-ray diffraction precession camera is described. The instrument appears applicable to single crystal studies to pressures as high as at least 30 kilobars and temperatures of at least 250 °C. Application of the instrument is illustrated by single crystal studies of ice VI and ice VII. Unit cell parameters are given for these two forms of ice. Further modifications and applications are discussed.

Key Words: High pressure, single crystal, x-ray diffraction, ice VI, ice VII, water, calcite.

1. Introduction

X-ray diffraction of materials under high pressures presents obvious experimental problems arising from the necessity of using a vessel which is transparent to x rays, but sufficiently strong to contain the pressures desired. Jacobs [*1*][1] fabricated a steel vessel equipped with beryllium windows and used helium as the pressure medium in his pioneering studies, but little additional progress was made until Lawson [*2*] conceived and used the diamond pressure vessel. Imposing progress has been achieved in recent years, and the problem of x-ray diffraction appears to be solved in principle up to pressures as high as several hundred kilobars with accompanying temperatures as high as 1000 °C [*3*, *4*, *5*]. In practice, however, the diffraction data are limited in diffraction angle and further to those reflections sufficiently strong to override the unavoidable background arising from scattering by the pressure cell itself. All significant work, to date, involves powder x-ray diffraction and, in view of the present limitations of the methods, there is little promise that unequivocal structures of any high pressure phases, except those of the utmost simplicity, can result from such methods.

Some high-pressure polymorphs can be stabilized at 1 bar by quenching to low temperatures while still under pressure. Both powder and single-crystal x-ray diffraction studies [*6–12*] have been made on several such materials in the metastable state. As it appears that only a limited number of presently known high pressure polymorphs are quenchable, there is a need for producing and studying single crystals of high pressure phases in their ranges of stability by means of x rays. This paper is a preliminary report of techniques developed for single-crystal x-ray diffraction at high pressures.

[1] Italicized figures in brackets indicate the literature references at the end of this paper.

2. Apparatus and Experimental Method

2.1. Apparatus

The instrument used for single crystal studies is the diamond-anvil high-pressure cell developed at NBS. This cell has been used here and in other laboratories for spectroscopy, microscopy, and powder diffraction studies [*13*, *14*, *15*]. A technique for mounting a metal gasket between the diamond anvil faces was developed by Van Valkenburg [*16*] which permits the application of pressure to liquids. Using this technique it is possible to grow single crystals from liquids under pressure or to subject a single crystal immersed in the liquid to purely hydrostatic pressure. The modifications of the cell and the ordinary precession camera to permit high-pressure single crystal studies are as follows:

The original cell designed for spectroscopy [*13*] has been improved and is shown in figure 1. The instrument has opposed diamond anvils, A, to generate pressure. The anvils are fabricated from gem quality diamonds by grinding small flat surfaces approximately 0.6 mm and 1.2 mm in diameter parallel to the table faces. The diamonds are seated on their table faces in recesses in metal plates, B, that are held to cylinders, C, by means of two screws 180° apart. Two other screws at an angle of 90° to the holding screws permit alinement of the diamond anvil surfaces. The cylinders fit snugly into bearing, D, which has a shoulder at one end to support the thrust applied to the cylinder. The thrust which forces the anvils together is supplied by plate, E, by means of spring, F, acting through top plate, G, and lever arms, H. The diamond support plates, B, have always been made of stainless steel, but, for reasons to be discussed later, have been replaced by high purity beryllium plates. In both cases, a central hole is drilled in each plate to permit microscopic

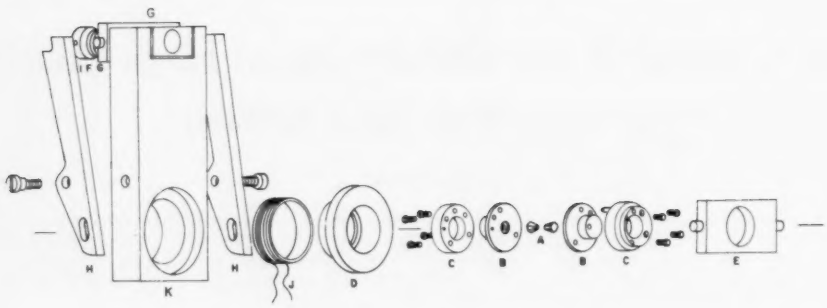

FIGURE 1. *Construction details of diamond cell (not to scale).*

observation of the specimen. To permit the entry or exit of x rays at higher angles, it was necessary to machine the stainless steel plates out at an angle of about 45°. Beryllium metal is relatively transparent to the x rays used here, and angular relief is not required. Due to spatial limitations the usual knurled knob on the screw, was replaced with a disk, I, which could be turned by means of a removable crank. Elevated temperatures were obtained by means of a small furnace, J. The furnace was made by winding Nichrome wire on a ceramic sleeve which fit snugly over the outside of D and inside the block, K. Temperature was recorded and controlled by means of a thermocouple inserted through a small hole in one of the cylinders, C, and plate, B, so as to be in direct contact with the metal gasket placed between the diamonds. An automatic recording-controlling unit was used to monitor temperatures.

It was necessary to modify the commercial precession camera to sustain the weight of the diamond cell. The existing crystal bearing assembly was eliminated by removing the mounting pillar and replaced by a sturdier unit constructed of aluminum to minimize its weight. An aluminum alloy shaft 1 in. in diameter was coupled to the film precession shaft as in the original camera. A large graduated flange was fitted over the end of the shaft and locked in place by means of set screws. This flange replaced the original "dial." A modified goniometer head was fastened to the other end of the flange. This provided only a single arc correction in an approximate horizontal plane. The two sections of this arc were also locked together with set screws. The customary vertical arc could not be accommodated in the available space and was eliminated. A stout horizontal bar clamped to the arc correcting unit was used to mount the diamond cell. This bar could be moved on a track with positioning screws to permit adjustment in the direction parallel to the x-ray beam. Vertical motion of the cell was achieved by means of a plate fastened to the diamond cell with slotted screw holes and sliding on a vertical track. The cell was clamped to the horizontal bar by screws into this plate. The screw holes through the horizontal bar were also slotted to permit the cell to slide on a track on the bar. This assembly permitted translation along three mutually perpendicular axes, and rotation about two mutually perpendicular axes. Because of interference between the cell and the x-ray tube or the collimator support, and limitations imposed by the metal of the cell cutting off the x-ray beam, maximum angular corrections of the order of $\pm 15°$ were permitted.

On assembly it was necessary to aline the new precession axis and the diamond cell to this precession axis. Most of the operations required are obvious and only the operations required to locate the specimen on the precession axis will be described. It was found that vertical and lateral adjustments were most easily initiated by visual alinement of the gasket hole with the collimator with $\bar{\mu}=0$. The gasket hole can be observed through the diamond. Refinements in these adjustments were made by maximizing the intensity in the spot produced by the x rays on a fluorescent screen placed behind the diamond cell. The intensity was first maximized at $\bar{\mu}=0$ and final adjustments were made at higher values of $\bar{\mu}$. The adjustment of the cell in the direction parallel to the x-ray beam was achieved by eliminating doubling of diffracted spots.

In use, it was expedient to remove the cell frequently for microscopic observation, and it was found to be essential to provide a means of ensuring that the cell was replaced in the same position to eliminate the need for realinement. This was achieved by means of the track on the horizontal bar which fixed the vertical and one lateral position and by means of metal stops on the bar which fixed the other lateral position. With these guides the cell could be removed

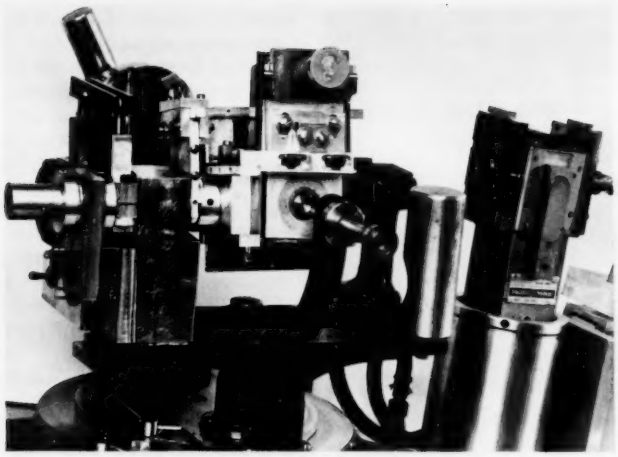

FIGURE 2. *Assembled single crystal precession unit.*

and replaced in a few seconds with no alinement adjustments required. The mounted cell is shown in figure 2.

For the diamond cell and camera used here it was found that with dial and arc readings near zero, the maximum useful value of $\bar{\mu}$ was about 20° with steel plates and 30° with beryllium plates. As the dial and arc values increased the maximum useful $\bar{\mu}$ value decreased. With the beryllium plates, however, values of 20° were easily obtained at the maximum arc and dial settings available.

2.2. Sample Preparation

The initial step in sample preparation involves fabricating the metal gasket. A thin sheet of metal (0.010 in. × 0.25 in. × 0.25 in.) is subjected to an initial compression between the diamond anvils to produce a well-defined indentation of the smaller of the two diamond surfaces. The pressure required for this operation must be adjusted to the properties of the gasket material and may vary from 5 kbar–60 kbar for different metals. Under a low power microscope a small punch mark is made in the *center* of the indentation and a small hole (No. 80 drill) is drilled through the gasket using the punch mark for centering. For pressure work above about 15 kbar it is essential that this hole be centered in the indentation to minimize the failure of the gasket; at lower pressures the centering requirement is less stringent. The burrs formed in drilling are removed with a small jeweller's file and the gasket is placed over the small diamond using the indentation as a guide. In this operation the cylinder containing the small diamond should be in position in the diamond cell with the diamond anvil face uppermost. If a liquid is to be studied a small drop of liquid is placed on top of the gasket in contact with the hole, the cylinder with the larger diamond inserted and the cell carefully assembled to avoid displacing the gasket. If a solid is to be studied, the selected single crystal may be placed in the hole and oriented on the diamond surface with a small needle before the hydraulic liquid is applied or the liquid may be applied first and the crystal inserted through the liquid. In either case difficulties are to be expected in maintaining proper alinement of the crystal during the assembly of the cell and the initial application of pressure. One technique used here involves cementing the gasket and the crystal in position by means of thin Canada balsam before assembly. However, cements are considered to be undesirable because they interfere with microscopic observations and may prove to be a source of pressure gradients.

Liquids which have been used successfully are water, glycerine, methanol, and Varsol. Both water and Varsol crystallize at moderate pressures, but glycerine and methanol or glycerine-water mixtures apparently do not crystallize to about 30 kbar. Glycerine proves to be sufficiently viscous to prevent appreciable motion of a crystal during the assembly process. Of these liquids, water, glycerine, and methanol are relatively incompressible, a matter of some importance because the crystal is crushed if it comes in contact with both diamond anvil surfaces simultaneously.

Some iron and nickel alloys serve to make satisfactory gaskets provided pressures above about 15 to 20 kbar are not required. Brass and aluminum alloys are not useful to these pressures but might prove useful at lower pressures. Above about 20 kbar problems involving gasket blowout are experienced, presumably because the strength of the metal and the diamond-metal friction is exceeded by the pressure exerted by the liquid. Two solutions are indicated, one to increase the strength of the metal gasket, the other to increase the surface area of the diamonds. Both techniques appear to be effective.

784-657 O-65-3

When molybdenum metal gaskets were used no blowouts were experienced. Molybdenum appears to be more difficult to handle mechanically but is very ductile under pressure (see Bridgman [17]). When the diameter of the smaller diamond was increased from 0.6 mm to 0.8 mm no blowouts were experienced using a nickel alloy gasket. The optimum gasket thickness for the diamonds used here appears to be about 0.010 in. Thicker gaskets have been used but do not perform satisfactorily, presumably because of the nonuniform shape of the smaller diamond. This diamond penetrates the gasket and appears to produce nonuniform stresses in the metal resulting in distortion and frequent blowout of the gasket hole. Gaskets 0.005 in. in thickness perform satisfactorily but provide a smaller available volume.

Initally, experiments were conducted using Mo Kα radiation. Under these conditions orientation photographs were obtained in 1/4-hr with ordinary x-ray film. With this radiation, however, it was found that cone axis, and upper level photographs were not satisfactory because the diffracted beams at higher angles were blocked by the cylinders or the instrument itself. A marked improvement in quantity of data obtained has resulted from using Ag Kα radiation which has a shorter wavelength (0.5609 Å versus 0.7107 Å). With Ag radiation useful cone axis and upper level photographs as high as the second level have been obtained with Fd* ≈ 4. Using Ag radiation, however, some sacrifice in exposure time is required. By using fast film (such as Kodak No Screen or DuPont Cronex III) in conjunction with fluorescent screens (Cronex CB 2, Ilford, or Radelin TF)[2] placed behind the film, orientation photographs can be made in 1/4-hr. Exposures are increased to at least 1 hr without the fluorescent screen.

It should be noted that the problem of collimation is simplified by use of a metal gasket that is opaque to the x rays. The hole in the gasket functions as a second pinhole and the external collimator need only contain a single pinhole. Use of the gasket as part of the collimating system produces diffraction rings from the metal in the resulting pattern. These rings have not caused any difficulties in interpreting the films. Extensive collimation of the beam before it is incident on the specimen and centering of the beam in the gasket hole can be used to eliminate diffraction rings from the metal. However, this technique results in a marked increase in exposure time which does not appear to be justified by the results.

3. Results

Initial studies using this instrument were made on materials which were crystalline solids at 1 bar and had known transitions at elevated pressures. The experimental technique used was to orient a crystallographic plane of the low pressure form using the precession camera. The pressure cell was then removed from the camera and mounted on a polarizing microscope. The pressure was increased slowly until the transition was observed by noting an abrupt change in birefringence or dimensions or a fracturing of the crystal. If the crystal remained intact in the high pressure form, the cell was returned to the camera for precession photographs. Under the conditions used to date, only one material of those studied appears to remain in single crystal form through the transition. The transition $CaCO_3$ (calcite) $\rightarrow CaCO_3$ II, [18] occurs with a marked change in birefringence and the crystal frequently remains intact. The transition $CaCO_3$II $-CaCO_3$III always results in a polycrystalline specimen. Transitions in KNO_3 [19] and the alkali halides [20] invariably produced polycrystalline products and no transition could be detected in KIO_4 [21].

In only one experiment with calcite was it possible to obtain a photograph of a densely populated plane of the $CaCO_3$II form. Zero level and cone axis photographs could be interpreted on the basis of a cell with dimensions $a = 4.97$ Å, $b = 7.72$ Å, and $c = 13.25$ Å with the a and b axes orthogonal. No information on any other angles or on upper levels could be obtained. Characteristic absences $h + k = 2n + 1$ were observed on the zero level photograph. Davis [22] has reported powder diffraction data on $CaCO_3$III and noted that $CaCO_3$II gave diffraction data similar to ordinary calcite except that the 113 reflection was missing in $CaCO_3$II. With the parameters found here and assuming an orthorhombic cell, it is possible to index almost all the lines reported for $CaCO_3$I (calcite), $CaCO_3$II, and $CaCO_3$III within the probable errors of the data. Further study is necessary before this situation can be cleared up. However, calcite crystals present problems in orientation because of their cleavage characteristics and it was decided to defer further studies until an improved instrument becomes available.

From the limited studies conducted here on solid-solid transitions at room temperature in single crystals, it appears that rentention of the single crystal form through a high pressure transition will not occur as frequently as originally anticipated. Other techniques for production of high pressure polymorphs in single crystal form are available, such as crystallization from solution or from a melt under conditions of stability of the desired polymorph. Both techniques are possible with the present instrument which has an upper temperature limit of operation above 250 °C. Neither method has been attempted because of the great ease with which single crystals may be grown from materials normally liquid at 1 bar and room temperature and current interest in the structure of such crystals.

3.1. Ice

Bridgman [23, 24] has shown that six forms of ice are formed under pressure. Of these six forms only two, ice VI and ice VII, are formed from water at or

[2] Certain commercial materials and equipment are identified in this paper in order to adequately specify the experimental procedure. In no case does such identification imply recommendation or endorsement by the National Bureau of Standards, nor does it imply that the material or equipment identified is necessarily the best available for the purpose.

above room temperature. Ice VI crystallizes from water at room temperature and approximately 9 kbar and ice VII forms at pressures above about 22 kbar and 82 °C—the VI–VII–L triple point. Both ice VI and ice VII can be grown as single crystals in the diamond cell, ice VI growing readily but ice VII with considerable difficulty.

3.1.1. Ice VI

Powder diffraction data for ice VI have been reported by Bertie, Calvert, and Whalley [8] at 90 °K and 1 bar and by Kamb and Davis [25] at −50 °C and 8 kbar. Both reports agree reasonably well on the powder lines and relative intensities when allowance is made for the different conditions of the two measurements. From single crystal studies here a preliminary report has been given for a unit cell which can be used to index the observed powder diffraction data [26].

Typical precession photographs of a single crystal of ice VI are shown in figures 3–7, with figures 3, 4, and 5 being made with steel plates on the cylinders and figures 6 and 7 with beryllium plates. A typical orientation photograph using unfiltered Ag radiation with a fluorescent screen is shown in figure 3. The exposure time is ½-hr with $\bar{\mu}=10°$. The intense streaks and loops are contributed by the diamonds, the diffraction rings by the metal gasket, and the narrow streaks by ice VI. A zero level photograph using Pd filtered Ag radiation is shown in figure 4. This is a 72 hr exposure with $\bar{\mu}=16°$ and a layer level screen 11.5 mm in diameter at a spacing of 40 mm. It is apparent that the filter and the layer level screen eliminate most of the diamond interference. It will be observed that diffraction spots in the 4th quadrant of this photograph are weaker than those in the 2d quadrant as a result of shadowing by the instrument itself. This occurred because of the angular correction required to orient the crystallographic plane. The first level spots are diffracted at higher angles than those on the zero level and the shadowing by the instrument makes it much more difficult to photograph these levels as shown by figure 5. This is the 1st level corresponding to figure 4 and is a 72 hr exposure with $\bar{\mu}=10°$. There are several rows of diffraction spots in this photograph concentrated principally in the 2d quadrant. The third quadrant which was slightly shadowed in the zero level photograph is now completely empty of diffraction spots. The shadowing restricts both the diffraction angle and the precession angle and for this reason it was decided to replace the steel plates, B, of figure 1 with beryllium plates. The effects of the substitution may be ascertained by comparing figures 4 and 5 with figures 6 and 7 which made use of the beryllium plates. The latter two photographs are 48 hr exposures with $\bar{\mu}=22°$ and $\bar{\mu}=10°$ respectively. A higher background is noted in the latter two photographs presumably arising from incoherent scattering by the approximately ½-in. of polycrystalline Be traversed by the x-ray beam.

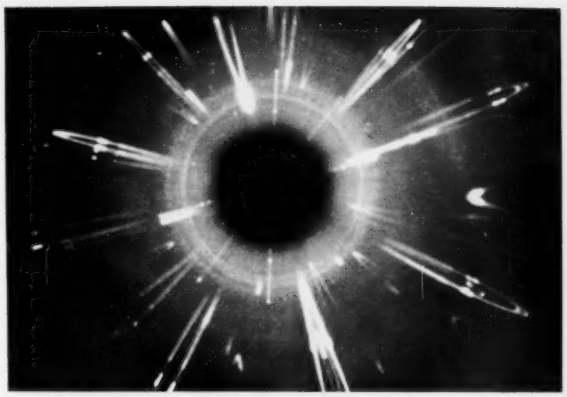

FIGURE 3. *Typical orientation photograph (unfiltered Ag radiation using fluorescent screen; $\bar{\mu}=10°$; 1/2 hr exposure.*

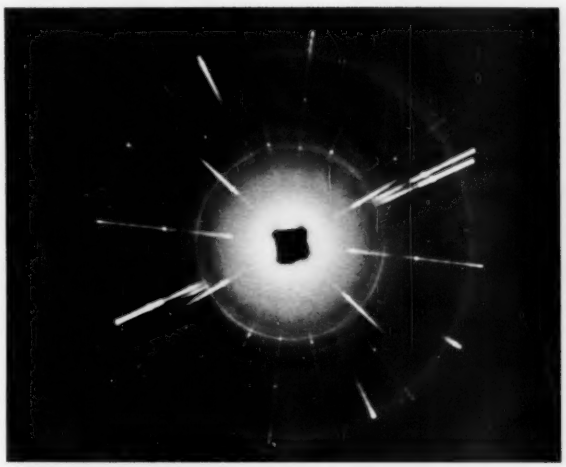

FIGURE 4. *Ice VI—*hk0 *photograph with steel plates (Pd filtered Ag radiation; $\bar{\mu}=16°$; 72 hr exposure).*

However, no appreciable shadowing is apparent on either photograph. With the beryllium plates shadowing becomes important on the 2d level of this crystal but even on this level several reflections were obtained whereas none were obtained with the steel plates. It is of interest to note the threefold diamond axis in figure 6.

Final answers on the unit cell and symmetry for ice VI have not been obtained to date. The unit cell dimensions at room temperature and approximately 9 kbar are $a=8.38$ Å, $b=6.17$ Å, $c=8.71$ Å with uncertainties of 0.05 Å in all cases. It is assumed that these axes are orthogonal. From the $hk0$ films systematic absences are $hk0$, $h=2n+1$, and $k=2n+1$. From $hk1$, systematic absences are $h+l=2n+1$. From upper level photographs and upper level loops seen on zero level photographs it appears that a is a true twofold axis but b is not. To give an unequivocal space group requires more facility of orienting

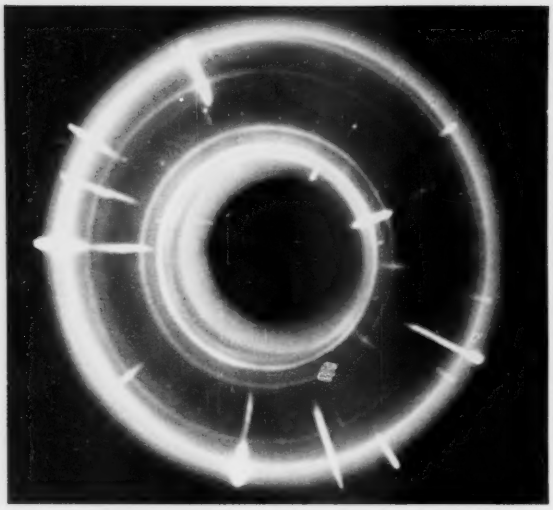

FIGURE 5. *Ice VI—*hk1 *photograph with steel plates (Pd filtered Ag radiation; $\bar{\mu}=10°$; 72 hr exposure).*

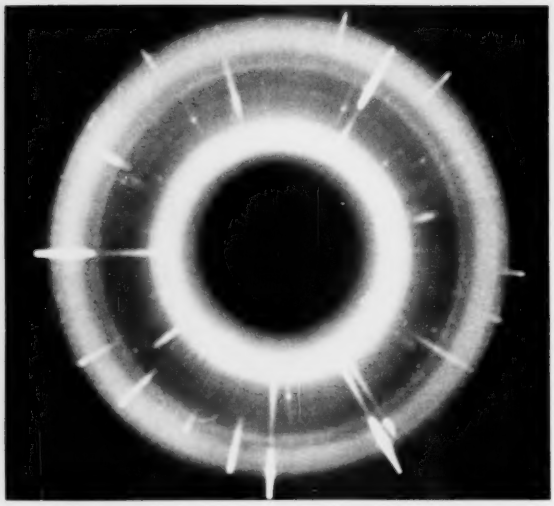

FIGURE 7. *Ice VI—*hk1 *photograph using beryllium plates (Pd filtered Ag radiation; $\bar{\mu}=10°$; 48 hr exposure).*

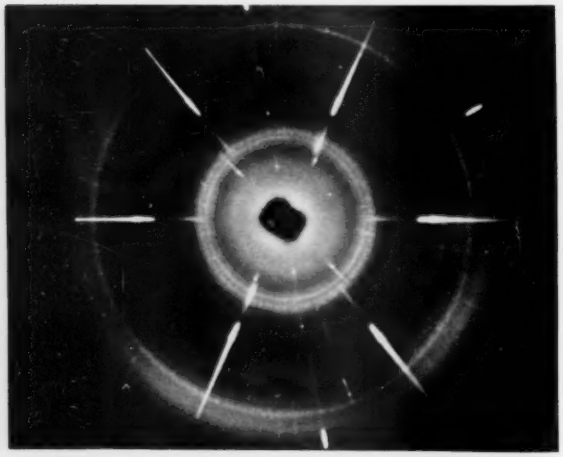

FIGURE 6. *Ice VI—*hk0 *photograph using beryllium plates (Pd filtered Ag radiation; $\bar{\mu}=22°$; 48 hr exposure).*

the crystal and less difficulty with shadow produced by the cell. A new camera now under construction is expected to facilitate solution of this problem.

3.1.2. Ice VII

Bertie, Calvert, and Whalley [8] and Kamb and Davis [25] have reported powder diffraction data for ice VII. The former authors worked at 90 °K and 1 bar and the latter at −50 °C and 25 kbar. Bertie, Calvert, and Whalley reported more reflections than Kamb and Davis, but noted that their strong reflections could be indexed in the cubic system. Kamb and Davis concluded that all their reflections were consistent with a body-centered cubic cell with $a=3.30$ Å, and they have proposed this structure for ice VII. Single crystal studies of ice VII in this laboratory arrived at identical conclusions at about the same time.

Single crystals of ice VII were grown in the diamond cell at approximately 90 °C and 25 kbar. The crystal grew as an anhedral spherical globule and was cooled to room temperature for study. It was found that very slow cooling was essential to prevent fracturing the crystal. Three different orientations of ice VII have been studied showing reciprocal lattice, planes perpendicular to the [100] and the [111] axes, and a plane containing the [110] and [121] axes. This latter plane was derived from the orientation perpendicular to the [111] axis by angular corrections consistent with the body-centered cell proposed by Kamb and Davis [25]. There are few reflections observed and the intensities decrease very rapidly with increasing order as noted by Kamb and Davis [25]. No weak reflections indicative of lower symmetry or superlattice have been observed, although it should be noted that the small dimensions of the unit cell precluded upper level photographs. From the present data, it is concluded that the cell is cubic with $a=3.40\pm0.05$ Å. Systematic absences $h+k+l=2n+1$ indicate a body-centered cell.

Bridgman [27] observed that water at 25 °C undergoes a change in volume of 0.359 cm³/g between 1 bar and 25 kbar. Therefore, the measured density of ice VII at 25 kbar and 25 °C is 1.56 g/cm³. From the dimensions of the unit cell obtained here contain-

ing two molecules of water the calculated density is 1.51 g/cm³. The single crystal data, therefore, corroborate the body-centered cubic structure proposed for ice VII by Kamb and Davis [25].

4. Conclusions

The present studies have shown that successful single-crystal x-ray diffraction work at high pressures is possible to pressures of at least 30 kbar. Successful structure analyses and space group determinations require more data and greater precision and facility of operation than the present precession camera can provide. A new goniometer head providing all the usual angular and translational motions and designed to support the weight of the diamond cell is being constructed. In addition, a new diamond cell constructed entirely of high purity beryllium metal is being fabricated.

Note added in proof: In relation to the structure of ice VI (see section 3.1.1) Kamb has recently published (Nature **150** 205, (1965)), x-ray diffraction data on ice VI obtained at 1 bar and −175 °C. He concluded that the cell was tetragonal with dimension $a = 6.27$ Å and $c = 5.79$ Å. This cell differs from the preliminary cell presented here although the two cells are related. However, there is sufficient difference that the cell proposed by Kamb cannot index both the 3.4 Å and 3.6 Å lines reported in the powder pattern by Bertie, Calvert, and Whalley [8] which the present cell can do. We have recently obtained an improved cell and orienting device. The final answer to the cell of ice VI under equilibrium conditions has not been obtained, but, by reorienting about our b axis we have obtained a zero level pattern which shows a four-fold axis of 3.11 Å which is compatible within the limits of error with Kamb's 6.27 Å (2×3.11 Å $= 6.22$ Å). Further studies are in progress.

(Paper 69C4–208)

5. References

[1] R. B. Jacobs, Phys. Rev. **54,** 325, 468 (1938).
[2] A. W. Lawson and T. Y. Tang, Rev. Sci. Instr. **21,** 815 (1950).
[3] J. C. Jamieson and A. W. Lawson, J. Appl. Phys. **33,** 776 (1962).
[4] J. D. Barnett and H. T. Hall, Rev. Sci. Instr. **35,** 175 (1964).
[5] E. A. Perez-Albuerne, K. F. Forsgren, and H. G. Drickamer, Rev. Sci. Instr. **35,** 29 (1964).
[6] R. L. McFarlan, J. Chem. Phys. **4,** 60, 253 (1936).
[7] J. E. Bertie, L. D. Calvert, and E. Whalley, J. Chem. Phys. **38,** 840 (1963).
[8] J. E. Bertie, L. D. Calvert, and E. Whalley, Canad. J. Chem. **42,** 1373 (1964).
[9] R. H. Wentorf and J. S. Kasper, Sci. **139,** 338 (1963).
[10] F. P. Bundy and J. S. Kasper, Sci. **139,** 340 (1963).
[11] C. Bates, F. Dachille, and R. Roy, Sci. **147,** 860 (1965).
[12] B. Kamb, Acta Cryst. **17,** 1437 (1964).
[13] C. E. Weir, E. R. Lippincott, A. Van Valkenburg, and E. N. Bunting, J. Res. NBS **63A** (Phys. and Chem.) No. 1, 55 (1959).
[14] A. Van Valkenburg, Rev. Sci. Instr. **33,** 1462 (1962).
[15] G. J. Piermarini and C. E. Weir, J. Res. NBS **66A** (Phys. and Chem.) No. 4, 325 (1962).
[16] A. Van Valkenburg, unpublished.
[17] P. W. Bridgman, Large Plastic Flow and Fracture (McGraw-Hill Book Co., New York, N.Y. 1952).
[18] P. W. Bridgman, Am. J. Sci. **237,** 7 (1939).
[19] P. W. Bridgman, Pro. Am. Acad. Arts & Sci. **51,** 581 (1916).
[20] P. W. Bridgman, Pro. Am. Acad. Arts & Sci. **74,** 21 (1940).
[21] P. W. Bridgman, Pro. Am. Acad. Arts & Sci. **72,** 45 (1937).
[22] B. L. Davis, Sci. **145,** 489 (1964).
[23] P. W. Bridgman, Pro. Am. Acad. Arts & Sci. **47,** 441 (1911).
[24] P. W. Bridgman, J. Chem. Phys. **5,** 964 (1937).
[25] B. Kamb and B. L. Davis, Pro. Nat. Acad. Sci. **52,** 1433 (1964).
[26] S. Block, C. Weir, and G. J. Piermarini, Sci. **148,** 947 (1965).
[27] P. W. Bridgman, Pro. Am. Acad. Arts & Sci. **74,** 399 (1942).

JOURNAL OF RESEARCH of the National Bureau of Standards—C. Engineering and Instrumentation
Vol. 69C, No. 4, October–December 1965

The Sondheimer-Wilson-Kohler Formula in Platinum Resistance Thermometry

R. J. Corruccini

Institute for Materials Research, National Bureau of Standards, Boulder, Colo.

(June 7, 1965)

An attempt was made to determine the ideal resistivity versus temperature function for platinum by a parameter-variation method using the Sondheimer-Wilson-Kohler formula for the deviation from Matthiessen's rule. At the same time a test of the applicability of the SWK formula for practical thermometry was made by examining the accuracy with which it could fit the resistance-temperature functions of selected thermometers, the characteristics of which were restricted in a manner believed to favor their accurate representation. No ideal resistivity function could be found such that most of the thermometers could be accurately represented.

Key Words: Cryogenic, electrical resistivity, low temperature, platinum, resistance thermometry, temperature measurement, thermometry.

1. Introduction

The resistivity of a metal can be expressed by the formula

$$\rho_T = \rho_0 + \rho_{iT} + \Delta_T \tag{1}$$

where ρ_0 is the imperfection-dependent resistivity at $T=0$, ρ_{iT} is the temperature-dependent "ideal" resistivity of the hypothetical perfect lattice, and Δ_T is a small term resulting from the interaction of defect and lattice scattering of the electrons. Sondheimer and Wilson [1][1] showed on the basis of a two conduction-band model that

$$\Delta_T = \frac{\rho_{iT}\rho_0}{a\rho_{iT} + b\rho_0} \tag{2}$$

and Kohler [2] obtained the same formula on more general grounds. In either treatment, the coefficients a and b are positive quantities and may be functions of temperature, but their forms have not been established from theory.

Equation (2), with a and b taken to be constants, was first applied to platinum resistance thermometry by Schultz [3]. It has recently received considerable attention as a device for establishing a platinum resistance scale of low temperatures [4]. A very extensive analysis of its application to this field has been made by Berry [5] who showed that it did not apply with sufficient accuracy to most of the thermometers considered or even to most of those of high purity; i.e., having high values of the coefficient, $\alpha \equiv (R_{373.15} - R_{273.15})/100R_{273.15}$, or low values of the reduced residual resistance, $W_0 \equiv R_0/R_{273.15}$.

[1] Figures in brackets indicate the literature references at the end of this paper.

In this paper we attempt to determine the ideal resistivity function by a new method; also we test the applicability of the SWK formula to a rather homogeneous group of high-purity thermometers that have been previously correlated by other means [6]. Some preliminary work along the lines of the present paper was reported earlier [6].

2. Procedures

2.1. Reduced Form of the SWK Equation

Equations (1) and (2) with a and b taken to be constants are first transformed into relations involving resistance ratios. We follow Schultz [3] but use the notation of Berry [5] where applicable. Equation (1) becomes

$$W_T = W_{iT} + W_0(1 - W_{iT})(1 + \Gamma_T) \tag{3}$$

where

$$W_T \equiv R_T/R_{273.15}$$

$$W_{iT} \equiv R_{iT}/R_{i\,273.15}$$

$$W_0 \equiv R_0/R_{273.15}$$

and

$$\Gamma_T = (\Delta_T - \Delta_{273.15}W_{iT})/\rho_{273.15}W_0(1 - W_{iT}).$$

Introduction of eq (2) leads to

$$(\Gamma_T)_{SWK} = AW_{iT}/(1 + CW_{iT}) \tag{4}$$

in which A and C are constants which can be evaluated

if the resistance is known at any two temperatures, T_1 and T_2, other than 0 and 273.15 °K. The following expressions are found for A and C:

$$C=\frac{\Gamma_1-\Gamma_2 W_{i1}/W_{i2}}{(\Gamma_2-\Gamma_1)W_{i1}}$$

$$A=\Gamma_2(1+CW_{i2})/W_{i2}.$$

The subscripts 1 and 2 refer, respectively, to T_1 and T_2. The constants A and C are related to the SWK parameters by the following close approximations:

$$a \approx C/A$$

$$b \approx 1/AW_0.$$

In the calculations to be described, T_1 and T_2 were always taken to be 20 and 90 °K; i.e., approximately the boiling points of hydrogen and oxygen, respectively.

2.2. The Thermometers

These consisted of 34 commercially made capsule-type thermometers plus thermometer T4 of the National Research Council, Canada. They are more fully described in the earlier paper [6]. All of the calibration data were expressed on the NBS 1955 temperature scale. The group is of high purity as indicated by $\alpha > 0.003924$ and $W_0(\text{estd.}) < 7\times10^{-4}$. The success with which they were correlated by the simpler empirical method of reference 6 suggested that they were rather uniform with regard to the forms of their deviations from Matthiessen's rule and thus would provide as favorable a practical test of the SWK formula as one could reasonably hope to obtain. The thermometers are referred to by identification numbers from 1 to 35 assigned in order of increasing $W_{20.263}$.

2.3. The Residual Resistance Ratio W_0

Experimental values of $W_{4.2}$ were available for five thermometers. These were adjusted to W_0 using the data in Berry's figure 1. For the remaining ones, W_0 was estimated from data in the region 10 to 20 °K using Method 1 in Berry's appendix III.

2.4. The Ideal Resistance Ratio Function W_{iT}

The function W_{iT} for platinum has been estimated by various methods. A summary and discussion was given by Berry who indicated objections to the various earlier methods. He derived a new function, slightly different from the others. In the region 10 to 90 °K, this was found by extrapolating plots of W_T-W_0 versus W_0 for a large number of thermometers to $W_0=0$. Since the values of W_T-W_0 unfortunately lay in a band rather than on a line, only a few selected thermometers having low values of W_T-W_0 were used in making the extrapolation. Correspondingly, when Berry fitted the SWK formula using this W_{iT} function to the various thermometers, the fit was satisfactory only for those few that had been used to derive the W_{iT} function.

The validity of the SWK model for the present group of thermometers is here tested by a different method, as follows. One may derive various arbitrary W_{iT} functions from the W_T function of any one thermometer via eqs (3) and (4) by assuming various values of its parameters A and C. Equations (3) and (4) can then be fitted to all of the remaining thermometers at 20 and 90 °K using these various W_{iT} functions in turn, and the errors in the representations of W_T at other temperatures can be examined. If it is supposed that the SWK formula holds for the group, then it should be possible to find in this way a particular W_{iT} function such that all of the remaining thermometers except the one used to generate the W_{iT} functions are accurately fitted. Furthermore if various thermometers are used in turn to generate such an optimum W_{iT} function, then the various optimum W_{iT} functions should be found to be all identical and therefore equal to the "true" W_{iT} function.

To carry out this test, nine thermometers were selected which, on the basis of earlier work [6], were judged to be representative of the set of thirty-five. The five of these for which experimental values of $W_{4.2}$ were available were used to generate the trial W_{iT} functions.

3. Results

3.1. The Function W_{iT}

When the procedure just described was carried out it was found that there existed a spectrum of suitable W_{iT} functions. In going from one to another of these functions, the identities of the thermometers for which the fit was least satisfactory changed, as did the temperatures at which the errors were largest, but no uniquely superior fit of all the thermometers could be found. In figure 1 are shown some of the better W_{iT} functions referenced to Berry's W_{iT} function as a base line.

The fitting errors (see the next section) were roughly an order of magnitude larger than the precision with which the resistance thermometers are believed to have been calibrated. Consequently, the variation in W_{iT} found by the present method is an artifact of the SWK model and is not chargeable to experimental error.

3.2. Accuracy of the SWK Equation With Constant Coefficients

The quality of the better fits obtained using W_{iT} functions derived by the method of section 2.4 may be summarized by stating that the maximum temperature error of the nine representative thermometers in the interval, 20 to 273.15 °K, was never much less than 20 mdeg, and the average of the maximum errors of the thermometers was never much less than 10 mdeg. In

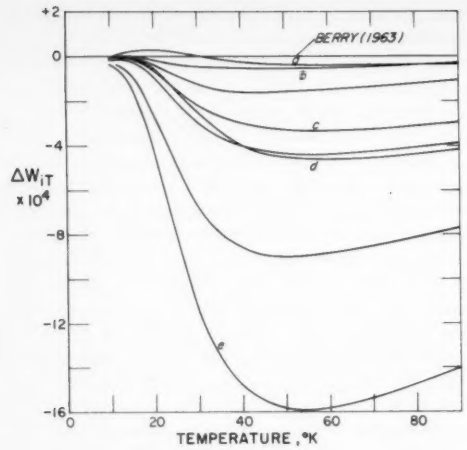

FIGURE 1. *Selected useable* W_{iT} *functions plotted relative to that of Berry* [5].

(The letters, a-b-c-d-e, identify functions referred to in table 1.)

table 1 are summarized the errors of the SWK formula resulting from use of five of the better fitting W_{iT} functions of figure 1. For comparison, Berry's W_{iT} function was also used. In the last two rows are given the corresponding errors of the simple empirical method evaluated earlier [6].

TABLE 1. *Accuracy of the SWK formula compared to an empirical method of interpolation*

Method of interpolation	Max. temp. error	Average $\lvert\Delta T_{max}\rvert$[a]	Range examined
SWK eqs (3–4) using the following W_{iT} functions:	*mdeg*	*mdeg*	°K
a. Figure 1	−17.0	8.5	20–273
b. Figure 1	+20.3	12.4	20–273
c. Figure 1	+21.3	10.6	20–273
d. Figure 1	−18.4	8.6	20–273
e. Figure 1	−21.7	10.6	20–273
Berry [5]	+27.1	12.8	20–273
Berry [5]	+27.1	12.7	20–90
Empirical method[b]	+8.6	3.6	20–273
Do	−4.8	2.2	20–90

[a] Average of the maximum errors of the nine representative thermometers.
[b] Reference 6, eq (10) using 20, 90, and 273.15 °K as calibration points.

All earlier studies of the resistance-temperature relation of platinum have encountered exceptional difficulties in representing it accurately in terms of temperature errors below 20 °K. It might reasonably be supposed that the SWK formula would be advantageous here because of its theoretical foundation and the constraint imposed on its behavior at the lowest temperatures by use of the residual resistance. However, its behavior below 20° also is unsatisfactory inasmuch as the error at 10 °K was usually of the order of 0.1 deg.

3.3. Further Characterization of the Thermometers

Following Berry, we may characterize the thermometers via the function $(\Gamma_T)_{exptl}$, calculated from eq (3) using the experimental values of W_T, i.e.,

$$(\Gamma_T)_{exptl} \equiv \frac{W_T - W_{iT}}{(1 - W_{iT})W_0} - 1.$$

This function, if it is to be fitted by eq (4), must rise monotonically—at first in proportion to W_{iT}, i.e, roughly as T^5—and approach an asymptotic limit. Berry found that the thermometers which would be well represented could be identified as those with (a) $\Gamma_{90} < 0.35$ (Γ_{90} approximates the high-temperature limit of Γ_T), (b) $W_0 < 1 \times 10^{-3}$, (c) monotonically rising curves of Γ_T. Only about 20 percent of the thermometers examined by him met all three requirements.

It will be recognized that conditions (a) and (c) test only the *uniformity* of the group. They are not meaningful criteria of "normal" versus "anomalous" behavior inasmuch as the behavior displayed depends entirely on the form of the adopted W_{iT} function.

The present group of thermometers was examined in the above way using Berry's W_{iT} function. All of the thermometers met criterion (b). Eighteen out of the 35 met criterion (a). Fifteen of these 18, as well as two of the others, failed to strictly meet criterion (c). However only five of these (consisting of the thermometers with the lowest values of Γ_{90}) showed marked maxima in $(\Gamma_T)_{exptl}$. If a requirement based on calibration at common fixed points were to be adopted for the purpose of excluding thermometers having maxima in Γ_T (e.g., $\Gamma_{90} > \Gamma_{54} > \Gamma_{27} > \Gamma_{20}$), only these five would be excluded. Had members of this set of five been excluded from the nine used for most of the calculations, the SWK fits would have been improved for certain of the W_{iT} functions derived and selected by the parameter-variation method, but would still have been inferior to that given by the empirical method of reference 6. The average fit of the SWK formula using Berry's W_{iT} function would actually have worsened.

Figure 2 shows a sampling of the $(\Gamma_T)_{exptl}$ curves. Numbers 17, 31, 5, 34, 23, and 11 are from the selected group of nine used for most of the calculations. Number 29 also was a typical curve; however, number 12 was unique. Numbers 11 and 29 provided reference functions used in the empirical method of reference 6. Numbers 23, 31, and 34 were used in a preliminary study [7] in which it was found that they could be represented within about 1 mdeg by the method of reference 6.

Table 2 lists the SWK parameters of the selected group of nine representative thermometers used in the derivation of W_{iT} and in examining the fit of the SWK equations. It may be compared with Berry's table IV. The range of the parameters a and b is very nearly the same as that covered by Berry although the range of W_0 is much narrower.

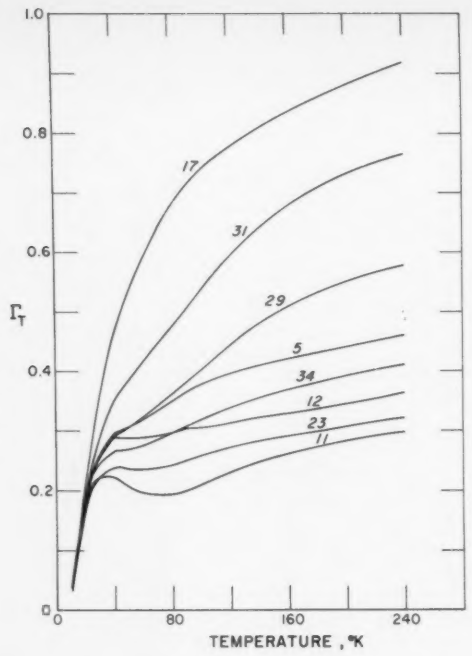

FIGURE 2. *Curves of* $(\Gamma_T)_{expt.}$ *for selected thermometers calculated using Berry's* W_{iT} *function.*

(The curves are labeled with the identification numbers of the thermometers.)

TABLE 2. *SWK parameters of the selected thermometers*

Thermometer number	$W_0 \times 10^6$	A	C	$\frac{1}{a}\left(=\frac{A}{C}\right)$	$\frac{b}{a}\left(=\frac{1}{CW_0}\right)$
2[a]	427	110	146	0.75	16.0
17	512	83	113	.74	17.4
31	666	86	166	.52	9.0
5	468	95	251	.38	8.5
34	681	135	430	.32	3.4
23	655	134	529	.25	2.9
10	485	231	926	.25	2.2
1	398	146	662	.22	3.8
11	498	386	1980	.19	1.0

[a]Thermometer T4 of National Research Council, Canada.

4. Discussion and Conclusions

The application of the SWK formula to platinum resistance thermometry has been based on the reasonable expectations that, because of its theoretical foundations, it should accurately represent a wider range of platinum purities and a wider range of temperatures than could purely empirical correlations. The work of Berry and others has already dashed these expectations. The failure of the present study to obtain a unique ideal resistivity function from the SWK model with constant coefficients as well as the failure to fit the model to any major part of the data used within the precision of those data indicate that the model has only qualitative significance. This supports the conclusions already reached.

Thus the present study is of use mainly in examining the question: Would the SWK formula have some special usefulness if the characteristics of the thermometers were narrowly restricted? The present thermometers have narrowly restricted α and W_0 values and are of uniform origin and style of construction. It has been shown that they can be accurately represented from 20 to 90 °K by a simple empirical method [6] using the same calibration temperatures as the present study except that the residual resistance is not required. Thus by these various criteria the present thermometers appear to be a quite homogeneous group. A correlation scheme that required any further restrictions on acceptable thermometer characteristics would not be justifiable on practical grounds. Yet the present study shows that the thermometers considered are a diverse group when categorized according to any of the following: (1) shape of the Γ_T function obtained using Berry's W_{iT} function, (2) magnitude of the SWK parameters, such as a, and (3) accuracy with which the SWK formula fits their resistance-temperature functions. Consequently, it seems unlikely that the SWK formula has any practical utility for accurate thermometry or for classification of thermometers into acceptable and unacceptable types.

The assistance of William J. Hall and Hans M. Roder in programming the calculations for automatic computation is gratefully acknowledged.

5. References

[1] E. H. Sondheimer and A. H. Wilson, Proc. Roy. Soc. (London), **A190,** 449 (1947).
[2] M. Kohler, Z. Physik **126,** 495 (1949).
[3] H. Schultz, Z. angew. Physik **9,** 465 (1957).
[4] See papers by Corruccini, Harper et al., Sharevskaya et al., and Van Dijk in Temperature, Its Measurement and Control in Science and Industry, C. M. Herzfeld, ed. (Reinhold Publishing Corp., New York, 1962), Vol. **3,** Part 1, Section VII, Platinum Resistance Thermometer Scale, 10 to 90 °K.
[5] R. J. Berry, Can. J. Phys. **41,** 946 (1963).
[6] R. J. Corruccini, Temperature, Its Measurement and Control in Science and Industry, C. M. Herzfeld, ed. (Reinhold Publishing Corp., New York, 1962), Vol. **3,** Part 1, p. 329.
[7] R. J. Corruccini, Rev. Sci. Instr. **31,** 637 (1960).

(Paper 69C4–209)

JOURNAL OF RESEARCH of the National Bureau of Standards—C. Engineering and Instrumentation
Vol. 69C, No. 4, October–December 1965

Stress Analysis of Tape-Wound Magnet Coils*

Jesse Hord

Institute for Materials Research, National Bureau of Standards, Boulder, Colo.

(June 14, 1965)

A liquid hydrogen cooled, tape-wound, axially segmented, high-purity aluminum electromagnet has been built and tested to 95 kilogauss with a magnet power consumption of 22 kilowatts. Formulae for the axial, radial, and circumferential stress components in this type coil are derived under the assumptions of isotropy and homogeneity. Both plane strain and plane stress analyses are given. The hoop stress is also derived from the "floating shell" concept using thin shell theory. The formulae from these analyses and thick-wall cylinder theory are used to calculate the hoop stresses in the experimental coil, and the results are presented for comparison. The theoretical burst field of a monolithic cylindrical coil disk is derived.

Key Words: Axial stress, burst field, circumferential stress, cryogenic electromagnets, electromagnets, magnetic body forces, magnetic field, plane strain, plane stress.

1. Introduction

Many current research programs require the application of high magnetic fields. Plasma containment, heating, and acceleration are examples. Cryogenic electromagnets are rapidly becoming the most convenient, economical means of producing these high fields. Purcell and Payne [1][1] have discussed the advantages of cryogenic electromagnets and described in detail the coil construction treated herein.

The maximum field attainable with an electromagnet is limited by the mechanical strength of the coil. The field strength obtained with a given coolant system and magnet power supply may also be limited by the heat transfer efficiency and heat capacity of the coolant and the conductor resistivity. Therefore, optimum coil design requires simultaneous consideration of stresses, heat transfer, and conductor resistivity. The first of these is of sufficient importance to be treated separately in this paper.

In high-field magnets, the mechanical stresses may burst the coil. The coil may also fail by localized yielding which can result in increased coil resistance and electrical shorting. Therefore, it is necessary to determine the stress field for a specific magnet construction. The coil construction of particular interest here is the stack of tape-wound epoxy-bound cylindrical disks. The coil disks are alternately stacked with fiber disks which provide electrical insulation and sector-like openings for radial coolant passages. The stack of coil disks and separators is shown on figure 1. This photograph was taken following electrical and intermediate structural failure of the magnet

*This study was conducted on Contract AT–(49–2)–1165 for the U.S. Atomic Energy Commission, PROJECT SHERWOOD.

[1] Figures in brackets indicate the literature references at the end of this paper.

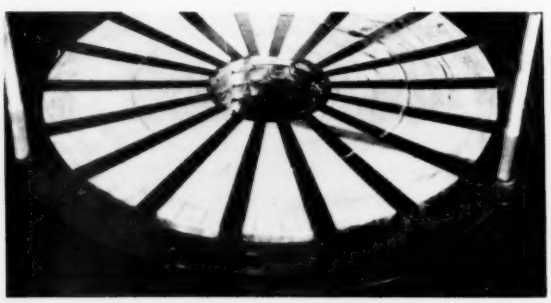

FIGURE 1. *Stack of magnet coil disks and disk separators with top four coil disks removed (after electrical and intermediate structural failure of the magnet at 95 kG).*

at 95 kilogauss (kG). The foil conductor is assumed to be tightly wound with alternate layers of paper insulation and then vacuum impregnated with epoxy resin to form a monolithic cylindrical disk. The paper and epoxy combined are not permitted to exceed 5 percent of the disk volume. The epoxy-paper tensile and compressive yield strengths exceed those of the conductor. This construction technique yields to the simplified analysis of an isotropic, homogeneous cylindrical disk. Although the epoxy-bound laminated construction cannot be perfectly isotropic, the assumption of isotropy is considered representative of the coil construction. These cylindrical coil disks are analyzed herein and formulae are developed for the axial, radial, and circumferential stress components. The radial and circumferential stress components are derived under the assumptions of both plane stress and plane strain. The hoop stress is also developed from the "floating shell" concept which assumes that each turn of the coil disk is an individual thin wall cylinder. This type analysis should be appropriate for loosely wound, poorly bonded coil disks. The formulation for predicting the burst field of a monolithic cylindrical coil disk is also developed. Stress and burst field design curves based on the analyses are presented.

Magnet stresses have been given considerable attention in the literature. For the most part, only the circumferential (hoop) stress component has been examined. This is reasonably justifiable since the circumferential stress is the largest component. Post and Taylor [2] point out that the magnetic pressure is proportional to $B_z^2/8\pi$, where B_z is the axial field component. They show that the main incremental body forces are proportional to the radial derivative of the magnetic pressure. Bitter [3] extends the magnetic pressure concept to a very useful form by assuming the coil to be a thick wall cylinder with internal pressure $B_0^2/8\pi$ (B_0 is the field at the geometric center of the coil). This calculation scheme is quick and easy to use and, as will be shown later, provides a rough estimate of the coil hoop stresses. However, it should be noted that this calculation scheme is valid only for the hoop stress (σ_c) component. If a shear failure theory is to be assumed for the coil, it is necessary to also know the axial (σ_z) and radial (σ_r) stress components. If the maximum normal stress failure theory is employed, then σ_c will suffice. It will be shown herein that σ_z is not negligible and can cause coil failure or excessive deformation under the disk separators.

Detailed stress analyses for various type magnets have been given by Cockcroft [4], Daniels [5], Giauque and Lyon [6], and Wells et al., [7]. None of these are deemed applicable to the magnet construction of interest for the following reasons: Cockcroft [4] assumed that the magnetic body forces were balanced at the outer periphery by an external pressure. This may be true for coils rigidly reinforced at the outer edge but no reinforcement was used for the coils described here. Cockcroft also made the simplifying assumption that the solenoid was a homogeneous, isotropic body, but neglected the largest stress component (σ_c) in his analysis. In addition, the formulae developed are dependent upon the calculation of the mutual inductance of a solid coil and a circle in the end plane. Although tables are given for specified variations in coil geometrical parameters, the calculation is laborious. Daniels [5] also utilizes the mutual inductance of one turn with the entire coil to derive stress formulae for coils fabricated by stacking tape-wound cylindrical disks. Since the disks were not considered to be structurally reinforced, the problem is similar to the one under consideration in this paper. Daniels [5] considered the problem as two dimensional and ignored stresses in the axial (Z) direction. The windings are assumed to be homogeneous and anisotropic because the coil was fabricated with nylon insulation between adjacent turns, and the composite was not integrally bonded in any way. It is assumed that the coil cannot unwind due to friction between adjacent turns. Daniels [5] includes the all-important hoop stress and the conditions of stress compatibility in the analysis. It is concluded that each turn of the coil is in equilibrium under its own body forces and that axial compression does not affect the magnitude of the stresses in the radial and circumferential directions. Daniels [5] also concludes that evaluation of the formulae developed is very laborious and suggests experimentation with models as an alternative to calculating the stresses. Giauque and Lyon [6] treat the problem of helical-wound cylindrical coils. Each helical layer of the solenoid was separated

by an electrical insulating material which also defined the cooling fluid annuli. Thus, the coil could not provide uniformly distributed resistance to radial forces and was prevented from unwinding only by frictional drag or deformation of the conductor. Each helical layer of the coil is assumed to be self-supporting until the stresses in the conductor exceed the conductor yield strength. Giauque and Lyon [6] also use the mutual inductance method in the development of formulae for the axial and circumferential stress components. A simplified expression for the calculation of the mutual inductance between current element and coil is given for nonhomogeneous coils. This simplified expression is reported to be useful for the quick evaluation of maximum stresses in a design feasibility study. Under the foregoing assumptions Giauque and Lyon [6] neglect the radial stress component, assume a maximum normal strain failure theory, utilize the mathematical expression for calculating mutual inductance, and derive very useful equations for the hoop, axial, and failure stresses in unbonded helical-layer cylindrical coils. Wells et al., [7] have extensively examined the distribution of magnetic forces in toroidal solenoids. Wells [8] has also developed very useful formulae for the computation of hoop and radial stresses in Bitter magnets (current density is inversely proportional to the coil radius). The stress formulae developed herein are dependent upon the magnetic flux density (B). The recent data of Brown et al., [9, 10] provide numerical values of B for any solenoid. Therefore, stress calculations using the derived expressions are simplified.

2. Analysis

2.1 Nomenclature

B = vector magnetic flux density
B_0 = magnetic flux density at the geometric center of the coil
C = constant of integration
E = Young's modulus of elasticity
F = force generated by magnetic field
I = current per turn of conductor
J = current density in conductor
L = half length of cylindrical coil
m = absolute value of the slope of B_z/B_0 versus γ plot
N = number of turns in coil
p_m = magnetic pressure
r = radius at some turn in the coil (radial coordinate)
r_i = inside radius of coil
r_0 = outside radius of coil
t = wall thickness of a thin cylinder
u = measure of radial displacement
V = conductor volume
y = absolute value of B_z/B_0 at $r = r_i (\gamma = 1)$
Z = denotes distance along axis from center of coil (axial coordinate).

a. Greek

α = ratio of outer to inner coil radius ($= r_0/r_i$)
β = ratio of coil half length to inner coil radius ($= L/r_i$)
γ = ratio of turn radius to coil inner radius ($= r/r_i$)
ϵ = unit strain in conductor
θ = circumferential coordinate
μ = Poisson's ratio
σ = unit stress in conductor

σ_y = yield stress of conductor
Φ = magnetic flux geometry parameter

$$\left\{ \equiv \frac{\beta}{\alpha - 1} \ln \left(\frac{\alpha + \sqrt{\alpha^2 + \beta^2}}{1 + \sqrt{1 + \beta^2}} \right) \right\}.$$

b. Subscripts

c = denotes circumferential direction
r = denotes radial direction
z = denotes axial direction

c. Superscripts

$*$ = denotes plane strain condition

Λ = denotes maximum (peak) value

$\overline{\ }$ = denotes average value.

The analysis is performed under the following general assumptions: (1) The tape-wound, epoxy-bound axially segmented cylindrical coil is considered to be homogeneous and isotropic in each disk. (2) The radial and circumferential stresses are derived under the assumptions of plane stress and plane strain. The coil is comprised of a stack of relatively thin disks which are separated by a disk-shaped insulating material with sector-like openings for coolant flow. Therefore, it would be extremely difficult to exactly determine the effect of axial compression on the radial and hoop stresses. The assumption of plane stress is judged most applicable since the major portion of each disk face is exposed to coolant. Axial stresses due to axial magnetic force are transmitted from disk-to-disk via the spokes in the disk separators. The axial compression is magnified by the reduction in compression area under the disk separators. (3) The coil is symmetrical with symmetrical flux distribution and uniform current density. (4) Frictional drag under the spokes of the disk separators does not resist radial deformation of the conductor. (5) Buckling or warping of the disk does not occur. This also means that no bending takes place between spokes of the disk separators (due to axial compression). (6) The stress formulae developed are applicable only so long as the conductor stress remains below the proportional limit. (7) The maximum normal stress failure theory is chosen because the hoop stress component dominates. The maximum normal strain or maximum shearing stress failure theory is more applicable to the conductor material immediately below the separator spokes; however, the material under the spokes comprises a small portion of the disk volume, and the high compressive stresses can be redistributed to the unstressed conductor.

Consider the cross section of a coil with a magnetic flux linkage as shown in figure 2a. The horizontal (radial) component (1) of the vector field induces vertical (axial) forces on the conductor. The axial component (2) of the magnetic field induces radial forces on the conductor. The distribution of the axial field component across the solenoid radius is shown on figure 2b. The field variation along the solenoid axis is shown in figure 2c and the radial field distribution on figure 2d. The axial field creates the bursting effect and varies almost linearly across the coil radius. The radial field is nearly sinusoidal over the coil radius and increases with distance along the axis (Z) for $Z < L$. Now the incremental force on a conductor segment in a magnetic field is given as

$$\frac{dF}{dV} = \frac{BJ}{10}. \tag{1a}$$

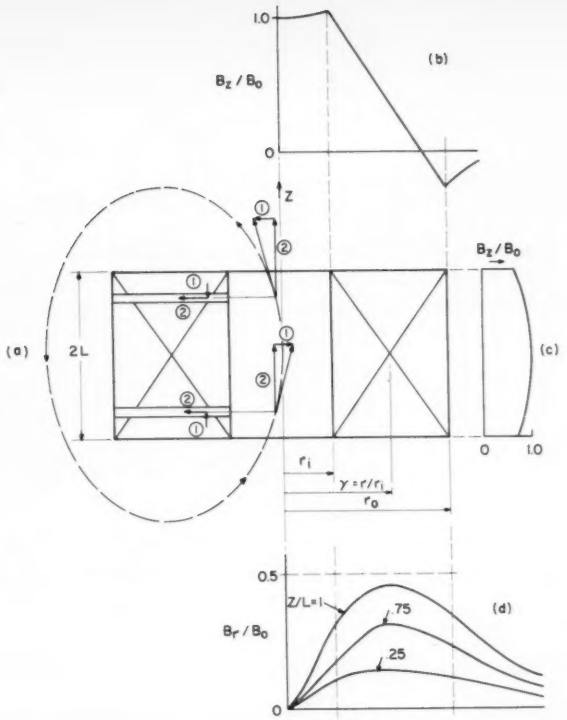

FIGURE 2. *(a) Cross section of solenoid showing magnetic flux components and associated body forces. (b) Distribution of the axial field component over the coil radius. (c) Distribution of the axial field component over the coil axis. (d) Variation of the radial field component with radial and axial position.*

The current density for the solenoid in figure 2a is

$$J = \frac{NI}{2L(r_0 - r_i)}. \tag{1b}$$

Also, the field at the geometric center of the coil may be written,

$$B_0 = \frac{4\pi NI}{10(2L)}\,\Phi. \tag{1c}$$

Combining eqs (1a), (1b), and (1c) we obtain the magnetic body force per unit volume of conductor;

$$\frac{dF}{dV} = \frac{BB_0}{4\pi(r_0 - r_i)\Phi}. \tag{2a}$$

The radial force component is

$$\frac{dF_r}{dV} = \frac{B_z B_0}{4\pi(r_0 - r_i)\Phi}, \tag{2b}$$

and the axial force component is

$$\frac{dF_z}{dV} = \frac{B_r B_0}{4\pi(r_0 - r_i)\Phi}. \tag{2c}$$

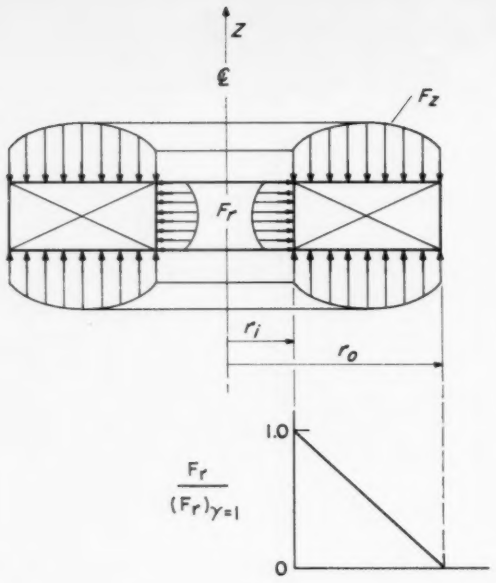

FIGURE 3. *Distribution of magnetic body forces on a coil disk at midplane* (Z/L = 0).

Equations (2b) and (2c) are valid for any point in the coil cross section. Equations (2b) and (2c) indicate that the radial and axial forces are linearly proportional to the field components. Referring to the field distributions in figure 2, we can sketch the loading imposed on a typical disk in the coil. The distribution of the magnetic body forces is illustrated on figure 3.

Radial equilibrium of a differential element of conductor with magnetic body force $\frac{dF_r}{dV}$ is satisfied by

$$\sigma_\theta - \sigma_r - r\frac{d\sigma_r}{dr} = r\frac{dF_r}{dV}. \tag{3}$$

See Timoshenko and Goodier [11].

2.2. Plane Stress

For the condition of plane stress $\sigma_z = 0$. Hooke's law for the condition of plane stress may be written [12] in terms of stress and displacement as follows:

$$\sigma_\theta = \frac{E}{(1-\mu^2)}\left\{\frac{u}{r} + \mu\frac{du}{dr}\right\}, \tag{4a}$$

$$\sigma_r = \frac{E}{(1-\mu^2)}\left\{\frac{du}{dr} + \mu\frac{u}{r}\right\}. \tag{4b}$$

Combining eqs (3) and (4) we obtain the equilibrium equation in terms of displacement

$$\frac{d^2u}{dr^2} + \frac{1}{r}\frac{du}{dr} - \frac{u}{r^2} = -\left(\frac{dF_r}{dV}\right)\frac{(1-\mu^2)}{E}. \tag{5}$$

Equation (2b) must now be evaluated in order to solve this differential equation. It will be shown

later that $B_z = B_0\left(\frac{r_0 - r}{r_0 - r_i}\right)$ provides fair results in computing the stresses at the midplane; however, to maintain generality we shall let

$$B_z = B_0[\gamma + m(1-\gamma)], \tag{6a}$$

where γ = the value of B_z/B_0 at $r = r_i$ (fig. 2b), and m = absolute value of the slope of B_z/B_0 (fig. 2b). Combining eqs (2b) and (6a) we obtain

$$\frac{dF_r}{dV} = \frac{B_0^2[\gamma + m(1-\gamma)]}{4\pi(r_0 - r_i)\Phi}. \tag{6b}$$

Substitution of eq (6b) into eq (5) yields

$$\frac{d^2u}{dr^2} + \frac{1}{r}\frac{du}{dr} - \frac{u}{r^2} = K[\gamma + m(1-\gamma)], \tag{7a}$$

where

$$K \equiv -\frac{B_0^2(1-\mu^2)}{4\pi E r_i(\alpha - 1)\Phi}. \tag{7b}$$

The left side of eq (7a) is recognized as Euler's equation and the complementary solution is written

$$u_1 = C_1 r + \frac{C_2}{r}. \tag{8a}$$

The particular solution to eq (7a) is

$$u_2 = Kr^2\left\{\frac{(\gamma + m)}{3} - \frac{mr}{8r_i}\right\}. \tag{8b}$$

and $u = u_1 + u_2$. The constants of integration C_1 and C_2 are evaluated from the boundary conditions $\sigma_r = 0$ at the inner and outer radii of the disk. Invoking these boundary conditions and combining eqs (4b) and (8) we obtain

$$C_1 = -\frac{KQ_1 r_i}{24},\ C_2 = -\frac{KQ_2 r_i^3}{24},$$

where $Q_1 \equiv \left(\frac{1}{1+\mu}\right)\{Q_2(1-\mu) + 8\gamma(\mu+2) + m(7+5\mu)\}$, and

$$Q_2 \equiv \left(\frac{\alpha^2}{\alpha^2 - 1}\right)\left(\frac{1}{\mu - 1}\right)\{8\gamma(\mu+2)(1-\alpha) + m[(7+5\mu) - 8\alpha(\mu+2) + \alpha^2(9+3\mu)]\}.$$

Substituting into eqs (4) we obtain the following formulae:

$$\sigma_c = \frac{B_0^2}{96\pi(\alpha-1)\Phi}\left\{Q_1(1+\mu) + Q_2\frac{(1-\mu)}{\gamma^2} + 3m\gamma^2(1+3\mu) - 8\gamma(\gamma+m)(1+2\mu)\right\}, \tag{9a}$$

$$\sigma_r = \frac{B_0^2}{96\pi(\alpha-1)\Phi}\left\{Q_1(1+\mu) - Q_2\frac{(1-\mu)}{\gamma^2} + 3m\gamma^2(\mu+3) - 8\gamma(\gamma+m)(\mu+2)\right\}. \tag{9b}$$

The stresses are in dynes/cm^2 when B_0 is expressed in gauss. To convert to psi multiply $B_0^2 \times 14.5 \times 10^{-6}$.

784-657 O-65-4

2.3. Plane Strain

For the case of plane strain $\epsilon_z = 0$. Pursuing the method used in deriving the plane stress formulae we obtain for plane strain,

$$\sigma_c^* = \frac{B_0^2}{96\pi(\alpha-1)(\mu-1)\Phi}\left\{Q_1^* - Q_2^*\frac{(1-2\mu)}{\gamma^2} + 8\gamma(y+m)(1+\mu) - 3m\gamma^2(1+2\mu)\right\}, \tag{10a}$$

$$\sigma_r^* = \frac{B_0^2}{96\pi(\alpha-1)(\mu-1)\Phi}\left\{Q_1^* - Q_2^*\frac{(2\mu-1)}{\gamma^2} + 8\gamma(y+m)(2-\mu) - 3m\gamma^2(3-2\mu)\right\}, \tag{10b}$$

where

$$Q_1^* \equiv -8y(2-\mu)\left(\frac{\alpha^2}{\alpha+1}+1\right) + m(7-2\mu)\left(\frac{1}{\alpha^2-1}\right) - \frac{m\alpha^2}{\alpha^2-1}\{8\alpha(2-\mu)$$

$$+ 3\alpha^2(2\mu-3)\}, \text{ and } Q_2^* \equiv \frac{\alpha^2}{(\alpha^2-1)(2\mu-1)}\{8y(2-\mu)(1-\alpha) + m[(7-2\mu) - 8\alpha(2-\mu)$$

$$-3\alpha^2(2\mu-3)]\}.$$

2.4. Simplified Plane Stress

If the hoop stress at the midplane only is desired for design calculations some simplifying assumptions can be made.

$$\text{Set } B_z = B_0\left(\frac{r_0-r}{r_0-r_i}\right),$$

which requires that $y=1$ and $m=\frac{1}{\alpha-1}$ in eqs (9). The resultant equations are

$$\sigma_c = \frac{B_0^2}{96\pi(\alpha-1)\Phi}\left\{\psi_1(1+\mu) + \psi_2\left(\frac{1-\mu}{\gamma^2}\right) + \frac{3\gamma^2(1+3\mu)}{\alpha-1} - 8\gamma\left(\frac{\alpha}{\alpha-1}\right)(1+2\mu)\right\}, \tag{11a}$$

$$\sigma_r = \frac{B_0^2}{96\pi(\alpha-1)\Phi}\left\{\psi_1(1+\mu) - \psi_2\left(\frac{1-\mu}{\gamma^2}\right) + \frac{3\gamma^2(\mu+3)}{\alpha-1} - 8\gamma\left(\frac{\alpha}{\alpha-1}\right)(\mu+2)\right\}, \tag{11b}$$

where $\psi_1 \equiv \left(\frac{1}{1+\mu}\right)\left\{\psi_2(1-\mu) + 8(\mu+2) + \left(\frac{1}{\alpha-1}\right)(7+5\mu)\right\}$,

and $\psi_2 \equiv \left(\frac{1}{\mu-1}\right)\left(\frac{1}{\alpha-1}\right)\left(\frac{\alpha^2}{\alpha^2-1}\right)\{8\alpha(\mu+2) - \alpha^2(5\mu+7) - 3\mu - 9\}$.

2.5. Bitter Method

Bitter [3] has suggested the use of formulae for the thick-wall cylinder subjected to internal pressure $B_0^2/8\pi$. Utilizing this method we obtain for stresses at the coil midplane,

$$\sigma_c = \frac{B_0^2}{8\pi}\frac{1+(\alpha/\gamma)^2}{\alpha^2-1}, \tag{12a}$$

$$\sigma_r = \frac{B_0^2}{8\pi}\frac{1-(\alpha/\gamma)^2}{\alpha^2-1}. \tag{12b}$$

As mentioned earlier, eq (12b) is not applicable because the boundary condition at the inner radius is not satisfied.

2.6. Floating Shell Method

The magnet fabricated at NBS admitted annular cracks of light upon completion, indicating imperfect epoxy impregnation. Thus, it seems worthwhile to calculate the hoop stresses as if each conductor turn is self-supporting and unrestrained, but closed as in a thin wall cylinder. The magnetic pressure may be written

$$dp_m = \frac{dF_r}{dA} = \left(\frac{dF_r}{dV}\right) dr. \tag{13a}$$

Restricting this calculation to the midplane we set

$$B_z = B_0 \left(\frac{r_0 - r}{r_0 - r_i}\right),$$

$dr = t$, $dp_m = \Delta p_m$, and combine eqs (2b) and (13a) with thin shell theory to obtain

$$\sigma_c = \frac{B_0^2 \gamma(\alpha - \gamma)}{4\pi(\alpha - 1)^2 \Phi}. \tag{13b}$$

This hoop stress reaches a maximum at the radius $r = r_0/2$. Then by the floating shell method the maximum hoop stress

$$(\hat{\sigma}_c)_{\gamma=\frac{\alpha}{2}} = \frac{B_0^2}{16\pi\Phi}\left(\frac{\alpha}{\alpha - 1}\right)^2. \tag{14}$$

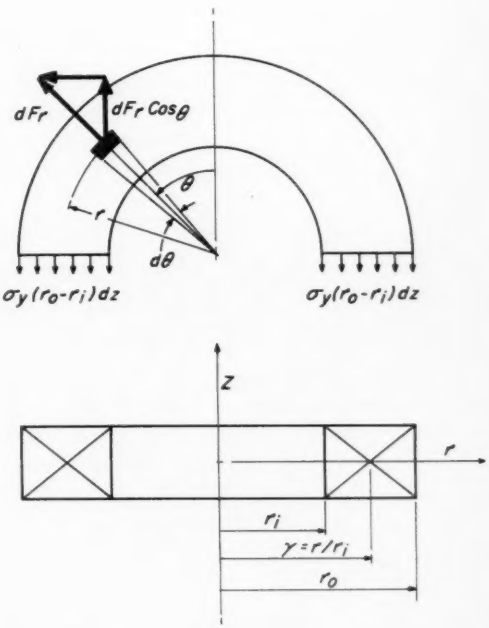

FIGURE 4. *Equilibrium of a coil disk when the entire cross section of the disk is stressed to the yield point.*

784-657 O-65-5

2.7. Burst Strength of Monolithic Disks

It is assumed that failure occurs when the coil material becomes plastic throughout. Although it has not yet been demonstrated, σ_z and σ_r are relatively low compared to σ_c, and therefore the maximum normal stress failure theory is selected. Referring to figure 4, equilibrium is satisfied when

$$2\sigma_y(r_0-r_i)dz=\int_V dF_r\cos\theta. \tag{15a}$$

Choosing unity thickness ($dz=1$) and combining eq (6b) and (15a) and performing the integration we obtain the theoretical bursting field

$$B_0^2=\frac{1.73(\alpha-1)^2\sigma_y\Phi}{(\gamma+m)(\alpha^2-1)-\frac{2m}{3}(\alpha^3-1)}, \tag{15b}$$

where B_0 is in kG and σ_y in pounds per square inch.

If for the sake of simplicity we substitute $\gamma=1$; $m=1/(\alpha-1)$ into eq (15b), the bursting field at the midplane is

$$B_0^2=\frac{5.2(\alpha-1)\sigma_y\Phi}{(\alpha+2)}. \tag{15c}$$

2.8. Axial Compression

The axial magnetic body forces are transmitted from disk to disk by the spokes of the disk separators. Thus, the forces are additive from the ends to the center so that the disk in the midplane must support the axial body forces of the entire coil. Axial equilibrium of a differential element requires that

$$\frac{d\sigma_z}{dz}=\frac{dF_z}{dV}. \tag{16}$$

In order to obtain σ_z we must evaluate $B_r(r, z)$ in eq (2c). It will be shown in the sample calculations which follow that the radial field component is approximated by an expression of the form

$$\frac{B_r}{B_0}=K_0+(\hat{K}-K_0)\left\{\sin\pi\left(\frac{\gamma-1}{\alpha-1}\right)\right\}, \tag{17a}$$

where $K_0\equiv\left\{\frac{(B_r/B_0)_{\gamma=1}+(B_r/B_0)_{\gamma=\alpha}}{2}\right\}$ for each Z/L of a fixed coil geometry, and $\hat{K}\equiv\left(\frac{B_r}{B_0}\right)_{\gamma=\frac{\alpha+1}{2}}$ (peak value of B_r/B_0 for each Z/L of a fixed coil geometry). K_0 and $\hat{K}-K_0$ can be linearly related to the axial dimension Z by;

$$K_0=m_1Z/L, \qquad \hat{K}-K_0=m_2Z/L, \tag{17b}$$

where m_1 is the slope of the K_0 versus Z/L plot, and m_2 is the slope of the $(\hat{K}-K_0)$ versus Z/L plot for a fixed coil geometry. Combining eqs (17a) and (17b) we obtain for the radial field,

$$\frac{B_r}{B_0}=\frac{Z}{L}\left\{m_1+m_2\sin\pi\left(\frac{\gamma-1}{\alpha-1}\right)\right\}. \tag{17c}$$

Combining eqs (2c), (16), (17c) and performing the integration the axial stress is derived,

$$\sigma_z = \frac{B_0^2 Z^2}{8\pi L r_i(\alpha-1)\Phi}\left\{m_1 + m_2 \sin \pi\left(\frac{\gamma-1}{\alpha-1}\right)\right\} + f(r) + C. \tag{18a}$$

Since external forces are not being considered $C=0$ and $f(r)$ is obtained from the boundary condition $(\sigma_z)_{Z=L}=0$. Performing the indicated algebra we arrive at a solution for the axial compressive stress

$$\sigma_z = -\frac{\beta B_0^2(L^2-Z^2)}{8\pi L^2(\alpha-1)\Phi}\left\{m_1 + m_2 \sin \pi\left(\frac{\gamma-1}{\alpha-1}\right)\right\}. \tag{18b}$$

This expression is applicable throughout the axial dimension of the coil. The axial stresses are largest at $Z=0$, and

$$(\sigma_z)_{Z=0} = -\frac{\beta B_0^2}{8\pi(\alpha-1)\Phi}\left\{m_1 + m_2 \sin \pi\left(\frac{\gamma-1}{\alpha-1}\right)\right\}. \tag{18c}$$

The radius at which $(\sigma_z)_{Z=0}$ becomes maximum is $\gamma = \frac{\alpha+1}{2}$. Assuming that each disk acts as a rigid plate so that the axial stress is equally distributed we find the average axial stress $(\bar{\sigma}_z)$ from

$$\bar{\sigma}_z = \frac{1}{\alpha-1}\int_1^\alpha \sigma_z d\gamma. \tag{19a}$$

Performing the indicated integration on eqs (18b) and (18c) we obtain

$$\bar{\sigma}_z = -\frac{\beta B_0^2(L^2-Z^2)}{8\pi L^2(\alpha-1)\Phi}\left\{m_1 + \frac{2m_2}{\pi}\right\}, \tag{19b}$$

and

$$(\bar{\sigma}_z)_{Z=0} = -\frac{\beta B_0^2}{8\pi(\alpha-1)\Phi}\left\{m_1 + \frac{2m_2}{\pi}\right\}. \tag{19c}$$

In order to obtain the maximum average compressive stress under the spokes of the disk separators at the midplane we need only to multiply the results of eq (19c) by the area magnification ratio $(A_{\text{disk}}/A_{\text{spokes}})$.

2.9. Sample Calculations

In order to compare the various formulae and illustrate their use, sample calculations are performed for the coil geometry of the NBS magnet.

$\alpha = \frac{r_0}{r_i} = 3.67$; $\beta = \frac{L}{r_i} = 1.87$; $r_i = 1.5$ in.; $r_0 = 5.5$ in.; $L = 2.8$ in.; $\mu = 0.33$ (aluminum); $\sigma_y = 4500$ psi; $\Phi = 0.64$. To evaluate eqs (9), (10), and (18c) we must determine the values of y, m, m_1, and m_2. All calculations will be performed for the midplane ($Z=0$) where the stresses are largest. All data for the radial and axial field components are taken from the tabulations of Brown et al., [9]. Brown and Flax [10] recently presented a graphical method for determining the magnetic field components of any finite coil by superposition of four semi-infinite solenoids. The axial field component (B_z/B_0) is plotted for various coil parameters (α, β) in figure 5. The dotted line indicates the extrapolated curve chosen to fit the coil parameters of the NBS magnet. Since β is shown to have little effect on the slope, the selection of the dotted line is based on linear extrapolation between the curves for $\alpha=3$ and $\alpha=4$. From figure 5 we obtain $y=1.04$ and $|m|=0.45$.

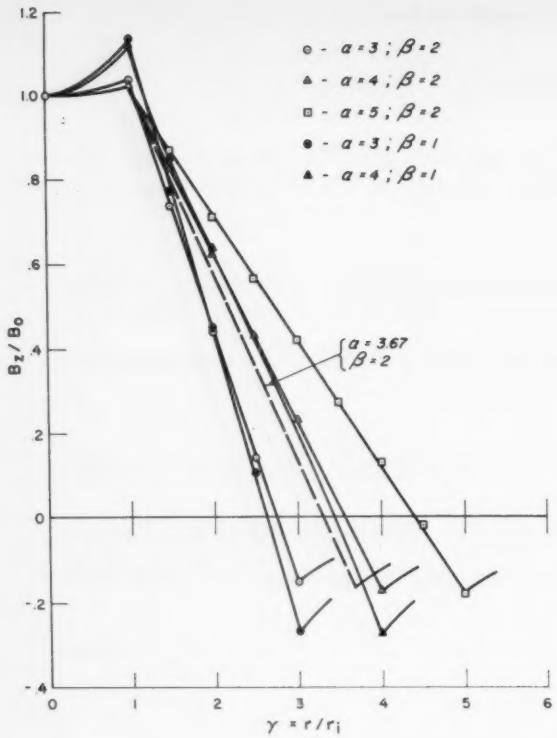

FIGURE 5. *Variation of midplane axial field with coil geometry.*

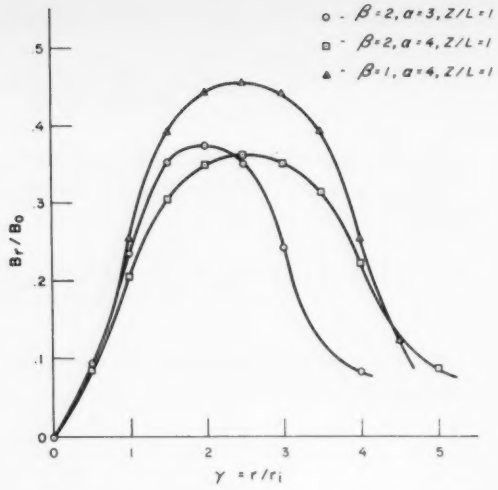

FIGURE 6. *Variation of end-plane radial field with coil geometry.*

On figure 6 is plotted the radial field component for various coil parameters. It is difficult to extend these curves to intermediate values of α and β. The effect of smaller β is to increase the magnitude of B_r/B_0 with little phase shift. Thus we plot on figure 7 the B_r/B_0 data for $\alpha=4, \beta=2$, and various Z/L. We note that the curves are essentially sinusoidal from $\gamma=1$ to $\gamma=4=\alpha$. Recalling that

$$K_0 \equiv \left\{\left(\frac{B_r}{B_0}\right)_{\gamma=1} + \left(\frac{B_r}{B_0}\right)_{\gamma=\alpha}\right\}\frac{1}{2},$$

and

$$\hat{K} \equiv \left(\frac{B_r}{B_0}\right)_{\gamma=\frac{\alpha+1}{2}},$$

we plot K_0 and $(\hat{K}-K_0)$ against Z/L on figure 8. From the K_0 plot we obtain the slope $m_1=0.213$, and from the $(\hat{K}-K_0)$ curve we obtain the slope $m_2=0.15$. Substituting these values of m_1 and m_2 into eq (17a) we check on the validity of the assumptions. The B_r/B_0 is calculated from eq (17a) and plotted on figure 7 for comparison. The calculated values plot high for lower values of Z/L; however, recall that the effect of a lower β (fig. 6) is to increase the B_r/B_0. Also, the fit is good for higher Z/L where the largest body forces are generated. The various formulae are evaluated and plotted for comparison on figure 9. From eqs (15b) and (15c) we calculate the bursting field as 93 kG and 84 kG, respectively. Using eq (19c) and an area magnification ratio of 4.4 we obtain

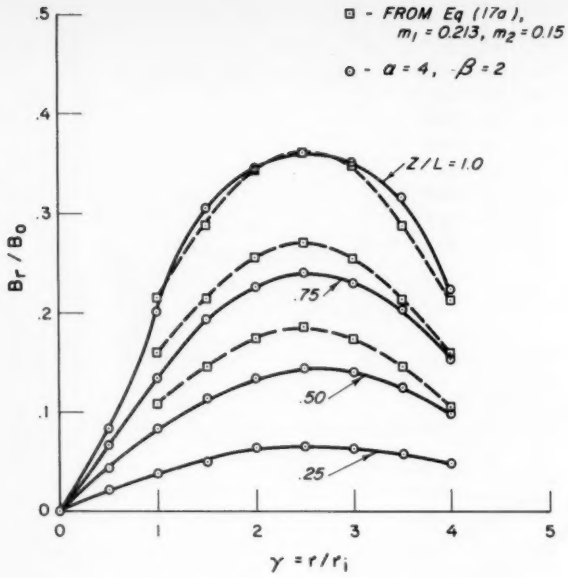

FIGURE 7. *Radial field as a function of axial position for a fixed coil geometry* ($\alpha = 4$, $\beta = 2$).

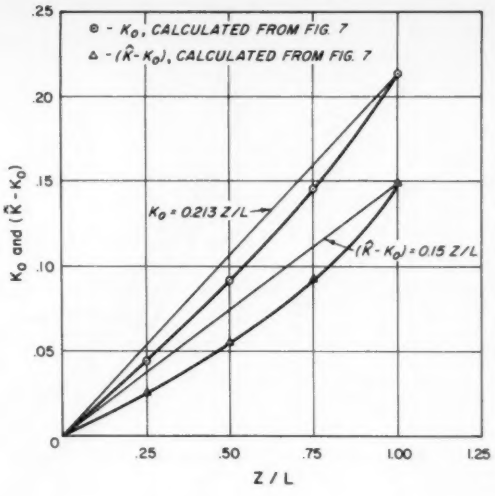

FIGURE 8. K_0 *and* $(\hat{K} - K_0)$ *as a function of axial position for a fixed coil geometry* ($\alpha = 4$, $\beta = 2$).

the average axial stress (psi) under the separator spokes as $-0.843\ B_0^2$ (B_0 in kG). The maximum hoop stress [$(\sigma_c)_{\gamma=1}$ from eq (11a)] is plotted for various coil parameters (α, β) on figure 10. Figure 11 shows the bursting field [B_0 from eq (15c)] as a function of α and β.

2.10. NBS Magnet Failure

The NBS tape-wound aluminum magnet failed electrically with intermediate structural damage at 95 kG. The magnet failure is attributed to excessive deformation at the outer radii which normally precedes bursting. Therefore, the failure field should not be much different from the actual burst field. The failure field agrees well with the 93 kG burst field calculated from eq (15b). The actual burst field is expected to exceed the theoretical value due to the frictional restraint of the axial compression (which was neglected in the analysis). Eight of the fourteen disks suffered circumferential cracks at radii of about 3.75 in. indicating excessive deformation at the outer radii and structural inhomogenieties. Some of the cracks were 0.125 in. wide. There is evidence of some radial deformation over the entire coil radii. The deformation of individual coil disks varied with coil axial position. The disks nearest the coil midplane were exposed to the largest magnetic pressure and suffered greater damage. The pronounced failure at an intermediate radius has been attributed to an intrinsic weakness in the coil disk construction. Several of the disks were rather loosely wound, and consequently some sizeable voids in the outer turns of the disk were epoxy-filled. All of the disks that failed possessed these voids from which the circumferential cracks propagated. Other disks in the coil had been tightly wound and suffered little or uniform stress damage. It would be quite difficult to determine what type structure the loosely wound epoxy-bound disk construction represents; however, it is estimated that the stresses should be intermediate to floating shell and plane stress analyses. The hoop stresses for the floating shell (eq (13b)) and simplified plane stress (eq (11a)) conditions are superimposed on the conductor yield strength

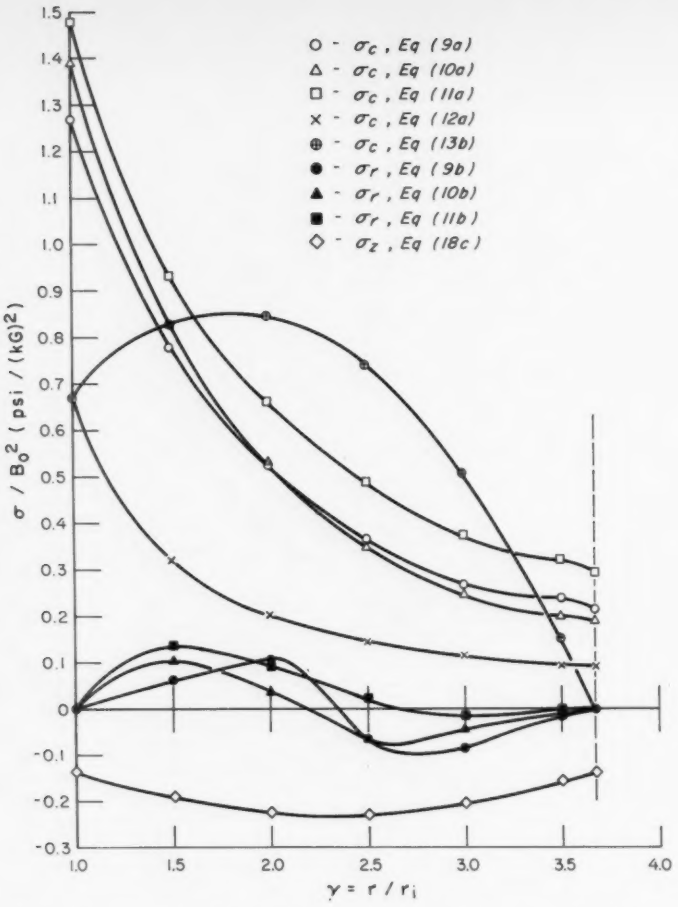

FIGURE 9. *Circumferential, radial and axial stress distributions at the midplane for the NBS magnet ($\alpha = 3.67$, $\beta = 1.87$) as computed from the various theories discussed.*

on figure 12. The variation in radii at which failure occurred is also indicated on figure 12. The conductor yield strength (0.2% offset) was experimentally determined to be 3300 psi at room temperature. The yield strength was then inferred to be 4500 psi at 20 °K (the operating temperature of the magnet). The actual strength of the material throughout the coil was unknown because the magnet had been tested at fields up to 70 kG several times prior to the 95 kG test. Thus, the material in the inner turns had been strain-hardened. Increased magnet resistance substantiated strain-hardening. The cyclic effect of strain on resistance and strength is under study; however, it is well known that the yield strength of pure aluminums can be increased three-fold at 20 °K by strain-hardening. A three-fold increase in yield strength of the inner turns of the coil disks would explain the circumferential cracks at intermediate radii when the magnetic field was increased from 70 to 95 kG. The epoxy voids provided the inherent weakness to permit the outer turns to expand radially outward from the strain-hardened inner turns. From figure 12 one could only conclude that the loosely wound turns of the epoxy-bound disks conformed more closely to the floating shell analogy. The shaded area on figure 12 indicates the region where the actual stresses for the loosely wound coils may plot. Some of the disks near the midplane were also badly damaged by axial compression. Extrusion of the conductor into the flow passages varied from 0.001

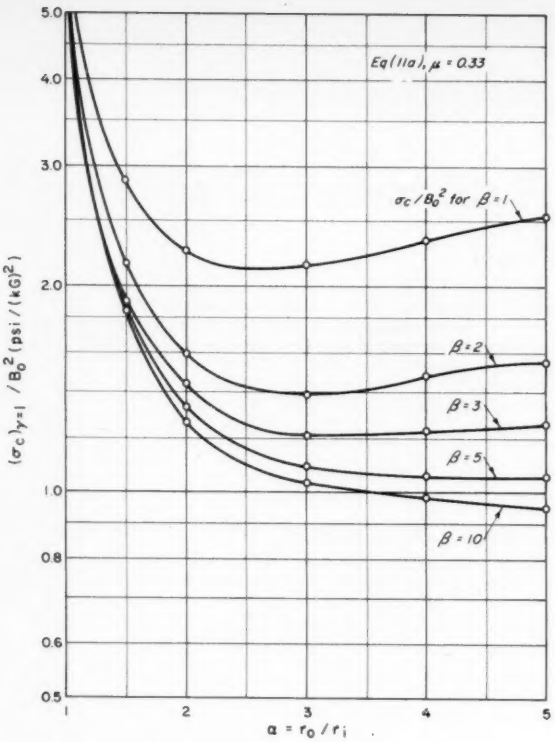

FIGURE 10. *Maximum hoop stress as a function of the coil parameters, α, β.*

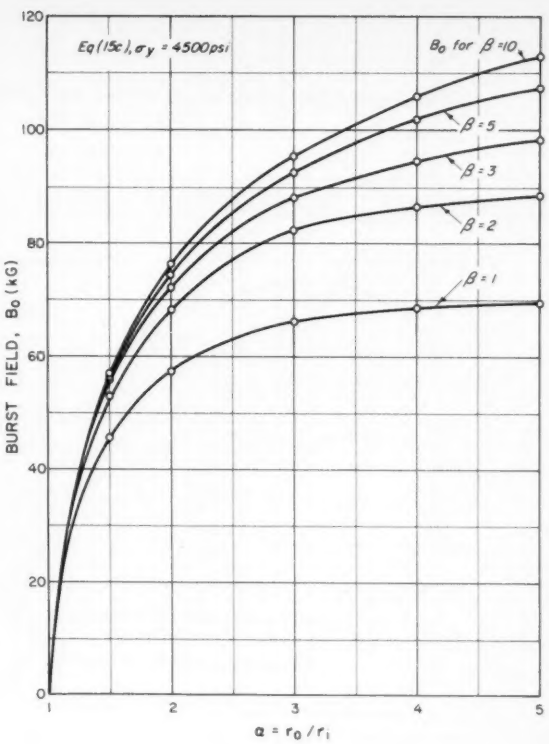

FIGURE 11. *Burst field as a function of the coil parameters, α, β.*

to 0.014 inches depending upon the disk axial position and the apparent aluminum-epoxy composite strength. Although the disks are separated by 0.025 inch fiber spacers a 0.004 in. feeler gage could not be inserted in some of the flow passages upon post-run inspection.

3. Conclusions

For quick design computations the method of Bitter, eq (12a), though nonconservative, is by far the most convenient. If a more precise analysis of both circumferential and axial stresses is desired eqs (9a) and (18c) are recommended. Equation (11a) is more convenient than eq (9a) and provides conservative results for hoop stress calculations.

Equation (13b) is suggested for hoop stress calculations on coils which are loosely wound and not integrally bound. The radial stress component is so small that it can be neglected in the coil construction described herein. Equation (11b) is recommended for those coil constructions where the radial stress is pertinent. Equation (15b) predicts the burst field of the tape-wound coil disks with reasonable precision. Equation (15b) and the simplified eq (15c) predict burst fields lower than those to be expected in practice. The actual burst field of a coil may be increased by strain-hardening the conductor through cyclic testing to the requisite fields.

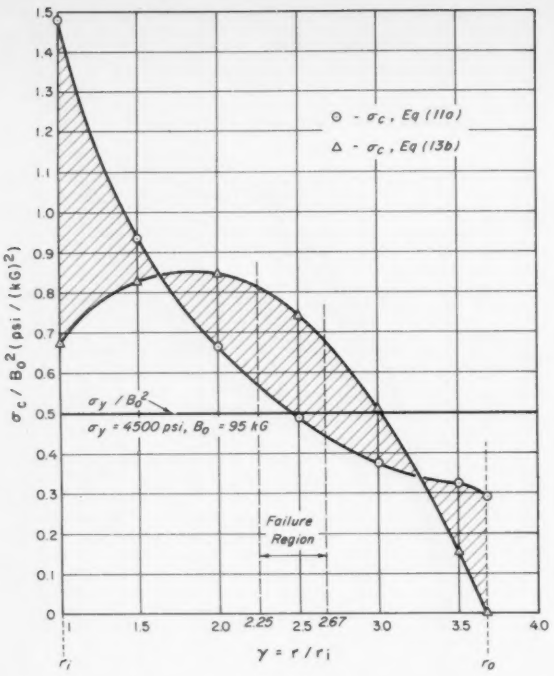

FIGURE 12. *Hoop stresses (as computed from the most dissimilar theories) and yield strength are superimposed on the failure radii of the NBS magnet.*

The author acknowledges the capable assistance of Larry L. Sparks and Jerry C. Jellison in performing the magnet experiments. Special recognition is due Vincent D. Arp for several fruitful discussions and ideas which are reflected throughout the text.

4. References

[1] J. R. Purcell and E. G. Payne, High-field liquid H_2-cooled aluminum-wound magnet, Rev. Sci. Instr. **34,** 893 (Aug. 1963).
[2] R. F. Post and C. E. Taylor, Air core cryogenic magnet coils for fusion research and high-energy nuclear physics Applications, Advan. Cryog. Eng. **5,** 13 (Plenum Press, Inc., New York, N.Y., 1960).
[3] F. Bitter, High Magnetic Fields, p. 85 (John Wiley and Sons, Inc., New York, N.Y., 1962).
[4] J. D. Cockcroft, The Design of coils for the production of strong magnetic fields, Phil. Trans. Roy. Soc. **227,** 317 (1928).
[5] J. M. Daniels, High power solenoids; stresses and stability, Brit. J. Appl. Phys. **4,** 50 (1953).
[6] W. F. Giauque and D. N. Lyon, Design of a 100-kilogauss 4-inch core solenoid for continuous operation, Rev. Sci. Instr. **31,** 374 (1960).
[7] D. R. Wells, R. G. Mills, A. Bahr, and R. L. Peskin, Project Matterhorn, Tech. Memo. No. III (1960), unpublished.
[8] D. R. Wells, Project Matterhorn, Tech. Memo. No. 30, NYO–6375 (1956), unpublished.
[9] Gerald V. Brown, Lawrence Flax, Eugene C. Itean, and James C. Laurence, Axial and Radial Magnetic Fields of Thick, Finite-Length Solenoids, NASA TR–R170 (December 1963).
[10] Gerald V. Brown and Lawrence Flax, Superposition of semi-infinite solenoids for calculating magnetic fields of thick solenoids, J. Appl. Phys. **35,** 1764 (June 1964).
[11] S. Timoshenko and J. N. Goodier, Theory of Elasticity, p. 58, 2d ed. (McGraw-Hill Book Company, Inc., New York, N.Y. 1951).
[12] S. Timoshenko, Strength of Materials, p. 207, 3d ed. (D. Van Nostrand Company, Inc., Princeton, New Jersey, 1956).

(Paper 69C4–210)

JOURNAL OF RESEARCH of the National Bureau of Standards—C. Engineering and Instrumentation
Vol. 69C, No. 4, October–December 1965

Centerline Correction for Precision Roughness Specimens

J. L. Chamberlin

(May 24, 1965)

In graphic determinations of roughness height (a measure of surface texture) a specific centerline about which the total area is measured is required. The first approximation of the position of this centerline is subjective and a repositioning was generally required. Here presented is a method for determining the roughness height without resorting to an additional area measurement.

Key Words: Centerline corrections, precision roughness specimens, roughness height.

Roughness height, one measure of the texture of a surface, is the arithmetic average deviation of the undulations of the surface, and is expressed by

$$R_a = \frac{1}{L}\int_0^L |y|dx \qquad (1)$$

where

R_a is the roughness height,
L is the length over which the roughness height is measured,
y is the amplitude of the undulations measured normal to their centerline, and
dx is the infinitesimal length measured along the centerline.

For uniform repetitive wave forms, like those comprising a precision roughness specimen, the centerline is taken as a line parallel to the general direction of the profile section of the surface tested, and so positioned that the area contained between it and those portions of the surface's profile which lie above it are equal to the area between it and the profile portions lying below it.

The length over which the roughness height is determined is generally taken as equal to a roughness-width cutoff or some whole multiple thereof. The roughness-width cutoff is the greatest spacing of repetitive surface irregularities which are to be included in the measurement for roughness height.

In the calibration of precision roughness specimens a graphical interpretation of roughness height is often employed. This results from performing the indicated integration of the roughness height defining eq (1). This integrated form is

$$R_a = \frac{1}{L}(A_T + A_B) \qquad (2)$$

where

A_T is the area between the centerline and that portion of the profile lying above it;
A_B is the area between the centerline and that portion of the profile lying below it.

In practice the surface to be measured is recorded using a surface finish analyzer. Such analyzers slowly traverse a sharp stylus across the surface. The undulation of this stylus relative to a straight datum is amplified and recorded, resulting in a magnified profile section of the surface. A centerline is positioned on this recording by visual estimation, and the length over which roughness height is to be determined is marked off to the nearest whole cycle of the undulations. The areas above and below the centerline are then planimetrically determined. If the measured areas are the same then application of eq (2), being mindful of the appropriate recorder magnifications, yields the roughness height. If the measured areas are not the same then it has been general practice to reposition the centerline and redetermine the areas.

If three conditions are met, this remeasurement may be circumvented by making a correction for the malplacement of the centerline. These conditions are as follows: First, the profile traced is comprised of uniform, repetitive wave forms; second, a minimal amount of waviness is present; and third, the difference between measured areas is small compared to their sum. Waviness is the long wavelength undulations of the surface upon which the repetitive wave forms are superimposed.

For consideration as a precision roughness specimen the first and second conditions must exist. The third condition follows as a natural consequence of the first two conditions since the more uniform the specimen, the easier it is to position the centerline. On typical specimens it is common to have the difference in areas less than 5 percent of the total area on the first visual estimation of the centerline position.

The required correction also is obtained as a consequence of the above conditions. That is, the roughness height of a specimen may be obtained from the measured areas and a knowledge of other surface parameters. In this development the measured values are primed and the desired values are not. Thus, the total measured area, A', is

$$A' = A'_T + A'_B \tag{3}$$

and the desired total area for the roughness height, A, is

$$A = A_T + A_B. \tag{4}$$

The error, E, in determining the correct area for application of eq (2) is

$$E = A - A' = A_T + A_B - (A'_T + A'_B). \tag{5}$$

The total correction is equal to the sum of the individual corrections of each cycle making up the length tested, or n times the average correction where n is the number of cycles in the length investigated. In this development figure 1 is to represent the average cycle and the corrections are developed for this case.

For the small correction to the total area involved it is sufficient to consider areas $a'abb'$ and $b'bcc'$ as trapezoids with altitude Δy.

The area above the centerline is for a single cycle

$$a_T = a'_T - \frac{\Delta y}{2}[(b'-a') + (b-a)] \tag{6}$$

and below the centerline

$$a_B = a'_B + \frac{\Delta y}{2}[(c'-b') + (c-b)] \tag{7}$$

where Δy is positive when

$$A'_T > A'_B.$$

(The lower case represents a measure referred to the single average cycle.) The error is thus

$$E = n\left\{-\frac{\Delta y}{2}[(b'-a') + (b-a)] + \frac{\Delta y}{2}[(c'-b') + (c-b)]\right\}. \tag{8}$$

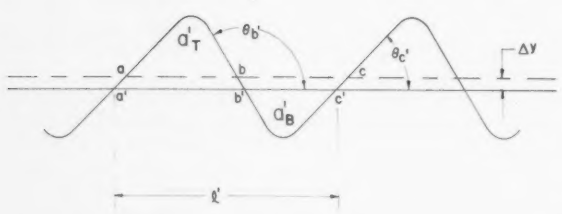

FIGURE 1. *Representation of the average cycle of a precision roughness specimen as measured about a malplaced centerline.*

But

$$(b-a) = (c-a) - (c-b)$$
$$(b'-a') = (c'-a') - (c'-b')$$
$$(c'-a') = (c-a) = l' = L'/n$$

and

$$(c-b) = (c'-b') + \Delta y(\cot\theta_{c'} - \cot\theta_{b'}). \tag{9}$$

Thus, the error becomes, upon substitution of eqs (9),

$$E = n\{-\Delta y[l' - 2(c'-b') - \Delta y(\cot\theta_{c'} - \cot\theta_{b'})]\} \tag{10}$$

By definition

$$A_T - A_B = 0$$

and

$$A'_T - A'_B = \Delta A'. \tag{11}$$

Therefore the measured area difference is

$$\Delta A' = \frac{n\Delta y}{2}[(b'-a') + (b-a) + (c'-b') + (c-b)]$$

or upon reduction

$$\Delta A' = L'\Delta y. \tag{12}$$

The area required for the roughness determination is therefore

$$A = A' - \frac{\Delta A'}{L'} n[l' - 2(c'-b') - \frac{\Delta A'}{L'}(\cot\theta_{c'} - \cot\theta_{b'})]. \tag{13}$$

The desired roughness height based on measurements made with a malplaced centerline is therefore

$$R_a = R_{a'} - \frac{\Delta A'}{L'}\left[1 - \frac{2(c'-b')}{L'/n} - \frac{\Delta A'}{L'}\frac{(\cot\theta_{c'} - \cot\theta_{b'})}{L'/n}\right]. \tag{14}$$

In practice the parameters of the average cycle used in the adjustment of the roughness height are the averages of individual values measured at points randomly chosen along the trace. Because of the uniformity of most precision roughness specimens it is satisfactory to use the cotangent of the average angle rather than the average cotangent of the angles. For example, the cotangent of the average angle and the average cotangent of the angles for four precision roughness specimens that were being tested during

the writing of this paper are shown in table 1. The values given are for five individual measurements made along the recorded trace. The recorded traces contained eight cycles for specimens 1 and 2 and ten cycles for specimens 3 and 4.

TABLE 1

Specimen	$\cot \bar{\theta}_{b'}$	$\overline{\cot \theta_{b'}}$	Range of $\theta_{b'}$	$\cot \bar{\theta}_{c'}$	$\overline{\cot \theta_{c'}}$	Range of $\theta_{c'}$
			Degree			*Degree*
1	−0.895	−0.896	3.2	1.155	1.155	1.5
2	−.887	−.888	2.4	1.108	1.111	5.9
3	−.202	−.202	2.2	0.233	0.233	1.5
4	−.186	−.186	2.2	.246	.247	4.1

To illustrate the use of the correcting equation, the roughness height of a trace similar to that shown in figure 2 was measured using a visually estimated centerline and four malplaced lines. The malplaced lines were approximately 0.05 and 0.10 in. above and below the centerline. The results are tabulated in table 2.

TABLE 2

Position	$A_{T'}$	$A_{B'}$	L'	$(\overline{c'-b'})$	$\cot \bar{\theta}_{b'}$	$\cot \bar{\theta}_{c'}$	$R_{a'}$	R_a
	sq. inches	*sq. inches*	*Inches*	*Inch*			*Inch*	*Inch*
0.10 in. above	1.378	2.123	7.523	0.512	−0.1475	0.3344	0.465_8	0.461_6
0.05 in. above	1.612	1.872	7.521	.483	−.1514	.3211	$.463_2$	$.462_9$
Centerline	1.775	1.704	7.524	.462	−.1530	.3213	$.462_4$	$.462_4$
0.05 in. below	1.932	1.567	7.527	.442	−.1534	.3276	$.464_9$	$.463_1$
0.10 in. below	2.131	1.383	7.526	.421	−.1562	.3325	$.466_9$	$.461_6$

Each of the average values is based on eight individual measurements. The trace contained eight cycles.

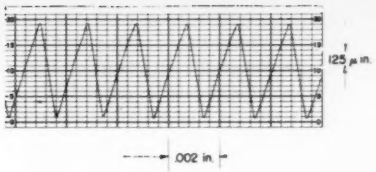

FIGURE 2. *Typical trace of the precision roughness specimen used in illustrating the correcting equation.*

To obtain the specimen's roughness height, the roughness height obtained from measurement on the recorded trace needs to be divided by the vertical magnification of the recorder. In this example, the vertical magnification was 2112 ×.

In this example 24 min were required to position a line and measure the areas about it. It required 17 min to measure the various parameters and to calculate the correction. A time savings of 29 percent could have been achieved in this case over repositioning for a malplaced centerline.

The use of this correcting equation has eliminated the centerline repositioning for graphic roughness height determinations. The time required to measure the necessary parameters is less than that required to reposition the centerline and make a new planimetric determination. Depending upon the complexity of the trace being measured, time savings up to 75 percent are possible.

(Paper 69C4–211)

JOURNAL OF RESEARCH of the National Bureau of Standards—C. Engineering and Instrumentation
Vol. 69C, No. 4, October–December 1965

Electric Currents and Potentials Resulting From the Flow of Charged Liquid Hydrocarbons Through Short Pipes

M. R. Shafer, D. W. Baker, and K. R. Benson

(June 21, 1965)

The electrical currents and potentials produced in pipes of intermediate and very high resistivities, by the flow of a charged liquid hydrocarbon have been investigated. The maximum pipe currents to the ground were in the range 1 to 6 microamperes. Depending upon the electrical resistance of the pipes, these currents produced potentials ranging from essentially zero to values in excess of 30,000 volts which were sufficiently severe to cause electrical breakdown and arcs within some of the pipes under investigation. It is concluded that hazardous pipe potentials, resulting from static electricity, can be eliminated in practical applications if the electrical resistance from each and any portion of the interior surface of the pipe to the ground does not exceed about 10^7 ohms.

Key Words: Breakdown, charged liquid hydrocarbons, charging tendency, charge separation, current, filters, inner liner, petroleum liquids, potential, relaxation, resistance, static electricity, tetrafluoroethylene tubing.

1. Introduction

The petroleum industry has long been concerned with the problem of static electricity resulting from the flow of relatively nonconducting liquid hydrocarbons through pipes, filters, and other components. Considerable literature is available which considers methods by which such charges are produced and the hazards arising from the introduction of electrically charged petroleum liquids into receiving tanks, as frequently occurs during refinery and fueling operations.

Problems related to the electrical currents and potentials produced in pipes and hoses through which charged petroleum liquids flow have not been investigated thoroughly. Carruthers and Marsh [1][1] and Carruthers and Wigley [2] considered this problem recently and developed equations relating the currents and potentials produced with the electrical resistance of the pipe, the electrical characteristics of the fuel and its velocity. Experimental checks were performed using pipes of essentially infinite and zero electrical resistance. Although these conditions were well suited for investigations of charge relaxation, neither condition provided experimental verification of the potentials produced in pipes having large, but not infinite, values of electrical resistance.

Under the sponsorship of the Department of the Navy, Bureau of Naval Weapons, the National Bureau of Standards has conducted an investigation to determine the desirable electrical resistance characteristics of hoses used to interconnect the various fuel handling components of aircraft and other internal combustion engines. It is believed that some of the results of the investigation are of sufficient general interest for presentation here as they provide further experimental verification of the theory and ideas presented in [1] and [2] and their Discussions.

The experimental investigations to be described were concerned primarily with a determination of the magnitude of electrical currents and voltages encountered in pipes of intermediate and very high resistivities through which electrically charged liquid petroleum flows. The pipes had a nominal inside diameter of 0.875-in. and lengths in the range of 20 to 48 in. Flowrates of 5 to 30 gal per minute were used with fuels having conductivities of 8 to 200 picomho per meter. Pipe currents to the ground encompassed the range 10^{-8} to 6×10^{-6} A. Depending upon the electrical resistance of the pipes, these currents produced potentials ranging from essentially zero to values in excess of 30,000 V, which were sufficiently high to cause electrical breakdown and arcs within some of the pipes under test.

2. Theoretical Considerations

Consider a pipe of length L, as shown in figure 1, through which a relatively nonconducting liquid is flowing at a mean axial velocity v. The liquid entering the section may or may not contain a significant initial charge q_i per unit length of pipe which corresponds to a convection current $I_i=q_iv$ entering the section under consideration. Likewise the liquid leaves the pipe with a charge q_u per unit length of

[1] Figures in brackets indicate the literature references on page 316.

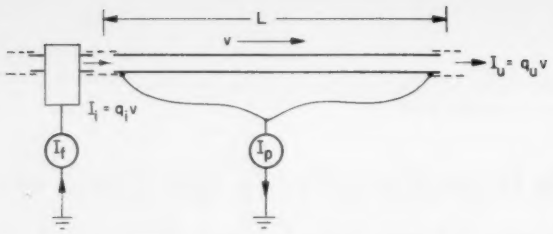

FIGURE 1. *Electric currents resulting from the flow of a fluid.*

pipe causing an exit convection current $I_u = q_u v$. As discussed in [1], the value of q_u and hence I_u is dependent upon: the magnitude of I_i, the resistivity of the fuel, the residence time, t, during which the fuel remains within the length of pipe, and the amount of charge separation which occurs at the fuel-pipe interface.

The equilibrium current $I_p = I_i - I_u$, flowing from the pipe to the ground, is a direct measure of the net rate at which charges are deposited on the interior surface of the pipe during passage of the fuel. It is conveniently measured by electrically insulating the pipe section from the remainder of the flow circuit and from the ground, and electrically connecting each end of this section to the ground through a suitable ammeter.

Convenient instrumentation for the direct measure of I_i is not available. However, when a charge-producing component such as a microfilter is placed immediately upstream of the test section, the current I_f between the filter and the ground is approximately equal to I_i. This filter current is conveniently measured by an ammeter if the filter is electrically insulated from the remainder of the flow circuit. Thus, $I_f = I_i$ provided the fuel entering the filter is essentially uncharged.

The relation between I_p and I_i, as developed in the appendix, is

$$I_p = (I_i - I_0)(1 - e^{-\lambda}) \tag{1}$$

where I_0 is the convection current that would emerge with the liquid from an infinitely long pipe under the same conditions. If I_i is caused by a filter placed immediately upstream from the test section and is large compared to I_0, then the relation

$$I_p \approx I_f(1 - e^{-\lambda}) \tag{2}$$

should be correct for the more severe charging conditions.

The term λ is the ratio of resistance time, L/v, of the liquid in the pipe to relaxation time, τ, of the liquid. Relaxation time is the time required for the charge existing in the stationary fuel to be reduced 63 percent in magnitude by electrostatic forces.

Considering a pipe grounded at each end, an approximate relation for the maximum potential developed on the pipe wall, as a result of current I_p, is

$$V_{max} = 0.1\, R_T I_p, \tag{3}$$

where R_T is the end-to-end resistance. Commencing with an expression from [1] for the voltage developed on the pipe wall at any distance from the inlet, this relation has been developed in the appendix subject to the following assumptions:

(a) The ratio λ has numerical value less than 6.

(b) The electrical resistance R_T of the pipe is small compared to that of the liquid contained within the pipe.

The constant 0.1 of eq (3) varies through the approximate range 0.08 to 0.13 for values of $\lambda < 6$. Values of $\lambda > 6$ are encountered only with long pipes, fuel of very high conductivities, or very low fuel velocities for which conditions nearly all of the separation of charges, q_i, occurs near the entrance of the pipe. Values of $\lambda < 6$ are those normally encountered during the flow of liquid petroleum products, and a constant factor of 0.1 can be selected for this range of λ with little sacrifice in accuracy.

The assumption that pipe resistance R_T is small compared to that of the liquid within the pipe is valid for pipes having resistances no greater than 10^{10} Ω per linear inch of length even when fuels having conductivities as large as 200 pmho/m are involved. Pipes having higher electrical resistances are not considered desirable because of the possibility of electrical discharges resulting from the extremely high voltages produced. Thus, it is believed the assumptions involved in deriving the approximate relation expressed in eq (3) are valid as far as practical applications are concerned.

It is of interest to note that eq (3) is essentially identical to the relation $V_{max} = 0.106(I_i - I_0)R_T$ which was presented by Dr. Klinkenberg in the Discussion of [2].

Data were obtained during these experiments which verifies eqs (2) and (3) using pipe specimens having R_T values in the range zero to 10^{10} Ω. Also, the influence of the electrical resistance of the pipe on the current I_p was investigated; and the electrical breakdown phenomena which occur when large values of I_p are encountered in pipes having extremely high values of R_T were observed.

3. Experimental Apparatus

The flow circuit, shown in figure 2, included a supply tank containing 50 gal of naptha and a centrifugal pump of 30 gpm capacity. The flow then passed through a suitable flowmeter into the microfilter used for the generation of the initial charge q_i. A by-pass valve was installed to provide a method of directing the flow through or around the filter as desired. The pipe sample under test was connected immediately downstream from the filter and the fuel then returned through a flow control valve to either the supply or receiver tank as desired. Each end of the pipe sample, as well as the entrance connection to the

filter, was electrically insulated from the flow system by short lengths of nonconductive tetrafluoroethylene (TFE) tubing. Short adapters, of metal tubing, were used as connectors between the ends of the test pipe and the insulating tubing. They were inserted into the ends of the test pipe to a depth of about one inch, thus forming internal electrodes. These two electrodes were electrically connected to each other and to the ground through an ammeter for the measurement of I_p. Likewise, the filter was connected to the ground through another ammeter for the measurement of I_f. All other portions of the flow system were constructed from conductive materials and grounded as in normal service.

The liquid used throughout the tests was a water-white, hydrocarbon naptha designated as MIL–F–7024A, Type II. This naptha has a 60/60 °F specific gravity of 0.771, a kinematic viscosity at 80 °F of about 1.2 centistokes, an initial distillation point above 300 °F, and a flash point above 100 °F. The electrical conductivity of the naptha as received, in 55-gal drums, at our laboratory is about 1 pmho/m. Contaminants were added to obtain the appreciable filter charging effects required.

Two different filters were used. Each had an external metal body containing a phenolic resin impregnated paper element. One filter had a 25-μm size element of a pleated design containing a total of 35 pleats 1-in. deep by 4.5-in. long giving a total filter surface area of about 300 in.^{2} The nominal flow rating of this element was 25 gpm with a fuel of 1 centistroke viscosity. The second filter had a 10-μm size element of a stacked-paper washer design having a length of 4 in., an outside diameter of 1.5 in., giving a total filter surface area of about 18 in.^{2} This element had a nominal flow rating of 5 gpm with a fuel of 1 centistoke viscosity. Both of these filters and their elements were identical in size and design to those commonly used in fuel systems of some internal combustion engines.

The ammeters used for the measurement of I_f and I_p were multipurpose electrometers having a range 10^{-13} to 3 A full scale. The voltage drop of these instruments never exceeded 1 V during the measurement of current.

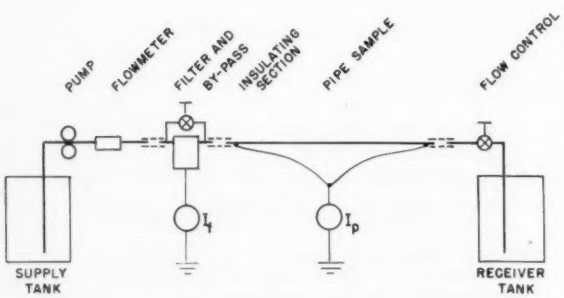

FIGURE 2. *Diagram of the flow circuit.*

Pipe potentials of less than 100 V were measured with a multipurpose electrometer having a resistance to ground of the order of 10^{14} Ω. Voltages in the range 100 to 10,000 V were measured with electrostatic voltmeters having resistances to ground of the order of 10^{16} Ω. No attempts were made to measure potentials exceeding 10,000 V as corona effects with the resulting breakdown of resistance were always encountered in this region.

Pin-type probes were constructed for the measurement of the potentials developed on the inner surfaces of the pipe walls. As will be discussed in detail, the test specimens were tetrafluoroethylene (TFE) tubing containing an inner liner of intermediate resistivity and having a total wall thickness of 0.040-in. The probes contained pin points about 0.06-in. long and were inserted through the tubing from the outside, thus puncturing and making electrical contact with the inside conductive liner of the pipe. Two pins pierced the wall at each probe location.

Fuel conductivities were determined by a conductivity cell constructed in accordance with figure 8 of reference [3]. The actual plate separation was 7.9 mm. A constant test potential of 150 V dc was used resulting in a test potential gradient of 19 V/mm. Significant polarization was obtained during the determination of fuel conductivities as evidenced by a considerable and continuous decrease in current with time under the condition of a constant applied voltage. For comparative purposes, the current used to compute fuel conductivity was that occurring 30 sec after applying the test voltage to the cell. Experience with this and other methods of conductivity measurement indicates that the determination of fuel conductivity is not an exact art.

4. Test Specimens

The pipe samples used during the investigation had nominal inside diameters of 0.875-in. and their lengths were in the range 20 to 48 in. One sample was a 22-in. length of stainless steel tubing which for purposes of this investigation is considered to have zero electrical resistance. All of the other samples were formed from the thermoplastic tetrafluoroethylene (TFE) which in a pure state has a volume resistivity $> 10^{18}$ Ω-cm. Each sample of TFE pipe had a wall thickness of about 0.040-in. The dielectric strength of the pure TFE was such that electrical breakdown would not occur when a potential of 30,000 V dc was applied across the wall.

Experimental samples of intermediate resistivity TFE tube were produced for use in this investigation by members of the aircraft hose industry. These differed from conventional, pure TFE in that each contained an inner layer to which small amounts of carbon had been added. This resulted in an inner liner of moderate conductivity, about 0.010-in. thick, extending the full length of the pipe and attached to and surrounded by an outer wall of nonconductive TFE about 0.030-in. thick. Thus, electrical conduction was in the longitudinal direction only.

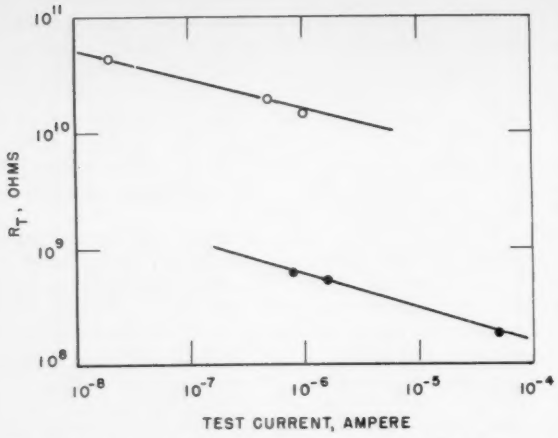

FIGURE 3. *End-to-end resistance of two samples of TFE pipe with carbon inner liners showing the variation in resistance with current.*

○ Sample A. ● Sample B

Pipes made in this manner have a voltage dependent, nonlinear, electrical resistance which tends to decrease appreciably with increased potential gradient. Thus, in performing tests to determine the ohmic resistances of the samples, it was found that current is a nonlinear function of the applied voltage. Typical results of end-to-end resistance tests of two of the pipe samples, 36 in. long, are shown in figure 3. These resistance values were obtained by applying selected constant test potentials across the pipe sections and measuring the resulting current. Unless stated otherwise, R_T values listed in this paper are those obtained with a test current of 1μA.

5. Tests and Results

5.1. Fuel Contamination and Filter Charging Tendency

Initial tests were conducted to investigate the relation between fuel contamination and the charging tendency of paper microfilters. The flow circuit, as shown in figure 2, utilized a two-tank system to enable use of one tank for supply and the other as a receiver. This system is desirable for experiments with fuels of low conductivities as it ensures uncharged fuel entering the pump inlet line. Thus, service operating conditions are duplicated closely. In these tests, a 48-in. length of semiconductive TFE tube ($R_T = 50\text{M}\Omega$) was used as the pipe sample, and the filter current, I_f, and pipe current I_p to the ground were measured.

The naptha had an initial conductivity of about 1 pmho/m. The two contaminants investigated were asphaltenes and a commercial antistatic compound (ASC). Fuel conductivities in the range 2 to 200 pmho/m were obtained by varying the concentration of these two materials. The asphaltenes were dispersed quickly and evenly throughout the test naptha by first dissolving in isopropylbenzene (Cumene). In order to generate large charging currents, these initial tests were performed with the 5-gpm stacked paper filter at a flowrate of 8 gpm through the filter. This corresponds to an average velocity of 4 ft/sec across the section of the 0.875 i. d. TFE pipe specimen.

The results of the stacked-paper filter charging tendency tests are shown in figure 4, a plot of filter current versus the fuel conductivity. Contamination with asphaltenes gave very significant filter charging currents with fuel conductivities above 10 pmho/m. The maximum charging tendency obtained by contamination with the antistatic compound (ASC) was only about 1/25 of that obtained with the asphaltenes under identical test conditions. Also, with the ASC contaminant, charging tendency decreased rapidly to a low value as conductivity exceeded 100 pmho/m. One additional point on figure 4 shows the effect of adding a small amount of the ASC to the asphaltenes mixture having an original conductivity of about 200 pmho/m. A considerable decrease in charging tendency was noted with a relatively small increase in fuel conductivity.

The charging tendency of the napthas containing the asphaltenes and ASC contaminants were also studied using the apparatus described on page 50 of reference [3]. Briefly, this provides a method of determining the amount of electric charge produced as a fuel flows by gravity through a steel capillary having an inside diameter of 3 mm and a length of

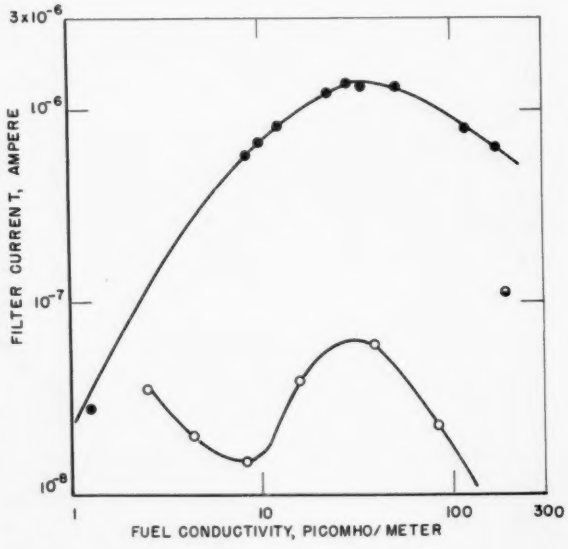

FIGURE 4. *Charging tendency of a stacked-paper filter at a constant flowrate of 8 gpm showing the influence of fuel conductivity with two different fuel contaminants.*

● Asphaltenes. ○ ASC Antistatic Compound. ◒ Asphaltenes plus ASC.

0.5 m. No relationship was found to exist between charging tendencies obtained with the paper filter as compared to those obtained using the steel capillary. In fact, the ASC contaminant gave approximately the same charging tendencies in the steel capillary as was obtained with asphaltene contamination.

Also in tests of other fuels having conductivities of 84 and 165 pmho/m caused by unknown contaminants, relatively insignificant charging tendencies were indicated by tests with the steel capillary while extremely large charging currents were obtained when the same fuels flowed through paper microfilters.

Thus, the investigation of the relation between contamination, fuel conductivity, and charging tendency showed that the charging tendency of a given liquid hydrocarbon is not related to fuel conductivity alone. Rather, as might be expected, it is dependent upon both the material and the amount of the contaminant in the liquid and upon the wall material at the liquid-wall interface. The investigation also showed that maximum charging tendency in microfilters will likely occur when fuel conductivity exceeds 10 pmho/m.

5.2. Preliminary Tests With Various Pipe Samples

Preliminary experiments were conducted with various pipe samples to determine: (a) the magnitude of pipe currents to be expected from pipes installed immediately downstream from the microfilters; (b) the influence of flowrate upon these pipe currents; and (c) whether the electrical conductivity of the pipe had a significant influence upon these currents. Fuel having a conductivity of 165 pmho/m was used throughout the preliminary tests. Pipe current, I_p, was measured, but unfortunately, the filter current, I_f, was not measured during the preliminary tests. However, an effort was made to keep the test conditions the same as the different pipe specimens were investigated. Thus, it can be assumed that the convection currents, I_i, entering the different test specimens were approximately equal at identical flowrate conditions. Only the pleated-paper filter was used during these tests. The filter by-pass valve in figure 2 was closed; thus all flow passed through the filter.

The pipe specimens selected for the preliminary tests all had a length of 22 in. These included a stainless steel tube and two samples of TFE pipe containing carbon inner liners having R_T values of 10^6 and 10^9 Ω. Voltage measurements were not made and the pin-type probes were not applied to the test samples.

The results of the preliminary tests are shown in figure 5. It is seen that I_p increased significantly with flowrate and that the largest values observed were in the range 2 to 6 μA. Also, the pipe currents were about equal in magnitude for all values of pipe resistance investigated. Thus, it was verified (as might be expected) that pipe resistance has very little influence, if any, upon the rate of relaxation of charges from the charged fuel to the walls of the pipe.

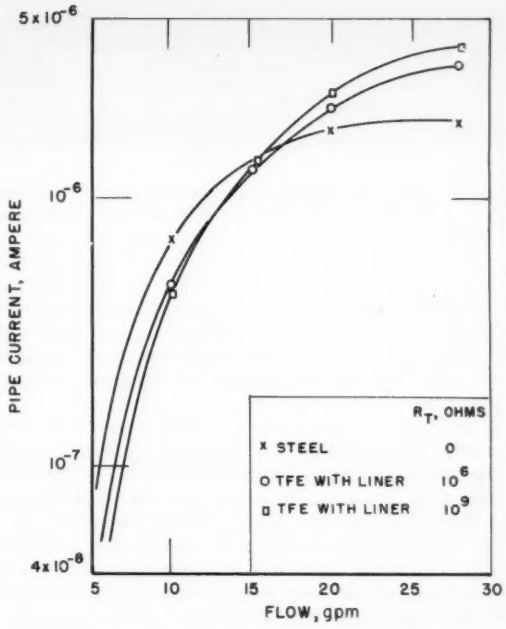

FIGURE 5. *Current to the ground from pipes of different resistivities, as influenced by flowrate (each pipe 22-in. long installed downstream from a pleated-paper filter, fuel conductivity 165 pmho/m).*

5.3. Electrical Breakdown in Nonconductive Pipes

When a nonconductive TFE pipe sample 22-in. long, was inserted in this same flow circuit, electrical sparks and other discharges occurring from the sample were observed. Also pinhole punctures appeared in the walls of the sample through which fuel slowly seeped to the atmosphere. The conditions leading to the electrical breakdown of the pure TFE pipe follow.

An unpunctured, translucent sample of bare TFE pipe 22-in. long, wall thickness 0.040-in., was installed downstream from a paper microfilter. The sample was electrically insulated from the remainder of the flow system by short lengths of TFE tubing. Short metal adapters were inserted between each end of the sample and the insulating tubing. These two adapters were electrically connected to each other and to the ground. A probe for measuring electrostatic potential was installed on the outside at the center of the sample. This consisted of a TFE insulator bushing, 0.25-in. wall thickness, having an aluminum foil strip wrapped around the exterior and connected to an electrostatic voltmeter. There was no other grounded metallic object close to the TFE pipe.

With the room darkened so electrical discharges could be seen more readily and using a fuel having a conductivity of about 165 pmho/m, flow through the system was quickly adjusted to 15 gpm at 25 psig.

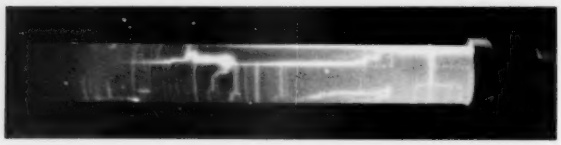

FIGURE 6. *Electrical discharges in a pure TFE pipe connected downstream from a pleated-paper filter (flowrate 15 gpm, fuel conductivity 165 pmho/m).*

The electrostatic voltmeter rose rapidly to a maximum of about 8 kV and then oscillated about this value indicating that some electrical discharges were likely occurring. These preliminary discharges were not visible in the darkened room.

After a period ranging from about 1 to 4 min at this constant flow condition, a very bright electrical discharge took place inside of the pipe. It consisted of bright flashes running lengthwise inside of the tube with numerous lateral flahses branching off as shown in the photograph of figure 6. After this initial discharge, the voltmeter oscillated about the 5 kV point, and the wall of the test pipe contained numerous pinhole punctures through which fuel slowly seeped.

Light for the photograph of figure 6 was obtained entirely from the electrical discharge which took place within the translucent pipe sample. The actual portion of the pipe shown is the upstream part with the entrance to the left and the TFE insulator bushing of the voltage probe at the right. The scale of the picture may be determined from the approximate tube diameter of 0.9-in.

Three pinhole punctures caused by the electrical discharge may be noted in figure 6. One is on the top of the pipe near the TFE insulator bushing. The second is the bright spot in the center of the pipe; and, the third is a bright spot at the bottom of the pipe towards the entrance end. None of these punctures were present prior to the initial breakdown.

When the TFE pipe was cut open to display the inner surface after the initial breakdown, the paths over which the numerous spark discharges occurred were observed. Rather wide and deep transverse and sometimes lateral paths were found to be centered about each pinhole puncture. Lighter paths branched off from these to cover practically the whole interior surface of the pipe with a rectangular network pattern in which the distance between paths was of the order of a few millimeters. The impression gained from this network is that of electrical charges draining along tributary paths to a central stream and thence to a puncture point. Also, it is believed that the paths traced by the spark discharges are proof that discharges such as are shown in figure 6 occur along the inner surface of the pipe and not in the liquid itself.

As flow continued after the initial breakdown, a glow discharge and sometimes small sparks were noted within the pipe centered about one or more of the punctured points. Electricity in the form of a purple corona discharge was seen streaming into the punctured points from the air. This corona discharge continued so long as the fuel flowed and its effect was to enlarge or erode the pinhole punctures.

Although not known definitely, it seems reasonable that the potentials existing just prior to breakdown may have been in the range 50 to 100 kV as this would likely be sufficient to cause the dielectric failure of the pipe wall. The electrical breakdown of nonconductive TFE pipe as described above is repeatable. It was observed in the same manner with numerous pipe samples, and other photographs of these initial breakdown flashes have been obtained.

5.4. Current-Voltage-Resistance Relationship

Three samples of TFE pipe with carbon inner liners, designated as A, B, and C, each having a length of 36 in., were selected for the investigation of the current, voltage, resistance relationship as expressed in eq (3). The end-to-end resistances R_T of samples A and B are given in figure 3. The resistances of samples A, B, and C were 14,000, 600, and 12 MΩ, respectively, with a test current of 1 μA. Using the flow circuit of figure 2, pipe current, I_p, filter current, I_f, and pipe potential, V_{max}, were measured. Pin-type probes described previously were placed on the test samples at distances of 9, 18, and 27 in. from the upstream end for the measurement of V_{max}. The potential between each of these three probes and the ground was measured with high impedance voltmeters for each flow condition established.

The hydrocarbon naptha had a conductivity of 84 pmho/m throughout these tests. Flow rates in the range 5 to 26 gpm were selected. These rates, in combination with the particular fuel conductivity and the inside pipe diameter of 0.875-in., resulted in values of λ in the range 1 to 6. Pipe currents, I_p, ranging from 2×10^{-10} to 3×10^{-6} A could be obtained conveniently by conducting tests with the filter by-pass valve both open and closed over the range of flowrates selected.

The results of these tests are summarized in figure 7, a log-log plot of the maximum pipe potential, V_{max}, determined from measurements at the three probes, as a function of the current, I_p, from the pipe to the ground. All of the pipe currents in figure 7 having a magnitude less than 10^{-7} A were negative. These were obtained with the filter by-pass valve open, a condition of minimum filter charging. It is believed these smaller currents all resulted from the separation of charges at the liquid-pipe interface. The pipe potentials corresponding to these small negative currents were also negative with the single exception of sample A at 5×10^{-10} A where positive readings of voltage were obtained. No explanation can be suggested for this single deviation, but it is of interest to note this test point does not lie on the straight line defined by the other points.

All I_p currents greater than 10^{-7} A were positive and were obtained with flow through the filter, i.e., the by-pass valve completely closed. These larger cur-

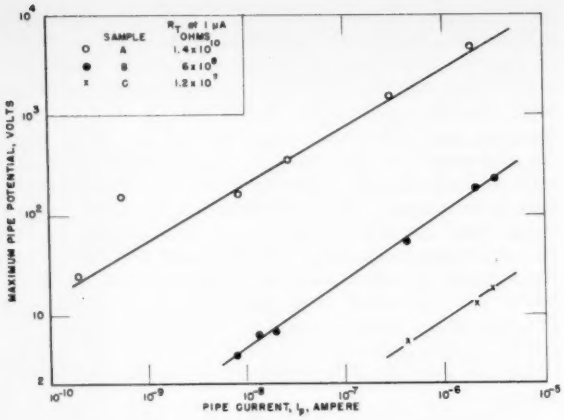

FIGURE 7. *Maximum potential versus pipe current in pipes with carbon inner liners (length 36 in., flowrate range 5 to 26 gpm, fuel conductivity 84 pmho/m).*

rents were the result of the separation from the fuel to the wall of the pipe of charges produced during flow through the filter. Also, all potentials resulting from the positive currents were likewise positive.

Still referring to figure 7, it is seen that one straight line for each pipe sample defines the test points quite closely and the slopes of these three lines are approximately equal. Also, the slopes are considerably less than 45°, indicating that the resistances of the three pipe samples were not constant, but tended to decrease with increasing voltage.

The experimentally determined maximum pipe potentials of figure 7 can be compared to those predicted by eq (3) provided R_T values corresponding to the pipe currents under consideration are used. Figure 3 gives these values for samples A and B. In selecting a value of R_T from this figure which corresponds to a designated I_p current, it is assumed that the net deposition of charges is relatively uniform lengthwise along the pipe. Thus, the average current existing in the wall of the pipe can be considered to be approximately 0.25 I_p. This is the current which has been used in obtaining values of R_T from figure 3.

The comparison of calculated and measured maximum pipe potentials for samples A and B is presented in table 1. Considering the practical difficulties involved in measuring R_T and V_{max} accurately it is believed that good agreement between the calculated and measured values was obtained. Certainly agreement such as this is quite adequate for the practical purpose of estimating potentials to be encountered in pipes through which a known current I_p to the ground is encountered. However, it must be realized that eq (3) applies only to the conditions in which the conductive portion of the pipe is in actual contact with the fuel throughout its length and the pipe is in electrical contact with the ground only at the two ends. Grounding of the conductive portion of the pipe at many locations throughout the length will of course result in lower voltages. Insulating the conductive portion of the pipe from the fuel will likely result in potentials having magnitudes sufficient to cause electrical breakdown.

TABLE 1. *Comparison of calculated and measured maximum pipe voltages*

Sample	I_p	R_T (fig. 3)	Maximum pipe voltage	
			Calculated $V_{max} = 0.1 R_T I_p$	Measured (fig. 7)
	Amperes	*Ohms*	*Volts*	*Volts*
A	10^{-7}	4×10^{10}	400	700
	10^{-6}	2.2×10^{10}	2,200	2,700
	10^{-3}	1.2×10^{10}	12,000	11,000
B	10^{-6}	9.3×10^{8}	90	100
	10^{-3}	4.7×10^{8}	470	490

5.5. Charge Relaxation in Short Pipes

Both filter current, I_f, and pipe current, I_p, were measured during the experiments reported in figures 4 and 7. During that portion of these tests in which the fuel passed through the filter, the values of I_f always exceeded 0.5 μA. These are very large compared to the currents generated at the fuel-pipe interface when the fuel bypassed the filter. Thus, for flow through the filter, it can be assumed that the measured I_p values are equivalent to the charges which migrated to the pipe wall during passage of the charged fuel through the pipe. Thus, data are available to verify eq (2), $I_p \approx I_f(1 - e^{-\lambda})$.

The results of this check of the relation $I_p \approx I_f(1-e^{-\lambda})$ are shown in figure 8. Each plotted point is the ratio

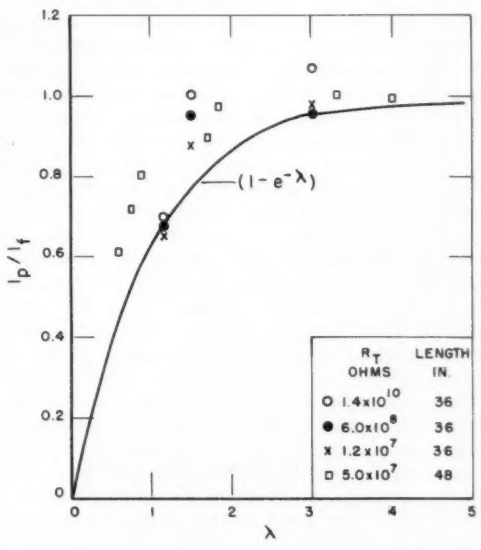

FIGURE 8. *Experimental verification of the relation* $I_p/I_f = (1 - e^{-\lambda})$ *for various pipe samples, flow rates, and fuel conductivities.*

I_p/I_f as calculated from the measured values of these two currents. The solid line represents the function $(1-e^{-\lambda})$ versus λ, computed from the relation $\lambda = L/v\tau$. Data corresponding to the three pipe samples 36-in. long were all obtained with a constant fuel conductivity of 84 pmho/m, and flowrate in the range 5 to 26 gpm. Data for the one pipe sample 48-in. long were obtained at a constant flow of 8 gpm with fuel conductivities in the range 11 to 200 pmho/m using asphaltenes as the contaminant. The few experimental points obtained for the λ range 5 to 10 are not included in this figure because these measured values of I_p/I_f were all within a few percent of unity. It is believed that the agreement shown in figure 8 is reasonable over the range of conditions encountered. However, some of the points indicate relaxation may at times occur more rapidly than predicted. Certainly these results help to verify that relaxation of a charged liquid flowing in a pipe is essentially independent of the electrical resistance of the pipe for resistance values in the range zero to about $10^{10}\ \Omega$.

It is believed, but not definitely known, that at least some of the deviations shown in figure 8 are related to the determination of fuel conductivity. Perhaps the effective conductivity of the charged fuel in the pipe can be influenced by the potential gradients existing. Thus, it is possible that present methods of determining fuel conductivity are not completely adequate for the experimental verification of the theoretical relations.

6. Discussion

The purpose of this section is to discuss and further emphasize those results leading to the desirable resistance characterisitcs of pipes and hoses through which charged liquid petroleum products may flow. It is believed that the experimental conditions of flowrate, and of pipe diameter, length, and installation downstream from microfilters duplicate closely conditions frequently encountered, especially in fuel systems of the larger size internal combustion engines. Admittedly, this investigation was concerned primarily with the more severe conditions rather than with average conditions. Also, the fuel conductivities of 84 and 165 pmho/m used during many of the tests are higher than those normally encountered. However, experiments with fuels of lower conductivities show that maximum filter charging effects usually occur in the conductivity range 10 to 200 pmho/m depending upon the filter design and the rate of flow. Experience has shown that conductivities in the range 10 to 30 pmho/m are encountered rather frequently in liquid petroleum fuels flowing into the engines.

Perhaps one point should be emphasized concerning fuel conductivity. In investigations concerned with the more severe filter charging conditions and the resultant currents and potentials in pipes installed downstream, it has been found, as shown in figure 4, that greatest electrification effects are obtained with fuels of moderate conductivities, range 10 to 200 pmho/m, rather than those having low conductivities of the order of one pmho/m. Therefore, elaborate precautions to remove absorbed water and as much of the contamination as possible are not necessary during investigations involving the generation of large filter charging currents. Nevertheless, in this connection some effects of water should be mentioned. As discussed in [3] and investigated briefly by the authors, ordinary tap water, which has relatively very high conductivity, does not increase fuel conductivity even when present to the extent of 5 percent or so. In fact, water frequently tends to leach out and reduce the amount of contaminant in a fuel with the resultant effect of a possibly large decrease in conductivity. Finally, water mixed with fuel, especially when dispersed in the form of droplets, usually increases electrification considerably during flow through pipes and filters.

It has been shown that electrical breakdown can occur when a charged fuel flows through nonconductive pipes. These phenomena are perhaps similar to the charging of an electrical condenser until the resulting potential gradients are sufficient to cause breakdown. Thereafter, depending upon the current and the particular materials involved, either a continuous discharge will be obtained through the breakdown path, or a series of intermittent discharges will result.

The question arises as to what happens when the nonconductive pipe has a sufficiently high dielectric strength so failure through the wall does not occur at the time of the arc discharge. An example of such conditions is described below.

Variable-area meters are used frequently in the laboratory for the flowrate measurement of hydrocarbon liquids. The metering tubes of these instruments are moulded of thick heavy glass, have a length in the range 1 to 3 ft, and frequently have no internal bonding wire or its equivalent. Occasionally such meters are connected downstream from microfilters which charge the fuel significantly under certain operating conditions.

It is rather well known that electrical discharges occur at times in glass-tube flowmeters so installed. Photographs of such discharges are very similar in appearance to figure 6 except that puncture or breakage of the glass pipe does not occur. Rather, the strong lengthwise spark terminates at any convenient metallic ground within the end of the glass tube. Numerous lateral flashes are noted also. Although not definitely known, it appears from photographs, that the electric arcs occur on the internal surfaces of the glass pipe. Arcs extending five or more inches up into the glass tubes have been observed under the more severe conditions.

The use of an internal bonding or ground wire in nonconducting pipes should reduce maximum potentials significantly and thus eliminate the possible hazard arising from electrical arc discharges. This internal bonding wire will likely have little, if any, influence upon the rate at which separation of charge from the highly charged fuel occurs.

The possibility of placing a conductive skin around the outside of nonconductive hoses was mentioned

in the Discussion of reference [2]. This idea may be practical provided the transverse leakage of electricity from the interior of the hose to the conducting skin does not puncture the wall. Experience has demonstrated this is not practical when applied to hoses containing a thin tube of pure TFE surrounded by an exterior, grounded, metal braid. In such hoses, discharges of electricity similar to that of figure 6, frequently puncture the TFE tube resulting in liquid leakage through the wall. One solution to the problem is the development of a practical inner liner or coating of moderate resistivity which would be grounded at each end of the hose.

Considering now the flow of a highly charged liquid hydrocarbon through a pipe of moderate resistivity, the experimental results help to verify that the rate of charge separation from the fuel to the pipe wall is essentially independent of the pipe material or of its electrical resistance. The relation $I_p = I_i(1 - e^{-\lambda})$ is in reasonable agreement with the experimental results provided I_i is large compared to I_0, where I_0 is the convection current flowing out with the fuel from an infinitely long pipe of the same material.

The maximum magnitudes of the currents I_p encountered in the investigation were in the range 1 to 6 μA. These are of the same order of magnitude and are in reasonable agreement with a possible maximum value of 10 μA cited at times in the literature. If a safety factor is desired, a maximum value of $I_p = 100$ μA will perhaps cover all operating conditions which could be encountered in practical applications.

The rather limited experiments indicate that the maximum voltages occurring in pipes can be predicted with reasonable accuracy by the relation $V_{max} = 0.1 R_T I_p$ provided $\lambda < 6$. According to eq (5) in the appendix and as shown in figure 9, for any given value of R_T and I_p, maximum potentials will be less for values of λ considerably greater than 6. However, such conditions are not usually encountered in practical applications. If potentials existing within pipes are not to exceed an arbitrary value of 1,000 V for a possible maximum pipe current of 100 μA, then the end-to-end resistance of the pipe may be computed as $R_T = 1{,}000/(0.1 \times 100 \times 10^{-6}) = 10^8$ Ω.

Thus, a value of R_T not to exceed about 10^8 Ω may be suggested for pipes and hoses intended for use with liquid hydrocarbons. It is believed this upper limit is sufficiently low to eliminate the hazard of spark discharges occurring either within or through the walls of hoses and pipes through which a liquid hydrocarbon flows. However, this suggested maximum value for R_T is subject to three conditions: (a) the pipe must be uniformly conductive throughout its length; (b) the conductive portion of the pipe must be in contact with the fuel throughout the length of the pipe; and (c) the conductive portion of the pipe must be electrically connected to the ground at each end of the pipe.

When conventional end fittings of aircraft hose are used as electrodes, the end-to-end resistance R_T is not a reliable parameter for specification purposes because it does not assure that the interior surface of the pipe is conductive and electrically connected to the ground. However, this requirement will be checked if the resistance from each and any portion of the interior surface of the pipe to the ground is measured instead of the end-to-end resistance. Consider an empty pipe grounded at each end. An internal electrode located at the center of this pipe has the effect of placing two $R_T/2$ resistances in parallel resulting in an effective resistance to the ground of $R_T/4$. With allowance for this, and considering orders of magnitude only, it is concluded that hazardous pipe potentials resulting from static electricity can be eliminated if the electrical resistance from each and any portion of the interior surface of the pipe to the ground does not exceed about 10^7 Ω. The use of an internal electrode in measuring the resistance of pipes and hoses will be inconvenient at times, but this method does provide an electrical path to the ground similar to that seen by the liquids contained within the pipe during normal usage.

It is acknowledged without reservation that the relations and ideas presented in [1] and [2] and their Discussions provided nearly all of the background material required for this investigation. It merely remained necessary to demonstrate that such relations and ideas were applicable to the particular problem under consideration. Thus, it is gratifying to be able to present additional experimental data which, for practical purposes, is in good agreement with the work of previous investigators.

7. Conclusions

1. High electrical charge densities can be produced in petroleum liquids having moderate to high electrical conductivities (10 or more pmho/m) when such liquids flow through conventional microfilters. However, the charging tendency of the liquid is not dependent upon fuel conductivity alone. Rather, it is dependent upon the amount and material of which the contaminant is composed and the material at the liquid-solid interface.

2. Maximum currents in the range one to 6 μA were obtained from the pipe to the ground when highly charged petroleum liquids flowed through short pipes or hoses. These comparatively large currents were caused by the migration to the wall of the pipe of the electrical charges contained within the charged fuel.

3. The rate of separation of electrical charges from the charged fuel is essentially independent of the pipe material and its electrical resistance.

4. When the rate of charge separation is sufficiently high in pipes constructed from nonconductive materials, electrical discharges in the form of sparks and arcs will occur. These discharges will originate on the inner surface of the pipe. They may be contained entirely within the pipe or may cause puncture or other failure of the pipe wall depending upon the pipe material, the wall thickness, and the ground locations involved.

5. Maximum potentials produced by static electric phenomena within pipes, grounded at each end, may be predicted with reasonable accuracy by a simple

relation provided the electrical resistance of the pipe and its current to the ground are known.

6. Considering pipes or hoses through which a highly charged petroleum liquid may flow, an electrical resistance from each and any portion of the interior surface of the pipe to the ground not exceeding about $10^7\ \Omega$ is adequate to limit pipe potentials resulting from static electricity to less than 1,000 V.

The financial support and personal interest shown during this program by the Navy Department, Bureau of Naval Weapons, is gratefully acknowledged. Also, the appreciation of the authors is hereby expressed for the considerable technical guidance received throughout the program from Francis Hermach of the Electricity Division of the National Bureau of Standards. Finally, the considerable contribution of industry in supplying experimental pipe samples for the investigation is also acknowledged.

8. References

[1] Carruthers, J. A. and Marsh, K. J., Charge relaxation in hydrocarbon liquids flowing through conducting and nonconducting pipes, J. Institute of Petroleum **48**, No. 462, June 1962, pp. 169–179.

[2] Carruthers, J. A. and Wigley, K. J., The estimation of electrostatic potentials, fields, and energies in a rectangular metal tank containing charged fuel, J. Institute of Petroleum **48**, No. 462, June 1962, pp. 180–195.

[3] Klinkenberg, A. and van der Minne, J. L. (ed), Electrostatics in the petroleum industry, Amsterdam: Elsevier, 1958.

9. Appendix

The object of this appendix is to develop an approximate relation for the maximum electrical potentials developed on the inner wall surface of pipes as a result of static electric phenomena caused by the flow of hydrocarbon liquids. Essentially this theory is a simplification of that developed by Carruthers and Marsh [1] subject to the assumptions that the electrical resistance of the pipe is low compared to that of the liquid and that the ratio of the residence time of the liquid in the pipe to the relaxation time of the liquid has a value less than 6. Both of these assumptions appear to be valid as applied to the more severe conditions likely to be encountered in practical applications.

I_f = current between the ground and the filter
$I_i = q_i v$ = convection current entering the pipe due to the flow of liquid containing an initial charge q_i per unit length of pipe
I_p = current flowing from the pipe to the ground
I_0 = convection current which would emerge with the liquid from an infinitely long pipe
L = length of pipe
$m = x/L$
$R_T = L/\beta$ = end-to-end resistance of the pipe
V_m = the potential on the inner wall of the pipe at a position $m = x/L$ from the pipe entrance
V_{max} = the maximum potential existing on the inner wall of the pipe
V_x = the potential on the inner wall of the pipe at a distance x from the pipe entrance
v = mean axial velocity of the liquid
x = distance along pipe from the entrance
β = conductance per unit length of pipe wall assuming the conductivity of the pipe wall is considerably greater than that of the liquid
$\lambda = L/v\tau$ = ratio of the residence time for the liquid in the pipe to the relaxation time of the liquid
τ = relaxation time of the liquid. Its value is computed from ee_0/k where k is liquid conductivity, e the dielectric constant of the liquid, and e_0 the electric constant of free space. When k is expressed in mho/m, τ in seconds, and e is taken as 2, $\tau = 17.7 \times 10^{-12}/k$.

Carruthers and Marsh [1] in a consideration of the potentials produced by the flow of hydrocarbon liquids have developed the expression

$$V_x = (I_i - I_0)\frac{v\tau}{\beta}\left[(1 - e^{-x/v\tau}) - \frac{x}{L}(1 - e^{-L/v\tau})\right] \qquad (1)$$

for the potential at any point of the cross section of liquid and pipe.

If it is assumed that the electrical resistance of the pipe is small compared to that of the liquid contained within the pipe, $R_T = L/\beta$, and by letting $m = x/L$ and $\lambda = L/v\tau$, eq (1) may be written as

$$V_m = (I_i - I_0)\frac{R_T}{\lambda}[(1 - e^{-m\lambda}) - m(1 - e^{-\lambda})]. \qquad (2)$$

Also in [1], the expression

$$I_u = I_i e^{-\lambda} + I_0(1 - e^{-\lambda}) \qquad (3)$$

is developed for the convection current, I_u, emerging with the liquid when the pipe is of finite length. This assumes both the relaxation of I_i and the generation of I_0 at the fuel-pipe interface are exponential processes. As shown in the discussion of figure 1, $I_u = I_i - I_p$, and from eq (3) the currents I_p, I_i, and I_0 are related by the expression

$$I_p = (I_i - I_0)(1 - e^{-\lambda}). \qquad (4)$$

Substituting for $(I_i - I_0)$ in eq (2) another expression

$$V_m = I_p \frac{R_T}{\lambda}\left[\frac{(1 - e^{-m\lambda})}{(1 - e^{-\lambda})} - m\right] = KI_pR_T \qquad (5)$$

is obtained for the potential at any point along the pipe.

Figure 9 shows K plotted as a function of λ for selected values of m. It is seen that K varies between 0.13 and 0.08 for values of λ less than 6. As λ becomes greater than 6, K decreases rapidly becoming less

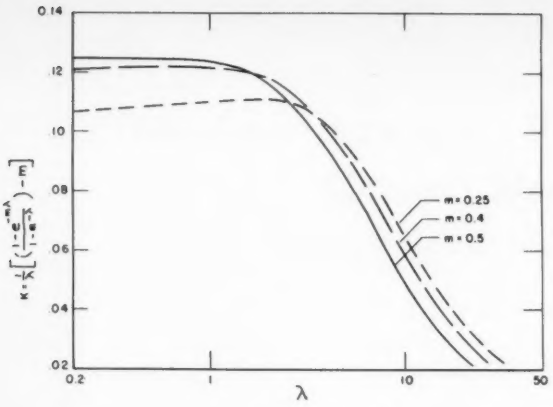

FIGURE 9. *The relation* $K=\frac{1}{\lambda}\left[\frac{(1-e^{-m\lambda})}{(1-e^{-\lambda})}-m\right]$ *as a function of* λ *for selected values of* m.

than 0.02 for $\lambda=50$. Values of λ exceeding 6 are encountered only with long pipes, fuels of very high conductivities, or very low fuel velocities; conditions in which nearly all of the charge relaxation occurs in a short upstream portion of the pipe. Values of λ less than 6 correspond to the more severe conditions encountered in practical applications. Therefore, with little sacrifice in accuracy an average value of $K=0.1$ can be used to obtain an approximate expression for the maximum potential produced in a pipe, and

$$V_{max}=0.1\ R_T I_p \tag{6}$$

where R_T is the end-to-end resistance of a pipe, grounded at each end, from which a current I_p is flowing to the ground.

(Paper 69C4–212)

JOURNAL OF RESEARCH of the National Bureau of Standards—C. Engineering and Instrumentation
Vol. 69C, No. 4, October–December 1965

A Transistor Screening Procedure Using Leakage Current Measurements

George T. Conrad, Jr., and Donald C. Shook

(July 27, 1965)

A study of the aging behavior of low-power germanium alloy switching transistors has revealed a relationship between small changes in junction leakage current, induced by a brief aging stress, and later deterioration in performance. This relationship may provide the basis for a nondestructive screening procedure which would serve to identify germanium alloy transistors likely to deteriorate through excessive growth of junction leakage current. The proposed screening procedure involves the determination of relatively small changes in junction leakage current, increases of the order of 15 percent or more, associated with 1,000 hours of aging at a shelf (bake) stress of 100 °C. Because the leakage current changes of interest are small, relatively high demands are placed upon measurement repeatability. There is evidence that transistors bearing identical type numbers but of different manufacture respond differently to the same screening procedures and would therefore require different screening limits.

Key Words: Aging behavior, alloy transistors, failure prediction, leakage current, screening procedures, temperature stress, transistor, transistor failure, transistor screening.

1. Summary

The data from a 20,000-hr transistor aging behavior study indicate that small changes in junction leakage current, induced by baking, provide a means for identification of units likely to deteriorate through growth of leakage current. A subsequent independent experiment, which included transistors of different manufacture, provided further evidence that this behavior may be generally characteristic of germanium alloy transistors. The second experiment also examined the effects of more stringent screening stresses.

2. Introduction

Studies of aging behavior of transistors are never free from many of the confounding effects which tend to degrade measurement repeatability. The data from recent experiments indicate that, generally, junction leakage current tends to decrease during early stages of aging. As aging continues, or as aging stresses are increased, the downward trend ultimately reverses. For some transistors, junction leakage currents were observed to increase from the outset. Those units exhibiting the largest increase formed a group which contained all (or nearly all, depending upon performance criteria) of the transistors which deteriorated more rapidly as aging continued. It appears that for these transistors, early increases in leakage current are a manifestation of a continuous process during which leakage current continues to increase, leading eventually to "failure." Since leakage-current degradation is not uncommon, careful observation of early changes in leakage current shows promise as a basis for a practical means of screening transistors to further improve transistor reliability.

The fractional changes in leakage current of interest are relatively small, and therefore all sources of variability in the measurement process are of concern. The inherent behavior of the device itself is one such source, and in some instances is the major source of variability. The measurement of transistor parameter values is not only dependent upon bias conditions and ambient temperature, but also upon the time duration of the measurement and upon the bias and temperature histories resulting from prior measurement and aging stresses. For example, voltage breakdown measurements using current-limited values even as low as 10 μA have been observed to commonly cause marked disturbances in the leakage current values, requiring several weeks for the effects to subside. Voltage breakdown measurements should be avoided wherever sensitive leakage current measurements are being made. As another example, the transfer of a transistor from an aging to a testing environment is accompanied by a shift in parameter values which usually requires several days to approach a new center value. This stabilization effect [1] appears repeatable for a given transistor but is not consistent among transistors. The above mentioned disturbances cannot, in general, be eliminated, but their effects may be substantially reduced by careful choice of operating procedures and test methods.

Similarly, the instability of measurement equipment, especially long-term drift, as well as variation in ambient temperature during measurement, introduces errors which cloud the meaningfulness of aging behavior data.

The National Bureau of Standards in cooperation with the Department of the Navy is conducting

[1] Zierdt, C. H., Jr., On importance of operating tests as compared to storage tests of transistors, The Solid State Journal **2**, No. 9, 21–27 (1961).

transistor aging studies in which every reasonable effort is being applied towards minimization of unwanted variability in the aging data through careful instrumentation, selection of test methods and procedures, and design of experiments. A key feature of the instrumentation for measurement of d-c parameters, for example, is close ambient-temperature control. The transistors are immersed in a "constant-temperature" recirculating air stream. The air stream temperature is centered at 25 °C and fluctuations are regulated within ±0.01 °C. Further precautions include replication of measurements coupled with computer analyses programmed to detect and identify questionable agreement between replications. This enables us to repeat questionable measurements, if necessary.

These and other precautions have helped to maintain a high level of equipment performance and measurement repeatability. A case in point is the record of temperature-sensitive leakage current measurements accumulated during the course of a three-year aging study wherein each of 10 "control" transistors was measured a total of over 3,000 times. Among these measurements are four sets of junction leakage current measurements, each set consisting of 300 recordings. These recordings were found to have gradually decreased approximately 1½ to 2 percent during the 3-year period. The major part of this decrease is traceable to creep of 0.08 °C in the calibration point of a thermometer due to stabilization of the glass bulb. Corrections for the gradual change in ambient temperature between each measurement period resulted in an estimated coefficient of variation of less than 1 percent. This performance record is consistent throughout the data and demonstrates the stability of the transistor-measurement system combination and serves as a measure of confidence which may be placed in the transistor aging data discussed in this paper.

3. First Experiment

The first of two experiments described in this paper provided a survey of the behavior of approximately 500 type 2N396 germanium alloy transistors in response to a wide range of aging stresses. The second experiment used approximately 100 transistors to explore more fully behavior in the 100 to 125 °C region and to introduce different types and manufacture of germanium alloy transistors into the study. All transistors had met stringent military requirements and were considered "high reliability" units.

A full reporting of the first experiment, in which over ¼ million measurements have been recorded, would be prohibitively lengthy. A brief description of the entire experiment, however, is given in the appendix. Attention is focused on that part of the experiment involving the four groups of transistors which were subjected to four different combinations of aging. Each combination was calculated to produce a junction temperature of 100 °C (identified as aging conditions 13, 14, 15, and 18 in table 3). This temperature lies roughly in the center of the aging-stress spectrum for the total experiment.

The 100 °C aging conditions are of particular interest because the small but significant changes in leakage current, occurring within the first 1,000 hr of aging, take on meaningful significance when compared with later aging behavior.

The aging conditions at 55 °C and below produced too little deterioration in 20,000 hr of aging to be of much value in testing relationships between early change and aging. Comparison of results for the different aging temperatures, however, were not inconsistent with the expectation that failure rates (and chemical activity) double for each approximately 10 °C increase in junction temperature. The volume of data from the lower stress conditions, 55 °C and below, provided assurance that the measurement system, as well as the transistors, was quite stable and factors affecting repeatability were in close control.

The aging conditions at 145 °C and above, on the other hand, caused relatively rapid deterioration, and in a few cases, total destruction occurred prior to the first measurement period, i.e., during the first 340 hr of aging. Further aging showed conclusively that the failure rates were too high to expect the data for these conditions to shed much light on the meaningfulness of small early changes.

For the reasons given above, the remainder of the discussion of the first experiment will be devoted to the behavior of the four groups consisting of 160 transistors aged with the junction temperature maintained at 100 °C for a total of 20,000 hr.

4. Data

Each of the four groups of 40 transistors was subjected to a different combination of ambient temperature and applied bias power. The four aging conditions are identified in table 3 of the appendix. Three of the conditions were essentially shelf aging at an ambient temperature of 100 °C; condition number 13 provided no bias power, condition 15 included a nominal 3 mW of power dissipation, and condition 18 subjected the collector-to-base junction to a reverse bias voltage stress of −24 V. The fourth aging condition provided a combination of 70 °C ambient temperature and 120 mW of power dissipation which was the power required to raise the junction temperature to an estimated 100 °C.

The general effect of the four 100 °C aging conditions was to cause only a very small and gradual increase in the dispersion of the electrical parameters with no perceptible trend in the modal values. For those transistors which eventually exhibited substantial degradation, the changes were mainly gradual and thus presented the problem as to when performance should be judged "unsatisfactory." Since no particular circuit applications with associated performance limits were involved, the basis for such a decision is necessarily arbitrary. The criteria selected are similar to those appearing in the specification for the environmental acceptance tests, IEBO (−10 V) or

ICBO (−10 V) greater than 10 μA or hFE (10 mA, −5 V) less than 20. Using these criteria, the performance of a total of 10 transistors became "unsatisfactory" during the 20,000 hr of aging at 100 °C. (The total elapsed time of the experiment, including the measurement periods, exceeds 3 years.)

The records of behavior of these 10 transistors have been scrutinized and a summary is given in table 1. On the left, the individual transistors are identified along with their respective aging conditions. The code numbers for the aging conditions are fully described in table 3 of the appendix. "Unsatisfactory" transistors appeared in all four conditions, and differences in the number of "unsatisfactory" units corresponding to each condition are not sufficiently large to be considered significant. For these reasons, and for the lack of any other substantial differences in observed transistor behavior between the four aging conditions, it was decided to combine the data for the subsequent analyses.

TABLE 1. *Summary of aging behavior of "unsatisfactory" transistors*

Transistor and plug No.	Aging condition	0-hr values of		Early changes			Hours of aging	Deterioration					
		IEBO	ICBO	Ratio values of IEBO or ICBO, whichever is larger				"Unsatisfactory" criteria			Character of deterioration		
				340-hr	1,000-hr	1,000-hr		hFE*	IEBO	ICBO	Avalanche	Ohmic leakage	Other
		μA	μA	0-hr	0-hr	340-hr		< 20	> 10 μA	> 10 μA			
8–1058	15	2.163	1.645	3.578	3.795	1.061	2.0 k		X		E		
3–1066	18	.9479	1.152	1/1.039	2.101	2.182	2.0 k			X		EC	
0–1040	13	1.107	1.612	1.218	1.737	1.426	3.4 k	X				EC	
0–1052	14	[v]2.191	1.496	3.658	3.854	1.054	11. k		X		E		
3–1064	18	1.361	1.489	1/1.106	1.213	1.342	11. k			X		C	
0–1050	14	[*]1.169	[*]2.873	1.041	1.066	1.024	14. k		X				[1]
8–1046	13	1.029	1.206	1/1.013	1/1.062	1/1.049	20. k		X				[2]
3–1068	18	.6595	.7854	1.014	1.064	1.049	20. k			X		C	
1–1070[1]	18	1.189	1.447	1/1.081	1/1.082	1.005	20. k			X		C	
2–1070	18	1.256	1.215	1.732	2.190	1.265	20. k		X			EC	

[1] Case leak detection test was applied after 20 khr to all of above transistors except 0–1050 and 8–1046. Only 1–1070 leaked; rate was $\approx 200 \times 10^{-8}$ std. cm³/s.
[v] Variable.
[*] Only 0-hr measurement was variable.

(1) Wafer was found to be cracked.
(2) Large and abrupt increase in emitter current.
"E" Indicates emitter and "C" collector junction.

Returning to table 1, the initial or 0-hr IEBO (−10 V) and ICBO (−10 V) values listed on the left were obtained before application of the aging stresses. The distribution of these values is not perceptibly different from that of the larger group of "satisfactory" transistors. Even the single maximum value listed would have been ineffective for screening, because at least 10 "satisfactory" transistors had larger values. We conclude therefore that these 0-hr values provide no effective means for identification of the "unsatisfactory" transistors.

Variability of the parameter values during measurement was another property of interest. A few of the 0-hr measurements in table 1 bear superscripts indicating that these measurements were classified as variable on the basis that the automatic digital voltmeter, which has a 2- to 3-sec conversion time, would not balance within 50 sec. This variability test was applied uniformly to all transistors throughout the experiment. There is no evidence that 0-hr measurement variability is uniquely related to deterioration. Over an extended period of aging, however, the time-series measurements indicated that consistently variable units exhibited more pronounced deterioration. The association was not so close (nor the technique amenable) as to favor the use of this criterion to screen potential failures.

In contrast to the ineffectiveness of the 0-hr leakage current measurements, *changes* in the value of junction leakage current observable within the first 1,000 hr of accelerated aging appear promising as a screening index. None of the other parameters in the experiment, measured or computed as listed in the appendix, appears to be as useful. For this reason the remainder of table 1 provides only for comparison between fractional changes in junction leakage current measurements and deterioration. Ratio values greater than unity indicate an increase in leakage current with time.

The ratio values given are the ratio of the 340-hr measurement divided by the 0-hr measurement, and the ratio of the 1,000-hr measurement divided by the 0-hr measurement. In each instance the ratio indicates the fractional change in junction leakage current; either the IEBO or ICBO change is listed, whichever is the larger. By thus combining the larger change into one table, a closer relationship between early fractional changes and deterioration in either junction is more apparent than if IEBO or ICBO were treated separately.

Although table 1 does not indicate which junction current is associated with the larger ratio value listed, the data reveal that with one exception, the junction associated with the larger ratio value was also the

junction which deteriorated and led to "unsatisfactory" performance. The one exception was transistor 0–1040, where "unsatisfactory" was indicated by hFE* becoming less than 20, first observed after 3.4 khr of aging. In the very next measurement period (4.7 khr), the ICBO value exceeded 10 μA, and it was the collector junction which exhibited the larger ratio value. The consistent correspondence between early changes and deterioration in the same junction argues for the existence of a determinative relationship.

5. Character of Deterioration in Performance

The "Hours of Aging" in table 1 indicate when the transistor was first observed not to have met performance criteria, and was thereby adjudged "unsatisfactory." In each instance there was an increase in leakage current. The nature of these increases suggested the three categories listed under "Character of Deterioration." Avalanche conduction was ascribed to two transistors which exhibited a several-fold increase in (emitter) junction leakage current at 10 V with essentially no associated increase at 2 V. Conduction by current multiplication was clearly present. The second, and most common form of deterioration, was a gradual increase in leakage current for both bias levels. Six transistors displayed this type of deterioration. For each measurement period the estimated intrinsic saturation current, which was found by extrapolation of the current versus voltage curve to estimate the saturation current at 0 V, remained relatively constant, thus indicating the presence of a linear (ohmic) relationship between bias voltage and observed leakage current. The third characteristic of deterioration, designated "other," applies to two transistors which became catastrophic failures. The first of these two transistors, number 0–1050, developed a collector-to-base and collector-to-emitter "short," which was apparently caused by a fractured wafer found by optical examination. The presence of the overt fault was observed after this transistor, as well as all other transistors under study, was remounted and soldered to a new type of high-temperature plug. The implied causal relationship, damage by remounting, is not so clear-cut as it might appear in light of the following considerations. First, the soldering and handling techniques had been checked in a preliminary experiment in which the effects of the same soldering techniques were found to produce no significant change (less than 1 percent) in leakage current. All transistors were monitored before and after remounting, and only 0–1050 showed a change. Second, earlier behavior of 0–1050 was suspect. The initial 2-V ICBO value was 12 μA, and the 10-V value was, oddly, only 3 μA. Both measurements were variable. Replicate ICBO measurements made later in the same day were also variable, but were near 1 μA. The initial higher values did not repeat. Measurements of hFE were variable and large. They became normal after 340 hr of aging. In fact, from the 340-hr measurement period until the time it was withdrawn from the experiment at 14 khr, transistor 0–1050 was one of the best-behaved units in its aging condition. The above observation would lead one to suspect the wafer was cracked in the beginning. Such a suspicion is not unreasonable, in view of the fact that six of the original 500 transistors received for this experiment were found to have fractured wafers.

The second transistor, 8–1046, exhibited an abrupt increase in emitter leakage current between 14 and 20 khr of aging, with no prior indication of impending deterioration. The resulting voltage-current relationship had the character of ohmic conduction (~ 10 kΩ), but differing from the six other transistors classified as having ohmic leakage in that the change appeared as an abrupt steplike increase. Unfortunately, in removing the case for optical examination, the transistor was damaged.

With the exceptions of transistors 0–1050 and 8–1046, which had previously had their cases removed, the "unsatisfactory" transistors were subjected to 125 °C mineral-oil gross-leak detection test and a helium fine-leak detection test. Only transistor 1–1070 was found to leak, and at a rate of approximately 200×10^{-8} std. cm^3/s. (He).

6. Changes in Leakage Current Related to Deterioration

Table 1 lists the values relating early fractional changes in junction leakage current to deterioration which led to "unsatisfactory" performance. It is of interest to note that the two transistors which exhibited the largest early fractional changes were the only two which later developed avalanche conduction. The large fractional change in leakage current occurred within the first 340 hr of aging.

The significance of the relationships between fractional changes and deterioration is more fully revealed in figures 1, 2, and 3. Figure 1 relates aging behavior to the fractional increase in junction leakage current associated with the first 340 hr of the aging stress. Both junction currents were measured, but only the larger of the two fractional changes was plotted. The distribution of the ratio values for the entire 160 transistors is shown by the major histogram. The smaller receding histograms show cumulatively the ratio values for those transistors which had become "unsatisfactory" by the time indicated. The crosshatch shows when a transistor was first observed to be "unsatisfactory."

Similarly, figure 2 relates the change produced by the first 1,000 hr of aging to later behavior. A comparison of the two figures shows that, in general, the 1,000-hr ratio values of the "unsatisfactory" units fall more consistently in the upper range of the ratio distribution than do the 340-hr ratio values. In figure 2, the correspondence between relatively high ratio values and deterioration is clearly more pronounced for those units which deteriorated more rapidly, as

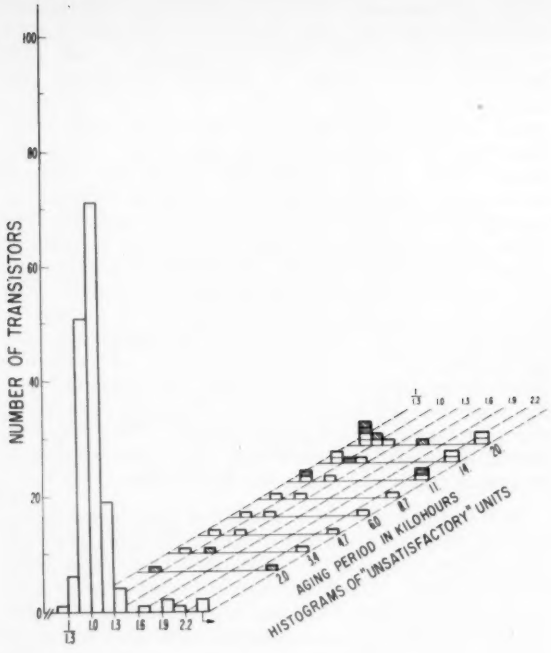

FIGURE 1. *Histogram of ratio values showing change in* IEBO *or* ICBO *after 340 hr of aging.*

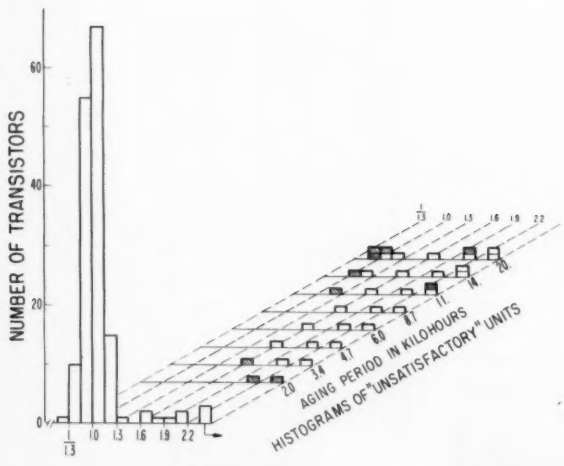

FIGURE 2. *Histogram of ratio values showing change in* IEBO *or* ICBO *after 1,000 hr of aging.*

shown by the histograms through 8.7 khr. The relationship becomes more tenuous for those units which last longer, as indicated by the histogram distributions spreading down scale with increasing time.

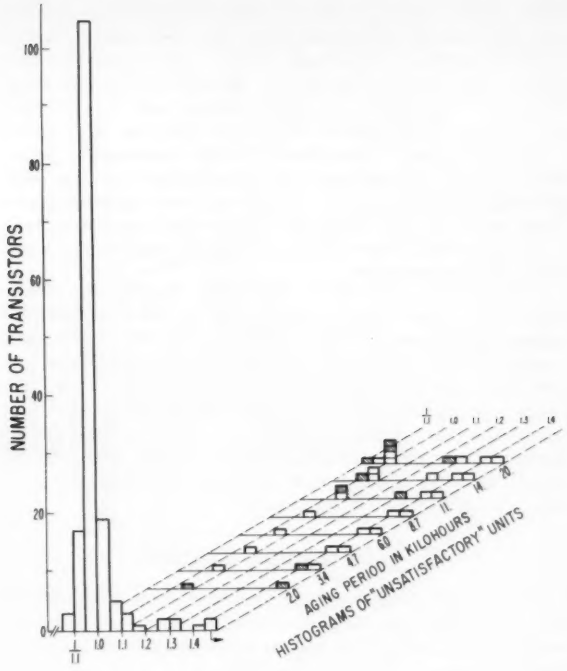

FIGURE 3. *Histogram of ratio values showing change in* IEBO *or* ICBO *between 340 and 1,000 hr of aging.*

Figure 3 relates the change observed between 340 and 1,000 hr of aging to later behavior, thereby excluding the more pronounced effects associated with the first several hundred hours of aging. The distribution of values was so much more compact that the class interval of figure 3 was reduced to roughly one-third that used in figures 1 and 2 in order to obtain a reasonable representation of the distribution.

The relationships in figures 1 through 3 suggest means for the identification of transistors likely to deteriorate. These data are based on 100 °C stress for screening as well as for subsequent aging. It should be borne in mind that this stress is higher than that which would normally be encountered in applications. A convenient and reasonable approximation may be made of expected aging performance by assuming that the rate of deterioration doubles for every 10 °C increase in junction temperature.[2] For example, the rate of deterioration at 55 °C may be conservatively estimated to be 1/10 that at 100 °C. Figures in this report, therefore, may serve to roughly approximate aging under more normal conditions (say 55 °C) by multiplying the time scale (associated with 100 °C aging conditions) by 10. Reexamining figure 2 with the expanded time scale in mind indicates that the

[2] Peck, D.S., Semiconductor Reliability Predictions from Life Distribution Data, ch. 5 of Semiconductor Reliability, edited by Shwop, J. E. and Sullivan, H. J. (Reinhold Pub. Corp., New York, 1961).

first three "unsatisfactory" units might have caused trouble in an application by not providing "satisfactory" service for at least 1 or 2 years. On the other hand, the remainder of the transistors would have become "unsatisfactory" only after a period of service in excess of 10 years. The fact that the first three "unsatisfactory" transistors have unusually large ratio values strengthens the expectation that the relationship between ratio values and later preformance may serve as the basis for a practical screening test to detect transistors likely to exhibit junction leakage current deterioration.

Since the suggested screening procedures stem from an *a posteriori* examination of all the data, no significant tests of the effectiveness of these procedures can be made using these same data. A second, smaller experiment described later in this paper provides a set of independent data which is used for this purpose. However, in order to demonstrate the observed relationships of the first experiment in a screening test context, an example of a screening analysis is presented.

7. A Screening Example

The ideal screening test serves a dual goal; one is to reject all units which would, in fact, fail to meet ensuing operational requirements for at least a specified period of time, and the other goal is to not reject any units which would meet such requirements. Failure to achieve the former goal through the erroneous acceptance and use of faulty units would lead to unreliable performance. Because this is of obvious and immediate concern to the consumer, this type of error is usually associated with a consumer's risk. On the other hand, failure to achieve the *latter* goal through the erroneous rejection of satisfactory units would directly penalize the producer of such units. This type of error is therefore associated with a producer's risk. It is evident that one or the other of these errors can be made as small as is desirable at the expense of increasing the other. A graphic view of the interplay between these two errors for various choices of performance time requirements and screening criteria is presented in figures 4, 5, and 6. The information was derived from figures 1, 2, and 3, respectively. The three groups of histograms in each figure illustrate the effects of choices of screening limits by application of three different magnitudes of fractional change upon which to base the decision to reject or accept individual transistors. The indicated sets of limits are arbitrary and were chosen so as to provide a reasonable basis for discussion.

Each bar in figures 4, 5, and 6 is a complete analysis in itself, relating screening results with aging performance. The screening test identifies those transistors to be rejected. The number of rejected units is indicated by the height of the bar above the axis. Superimposed on the bar is the aging performance record whereby the individual transistors are classified as "unsatisfactory" if they fail to meet the end-of-life requirements within the time period indicated on the abscissae. For example, the second bar from the left

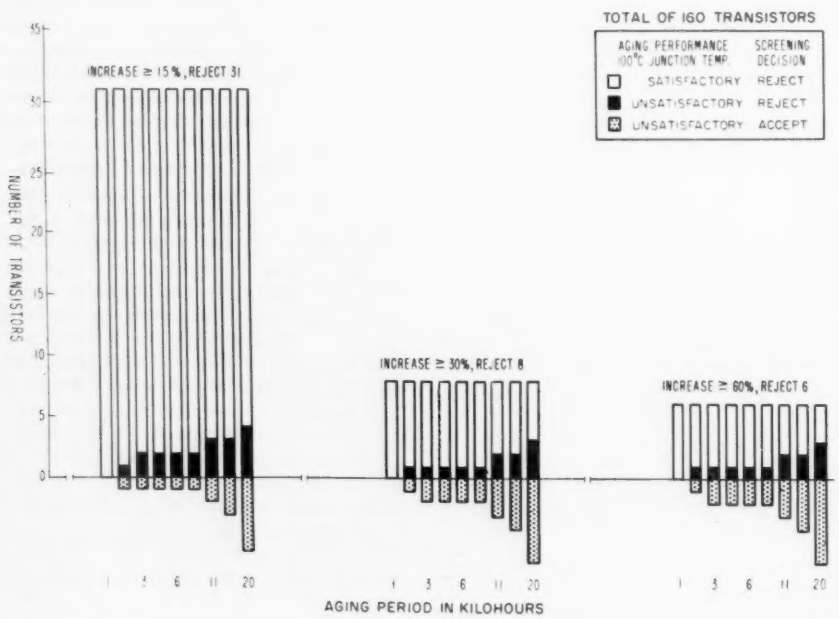

FIGURE 4. *Screening analyses using relative change in values of* IEBO *or* ICBO *after 340 hr of aging.*

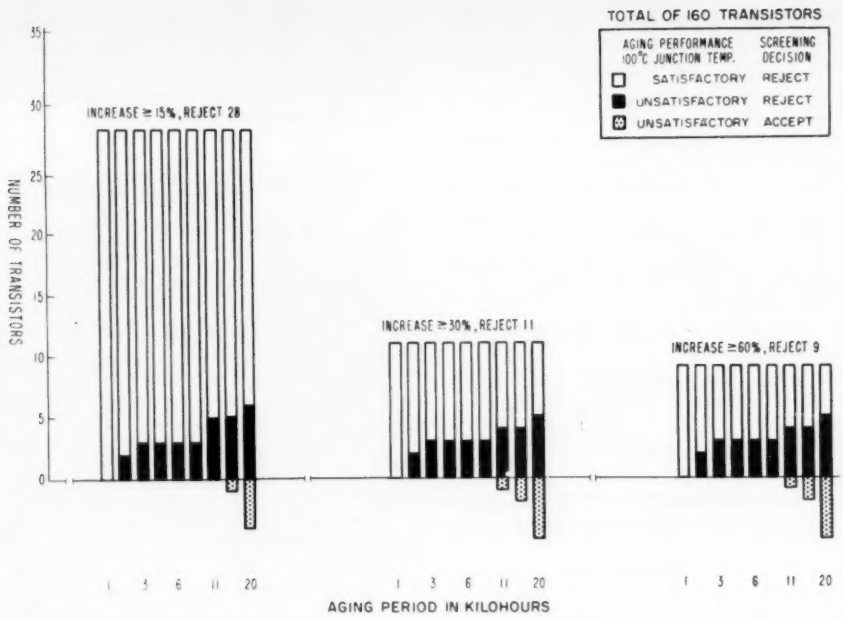

FIGURE 5. *Screening analyses using relative change in values of* IEBO *or* ICBO *after 1000 hr of aging.*

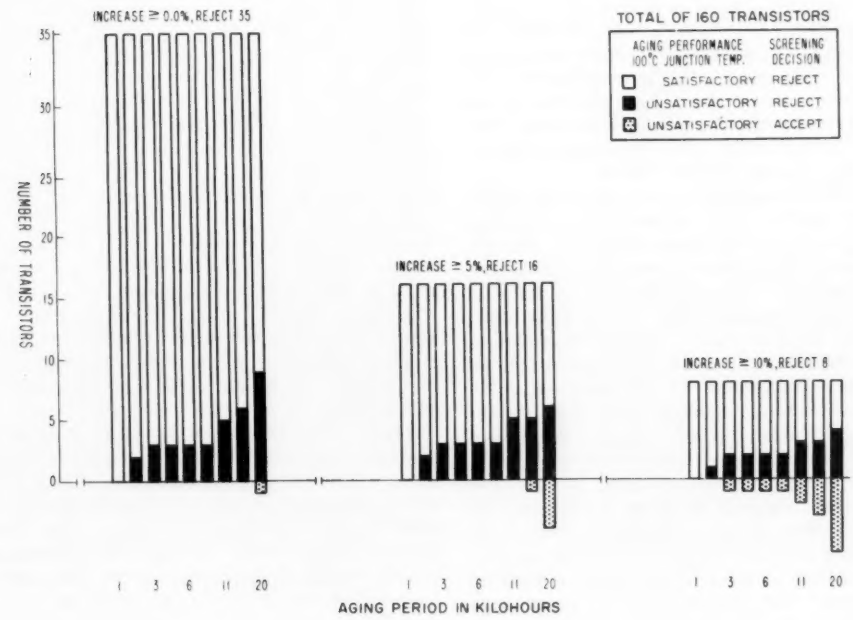

FIGURE 6. *Screening analyses using relative change in values of* IEBO *or* ICBO *between 340 and 1,000 of aging.*

in figure 4 indicates that after 340 hr of aging the junction leakage current (IEBO or ICBO) increased 15 percent or more in 31 of the transistors out of the total of 160. Two transistors out of the 160 were "unsatisfactory" after 2 khr of aging at 100 °C, one of which was within the group of 31 rejects and is represented by the black portion of the column. The second "unsatisfactory" transistor was not among the rejected groups and is represented by a dotted column extending below the axis. There remains, of course, the total number (128) of "satisfactory" units accepted correctly. The column in our example with the three area distinctions thus indicates:

1. By the height of the bar over the axis, the number (31) of transistors rejected;
2. by the white area, the number (30) of "satisfactory" units rejected in error, which is related to the "producer's risk";
3. by the black area, the number (1) of "unsatisfactory units rejected correctly;
4. by the dotted area, the number (1) of "unsatisfactory" units accepted in error, which is related to the "consumer's risk."

It is important to recognize that the time scales of figures 4, 5, and 6 refer to performance at 100 °C, a temperature which can be expected to produce more rapid aging than those ordinarily encountered in normal usage. Aging corresponding to a junction temperature of 55 °C would be more realistic and may be conservatively estimated by multiplying the time scale by a factor of ten. The basis for this procedure was discussed in the previous section.

A comparison of figures 4, 5, and 6 sets figure 4 apart by the relatively larger number of "unsatisfactory" units accepted (associated with "consumer's risk"), even though the corresponding errors associated with "producer's risk" are roughly comparable. It appears that a substantial reduction in the risk to the consumer is gained (without unduly increasing risk to the producer) by extending the screening stress to 1,000 hr rather than terminating at 340 hr.

There are several distinctions which should be noted between figures 5 and 6. The difference in screening results between the 5 percent steps of figure 6, despite the smaller increments, is more pronounced than that between the 15 percent steps of figure 5. This may have been expected because 340- to 1,000-hr ratio values of figure 6 form a more compact distribution (shown in figure 3) than the values for figure 5 (shown in figure 2). The effective use of the information in figure 6 requires a finer measurement distinction. The need for finer distinctions is obviously undesirable; as the necessary resolution approaches the magnitude of measurement error, the effectiveness of fine distinctions evaporates. Stated in other words, one of the desirable qualities of a screening parameter is that it have a broad distribution, and one of the essential qualities is that its dispersion be large relative to measurement error. For these reasons the criteria represented in figure 5 are favored. An additional desirable quality is the apparent lack of sensitivity of screening results to the choice of the ratio change, whether it be 30 or 60 percent.

On the basis of the factors discussed above, it was decided to eliminate the 340-hr measurement period and use only the observed relative change after being subjected to an accelerated aging stress for 1,000 hr, as illustrated in figure 5.

8. Second Experiment

The value of the screening concept discussed in this report depends, to a large extent, upon the relation of early-changes versus deterioration being a general behavioral characteristic, a characteristic which other types of transistors and transistors of different manufacture have in common. The completion of a modest second experiment tends to confirm that the relationship does exist for other types and manufacture of germanium alloy transistors.

As a sequel to the first experiment, a second was initiated, wherein approximately 125 °C junction temperature screening stress was applied for 1,000 hr and then reduced to 100 °C for continued aging. The parameters measured were identical, and the form of the data was similar to that of the first experiment. It was, therefore, a simple matter to apply the screening criteria to the data without foreknowledge of the actual performance. For this reason, and the fact that the data of the second experiment are independent of those used (in the first experiment) in development of the screening test, the second experiment provides a valid basis for evaluation of the effectiveness of the screening procedure.

The second experiment consisted of applying a screening test and then aging all units for nearly one year. The experiment included a group of 40 type R212 transistors of manufacture B, 40 of manufacture C, and 40 type 2N396 transistors of manufacture E. The 2N396 units are the same type and manufacture as those used in the first experiment. Furthermore, an effort was made to compare results of two different forms of screening stress. Half the transistors were exposed to a 1,000-hr bake screening stress of 125 °C with no applied power. The remaining half of the transistors were exposed to a contrasting screening stress having a low ambient temperature combined with a high power dissipation calculated to produce the same 125 °C junction temperature. The latter stress was obtained with an ambient temperature of −65 °C (which is a commonly accepted temperature test point) combined with the calculated bias power of 760 mW.

The calculations were based on measured values of thermal resistance. The thermal resistance of the units of manufacture B was somewhat higher than that of the other two groups. It was decided, since ratings were similar, to apply the same bias power for all three groups, even though the estimated rise in junction temperature would be approximately 5 percent greater for the units of manufacture B. This later proved to be a crucial decision resulting in rapid deterioration of units of manufacture B.

After completion of the two screening tests, the two groups were again subdivided, half of each group being

subjected to 6,000 hr of 100 °C shelf aging and the remaining half subjected similarly to power aging. The estimated 100 °C junction temperature for power aging was obtained with the combination of 70 °C ambient temperature and 120 mW of bias power (condition 14 in table 3).

Figure 7 summarizes the results of the 125 °C bake stress screening test. Similarly, figure 8 summarizes the results of the power stress screening test. The criterion for "satisfactory" performance was that IEBO and ICBO at 10 V must be no greater than 5 μA, as called for in the procurement specification for R212 transistors. Referring to the histograms, which show the distribution of fractional changes in junction leakage (IEBO or ICBO, whichever is the larger) induced by the screening stress, in figure 7 the pronounced mode lies below 1.0 and contrasts sharply with the bimodal distribution in figure 8, where both modes lie above 1.0. This indicates that the 125 °C shelf stress produced a reasonably uniform decrease in leakage current for all three manufacturers' transistors, whereas the nominal 125 °C power stress produced nonuniform increases in leakage current. The nonuniformity was due mainly to the R212 transistors of manufacture B exhibiting substantial deterioration; the leakage current increased in value to the extent that it exceeded 5 μA in 7 out of 20 transistors. Since these seven units no longer met the criterion for "satisfactory" performance, they were removed from the experiment. It is likely that the deterioration of these units was caused by excessively high junction temperature. As was mentioned earlier, the thermal resistance of the transistors of manufacture B was somewhat higher than that of the others and was calculated to produce a junction temperature more nearly 135 °C than the estimated 125 °C of the others. In sharp contrast to the above described deterioration under the power screening stress, the transistors of manufacture B exhibited the least degradation during the 125 °C shelf screening stress or the prolonged 100 °C shelf or power aging stress. The collective results of this experiment indicate that the effects of the power screening stress used was critically sensitive to the difference in thermal resistance and could have led to erroneous conclusions regarding the relative merits of the units of manufacture B. These results illustrate the possible hazards of applying uniformly, to a given type of transistor, excessive power as a means for screening or accelerating aging effects.

Referring again to figures 7 and 8, the relationship between fractional changes in leakage current and subsequent aging is shown for aging periods extending from 2,000 to 7,000 hr, as was done in a similar fashion in figures 1, 2, and 3. Although two aging conditions were used, a 100 °C bake stress and a 100 °C junction temperature obtained with applied power, the limited volume of data indicated no significant difference in aging behavior and, therefore, data from the two conditions were combined. The effectiveness of the screening process is illustrated in the two boxes in the upper portions of figures 7 and 8. The screening criterion of 1.6 ratio or greater, in the upper box, was

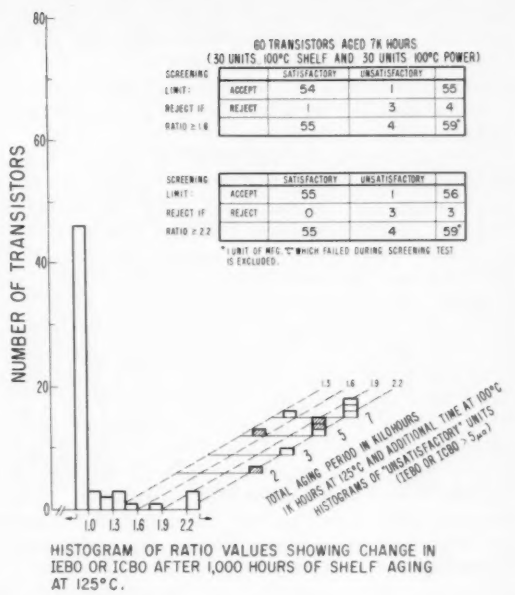
60 TRANSISTORS AGED 7K HOURS
(30 UNITS 100°C SHELF AND 30 UNITS 100°C POWER)
SCREENING LIMIT:
REJECT IF RATIO ≥ 1.6
SATISFACTORY
UNSATISFACTORY
ACCEPT 54 1 55
REJECT 1 3 4
55 4 59*
SCREENING LIMIT:
REJECT IF RATIO ≥ 2.2
ACCEPT 55 1 56
REJECT 0 3 3
55 4 59*
* 1 UNIT OF MFG "C" WHICH FAILED DURING SCREENING TEST IS EXCLUDED.
NUMBER OF TRANSISTORS
80
60
40
20
0
1.0 1.3 1.6 1.9 2.2
1.3 1.6 1.9 2.2
1 3 5 7
2
TOTAL AGING PERIOD IN KILOHOURS (1K HOURS AT 125°C AND ADDITIONAL TIME AT 100°C)
HISTOGRAMS OF "UNSATISFACTORY" UNITS (IEBO OR ICBO > 5μa)

HISTOGRAM OF RATIO VALUES SHOWING CHANGE IN IEBO OR ICBO AFTER 1,000 HOURS OF SHELF AGING AT 125°C.

FIGURE 7. *Analysis of 125 °C screening test (shelf).*

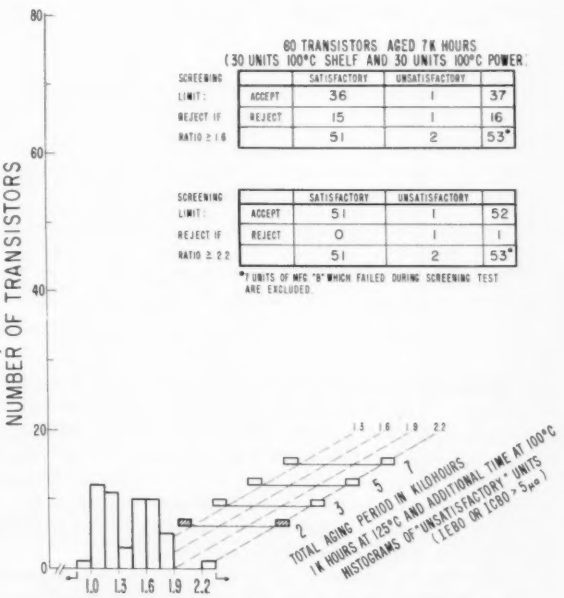
60 TRANSISTORS AGED 7K HOURS
(30 UNITS 100°C SHELF AND 30 UNITS 100°C POWER)
SCREENING LIMIT:
REJECT IF RATIO ≥ 1.6
SATISFACTORY
UNSATISFACTORY
ACCEPT 36 1 37
REJECT 15 1 16
51 2 53*
SCREENING LIMIT:
REJECT IF RATIO ≥ 2.2
ACCEPT 51 1 52
REJECT 0 1 1
51 2 53*
* 7 UNITS OF MFG "B" WHICH FAILED DURING SCREENING TEST ARE EXCLUDED.
NUMBER OF TRANSISTORS
80
60
40
20
0
1.0 1.3 1.6 1.9 2.2
1.3 1.6 1.9 2.2
1 3 5 7
2
TOTAL AGING PERIOD IN KILOHOURS (1K HOURS AT 125°C AND ADDITIONAL TIME AT 100°C)
HISTOGRAMS OF "UNSATISFACTORY" UNITS (IEBO OR ICBO > 5μa)

HISTOGRAM OF RATIO VALUES SHOWING CHANGE IN IEBO OR ICBO AFTER 1,000 HOURS OF POWER AGING AT ESTIMATED 125° JUNCTION TEMPERATURE.

FIGURE 8. *Analysis of 125 °C screening test (power).*

chosen because it is the largest of those used in the first experiment, and therefore allows comparison of the results. Since the screening stress was larger (125 °C), a second analysis was made using a larger value as a screening criterion. The second value, 2.2, was the largest one available without reprocessing the data and, fortunately, appears to be a reasonable choice.

The footnote under the boxes of figure 7 indicates that one unit of manufacture C failed, i.e., became "unsatisfactory," during the shelf screening test. Although such a failure may offhand appear to indicate rapid and destructive deterioration at 125 °C shelf stress (as was discussed for the 7 units of manufacture B which failed under the power screening stress), such a conclusion is surely questionable in light of the fact that one out of four of the same manufacturer's units also failed while subjected to 25 °C shelf storage, which was part of an experiment control.

Comparison of the screening summaries indicates superior results for the shelf-stress screen of figure 7. Such comparisons are usually difficult because of the several factors which should be considered. A better intuitive understanding may be reached for judging the effectiveness of the different screening tests by examining the summary in table 2. This table compares the relative number of "unsatisfactory" transistors present before screening with the number present after screening. An indication of the cost of the improvement through screening is given in terms of the relative number of "unsatisfactory" units rejected correctly compared to the total number rejected. The latter ratio indicates the (fractional) number of units rejected correctly.

TABLE 2. *Summary of effectiveness of screening tests*

Screening test (125 °C)		Relative number of "unsatisfactory" units present		Rejected correctly / Total rejected
Stress	Limit	Before screening	After screening	
Shelf	1.6	4/59 or 6.8%	1/55 or 1.8%	3/4 or 75%
	2.2		1/56 or 1.8%	3/3 or 100%
Power	1.6	2/53 or 3.8%	1/37 or 2.7%	1/16 or 6%
	2.2		1/52 or 1.9%	1/1 or 100%

This summary shows that for shelf stress screening, the two screening limits (1.6 and 2.2) were almost equally effective. For the power stress screening, however, the results were very sensitive to the choice of limit. The 2.2 value was preferred by far because the 1.6 limit caused 15 "satisfactory" units to be rejected in error. This is a relatively poor showing compared to the other three outcomes.

The results of the shelf screening test, even though the screening stress (125 °C) is somewhat more severe than that used in the first experiment (100 °C), support the general findings of the earlier experiment. The fractional change in leakage current appears to provide a useful measure of expected performance.

9. Conclusion

A study of the aging behavior of low-power germanium alloy switching transistors has revealed a relationship between small changes in junction leakage current, associated with a brief aging stress, and later deterioration in performance. Other parameters studied were ICES, ICER, ICEO, and 1 + hFB, which were measured, and the voltage sensitive component of the leakage current, the intrinsic leakage current, and hFE*, which were computed. With the possible exception of hFE*, none of these parameters appeared promising for stress-screening purposes.

These findings apply to transistors which had been accepted for stringent military requirements and were considered "high reliability" units. They had conformed to military acceptance specifications which had included a series of measurements on each device. It was not surprising, therefore, that the NBS 0-hr measurements proved to be of little value as a screening criterion. Even the variable or noisy character of some of the 0-hr measurements offered little hope as an indicator of expected performance. Shifts or jumps in parameter values while lightly tapping the transistor case, however, proved to be quite useful. Six type 2N396 transistors having fractured wafers or other mechanical faults were clearly identified while making preliminary measurements using this procedure, and were not included in the aging study.

The observed junction leakage current relationship to aging appears characteristic of several types and manufactures of germanium-alloy transistors. This relationship may provide the basis for a promising nondestructive screening procedure which would serve for the identification of germanium-alloy transistors likely to deteriorate through excessive growth in junction leakage current. Since leakage current deterioration has continued to be one of the more common forms of degradation in transistor performance, a screening procedure which is effective in guarding against such a fault would be of substantial value.

The proposed screening procedure involves the determination of relatively small changes in junction leakage current, increases of the order of 15 percent or more, associated with 1,000 hr of aging at a shelf (bake) stress of 100 °C. Because the leakage current changes of interest are small, high demands are placed upon measurement repeatability. A number of factors are important in maintaining the necessary long-term repeatability. There is need for operating procedures which provide a record of proof of stable performance through a history of frequent calibration and through a history of measurements on a group of "control" transistors. Also, the measurement procedure should treat each transistor alike. A stabilization or "soaking" period of a fixed duration (24 hr ± 2 hr) under measurement ambient conditions prior to measurement should be incorporated in the test procedure so as to minimize the transient recovery effects associated with the removal of the transistor from a high-temperature aging stress environment.

Relatively close ambient temperature control during measurement is essential. The very close control of ±0.01 °C of the NBS measurement facility, although proven to be a key feature in the aging studies, is unnecessarily stringent. Commercial equipment having control with ±0.1 or 0.2 °C is adequate for the leakage-current bake-stress screening described in this paper.

The initial choice of value of fractional change in junction leakage current as the screening limit is necessarily somewhat arbitrary. There is evidence that even transistors bearing identical type numbers but of different manufacture might require different screening limits. Once an initial choice is made, however, an *a posteriori* aging test of all rejected units and sample groups of accepted units is recommended as an evaluation procedure for monitoring the screening effectiveness and for improving the choice of screening limits. These procedures are now being followed at NBS in a further study of the proposed screening procedure as applied to much larger groups of transistors and to germanium transistors of different construction.

10. Appendix

A total of 516 germanium low-power alloy-junction switching-type transistors (type 2N396), obtained from a single manufacturer, were aged under 13 different combinations of ambient temperature, collector voltage, and collector current. The thirteen aging conditions are summarized in table 3, from which it may be seen that these conditions form an incomplete factorial experiment. Each condition is identified by a number in the lower left corner of each box. Each condition contained 40 transistors mounted on four plugs.

Immediately prior to being subjected to its aging environment, each transistor was measured twice, a morning group of 10 parameter measurements being replicated in the afternoon of the same day. During the course of the experiment, the transistors were periodically removed from their aging environments and the 10 parameters were measured four times before the aging treatments were again applied. The measurement period began with removal of the transistors from the aging environment, after which

Table 3 Aging Conditions

	T_j=25 °C	T_j=55 °C	T_j=100 °C	T_j=145 °C	T_j=200 °C	
V_{CB}=0v	PC=0mw, T_a=25 °C, ΔT_j=0 °C; STA/PLUG: 1/1000, 2/1002, 3/1004, 4/1006 1 (0,0,25)25	7	PC=0mw, T_a=100 °C, ΔT_j=0 °C; STA/PLUG: 5/1040, 6/1042, 7/1044, 8/1046 13 (0,0,100)100	19	PC=0mw, T_a=200 °C, ΔT_j=0 °C; STA/PLUG: 1/1098, 2/1098, 3/1904, 4/1906 25 (0,0,200)200	I_c=0ma
V_{CB}=3v	2	PC=120mw, T_a=25 °C, $\Delta T_j \approx$30 °C; STA/PLUG: 1/1016, 2/1018, 3/1020, 4/1022 8 (3,120,25)55	PC=120mw, T_a=70 °C, $\Delta T_j \approx$30 °C; STA/PLUG: 1/1048, 2/1050, 3/1052, 4/1054 14 (3,120,70)100	PC=120mw, T_a=115 °C, $\Delta T_j \approx$30 °C; STA/PLUG: 5/1072, 6/1074, 7/1076, 8/1078 20 (3,120,115)145	26	I_c=40ma
	3	PC=3mw, T_a=55 °C, $\Delta T_j \approx$1 °C; STA/PLUG: 5/1024, 6/1026, 7/1028, 8/1030 9 (3,3,55)55	PC=3mw, T_a=100 °C, $\Delta T_j \approx$1 °C; STA/PLUG: 5/1056, 6/1058, 7/1060, 8/1062 15 (3,3,100)100	PC=3mw, T_a=145 °C, $\Delta T_j \approx$1 °C; STA/PLUG: 1/1080, 2/1082, 3/1084, 4/1086 *21 (3,3,145)145	27	I_c=1ma
V_{CB}=12v	4	10	16	22	28	
	5	PC=480mw, T_a=-65 °C, $\Delta T_j \approx$120 °C; STA/PLUG: 1/1032, 2/1034, 3/1036, 4/1038 11 (12,480,-65)55	17	PC=480mw, T_a=25 °C, $\Delta T_j \approx$120 °C; STA/PLUG: 5/1088, 6/1090, 7/1092, 8/1094 23 (12,480,25)145	29	I_c=40ma
V_{CB}=24v	PC≈0mw, T_a=25 °C, ΔT_j=0 °C; STA/PLUG: 5/1008, 6/1010, 7/1012, 8/1014 6 (24,0,25)25	12	PC≈0mw, T_a=100 °C, ΔT_j=0 °C; STA/PLUG: 1/1064, 2/1066, 3/1068, 4/1070 18 (24,0,100)100	24	30	I_c=0ma

OVEN AND COLDBOX AMBIENT TEMPERATURE

-65 °C (4 PLUGS) +100 °C (12 PLUGS)
+25 °C (16 PLUGS) +115 °C (4 PLUGS)
+55 °C (4 PLUGS) +145 °C (4 PLUGS)
+70 °C (4 PLUGS) +200 °C (4 PLUGS)

POWER CONDITIONS

SHELF AGING (12 PLUGS)
0mw, 0ma, 24v (8 PLUGS)
3mw, 1ma, 3v (12 PLUGS)
120mw, 40ma, 3v (12 PLUGS)
480mw, 40ma, 12v (8 PLUGS)

NOTES

1—PLUG 1910 IS CONTROL PLUG
2—CONDITION 25 CONTAINS 4 PLUGS WITH MIXED WEEK OF MANUFACTURE.
3—(V_{CB}, PC, T_a)T_j IS CODING USED FOR BOTTOM LINE IN EACH CONDITION
*4—LEVEL OF CURRENT IN CONDITION 21 INCREASED TO 4ma, PC=12mw AND $\Delta T_j \approx$3 °C.

784-657 O-65-7

they were permitted to stabilize for 24 hr at 25 °C. During the morning of the second day of the measurement period, the 10 parameters were measured and a replicate set of measurements made during the afternoon. The transistors were then permitted to stabilize for an additional seven days, the a.m. and p.m. sets of measurements being repeated during the eighth day of the measurement period. A computer was used to compare the a.m. and p.m. replicate measurements and print out all which changed by more than 2 percent. This allowed all such measurements to be reviewed and, if necessary, repeated before returning the transistors to the aging environment.

The first three measurement periods, 340, 1,000, and 2,000 hr, were selected to correspond to those commonly used in aging schedules and specifications. The remaining periods were selected to provide approximately equal log-time intervals between the measurement periods. The intervals so determined are a fixed fraction of the elapsed time, and for this experiment, were roughly 40 percent of the elapsed time. This procedure gave the following total elapsed times at which the measurement periods fell: 3.4, 4.7, 6.0, 8.7, 11, 14, and 20 khr.

The d-c parameters measured, using automatic equipment, were as follows: IEBO and ICBO at 2 and 10 V; ICES, ICER (R = 10 kΩ), and ICEO at 10 V; normal and inverse 1 + hFB at 10 mA and 5 V. The tenth parameter, 1 + hfb, was measured using a 270-Hz small signal. From these measurements a number of additional parameters were computed. The computed parameters provided estimates of: the voltage-sensitive components of the leakage currents, the intrinsic leakage currents, and (1 + hFB)* (the asterisk indicating that the leakage current was subtracted from the measurement of 1 + hFB) and, finally, hFE*.

(Paper 69C4–213)

JOURNAL OF RESEARCH of the National Bureau of Standards—C. Engineering and Instrumentation
Vol. 69C, No. 4, October–December 1965

Publications of the National Bureau of Standards*

Selected Abstracts

Effect of hydrostatic pressure on the refractive indices of some solids, R. M. Waxler and C. E. Weir, *J. Res. NBS* **69A** (*Phys. and Chem.*), *No. 4, 325–333 (July–Aug. 1965), 70 cents.*
Measurements were made on refractive index changes with hydrostatic pressures between 1 bar and 1 kbar using the helium yellow line. The materials studied were: KBr, NaCl, LiF, diamond, MgO, quartz, Al_2O_3, and three silicate glasses. All the materials increased in refractive index with pressure except diamond, MgO, and Al_2O_3 which decreased, and LiF which did not change. The results were compared with photoelastic measurements, and Pockel's geometric theory of photoelasticity was substantiated as well as Mueller's physical theory. The data show that the ratio of change of polarizability with density is greater for solids having stronger interatomic repulsive forces. Volume and temperature coefficients of polarizability were evaluated for the cubic crystals and glasses. The thermo-optic behavior of crystals and glasses is discussed.

An absolute temperature scale from 4 °K to 20 °K determined from measurements with an acoustical thermometer, H. H. Plumb and G. Cataland, *J. Res, NBS* **69A** (*Phys. and Chem.*), *No. 4, 375–377 (July–Aug. 1965), 70 cents.*
At the National Bureau of Standards an acoustical thermometer has been used to obtain values of temperature at every degree from 5 to 20 °K as a basis for a temperature scale. This scale has been compared with four other temperature scales in the region from 10 to 20 °K. Since the acoustical thermometer is an entirely new approach to precision thermometry in this range the comparison of its resulting scale with scales based upon gas thermometry from 12 to 20 °K is significant. Indications of inaccuracies in equilibrium hydrogen vapor pressure scales, and also in the He^4 vapor pressure scale, are presented.

Current research on preservation of archival records on silver-gelatin type microfilm in roll form, C. S. McCamy and C. I. Pope, *J. Res NBS* **69A** (*Phys. and Chem.*), *No. 5, 385–396 (Sept.–Oct. 1965), 70 cents.*
This is a progress report on a study of aging blemishes on microfilm and measures to prevent their formation. Recommendations, based on current information, include: avoiding excessive densities, avoiding physical damage to the film, the use of potassium iodide in the fixer, thorough washing, uniform drying, storage at low temperature and humidity in sealed containers, avoidance of air-borne reactants, increased archival use of positive copies, and periodic inspection.

A wide-range (up to 10^{10}P) rotating cylinder viscometer, A. Napolitano, P. B. Macedo, E. G. Hawkins, *J. Res. NBS* **69A** (*Phys. and Chem.*), *No. 5, 449–455 (Sept.–Oct. 1965), 70 cents.*
The range of a high temperature rotating cylinder viscometer has been extended so that viscosity measurements can be made between 10^0 to 10^{10} poises to within 2 percent accuracy. This involves three different techniques. After a calibration constant has been determined for the apparatus in the standard oil range, the other two constants for the higher viscosities were self-determined. In making measurements at the low viscosities, 10^0 to 10^5 poises, the outer cylinder is rotated at constant speed and the torque measured on the inner cylinder; from $10^{4.5}$ to $10^{7.5}$ poises the inner cylinder is rotated through an angle and timed as it returns to its zero position, and from $10^{8.5}$ to 10^{10} poises the inner cylinder is driven through an angle at constant torque and timed as it traverses this angle. The Fulcher equation viscosity values obtained from previous measurements on Standard Glasses No. 710 and No. 711 by the fiber elongation and rotating cylinder methods have been compared with the present results.

Internal friction in ZrO_2 containing CaO, J. B. Wachtman, Jr., and W. C. Corwin, *J. Res. NBS* **69A** (*Phys. and Chem.*), *No. 5, 457–460 (Sept.–Oct. 1965), 70 cents.*
Internal friction was measured on polycrystalline ZrO_2 containing 4, 7, 10, 13, 16, and 20 mole percent CaO. In the range 10 to 20 percent a symmetrical internal friction peak occurs with its maximum at about 300 °C at 1 kHz; below 10 percent a nonsymmetrical peak occurs at somewhat higher temperature which may be associated with the presence of two phases. The symmetrical peak in as-sintered specimens has the same dependence on CaO content as that reported for electrical resistivity at 1000 °C and is probably caused by motion of oxygen vacancies. Annealing at 1000 °C for 1000 hours causes reduction of the peak height but with a different composition dependence from that reported for annealing of electrical resistivity. The results suggest that oxygen vacancies in calcia stabilized zirconia exist in several states of binding but that detailed models are likely to be complex.

On Kirchhoff's law and its generalized application to absorption and emission by cavities, F. J. Kelly, *J. Res. NBS* **69B** (*Math. and Math. Phys.*), *No. 3, 165–171 (July–Sept. 1965), 75 cents.*
Several authors have made the assumption that Kirchhoff's Law holds for the apparent local spectral emittance and apparent local spectral absorptance of any point on the interior surface of a cavity. The correctness of this assumption is demonstrated under certain general conditions, and its practical application to the calculation of the total flux absorbed by a cavity or spacecraft is discussed. A further application to the case of a nonisothermal cavity or spacecraft is derived. By this derivation an easy method for determining the total flux emitted from such a nonisothermal cavity is found when the distribution of the apparent local spectral emittance of the isothermal cavity is known. The economy and versatility of this method is shown by the calculation of the total flux emitted from a nonisothermal cylindrical cavity for several arbitrary cases of temperature distribution on the interior surface of the cavity. Finally, the integral equation for a diffuse cavity whose wall emittance varies with position on the wall is transformed to an equation having a symmetric kernel.

Ground-based passive probling using the microwave spectrum of oxygen, E. R. Westwater, *Radio Science J. Res. NBS/USNC–URSI* **69D,** *No. 9, 1201–1211 (Sept. 1965), $1.00.*
The determination of the kinetic temperature structure of the troposphere from ground-based measurements of oxygen emission spectra in the microwave region is discussed. Molecular absorption properties of oxygen and water vapor are reviewed. A new "inversion" technique is described. This technique uses a least squares-iteration solution which is applicable to Fredholm integral equations of the first kind. The inversion technique is used to reconstruct two types of tropospheric temperature profiles. The effects of certain types of errors in the brightness temperature on the derived temperature distribution are computed.

Response of NBS microwave refractometer cavities to atmospheric variations, R. O. Gilmer, R. E. McGavin, and B. R. Bean, *Radio Science J. Res. NBS/USNC–URSI* **69D,** *No. 9, 1213–1217 (Sept. 1965), $1.00.*
The sampling cavity of the NBS refractometers has been evaluated in a wind tunnel, a waterflow tunnel, and in the free atmosphere. The cavity is slightly velocity-sensitive. It is also aspect-sensitive, an error being introduced when the wind is oblique to the axis of the cavity affecting the level of the spectrum. The characteristic flushing length of the cavity in normal operation is estimated as 0.75 meters when the wind is into the cavity and considerably more when the wind is at an oblique angle. A modified cavity has been developed which appears to substantially improve the response of the refractometer.

Effects of rocket outgassing on rf experiments, W. Pfister and J. C. Ulwick, *Radio Science J. Res. NBS/USNC–URSI* **69D,** *No. 9, 1219–1225 (Sept. 1965), $1.00.*
Peculiarities in the results of electron density measurements with rockets were noticed on several occasions. They were found to be effects of rocket outgassing. When the fuel valves of Aerobee rockets are not shut after burnout, residual fuel leaks out and diffuses into the atmosphere. Electrons attach to the fuel and decrease in concentration while the positive ions are not affected. Outgassing effects were observed on probe experiments flown in rockets as well as on propagation experiments between rocket and ground. Quantitative estimates indicate that the leaking fuel is a very effective attaching agent. Some solid fuel rockets also show similar effects.

Measurement of group velocity of 17.8-kHz VLF radio waves, W. D. Westfall, *Radio Science J. Res. NBS/USNC–URSI* **69D,** *No. 9, 1235–1238 (Sept. 1965), $1.00.*
Group velocity of 17.8 kc/s VLF radio waves is determined by measuring the difference in time of arrival of the transmitted signals which travel over complementary great circle paths. The velocity is found to be 3.04×10^8 meters/second with an estimated error of approximately $\pm 0.10 \times 10^8$ meters/second. Differences in measurement technique and general environmental conditions between this experiment and a previous measurement of 18 kc/s group velocity which was made in 1949 is discussed.

Propagation of pulses in dispersive media, J. R. Wait, *Radio Science J. Res. NBS/USNC–URSI* **69D,** *No. 11, 1387–1401 (Nov. 1965), $1.00.*
The paper deals with various approximate procedures for calculating the distortion of a pulse after it has propagated through a dispersive channel such as a waveguide. The methods used for evaluating the integrals utilize a stationary phase principle. Both impulsive-type and quasi-monochromatic sources are considered. It is shown that, in most cases, the transient response may be obtained straightforwardly from the shape of the phase versus frequency characteristics of the system. Some attention is given to the complication which arises when the group velocity has an extremum as a function of frequency.

Interference rejection capability of a switched radiometer, R. E. Clapp, *Radio Science J. Res. NBS/USNC–URSI* **69D,** *No. 11, 1425–1429 (Nov. 1965), $1.00.*
The increasing congestion of the radio-frequency spectrum makes necessary a re-examination of current techniques used in radiometric receivers for radio astronomy. Square-wave switching, as currently used, modulates incoming CW signals and introduces sidebands which can intrude on the presently available windows in the spectrum. This effect can be treated as an apparent deterioration of an ideal square-sided filter. Examples are given, for different filter bandwidths and chopping frequencies. Where radiometry is interference-limited, sinusoidal chopping or a correlation technique avoiding chopping is strongly recommended.

Atmospheric breakdown limitations to optical maser propagation, R. G. Tomlinson, *Radio Science, J. Res. NBS/USNC–URSI* **69D,** *No. 11, 1431–*1433 *(Nov. 1965), $1.00.*
It is shown that air breakdown by focused optical maser pulses is dependent on gas pressure. It would appear that megawatt type pulses of 10 to 100 nanosecond duration could produce air breakdown.

Electrical engineering units and constants, *NBS Misc. Publ. 268 (June 1965), 10 cents a copy; $6.26 per 100 copies.*
This publication is a compilation of electrical engineering symbols and units and physical constants used in electrical engineering.

Examination of liquefied petroleum gas liquid-measuring devices, M. W. Jensen, *NBS Handb. 99 (Apr. 23, 1965), 35 cents.*
A manual for State and local weights and measures officials, describing the devices, testing equipment and its calibration, inspecting and testing procedures, and a reporting system.

Steel medicine cabinets, *NBS CS267–65 (Mar. 1, 1965), 10 cents.*
This Commercial Standard covers the requirements for materials, construction, finishes, accessories, minimum sizes, methods of test and the labeling of sliding-door and swinging-door steel medicine cabinets. Cabinets having a combination of mirror and enclosed sliding door shelves, and known variously as mirror vanity, vanity mirror and vanity shelves, or otherwise designated, are not covered by this standard.

Hide trim pattern for domestic cattlehides, *NBS CS268–65 (Apr. 4, 1965), 10 cents.*
This Commercial Standard covers the trimming of hides of the domestic bovine species generally described as "domestic packer cattlehide", and other comparable hides.

Phase and amplitude diversity in over-water transmissions at two microwave frequencies, H. B. Janes, A. W. Kirkpatrick, D. M. Waters, and D. Smith, *NBS Tech. Note 307 (Apr. 12, 1965), 40 cents.*
Propagation measurements at 9.4 and 9.2 Gc/s were made over a 47 km, line-of-sight, over-water path at Eleuthera Island in the Bahamas. The purpose was to study the signal amplitude and phase variations at the two frequencies, and in particular, the variations in the phase difference and amplitude ratio ("differential amplitude") of the two frequencies. The results include power spectra of phase and phase difference variations (from about 10^{-4} to 4 c/s) and cumulative distributions of amplitude, differential amplitude, and phase difference.

A bibliography of experimental saturation properties of the cryogenic fluids, N. A. Olien and L. A. Hall, *NBS Tech. Note 309 (Apr. 9, 1965), 60 cents.*
A bibliography of 507 references to experimental work is presented for the properties of the cryogenic fluids in the solid, liquid, and vapor phases at saturation. The cryogenic fluids included are helium, hydrogen, neon, nitrogen, oxygen, air, carbon monoxide, fluorine, argon, methane, and isotopes of helium, hydrogen, and methane. Each article has been reviewed and coded for properties, method of presentation of the data, and temperature range. An index lists each fluid in five categories: solid-solid transition, solid-liquid transition, solid-vapor transition, liquid-vapor transition, and triple point. For helium the liquid-liquid transition is also included. Each category is indexed by the properties: pressure-temperature data, density and heat capacity of all phases at saturation, and latent heats.

Watermarks for papermaking by electroforming, J. P. Young, *Tappi* **48,** *No. 1, 36A–37A (Jan. 1965); Metal Finishing* **63,** *No. 4, 79–82 (Apr. 1965).*
A process has been developed whereby a watermark is electroformed on a papermaking screen. The pattern of the watermark is first outlined on the screen by use of a photosensitive resist or by the use of a suitable resist and the silk screen process. The watermark is then formed directly on the screen with electrodeposited copper. This process allows transfer to the papermaking screen of any line or silhouette pattern, no matter how complicated, from a film transparency with a saving of time and skilled labor.

Latensification in radiographic emulsions, W. L. McLaughlin, *J. Photo. Sci.* **13,** *1–11 (1965).*
Latensification by means of post-exposures to selected wavelengths of light or near infrared is shown to provide as much as threefold enhancement of response of some commercial x-ray emulsions to ionizing photons. The sensitivity can be similarly enhanced by special development procedures. A combination of these techniques permits a five- or six-fold increase in sensitivity in the low-density region, for some emulsions. Spectral sensitivity changes in the x- and γ-ray response are small; no rate dependence is observed; variations in total density, however, are found with differences in delay period between exposure and post-exposure and between post-exposure and processing. The effects may be explained by the change in the size and location of development centers resulting in an improvement of development activity, and therefore in a larger number of developed grains. In some instances, there may be an increase in developed grain size.

On the information in a microphotograph, C. S. McCamy, *Appl. Opt.* **4,** *No. 4, 405–411 (Apr. 1965).*
The information concentration of a legible microphotograph made

at a reduction ratio of 1200 is computed to be over 2×10^6 bits/mm². Reasons are adduced for using a mosaic of squares having sides equal to the reciprocal of the resolving power, each being capable of assuming one of two density ranges, as a model of a high contrast material for the computation of information capacity. It follows that the information capacity is equal to the square of the resolving power. This relation gives values of information capacity in good accord with the values computed by the Jones theory. The information capacity of a Kodak High Resolution Plate is computed to be 3.25×10^6 bits/mm². That the product of reduction ratio times quality index equals the product of resolving power times the height of the lower case **e** in type to be copied is verified at the high reduction ratio, and this relationship is considered useful for engineering computations involving the copying of commonly used styles of type. The use of literal charts designed on the basis of information theory is suggested for the evaluation of microcopying systems.

Results of National Bureau of Standards corrosion investigation in disturbed and undisturbed soils, M. Romanoff, *Proc. Appalachian Underground Short Course, Tech. Bull.* **72,** *566–589 (West Virginia Univ., Morgantown, West Va., 1965).*
This paper gives (1) a summary of the extensive investigations which have been in progress at the National Bureau of Standards since 1922 on the corrosion of metals in a wide variety of soils for exposures up to 17 years, and (2) a summary of the results of inspections made on steel pilings after exposures up to 40 years in various underground structures.
The corrosion data show that there is an appreciable difference in the corrosion observed on steel pipe specimens buried at the test sites under disturbed soil conditions, and with that observed on steel pilings driven in undisturbed soils.

Technique for determining spin-lattice relaxation times, G. A. Candela and R. E. Mundy, *Rev. Sci. Instr.* **36,** *No. 3, 338–342 (Mar. 1965).*
Experiments were performed so that the actual change in the static direct current susceptibility of a paramagnetic material could be measured as a function of microwave power absorbed at electron spin resonance. The spin-lattice relaxation τ_1 can be expressed by

$$\tau_1 = \frac{(\chi_0 - \chi_s)}{P_a \Gamma_m} M_s B_{dc}^a$$

where P_a is the microwave power necessary to change the field independent static susceptibility from χ_0 to χ_s. χ_s is the steady state static susceptibility of the sample when it is absorbing P_a amount of microwave power. B_{dc} is the homogeneous dc field produced by the laboratory magnet, M_s is the weight of the sample, and Γ_m is the magnetic constant. The relaxation time is determined by directly measuring P_a, M_s B, χ_0, and χ_s/χ_0. The apparatus, the experimental techniques, and the accuracy of the measurements are described in some detail.

Two cases of stress corrosion cracking in copper tubing, H. L. Logan and G. M. Uginsky, *Materials Prot.* **4,** *No. 3, 79–80 (May 1965).*
A failure in annealed copper tubing used to transport natural gas from the main to an individual dwelling was investigated and found to be due to stress-corrosion cracking penetrating through the tubing wall from the exterior surface. A second failure also diagnosed as stress-corrosion cracking is also reported. In each case the area of failure had been encased in a section of steel pipe.

Nomographs for computing real, imaginary, and absolute values of vector ratios, H. S. Bowman, *Acoust. Soc. Am.* **37,** *No. 4, 751 (Apr. 1965).*
Two nomograms were designed and constructed to compute real, imaginary, and absolute values of two-dimensional vector ratios.

A study of errors in the measurement of microscopic spheres, C. P. Saylor, *Appl. Opt.* **4,** *No. 4, 477–486 (Apr. 1965).*
Uncertainties in the microscopical measurement of small spheres as influenced by index of refraction of the mount, focus, aperture, and resolution have been variously reported and denied. The present study was conducted with large spheres in order to disclose the basic phenomena, but with such optical conditions as would ordinarily be used for much smaller objects. The reality of each reported error is verified. The principal uncertainties originate in the geometrical optics of thick bodies, but these effects tend to be confused by limitations in resolving power.

Definition of "ampere" and "magnetic constant", C. H. Page, *Proc. IEEE* **53,** *No. 1, 100–101 (Jan. 1965).*
Confusion about the definition of the MKSA system of electrical units is related to two meanings of the word "ampere." This word refers to either the physical *measurement unit* of *current*, or the *abstract unit* in the mathematical representation of current.
The magnetic constant is defined as the proportionality constant in an equation representing the interaction force between current elements; assignment of a numerical value to this constant implicitly defines the physical ampere.

Electromagnetic measurement, H. W. Lance, *SPACE/AERONAUTICS Res. Develop. Handb.* **42,** *No. 4, 199–202 (1964–1965).*
Important recent developments in electromagnetic measurements are helping to fill a serious "measurements gap." Cesium beam frequency standards have been improved, and recently inaugurated LF and VLF standard frequency broadcasts permit improvements to be realized at receiving stations. In the low frequency region improved ratio devices (especially inductive voltage dividers) permit laboratories to perform a wide variety of measurements based upon relatively few reference standards. In the high frequency region improved coaxial connectors permit significant improvements in the accuracy of most types of measurements in coaxial systems. In the microwave region an accelerated radar standards program in the NBS Radio Standards Laboratory offers the probability of relief in this critical measurement area. The increasing maturity of the millimeter wave field and the extension of coherent radio measurement techniques to optical frequencies offer new challenges in electromagnetic measurements.

A test of analytical expressions for the thermal emissivity of shallow cylindrical cavities, F. J. Kelly and D. G. Moore, *Appl. Opt.* **4,** *No. 1, 31–40 (Jan. 1965).*
Analytical expressions for the directional thermal emissivity of a shallow cylindrical cavity were tested by means of room temperature reflectance measurements. The measurements were made by placing a paper-lined brass cavity of adjustable depth over the specimen opening of a recording spectrophotometer. Reflectance curves were obtained from 0.4 μ to 0.75 μ with the plunger positioned to give cavity depth-to-radius ratios of 0, 0.5, 1.0, 1.5, and 2.0. The resulting reflectances were then converted to emissivities through use of the relation that, for an opaque material, the emissivity is equal to one minus the reflectance. Two theoretical expressions predicted the emissivity of a cavity with a diffusely reflecting wall to within 0.01. A closed-form expression of Gouffé, which forms the basis of a shallow-hole method for measuring the emissivity of nonmetals at high temperatures, was in as good agreement with the experimental measurements as a more rigorous expression derived by a different approach. Sizable departures of the cavity walls from good diffusers had a negligible effect on the emissivity of the cavity at a depth-to-radius ratio of 0.5, but the effect of specular components became progressively greater as the cavity depth was increased.

A universal color language, K. L. Kelly, *Color Eng.* **3,** *No. 2, 16–21 (Mar.–Apr. 1965).*
A method of color designation which provides a universal means of color communication for people of varying technical and occupational backgrounds, using a newly available, basically different type of color chart.

High silica glass, quartz, and vitreous silica, J. S. Laufer, *J. Opt. Soc. Am.* **55,** *No. 4, 458–460 (Apr. 1965).*
A discussion of confusion in the literature caused by twenty-eight terms used to describe high silica glass, natural quartz, cultured quartz, and the two classes of vitreous silica. Five clearly defined terms are recommended to eliminate error or confusion whenever these materials are mentioned. Appropriateness of the chosen terms is discussed on the basis of structure of the materials.

Interference patterns in reverberant sound fields. II, R. V. Waterhouse and R. K. Cook, *J. Acoust. Soc. Am.* **37,** *No. 3, 424–428 (Mar. 1965).*

Contour charts are given of the sound fields near one, two, or three reflecting surfaces at right angles, for random sound incidence. The charts show contours of the mean-squared pressure in decibels as a function of position in the region within two wavelengths of the boundary surfaces. The boundary conditions at the reflecting planes are pressure-reflecting (normal velocity component equal to zero) or pressure-release (pressure equal to zero). By reciprocity, the charts also give the relative radiation resistance of a point source as a function of position near such reflectors. The formulas used are tabulated; they extend and in some places correct formulas given in an earlier paper [J. Acoust. Soc. Am. **27**, 247–258 (1955)]. The features of the sound fields near the reflectors are discussed, and some applications to acoustical measurements in reverberant sound fields are considered.

The use of terahertz photobeats for precise velocity-of-light measurement, Z. Bay and H. S. Boyne, *Proc. Enrico Fermi International School of Physics: Course No. XXXI Quantum Electronics and Coherent Light 1963, pp. 352–371 (1964).*

A method for the determination of the velocity of light using high frequency beats of the order 10^{12} cps between laser lines is discussed. The feasibility of accurately measuring the beat frequency by means of a special phototube similar in design to a fast cathode ray tube is examined in detail. It is shown that one might expect to measure beat frequencies as high as 1.6×10^{12} cps if there is no appreciable electron scattering in the photocathode. A determination of the wavelength separation $\Delta\lambda$ corresponding to the beat frequency ω can be made with a scanning Fabry-Perot interferometer of a few meters length in order to obtain a precision of one in 10^8 for the velocity of light.

Potential use of passive probing of atmospheric structure by thermal emissions at radio frequencies, B. R. Bean, E. R. Westwater, and R. L. Abbott, *(Proc. 1963 Intern. Symp. Humidity and Moisture, Washington, D.C.), Book, Humidity and Moisture. Measurement and Control in Science and Industry, Vol.* **2,** *Applications, Sec. VII, Paper 71, pp. 595–608 (Reinhold Publ. Corp., New York, N.Y., 1965).*

Microwave resonance lines of water vapor ($\nu = 22.235$ Gc/s) and oxygen (50 Gc/s $< \nu <$ 65 Gc/s) give rise to strong thermal emissions by the atmosphere in the microwave region. The intensity of these emissions depends on the water vapor and temperature distributions within the atmosphere. This paper explores the possibility of using ground-based radiation measurements of these thermal emissions to determine the gross water vapor and temperature profiles of the lower atmosphere.

Radio refractometry and its potential for humidity studies, R. E. McGavin and M.J. Vetter, *(Proc. 1963 Intern. Symp. Humidity and Moisture, Washington, D.C.), Book, Humidity and Moisture. Measurement and Control in Science and Industry, Vol.* **2,** *Applications, Sec. VII, Paper 66, pp. 553–560 (Reinhold Publ. Corp., New York, N.Y., 1965).*

Radio refractometers have been in use for the past decade. Their primary use has been in the investigation of the refractive index structure as applied to radio wave propagation. There has been considerable improvement in these devices in recent years and the present status of radio refractometery indicates broader application of these techniques. Since the radio refractive index is a function of pressure, temperature, and humidity, these devices can be converted to hygrometers when suitable compensation for temperature and pressure is applied. This technique has been used successfully by a number of investigators. The results of some of these investigations are reviewed.

The use of the radio refractometer to measure water vapor turbulence, B. R. Bean and R. E. McGavin, *(Proc. 1963 Intern. Symp. Humidity and Moisture, Washington, D.C.), Book, Humidity and Moisture. Measurement and Control in Science and Industry, Vol.* **2,** *Applications, Sec. VII, Paper 67, pp. 561–568 (Reinhold Publ. Corp., New York, N.Y., 1965).*

The turbulent transport of the radio refractive index is studied theoretically. This study indicates that, under a wide range of conditions, the turbulent fluxes of the radio refractive index and of the absolute humidity are linearly related.

The initial results of an experiment specifically designed to check this conclusion are in agreement with the theoretical analysis.

Emission spectroscopy, B. F. Scribner and M. Margoshes, Treatise on Analytical Chemistry, Ed. I. M. Kolthoff and P. J. Elving, *6, Pt. 1, Chapt. 64, pp 3347–3461 (Inter-Science Publ. Inc., New York, N.Y., 1965).*

The literature on optical emission spectrometry, including atomic absorption and flame photometry, is reviewed for the period since the last reviews which appeared in Analytical Chemistry in April, 1962. Attention is given to contributions of basic importance or to analytical applications that are new, unique, or extensive. The review is divided for convenience into sections including Books and Reviews, Spectral Descriptions and Classifications, Spectroscopic Instrumentation, Excitation, Standards and Calibration, Isotopic Analysis, Trace Analysis, Analysis of Gases, Analysis of Metals, Analysis of Non-Metals, and Literature Cited. The reference list totals 565.

Gas chromatographic determination of the moisture content of grain, E. L. Weise, R. W. Burke, and J. K. Taylor, *(Proc. 1963 Intern. Symp. Humidity and Moisture, Washington, D.C.), Book, Humidity and Moisture, Ed. A. Wexler, Vol.* **IV,** *Principles and Methods of Measuring Moisture in Liquids and Solids, Chapt. 1, pp. 3–6 (Reinhold Publ. Corp., New York, N.Y., 1965).*

Water is extracted from ground grain by anhydrous methanol as in the Karl Fischer titration method of Hart and Neustadt. Determination of water in the methanol extract by gas chromatography yields a value for the moisture in the grain. Various gas chromatographic columns and operating conditions were explored to find combinations suitable for the adequate separation and accurate determination of small amounts of water in large excesses of methanol. Comparison is made with the Karl Fischer method. This procedure should be applicable to other materials if (1) methanol will extract all of the water classed as "moisture" and (2) methanol does not extract substances that would coincide with either the methanol or water peaks on the chromatogram.

Oxidation of asphalt flux with oxides in nitrogen, P. G. Campbell and J. R. Wright, *Ind. Engr. Chem. Prod. Res. Develop.* **4,** *No. 2, 121–128 (June 1965).*

An asphalt flux of Southeastern U.S.A. origin was treated with various oxides of nitrogen as the oxidizing gases. Changes in physical and chemical properties were measured by infrared spectroscopy, softening points, and microviscometry. Reaction temperatures did not exceed 166 °C. and gas flow rates were well below those used in the commercial air-blowing of asphalts. Nitrous oxide and nitric oxide, alone, gave very little reaction. Nitrogen dioxide, photosensitized nitrogen dioxide, and a nitric oxide-oxygen mixture reacted rapidly with the asphalt flux to produce coating-grade asphalts. The reaction time needed to produce a given asphalt softening point with photosensitized nitrogen dioxide, for example, was 1/20 that needed for air alone. Coating-grade asphalts made with oxides of nitrogen were more stable to photo-oxidation, and to film rupture at any given rate of shear, than was the commercial asphalt from the same flux. A correlation was observed between the extent of photo-oxidation of exposed asphalts and the changes in viscoelastic properties.

Radiation-induced polymerization and other reactions of *n*-perfluoropentadiene-1, 4 at high temperature and pressure, D. W. Brown, J. E. Fearn, and R. E. Lowry, *J. Polymer Sci.* **3,** *Pt. 2, 1641–1660 (1965).*

The radiation-induced polymerization of *n*-perfluoropentadiene-1, 4 was studied between temperatures of 100 and 170 °C and pressures of 8,000 and 15,000 atm. Kinetic evidence indicates that polymerization occurs by a free radical reaction; the activation energy is between 14 and 17 kcal/mole and the activation entropy is -8 ± 5 e.u./mole. Transfer with monomer limits the number-average degree of polymerization to values of 40 or less except in special circumstances. Dimerization and double bond migration occur to some extent; *n*-perfluoropentadiene-1, 3 is formed in the latter process. It and the 1,4-diene copolymerize; the latter undergoes cyclic addition so that the polymers are soluble and have little perfluorovinyl unsaturation. The polymers are brittle if the fraction of 1, 3-diene in the polymer is less than 0.1. They are rubbery and of considerably higher molecular weight if the fraction of 1, 3-diene is greater than 0.4. The thermal stability of the polymers decreases as the content of 1, 3-diene increases.

Strength of fingernails, R. W. Young, S. B. Newman, and R. J. Capott, *J. Invest. Dermatol.* **44,** *No. 5, 358–360 (Dec. 23, 1964).*
A method is described for determining strength values on fingernails. Flexural stresses ranging up to 880 kilograms per square centimeter have been obtained by this technique. Data from fingernails of a number of subjects are shown to be in agreement with strength values for other keratinous materials. The use of this method as a tool for evaluating the effects of diet on fingernails is proposed.

A miniature helium turbo-expander for cryogenic refrigeration systems, M. T. Norton, (*Proc. XI Intern. Congress Refrigeration, Munich, Germany, Aug. 1963*), *Prog. Refrig. Sci. Technol.* **1,** *131–135 (1963).*
The Cryogenic Engineering Laboratory is investigating the use of small turbo-expanders, supported by gas bearings, which produce small amounts of refrigeration at 4.2 °K and 30 °K. The turbine and externally pressurized gas bearings used with the 4.2 °K system have previously been reported.
This paper describes a helium turbine expander designed for use in a closed cycle system. The turbine was designed to extract about 200 watts at 30 °K from the helium flow. The turbine is 7.9 mm in diameter, rotates at 9800 revolutions per second, and was designed for an inlet pressure of 4 atmospheres and a 4:1 pressure ratio. Tests covering pressure ratios from 4:1 to 6.4:1 indicate a peak efficiency of 65 percent. The turbine design philosophy and performance data of this turbine are given.

A waveguide noise standard, C. K. S. Miller, W. C. Daywitt, and E. Campbell, (*Proc. Intern. Measurements Conf.*), *Acta IMEKO* **3,** *371–382 (1964).*
Radio astronomy and noise measuring systems have laid heavy stress on the need for noise standards covering an increasingly larger frequency range. In response to this need, the National Bureau of Standards recently has completed work in National Standards and comparison systems for calibrating microwave noise sources in WR90 (8.2 to 12.4 Gc) and WR62 (12.4 to 18.0 Gc) waveguide. This availability has, in turn, placed more emphasis on the need for good interlaboratory noise standards. The gas-discharge noise tube makes a very stable, long-life source for use in an interlaboratory standard. However, the available noise source mounts examined did not have the required characteristics for use in this quality of standard. This paper discusses experimental data of gas-discharge noise sources gathered over a period of two years and indicates where improvements can be made. Using this knowledge, an experimental gas-discharge noise tube mount was designed and constructed. The data taken using this mount indicated that the new design was suitable for interlaboratory work and provided a possible means of using the improved mount with different gas tubes to form more than one standard.

A standard for extremely low values of spectral irradiance, R. Stair, W. B. Fussell, and W. E. Schneider, *Appl. Opt.* **4,** *No. 1, 85–89 (Jan. 1965).*
To serve the interests of workers in certain fields of extremely low irradiation such as is present in the air glow and in phosphorescent, fluorescent, biochemical, and associated areas, a standard of spectral irradiance of extremely low intensity has been set up. This standard, in effect, combines the NBS standard of spectral radiance with a small aperture which approximates a point source of radiant energy of known spectral distribution. This combination, with one or more convex mirrors, will supply extremely low, spectral irradiances in wavelength range 0.25 to 2.6 microns with an uncertainty of about 10 percent.

Commercial carbon composition resistors as pressure transducers, C. E. Miller, J. W. Dean, and T. M. Flynn, *Rev. Sci. Instr.* **36,** *231–232 (Feb. 1965).*
This paper presents the results of a recent series of pressure tests conducted on a group of commercial carbon composition resistors and discusses the possible application of the unique piezoresistive behavior of these resistors to pressure measurement.

Human engineering in the design of a console for the comparison of volt boxes, P. H. Lowrie, Jr., *19th Annual Instr. Soc. Am. Conf. and Exhibit, Preprint No. 12.1–3–64, pp. 1–8 (Oct. 12–15, 1964).*
Too often the human element is not given adequate consideration in the design of precise measuring equipment. The dependence upon the operator for the attainment of high measurement accuracies cannot be denied. This paper describes a calibration console in which the human engineering factors were given the same consideration as the technical requirements. In this system the operator is considered to be a decision maker, and those functions not requiring judgment are handled automatically by the console. Most of the calculations are performed automatically by internal circuits, and the results are displayed digitally upon command. The console is an illustration in point that the principles of human engineering are as applicable to the precise measurements found in the standards laboratory as they are to the production line. The paper discusses the features of the console and points out some of the pitfalls that may be encountered in a design of this type.

Maintenance of maring electronic equipment by personnel not trained in electronic maintenance, G. Shapiro and G. J. Rogers, *Proc. Annual Tanker Conf. American Petroleum Institute, pp. A–1–A–18 (June 1965).*
The fault isolation technique developed at the National Bureau of Standards for the Navy could be used aboard the ships of the Merchant Marine to permit the electronic equipment used on the bridge and in the engine room to be maintained at sea by the ship's officers. A more sophisticated version of the test instrument can be used to provide a maintenance log.
This maintenance technique is implemented by building the electronic system of functional modules, by providing test sockets at which each module's performance can be evaluated, and by using a test instrument which indicates that module performance is good if it is within prescribed limits, and bad if it is not. For the maintenance log, a different test instrument would be used to present performance information in quantitative terms.

Optical instrumentation for the biologist: microscopy, J. R. Meyer-Arendt, *Appl. Opt.* **4,** *No. 1, 1–9 (Jan. 1965).*
A great variety of optical instruments has been developed for use in biology. The microscope and its many special types are part of them. In this article, a survey is given on the history, development, current status, and future outlook of general microscopy, microspectroscopy, interference microscopy, and electron and x-ray microscopy.

Precision detector for complex insertion ratio measuring systems, C. M. Allred and R. A. Lawton, *IEEE Trans. Instr. Meas.* **IM–13,** *No. 2 & 3, 76–81 (June-Sept. 1964).*
A precision, low-noise, highly sensitive, synchronous rf detector is described that permits simultaneous phase and level nulling in complex insertion ratio measuring systems. This insertion ratio is a measure of both the phase shift and magnitude change produced by a network when inserted in a transmission path.

Stress corrosion cracking of metals, H. L. Logan, *Metals Engr. Quart.* **5,** *No. 2, 32–38 (May 1965).*
Stress-corrosion cracking results from a combination of high, but usually residual, tensile stresses and the chemical action of a specific but mild corrodent. The functions of the specific corrodent are to (a) form a protective film on the surface of the metal and (b) reduce the energy to form new surfaces at the crack tip. Cracking is initiated and propagated in part by an electrochemical process. Small anodes are formed at grain boundaries or on grain faces as the result of plastic deformation which either ruptures a protective film and/or produces a heterogeneous condition at the grain boundary or on the grain face. The unstrained material forms a large cathode. Cracking proceeds by an electrochemical process until the stress concentration becomes sufficiently large to trigger a fracture. In the early stages of crack propagation, fracture will be stopped by the energy requirements to plastically deform the material at the crack tip. Eventually the structure may fail by ductile fracture.
If upon deformation tangled arrays of dislocations are formed in the material, stress-corrosion cracking, if it develops, will be intercrystalline.
In face centered cubic material, if conditions of dislocation array, short range order and/or stacking fault energy prevent cross slip, stress corrosion cracking will most probably be transcrystalline.

The effect of a fatigue crack on the fatigue strength of an aluminum alloy, J. A. Bennett, *Mater. Res. Std.* **5,** *No. 5, 235–239 (May 1965).*

Specimens of 2024–T4 aluminum alloy were subjected to reversed bending at a stress amplitude of 40 ksi, and the loss of fatigue strength due to this stressing was evaluated by subsequent tests at lower stress amplitudes. The phenomenon of gas evolution was used to determine whether or not a crack had developed during the damaging stressing; it was found that prior to the development of a crack the fatigue strength was reduced only 10–20 percent but that a small crack caused a further 50–60 percent reduction. These results demonstrate the necessity for considering the two stages of a fatigue failure separately in attempting to evaluate cumulative damage in this material.

The role of cryogenics in the production of high and ultra-high vacuum, L. O. Mullen and M. J. Hiza, *Cryogenics* **4,** *No. 6, 387–294 (Dec. 1964).*

Many of the variables affecting the equilibrium pressure in a vacuum system are temperature dependent. This paper, oriented toward unbakeable and elastomer sealed systems, reviews the effects of some of these variables. Some recognized limitations of cryopumps and diffusion pumps at pressures in the low 10^{-10} torr range are pointed out.

A comparison between the National Bureau of Standards two-pressure humidity generator and the National Bureau of Standards hygrometer, S. Hasegawa, R. W. Hyland, and S. W. Rhodes, *(Proc. 1963 Intern. Symp. Humidity and Moisture, Washington, D.C.), Book, Humidity and Moisture. Measurement and Control in Science and Industry, Ed. A. Wexler, Vol.* **3,** *Fundamentals and Standards, Chapt. 22, pp. 455–459 (Reinhold Publ. Corp., New York, N.Y., 1965).*

A 3×3 Graeco-latin square experiment was used for testing four parameters of the National Bureau of Standards two-pressure humidity generator to determine which parameters influence the accuracy of the generator. The external saturator temperature, the saturation temperature, the saturator pressure, and the air flow were varied and the calculated mixing ratio of the generator was compared against the mixing ratio as measured with the National Bureau of Standards' standard gravimetric hygrometer.

The results show that for the highest accuracy, the National Bureau of Standards' pressure humidity apparatus has a maximum flow limitation of under five standard cubic feet per minute (scfm). Tentative values of the correction factor for the saturation pressure of pure water vapor when used to compute the humidity of water-air mixtures were obtained. The correction factor is a function of saturation temperature and pressure. It is estimated that the maximum uncertainty in the mixing ratio produced by the generator is 1/2 percent over a range of final saturator temperature of 25° to −20 °C and final saturator pressure of 0 to 60 psia.

A pneumatic bridge hygrometer for use as a working humidity standard, L. Greenspan, *(Proc. 1963 Intern. Symp. Humidity and Moisture, Washington, D.C.), Book, Humidity and Moisture. Measurement and Control in Science and Industry, Ed. A Wexler, Vol.* **3,** *Fundamentals and Standards, Chapt. 20, pp. 433–443 (Reinhold Publ. Corp., New York, N.Y., 1965).*

A pneumatic bridge, utilizing two sets of critical flow nozzles in series and arranged to form a network analogous to a Wheatstone bridge, is described. By inserting a desiccant between the two nozzles in one arm of the bridge and measuring the ensuing pressure difference across the bridge produced by the absorption of the water from the test gas in one arm of the bridge, a measure of the humidity of the test gas is obtained. The equation expressing the relationship between the bridge pressure ratio, I, and the mixing ratio, r, defined as the mass of water per mass of dry gas, is given by

$$I = 1 - \frac{1 + Kr}{(1 + r)^{1/2}(1 + r/E)^{1/2}}$$

where E is the ratio of the molecular weight of water to that of the dry test gas and K is an empirically determined constant. The bridge pressure ratio is the ratio of a measured pressure difference to the sum of two measured absolute pressures. This instrument may be calibrated against a suitable reference standard. When calibrated against the NBS gravimetric hygrometer, a value of $K = 20.62 \times 10^{-3}$ was obtained. The largest error measured, over the range of 0.15 to 19.1 mg of water vapor per gram of dry air, was 0.025 mg of water vapor per gram of dry air. The upper limit to the effect of random errors and possible systematic errors in terms of mixing ratio is estimated at 0.050 mg of water vapor per gram of dry air or 1/4 percent of full scale. The instrument was designed for use as a working or transfer standard for humidity measurements.

The international system of units, A. G. McNish, *Am. Soc. Quality Control Annual Tech. Conf. Trans. pp. 431–438 (1965).*

The International System of units is advantageous in engineering calculations because of its completeness and simplicity. No difficulty is experienced in its application in the United States although it is inconsistent with our customary units for length, mass and temperature.

The NBS standard hygrometer, A. Wexler and R. W. Hyland, *(Proc. 1963 Intern. Symp. Humidity and Moisture, Washington, D.C.), Book, Humidity and Moisture. Measurement and Control in Science and Industry, Ed. A. Wexler, Vol.* **3,** *Fundamentals and Standards, Chapt. 19, pp. 389–431 (Reinhold Publ. Corp., New York, N.Y., 1965).*

A gravimetric hygrometer is described that serves as the NBS standard instrument for the measurement of the moisture content of gases on an absolute basis in terms of mixing ratio (mass water vapor/unit mass of dry gas). The National Bureau of Standards and other laboratory reference and working instruments are intercompared and calibrated with this instrument. The measuring operation involves the absorption of the water vapor from a water vapor-gas mixture by a solid desiccant and the determination of the mass of this water vapor by precision weighing; it also involves the determination of the volume of the associated gas of known density by counting the fillings of two calibrated stainless steel cylinders. An automatic system permits the sampling of the test gas at any desired flow rate up to 2 lpm (STP) and for any desired number of fillings. The instrument provides a value of the mixing ratio averaged over the time interval of a test.

The construction and operation of the instrument is described. Discussions of the tests and calibrations of component parts, and of the sources of errors also are included. An analysis of the random and systematic errors effecting the overall accuracy in the determination of mixing ratio shows that if 0.60 g of water vapor is collected from moist air, then the estimated maximum uncertainty expected for mixing ratios between 27 mg/g and 0.19 mg/g is 12.7 parts in 10^4.

Characteristics of a Raman laser excited by an ordinary ruby laser, H. Takuma and D. A. Jennings, *Proc. IEEE* **53,** *No. 2, 146–149 (Feb. 1965).*

The stimulated Raman effect of benzene has been observed using an ordinary (non-giant) ruby laser. The buildup of oscillation at the ν_2, $2\nu_2$, $3\nu_2$, and $4\nu_2$ Stokes lines and also at the first ν_1 Stokes line and also at the first ν_1 Stokes line have been observed. The threshold exciting power for laser action in the ν_2 Stokes line has been measured to be 9.5 kW. A rate equation for the Raman laser has been given, and the constant for Raman scattering of benzene has been determined as $k = 9.5 \cdot 10^{-28}$ sec.$^{-1}$. The estimation based on the results of this investigation indicates that it is possible to construct a Raman laser of benzene using a He-Ne gas laser.

Drift-free Mössbauer spectrometer, F. C. Ruegg, J. J. Spijkerman, and J. R. DeVoe, *Rev. Sci. Instr.* **36,** *No. 3, 356–359 (Mar. 1965).*

In order to eliminate drifts encountered in electro-mechanical Mössbauer spectrometers, a drive has been developed which is drift free with regard to velocity as well as position. The spectrometer can be driven in two modes: constant acceleration and constant velocity. The constant acceleration input signal is the analog output of the address scalers of a multichannel analyzer running as a multi-scaler (time mode). The constant velocity is obtained from a photo-cell slit system which drives the input of the spectrometer with a rectangular wave. In both modes, the photocell system is used to eliminate all position drifts by starting each

new cycle from the same position. To analyze the velocity of the spectrometer a voltage to frequency converter and multichannel analyzer are used.

Elastic constants of cubic lead fluoride at room temperature, J. H. Wasilik and M. L. Wheat, *J. Appl. Phys.* **36,** *No. 3, Pt. 1, 791–793 (Mar. 1965).*

Using an ultrasonic pulse echo technique operating at frequencies ~ 10 Mc/sec, we have obtained the following elastic constants for cubic PbF_2: $C_{11}=8.88\times10^{11}$ dyn/cm², $C_{12}=4.72\times10^{11}$ dyn/cm², $C_{44}=2.454\times10^{11}$ dyn/cm² at 27 °C. From these data a Debye θ of 221.2 °K was calculated.

Electron microscopy and diffraction of synthetic corundum crystals. I. Pure aluminum oxide grown by the Verneuil process, D. G. Barber and N. J. Tighe, *Phil. Mag.* **11,** *No. 111, 495–512 (May 1965).*

Single crystal aluminum oxide has been chemically thinned by means of a jet-polishing device and examined in the electron microscope. During thinning, the crystals could be etch-pitted, and the relationship between etch-pits and dislocations has been investigated; etch-pits on subgrain boundaries are often unrepresentative of the dislocation density. The characteristics of thermally etched surfaces have also been studied, and the results of evaporation experiments in the microscope are presented.

The behaviour of dislocations in various plastically deformed crystals has been examined. Tangles of dislocations, commonly found in metals and in other ionic solids, are absent, and dislocation densities in glide bands are low. Grown-in dislocations apparently participate in the glide process; therefore, they are not strongly pinned by impurities at temperatures permitting plastic deformation. The occurrence of dislocation dipoles is taken as evidence for the existence of cross slipping of basal dislocations at temperatures below those required for slip on {1120} prism planes. No positive evidence for dislocation dissociations have been found and if splitting occurs, it must be small, indicating that the stacking fault energy is high.

Preliminary studies of dislocation motion in the microscope at temperatures ~ 1500 °C are reported and discussed.

Ice nucleation by photolyzed silver iodide, G. Burley, *Phil. Mag.* **10,** *527 (Sept. 1964).*

A progressive change of the shape of ice crystals nucleated by silver iodide particles at constant temperature has been found, with a linear dependence only on the cumulative time of exposure of the latter to light. The directional crystallographic properties of the photodeactivation process are applied to correlate this with the mechanism of epitaxial nucleation.

The absolute photometry of the zodiacal light, L. L. Smith, F. E. Roach, and R. W. Owen, *Planet. Space Sci.* **13,** *207–217 (Pergamon Press Ltd., Northern Ireland, 1965).*

Interpretation is made of photometric records obtained at the Haleakala Observatory during six nights between August 1961 and June 1962. An interference filter centered on wavelength 5300A was used. After allowance for the airglow continuum and the integrated starlight the residual was interpreted as due to zodiacal light. The brightness of the zodiacal light is tabulated for that part observable in the night sky. Graphical representations of the data illustrate the distribution of brightness in ecliptic coordinates. Evidence is presented supporting the existence of a terrestrial component superimposed photometrically on the general interplanetary component.

X-ray spectrochemical analysis of material: cement and dental alloys, B. L. Bean and B. W. Mulligan, *Am. Soc. Testing Mater. Spec. Tech. Publ. 373, Application of Advanced and Nuclear Physics to Testing Materials, pp. 25–45 (June 17, 1965).*

The application of X-ray spectrochemical analysis to various materials has undergone marked expansion in recent years. Special examples from the authors' experiences in the analysis of cements and dental materials are cited. Difficulties in presenting a representative sample to the primary X-ray beam are described, together with means for minimizing these difficulties. Interelement corrections for the X-ray analysis of cement are discussed. References are given to the work of numerous investigators in this field.

Measurement and standardization of LF to UHF electrical quantities. Sketch of recent world-wide developments, M. C. Selby, *Prog. Radio Sci. 1960–1963, Vol.* **I.** *Radio Standards and Measurements, pp. 45–55 (Elservier Publ. Co., Amsterdam, The Netherlands, 1965).*

An outline of world-wide activities and progress on measurement & standardization of electrical quantities over an approximate range of 30 Kc/s to 3 Gc/s is presented. The period covers approximately the years of 1960, 1961, and 1962. More prominent technical developments are noted and publication subjects in a number of countries are indicated to expose the apparent areas of more specific interest in these countries. Accelerating national and international organizational activities are also called attention to in order to show the degree of increasing attention to this subject. An attempt is made to present a digest which will be found more specific and more revealing than can be expected from a report of the International Chairman of URSI Commission I. On the other hand, it is far from the detailed account to be found in the national progress reports. The information on international organizational activities seems to be pointed out for the first time in these series of URSI reports.

Radio meteorology, J. W. Herbstreit, *Science* **147,** *No. 3653, 76–78 (Jan. 1, 1965).*

A report of the highlights of the 1964 World Conference on Radio Meteorology held at the National Bureau of Standards, September 14–18, 1964.

The use of electromagnetic signals emitted from nuclear explosions to study long-range VLF propagation, A. G. Jean and J. R. Wait, *J. Geophys. Res.* **70,** *No. 5, 1258–1251 (Mar. 1, 1965).*

Within recent years a number of reports [Newman, 1953; Kompaneets, 1958; United Nations, 1958] have been published which describe the electromagnetic radiation from a nuclear detonation. The phenomenon has been discussed at the conference of "experts" at Geneva at various intervals since the summer of 1958 [United Nations, 1958].

Other NBS Publications

Journal of Research 69A (Phys. and Chem.), No. 4 (July-Aug. 1965), 70 cents.

Correlation of successive atomic steps in crystals by relaxation mode analysis. A. D. Franklin.

Reduction of crystallographic point groups to subgroups by homogeneous stress. H. S. Peiser and J. B. Wachtman, Jr.

Effect of hydrostatic pressure on the refractive indices of some solids. R. M. Waxler and C. E. Weir. (See above abstracts).

Crystallization kinetics and polymorphic transformations in polybutene-1. J. Powers, J. D. Hoffman, J. J. Weeks, and F. A. Quinn, Jr.

Compliance-time-temperature relationships from indentation measurements on a pure-gum rubber vulcanizate. F. L. Roth, G. W. Bullman, and L. A. Wood.

Distribution function of the end-to-end distances of linear polymers with excluded volume effects. J. Mazur.

An additivity rule for the vapor pressure lowering of aqueous solutions. R. A. Robinson and V. E. Bower.

Franck-Condon factors to high vibrational quantum numbers V: O_2 band systems. R. W. Nicholls.

An absolute temperature scale from 4 °K to 20 °K determined from measurements with an acoustical thermometer. H. H. Plumb and G. Cataland. (See above abstracts).

Journal of Research 69A (Phys. and Chem.), No. 5 (Sept.-Oct. 1965), 70 cents.

Current research on preservation of archival records on silver-gelatin type microfilm in roll form. C. S. McCamy and C. I. Pope. (See above abstracts).

Franck-Condon factors to high quantum numbers VI: C_2 band systems. R. W. Nicholls.

Matrices of spin-orbit interaction in the electron configurations p^2d and p^4d. J. L. Tech and R. H. Garstang.

Heat of formation of calcium aluminate tricarbonate at 25 °C. H. A. Berman.

Vapor pressure and heat of sublimation of tungsten. R. Szwarc, E. R. Plante, and J. J. Diamond.

Heat capacity and enthalpy measurements on aluminum carbide (Al_4C_3) from 15 to 1173 °K. Thermodynamic properties from 0 to 2000 °K. G. T. Furukawa, T. B. Douglas, W. G. Saba, and A. C. Victor.

Properties of aqueous mixtures of pure salts: thermodynamics of the ternary system water-potassium chloride-barium chloride at 25 °C. R. A. Robinson and V. E. Bower.

A wide-range (up to 10^{10} P) rotating cylinder viscometer. A. Napolitano, P. B. Macedo, and E. G. Hawkins. (See above abstracts).

Internal friction in ZrO_2 containing CaO. J. B. Wachtman, Jr., and W. C. Corwin. (See above abstracts).

Splitting of equivalent points in noncentrosymmetric space groups into subsets under homogeneous stress. H. S. Peiser, J. B. Wachtman, Jr., F. A. Munley, and L. C. McCleary.

Inclusion of perfluoromethyl groups in the lattice of copolymers of tetrafluoroethylene and hexafluoropropylene. L. H. Bolz and R. K. Eby.

Journal of Research 69B (Math. and Math. Phys.), No. 3 (July-Sept. 1965), 75 cents.

A development of the theory of errors with reference to economy of time. M. D. Hersey. Prefatory note by Churchill Eisenhart.

Transversals and matroid partition. J. Edmonds and D. R. Fulkerson.

Some L_2 Markoff inequalities. L. F. Shampine.

Some theorems on the permanent. R. A. Brualdi and M. Newman.

On Kirchhoff's law and its generalized application to absorption and emission by cavities. F. J. Kelly. (See above abstracts).

On a relation between two-dimensional Fourier integrals and series of Hankel transforms. J. V. Cornacchio and R. P. Soni.

On convex metrics. C. Witzgall.

Some extensions of Banach's contraction theorem. P. R. Meyers.

A variant of the two-dimensional Riemann integral. A. J. Goldman.

The use of finite polynomial rings in the factorization of the general polynomial. D. B. Lloyd.

A primal (all-integer) integer programming algorithm. R. D. Young.

Radio Science J. Research NBS/USNC-URSI 69D, No. 9 (Sept. 1965), $1.00.

Ground-based passive probing using the microwave spectrum of oxygen. E. R. Westwater. (See above abstracts).

Response of NBS microwave refractometer cavities to atmospheric variations. R. O. Gilmer, R. E. McGavin, and B. R. Bean. (See above abstracts).

Effects of rocket outgassing on rf experiments. W. Pfister and J. C. Ulwick. (See above abstracts).

Further analysis of propagation of plasma waves in a "spoke-wheel" magnetic field. R. R. Gold.

Measurement of group velocity of 17.8-kHz VLF radio waves. W. D. Westfall. (See above abstracts).

On the radio noise level at low and very low frequencies in polar regions. T. S. Jørgensen.

Experimental study on the circular loop antenna immersed shallowly in a conducting medium. K. Iizuka.

Directivity of uniformly spaced optimum endfire arrays with equal sidelobes. M. T. Ma.

Extension of Fock theory for currents in the penumbra region. V. H. Weston.

Isometric-circle interpretation of bilinear transformation and its application to VSWR minimization. J. G. Rudolph and D. K. Cheng.

Magneto-ionic propagation in inhomogeneous media. Part I. Transverse propagation. B. K. Banerjea.

Magneto-ionic propagation in inhomogeneous media. Part II. Oblique propagation. B. K. Banerjea.

Editorial comment on the scientific papers of Lord Rayleigh (John William Strutt). J. R. Wait.

Radio Sci. J. Research NBS/USNC-URSI 69D, No. 10 (Oct. 1965), $1.00.

Irreversible power and radiation resistance of antennas in anisotropic ionized gases. K. S. H. Lee and C. H. Papas.

Scattering resonances of a cylindrical plasma. W. M. Leavens.

Radiation patterns from plasma enclosed cylindrical hypersonic vehicles. J. H. Harris, A. T. Villeneuve, and L. A. Broca.

The Schumann resonances. R. K. Cole, Jr.

Atmospheric radio noise bursts in the LF band at Bangalore. S. V. C. Aiya and K. N. Lakshminarayan.

Influence of finite ground conductivity on the propagation of VLF radio waves. J. R. Wait and K. P. Spies.

Model experiments on propagation of groundwaves across an abrupt boundary at perpendicular incidence. R. J. King and S. W. Maley.

Radio Science J. Research NBS/USNC-URSI 69D, No. 11 (Nov. 1965), $1.00.

Propagation of pulses in dispersive media. J. R. Wait. (See above abstracts).

An anisotropic electron velocity distribution for the cyclotron absorption of whistlers and VLF emissions. H. Guthart.

Nose whistler dispersion as a measure of magnetosphere electron temperature. H. Guthart.

Interference rejection capability of a switched radiometer. R. E. Clapp. (See above abstracts).

Atmospheric breakdown limitations to optical maser propagation. R. G. Tomlinson. (See above abstracts).

Phase steps and amplitude fading of VLF signals at dawn and dusk. D. Walker.

Propagation in a model terrestrial waveguide of nonuniform height theory and experiment. E. Bahar and J. R. Wait.

Comments on H. Volland's "Remarks on Austin's Formula." J. R. Wait.

The path integrals of LF/VLF wave hop theory. L. A. Berry and M. E. Chrisman.

Reactive loading of arbitrarily illuminated cylinders to minimize microwave backscatter. K. M. Chen.

On the statistical theory of electromagnetic waves in a fluctuating medium (II) Mathematical basis of the analogies to quantum field theory (a digest). K. Furutsu.

Ionospheric radio propagation, K. L. Davies, NBS Mono. 80 (Apr. 1965), $2.75.

Systems engineering in ceramics. Proceedings of a symposium April 19, 1964, NBS Misc. Publ. 267 (May 1, 1965), $2.00.

Transmission loss predictions for tropospheric communication circuits. P. L. Rice, A. G. Longley, K. A. Norton, and A. P. Barsis, NBS Tech. Note 101, Vol. I (May 7, 1965), $1.00.

Transmission loss predictions for tropospheric communication circuits. P. L. Rice, A. G. Longley, K. A. Norton, and A. P. Barsis, NBS Tech. Note 101, Vol. II (May 7, 1965), $1.00.

Research on crystal growth and characterization at the National Bureau of Standards July to December 1964, ed. H. F. McMurdie, NBS Tech. Note 260 (May 8, 1965), 50 cents.

Studies of solar flare effects and other ionospheric disturbances with a high frequency Doppler technique, V. Agy, D. M. Baker, and R. M. Jones, NBS Tech. Note 306, (Apr. 28, 1965), 75 cents.

Data reduction for stable auroral red arcs observed at Rapid City, South Dakota, J. E. Cruz, R. Davies, L. K. Droppleman, E. Marovich, L. R. Megill, M. H. Rees, L. Reisbeck, and F. E. Roach, NBS Tech. Note 308 (May 3, 1965), 50 cents.

Attenuation of the ground wave of a low frequency electromagnetic pulse, J. C. Morgenstern and J. R. Johler, NBS Tech. Note 310 (Apr. 1965), 30 cents.

On the effect of heavy ions on LF propagation, with special reference to a nuclear environment, J. R. Johler and L. A. Berry, NBS Tech. 313 (June 7, 1965), 45 cents.

Stability of two-phase annular flow in a vertical pipe, S. Jarvis, Jr., NBS Tech. Note 314 (June 7, 1965), 55 cents.

Selected tables of atomic spectra. Atomic energy levels and multiplet tables Si II, Si III, Si IV, C. E. Moore, NSRDS–NBS3, Sec. 1 (June 25, 1965), 35 cents.

A line-formula notation system for coordination compounds, P. M. McDonnell and R. F. Pasternack, J. Chem. Documentation **5**, No. 1, 56–60 (Feb. 1965).

Decyclization of cyclohexene, 4-methylcyclohexene, and 4-vinylcyclohexene in a single-pulse shock tube, W. Tsang, J. Chem. Phys. **42**, No. 5, 1805–1809 (Mar. 1, 1965).

Direct and inert-gas-sensitized radiolysis and photolysis of methane in the solid phase, P. Ausloos, R. E. Rebbert, and S. G. Lias, J. Chem. Phys. **42**, No. 2, 540–548 (Jan. 15, 1965).

Effect of electrical fields and density in the radiolysis of ethane, H. H. Carmichael, R. Gorden, Jr., and P. Ausloos, J. Chem. Phys. **42,** No. 1, 343–351 (Jan. 1, 1965).

Equilibrium pressures of oxygen over $MnO_2-Mn_2O_3$ at various temperatures, E. M. Otto, J. Electrochem. Soc. **112,** No. 4, 367–370 (Apr. 1965).

Hydrogen atom addition to olefins: Relative rates at the two carbon positions and derived heats of formation of several alkyl radicals, R. D. Kelley, R. Klein, and M. D. Scheer, J. Phys. Chem. **69,** No. 3, 905–908 (Mar. 1965).

Isotopic mixing in CO chemisorbed on tungsten. A kinetic study, T. E. Madey, J. T. Yates, Jr., and R. C. Stern, J. Chem. Phys. **42,** No. 1, 1372–1378 (Feb. 15, 1965).

Determination of the composition of complexes and their instability constant by calorimetry, I. The cuprocyanide complexes, A. Brenner, J. Electrochem. Soc. **112,** No. 6, 611–621 (June 1965).

Isotropic fractionation of uranium in sandstone, Powder River Basin, Wyoming, and Slick Rock District, Colorado, J. N. Rosholt, A. P. Butler, E. L. Garner, and W. R. Shields, Econ. Geol. **60,** No. 2, 199–213 (Mar.-Apr. 1965).

Mass spectrum of yttrium chloride vapor, J. D. McKinley, J. Chem. Phys. **42,** No. 6, 2245–2246 (Mar. 15, 1965).

Some new co-ordination compounds of copper (II) chloride, C. Reimann and G. Gordon, Nature **205,** No. 4974, 902–903 (Feb. 27, 1965).

Standardization of analytical data obtained with silver-silver chloride electrodes in methanol-water solvents, M. Paabo, R. G. Bates, and R. A. Robinson, Anal. Chem. **37,** 462–464 (1965).

Statistical design of experiments, W. J. Youden, Handbook on Metals Engineering-Design, American Society of Mechanical Engineers, ch. 3, Pt. 5, pp. 583–585 (McGraw-Hill Publ. Corp., New York, N.Y., 1965).

A uniqueness theorem for entire functions, R. F. DeMar, Proc. Am. Math. Soc. **16,** No. 1, 69–71 (Feb. 1965).

On a theorem concerning existence of interpolating functions, R. F. DeMar, Trans. Am. Math. Soc. **114,** No. 1, 23–29 (Jan. 1965).

PHYSICS

A proper accounting of conformation of a polymer near a surface, E. A. DiMarzio, J. Chem. Phys. **42,** No. 6, 2101–2106 (Mar. 1965).

Characteristics of the "synchrotron light" from the NBS-180 MeV machine, K. Codling and R. P. Madden, J. Appl. Phys. **36,** No. 2, 380–387 (Feb. 1965).

Dependence of the superconducting transition temperature on carrier concentration in semiconducting $SrTiO_3$, J. F. Schooley, W. R. Hosler, E. Ambler, J. H. Becker, M. L. Cohen, and C. S. Koonce, Phys. Rev. Letters **14,** No. 9, 305–307 (Mar. 1, 1965).

Direct observation of the optical anisotropy of the holmium nucleus, E. Ambler, E. G. Fuller, and H. Marshak, Phys. Rev. **138,** No. 1B, B117–B126 (Apr. 12, 1965).

Growth layers on ammonium dihydrogen phosphate, J. L. Torgesen and R. W. Jackson, Science **148,** No. 3672, 952–954 (May 14, 1965).

Influence of paramagnetic resonance on the static susceptibility. Spin-lattice relaxation time of cupric sulfate pentahydrate, G. A. Candela, J. Chem. Phys. **42,** No. 1, 113–117 (Jan. 1, 1965).

Line profiles in the far-uv absorption spectra of the rare gases, U. Fano and J. W. Cooper, Phys. Rev. **137,** No. 5A, A1364–A1379 (Mar. 1, 1965).

Low temperature magnetic transitions in some rare-earth trichlorides, J. C. Eisenstein, R. P. Hudson, and B. W. Mangum, Phys. Rev. **137,** No. 6A, A1886–A1895 (Mar. 15, 1965).

Multichannel resonances in the forward scattering of electrons by helium, G. E. Chamberlain, Phys. Rev. Letters **14,** No. 15, 581–582 (Apr. 12, 1965).

Nonlinear ambipolar diffusion of an isothermal plasma across a magnetic field, E. R. Mosburg, Jr., and K. B. Persson, Phys. Fluids **7,** No. 11, 1829–1833 (Nov. 1964).

Polymorphism in hydrogen iodide, F. A. Mauer, C. J. Keffer, R. B. Reeves, and D. W. Robinson, J. Chem. Phys. **42,** No. 4, 1465–1466 (Feb. 15, 1965).

Stability of traveling waves in lasers, J. A. White, Phys. Rev. **137,** No. 6A, A1651–A1654 (Mar. 15, 1965).

Temperature and mean free path dependence of the Ginzburg-Landau parameter, S. Gygax and R. H. Kropschot, Phys. Letters **12,** No. 1, 7–9 (Sept. 1, 1964).

The measurement of water vapor boundary layers in biological systems with a radio refractometer, D. M. Gates (Proc. 1963 Intern. Symp. Humidity and Moisture, Washington, D.C.), Book, Humidity and Moisture. Measurement and Control in Science and Industry. Vol. 2. Applications, Sec. I, Paper 5, pp. 33–38 (Reinhold Publ. Corp., New York, N.Y., 1965).

Two-electron excitation states in helium, R. P. Madden and K. Codling, Astrophys. J. **141,** No. 2, 362–375 (Feb. 15, 1965).

Cavity resonances for spherical earth with a concentric anisotropic shell, J. R. Wait, J. Atmos. Terres. Phys. **27,** 81–89 (1965).

Method of adjusting force constants and its application to H_2O, H_2CO, CH_2Cl, and their deuterated molecules, T. Shimanouchi and I. Suzuki, J. Chem. Phys. **42,** No. 1, 296–308 (Jan. 1, 1965).

On the twilight sodium emission-2. A theoretical model of sodium abundance, M. Gadsden, Ann. Geophys. **20,** No. 4, 383–396 (Oct.-Dec. 1964).

Quenching of the triplet state of acetone and biacetyl by azoalkanes, R. E. Rebbert and P. Ausloos, J. Am. Chem. Soc. **87,** 1847–1852 (May 5, 1965).

Vacuum-ultraviolet photolysis of ethane in liquid-nitrogen solution, J. A. Pirog and J. R. McNesby, J. Chem. Phys. **42,** No. 7, 2490–2494 (Apr. 1, 1965).

A simple method for measuring the amount of granular materials in sulfur mortars, C. L. Thompson, Mater. Res. Std. **5,** No. 5, 242–243 (May 1965).

Thermodynamic properties of neon from 25 to 300 °K between 0.1 and 200 atmospheres, R. D. McCarty and R. B. Stewart, Advances in Thermophysical Properties at Extreme Temperatures and Pressures, pp. 84–97, (Am. Soc. Mech. Engr., New York, N.Y., 1965).

Work function measurements on field emitters with prescribed orientation, J. W. Little, T. E. Madey, and R. Klein, J. Appl. Phys. **36,** No. 4, 1491–1492 (Apr. 1965).

A method for the computation of the error function of a complex variable, O. N. Strand, Math. Comp. **XIX,** No. 89, 127–129 (Jan. 1965).

Bounds for class numbers, M. Newman, Proc. Pure Mathematics, Vol. **VIII.** Theory of Numbers, pp. 70–77 (Am. Math. Soc., 1965).

Comment on The use of transforms to sum array factors, M. T. Ma, IEEE Trans. Ant. Prop. **AP-13,** No. 1, 174 (Jan. 1965).

Distribution of student's t in samples from a rectangular universe, M. M. Siddiqui, Rev. Intern. Stat. Inst. **32,** No. 3, 242–250 (1964).

Mathematical programming models for selection of diets to minimize weighted radionuclide intake, H. J. Bracken, Environmental Health Series: Radiological Health, Public Health Serv. Publ. 999–R–4 (Dept. Health, Education, and Welfare, Wash. D.C., Aug. 1963).

Letter to the Editor, C. H. Page, Metrologia **1,** No. 2, 73–74 (Apr. 1965).

The evolution of designed experiments, W. J. Youden, Proc. IBM Scientific Computing Symp. Statistics, pp. 59–67 (West Chester County, New York, Sept. 1963).

Adsorption of polymer molecules at low surface coverage, C. A. J. Hoeve, E. A. DiMarzio, and P. Peyser, J. Chem. Phys. **42,** No. 7, 2558–2563 (Apr. 1, 1965).

Determination of the probability distribution of the number of secondary electrons, Z. Bay and G. Papp, IEEE Trans. Nuclear Sci. **NS-11,** No. 3, 160 (June 1964); Elec. Commun. 40, No. 1, 134 (1965).

Effects of finite heat capacity on spin-lattice relaxation, R. L. Peterson, Phys. Rev. **137,** No. 5A, A1444–A1448 (Mar. 1, 1965).

Elastic resonances in electron scattering from He, Ne, Ar, Kr, Xe, and Hg, C. E. Kuyatt, J. A. Simpson, and S. R. Mielczarek, Phys. Rev. **138,** No. 2A, A385–A399 (Apr. 19, 1965).

Electron microscopy and diffraction of synthetic corundum crystals. I. Pure aluminum oxide grown by the Verneuil process, D. G. Barber and N. J. Tighe, Phil. Mag. **11,** No. 111, 495–512 (May 1965).

Electronic energy bands in $SrTiO_3$ and related oxide semiconductors, A. H. Kahn and A. J. Leyendecker, Proc. 1964 Intern. Conf. Physics of Semiconductors, Paris, pp. 33–39 (Physique des Semiconducteurs, Paris, France, 1964).

Identification of energy levels of negative ions, U. Fano and J. W. Cooper, Phys. Rev. **138,** No. 2A, A400–A402 (Apr. 19, 1965).

Influence of spin paramagnetism on superconductivity, R. A. Kamper, R. S. Collier, and Y. Ohori, Phys. Rev. **137,** 1A, A75–A77 (Jan. 4, 1965).

Interpretation of Ar^+-Ar collisions at 50 keV, U. Fano and W. Lichten, Phys. Rev. Letters **14,** No. 16, 627–629 (Apr. 19, 1965).

Longitude distribution of proton flares, C. S. Warwick, Astrophys. J. 141, No. 2, 500–504 (Feb. 15, 1965).

Mass-spectrometric study of photoionization, II. H_2, HD, and D_2, V. H. Dibeler, R. M. Reese, and M. Krauss, J. Chem. Phys. **42,** No. 6, 2045–2048 (Mar. 15, 1965).

Multiple-band conduction in n-type rutile (TiO_2), J. H. Becker and W. R. Hosler, Phys. Rev. **137,** No. 6A, A1872–A1877 (Mar. 15, 1965).

On the behavior of the compressibility along the critical isotherm, S. Y. Larsen and J. M. H. L. Sengers, Advances in Thermophysical Properties at Extreme Temperatures and Pressures, pp. 74–75, (Am. Soc. Mech. Engr., New York, N.Y., 1965).

On the validity of the Lorentz-Lorenz equation near the critical point, S. Y. Larsen, R. D. Mountain, and R. Zwansig, J. Chem. Phys. **42,** No. 6, 2187–2190 (Mar. 15, 1965).

Plans for proposed new tables of the thermodynamic properties of moist air, J. C. Davis, T. K. Faison, Jr., and P. R. Achenbach, (Proc. 1963 Intern. Symp. Humidity and Moisture, Wash., D. C.), Book, Humidity and Moisture, Measurement and Control in Science and Industry, ed. A. Wexler, Vol. **3.** Fundamentals and Standards, ch. 11, pp. 315–320 (Reinhold Publ. Corp., New York, N.Y., 1965).

Optical quenching of photoconductivity near the band edge in CdS, L. Grabner, Phys. Rev. Letters **14,** No. 14, 551–554 (Apr. 5, 1965).

Polar modes of lattice vibration and polaron coupling constants in rutile (TiO_2), D. M. Eagles, J. Phys. Chem. Solids **25,** No. 11, 1243–1251 (Nov. 1964).

Polaron coupling constants in $SrTiO_3$, D. M. Eagles, J. Phys. Chem. Solids **26,** No. 3, 672 (Mar. 1965).

Pressure dependence of the internal field at the ^{59}Co nucleus in a 99.5% Ni-0.5% Co alloy, L. H. Bennett, J. Appl. Phys. **36,** No. 3, Pt. 2, 942–943 (Mar. 1965).

Stimulated Brillouin scattering in the off-axis resonator, H. Takuma and D. A. Jennings, Appl. Phys. Letters. **5,** 239–241 (Dec. 1964).

Structure of electrodeposited lead dendrites, F. Ogburn, C. Bechtoldt, J. B. Morris, and A. deKoranyi, J. Electrochem. Soc. **112,** No. 6, 574–577 (June 1965).

SU(6) Clebsch-Gordan coefficients for the product 35×56, J. C. Carter, J. J. Coyne, and S. Meshkov, Phys. Rev. Letters **14,** No. 13, 523–526 (Mar. 29, 1965).

The correlation of experimental pressure-density-temperature and specific heat data for parahydrogen, H. M. Roder, L. A. Weber, and R. D. Goodwin, (Proc. XI Intern. Congress Refrigeration, Munich, Germany, Aug. 1963), Prog. Refrig. Sci. Technol. **1,** 187–191 (1963).

Transition from resonant to non-resonant line shape in microwave absorption, A. Ben-Reuven, Phys. Rev. Letters **14,** No. 10, 349–351 (Mar. 8, 1965).

Stratospheric moisture measurements using infrared spectroscopy, D. M. Gates, (Proc. 1963 Intern. Symp. Humidity and Moisture, Wash., D.C.), Book, Humidity and Moisture, Measurement and Control in Science and Industry, Vol. **2,** Applications, Sec. VI, pp. 446–449 (Reinhold Publ., Corp., New York, N.Y., 1965).

The uses of oblique ionograms in frequency utilization, K. Davies, ITU Telecommun. J. **31,** No. 10, pp. 1–7 (Oct. 1964).

Tropospheric propagation, P. L. Rice and J. W. Herbstreit, Advan. Electron. Electron Phys. **20,** 199–259 (1964).

**Publications for which a price is indicated are available by purchase from the Superintendent of Documents, U.S. Government Printing Office, Washington, D.C., 20402 (foreign postage, one-fourth additional). Reprints from outside journals and the NBS Journal of Research may often be obtained directly from the authors.*

JOURNAL OF RESEARCH of the National Bureau of Standards—C. Engineering and Instrumentation
Vol. 69C, No. 4, October–December 1965

INDEX TO VOLUME 69C

January to December 1965

A

Page

Adams, L. H., R. H. Waxler, Superimposed birefractory plates ... 103
Adiabatic calorimeter for the range 10 to 360 °K ... 19
Air capacitors, precision, voltage dependence ... 265

B

Baker, D. W., M. R. Shafer, K. R. Benson, Electric currents and potentials resulting from the flow of charged liquid hydrocarbons through short pipes ... 307
Benson, K. R., M. R. Shafer, D. W. Baker, Electric currents and potentials resulting from the flow of charged liquid hydrocarbons through short pipes ... 307
Berger, H. W., B. C. Cadoff, Polarographic analysis of titanium (IV)—EDTA complex: application to paint pigments ... 67
Bestul, A. B., K. F. Sterrett, D. H. Blackburn, S. S. Chang, J. Horman, An adiabatic calorimeter for the range 10 to 360 °K ... 19
Birefractory plates, superimposed ... 103
Blackburn, D. H., K. F. Sterrett, A. B. Bestul, S. S. Chang, J. Horman, An adiabatic calorimeter for the range 10 to 360 °K ... 19
Block, S., C. Weir, G. Piermarini, Single crystal x-ray diffraction at high pressures ... 275
Bowman, H. A., R. M. Schoonover, Cartesian diver as a density comparator ... 217
Broadhurst, M. G., A. J. Bur, Two-terminal dielectric measurements up to 6×10^9 Hz ... 165
Bur, A. J., M. G. Broadhurst, Two-terminal dielectric measurements up to 6×10^9 Hz ... 165

C

Cadoff, B. C., H. W. Berger, Polarographic analysis of titanium (IV)—EDTA complex: application to paint pigments ... 67
Caldwell, F. R., Temperatures of thermocouple reference junctions in an ice bath ... 95
Calorimeter, adiabatic, for the range 10 to 360 °K ... 19
Capacitor, improved ten-picofarad fused silica dielectric ... 173
Capacitors, precision air, voltage dependence ... 265
Cartesian diver as a density comparator ... 217
Cathodic protection and underground corrosion, soil resistivity as related ... 71
Centerable rotator for measuring properties of crystals ... 191
Centerline correction for precision roughness specimens ... 303
Chamberlin, J. L., Centerline correction for precision roughness specimens ... 303
Chang, S. S., K. F. Sterrett, D. H. Blackburn, A. B. Bestul, J. Horman, An adiabatic calorimeter for the range 10 to 360 °K ... 19
Chen, W. T., M. Waxman, A rugged null-type pressure transducer of high reproducibility for accurate gas phase PVT measurement ... 27
Comparator, density, Cartesian diver ... 217
Comparators for voltage transformer calibration at NBS ... 257
Compensated solenoid giving a uniform magnetic field over a large volume ... 49
Conductors, rectangular, exact inductance equations for, with applications to more complicated geometrics ... 127
Conrad, G. T., D. C. Shook, A transitor screening procedure using leakage current measurements ... 319
Construction of a Michelson interferometer for Fourier spectroscopy ... 5
Corrosion, underground, and cathodic protection, soil resistivity as related ... 71
Corruccini, R. J., The Sondheimer-Wilson-Kohler formula in platinum resistance thermometry ... 283
Cryogenic behavior of selected magnetic materials ... 225
Crystal, single, x-ray diffraction at high pressures ... 275
Crystals, centerable rotator for measuring properties ... 191
Cutkosky, R. D., L. H. Lee, An improved ten-picofarad fused silica dielectric capacitor ... 173
Cylinders, two intersecting, common volume ... 139

D

De, M., P. K. Mondal, Phase and amplitude contrast microscopy in partially coherent light ... 199
Detection and damping of thermal-acoustic oscillations in low-temperature measurements ... 35
Dielectric capacitor, improved ten-picofarad fused silica ... 173
Dielectric measurements, two-terminal, up to 6×10^9 Hz ... 165
Ditmars, D. A., G. T. Furukawa, Detection and damping of thermal-acoustic oscillations in low-temperature measurements ... 35
Driscol, R. L., C. Snow, A compensated solenoid giving a uniform magnetic field over a large volume ... 49

E

Edsinger, R. E., L. A. Guildner, The National Bureau of Standards gas thermometer II. Measurement of capacitance to a grounded surface with a transformer ratio-arm bridge ... 13
Electric currents and potentials resulting from the flow of charged liquid hydrocarbons through short pipes ... 307
Ellerbruch, D. A., Evaluation of a microwave phase measurement system ... 55
Equipment for single-crystal growth from the melt suitable for substances with a low melting point ... 195
Errors in the series-parallel buildup of four-terminal resistors ... 181
Evaluation of a microwave phase measurement system ... 55
Exact inductance equations for rectangular conductors with applications to more complicated geometries ... 127
Exposure time relations for Kossel microdiffraction photographs ... 213

F

Fourier spectroscopy, construction of a Michelson interferometer ... 5
Furukawa, G. T., D. A. Ditmars, Detection and damping of thermal-acoustic oscillations in low-temperature measurements ... 35

G

Gas phase PVT measurement, rugged null-type pressure transducer ... 27
Glasgow, A. R., A. T. Horton, Equipment for single-crystal growth from the melt suitable for substances with a low melting point ... 195
Gniewek, J. J., E. Ploge, Cryogenic behavior of selected magnetic materials ... 225
Guildner, L. A., R. E. Edsinger, The National Bureau of Standards gas thermometer II. Measurement capacitance to a grounded surface with a transformer ratio-arm bridge ... 13

H

Heat conduction, steady-state, in an exposed exterior column of rectangular cross section ... 145
Hoer, C., C. Love, Exact inductance equations for rectangular conductors with applications to more complicated geometries ... 127
Hord, J., Stress znalysis of tape-wound magnet coils ... 287
Horman, J., K. F. Sterrett, D. H. Blackburn, A. B. Bestul, S. S. Chang, An adiabatic calorimeter for the range 10 to 360 °K ... 19
Horton, A. T., A. R. Glasgow, Equipment for single-crystal growth from the melt suitable for substances with a low melting point ... 195
Hubbell, J. H., Common volume of two intersecting cylinders ... 139
Huntley, L. E., A self-calibrating instrument for measuring conductance at radio frequencies ... 115
Hydrocarbons, charged liquid, electric currents and potentials resulting from the flow through short pipes ... 307

I

Ice bath, temperature of thermocouple reference junctions ... 95
Improved ten-picofarad silica dielectric capacitor ... 173
Inductance equations, exact, for rectangular conductors with applications to more complicated geometries ... 127
Interferometer, wave front shearing, some applications ... 245

J

Johnson, A., Two picnometers of increased convenience and precision ... 1

K

Kossel microdiffraction photographs, exposure time relations ... 213

L

Lamperti, P. J., H. O. Wychoff, NBS free-air chamber for measurement of 10 to 60 kV x-rays ... 39
Leakage current measurements, a transitor screening procedure ... 319
Lee, L. H., R. D. Cutkosky, An improved ten-picofarad fused silica dielectric capacitor ... 173
Light, partially coherent, phase amplitude contrast microscopy ... 199
Love, C., C. Cletus, Exact inductance equations for rectangular conductors with applications to more complicated geometries ... 127
Lowey, H. B., C. P. Saylor, Centerable rotator for measuring properties of crystals ... 191
Low-temperature measurements, detection and damping of thermal-acoustic oscillations ... 35

M

Magnet coils, tape-wound, stress analysis ... 287
Magnetic materials, selected, cryogenic behavior ... 225
Michelson interferometer, construction of, for Fourier spectroscopy ... 5
Microdiffraction photographs, Kossel exposure time relations ... 213
Microwave phase measurement system, evaluation ... 55
Microscopy, phase and amplitude contrast in partially coherent light ... 199
Mondal, P. K., M. De, Phase and amplitude contrast microscopy in partially coherent light ... 199

N

NBS free-air chamber for measurement of 10 to 60 kV x-rays ... 39
Null-type pressure transducer of high reproducibility for accurate gas phase PVT measurement ... 27

P

Page, C. H., Errors in the series-parallel buildup of four-terminal resistors ... 181
Paint pigments, application: Polarographid analysis of titanium (IV)—EDTA complex ... 67

Page

Pearv, B. A., Steady-state heat conduction in an exposed exterior column of rectangular cross section 145
Phase and amplitude contrast microscopy in partially coherent light 199
Picnometers, two, of increased convenience and precision 1
Piermarini, G., C. Weir, S. Block, Single crystal x-ray diffraction at high pressures 275
Plates, birefractory, superimposed 103
Platinum resistance thermometry, the Sondheimer-Wilson-Kohler formula 283
Polarographic analysis of titanium (IV)—EDTA complex: application to paint pigments 67
Ploge, E. J., J. Gniewek, cryogenic behavior of selected magnetic materials 225
Precision air capacitors, voltage dependence 265
Precision method for evaluating primary aberrations of lenses with a Twyman interferometer 251

R

Radio frequencies, a self-calibrating instrument for measuring conductance 115
Resistors, four-terminal, errors in the series-parallel buildup 181
Rotator, centerable, for measuring properties of crystals 191
Rugged null-type pressure transducer of high reproducibility for accurate gas phase PVT measurement 27
Rundle, H. N., Construction of a Michelson interferometer for Fourier spectroscopy 5

S

Saunders, J. B., Precision method for evaluating primary aberrations of lenses with a Twyman interferometer 251
———, Some applications of the wave front shearing interferometer 245
Saylor, C. P., H. B. Lowey, Centerable rotator for measuring properties of crystals 191
Schoonover, R. M., H. A. Bowman, Cartesian diver as a density comparator 217
Schwerdtfeger, W. J., Soil resistivity as related to underground corrosion and cathodic protection 71
Screening procedure, transitor, using leakage current measurements 319
Self-calibrating instrument for measuring conductance at radio frequencies 115
Shafer, M. R., D. W. Baker, K. R. Benson, Electric currents and potentials resulting from the flow of charged liquid hydrocarbons through short pipes 307
Shields, J. Q., Voltage dependence of precision air capacitors 265
Shook, D. C., G. T. Conrad, A transitor screening procedure using leakage current measurements 319
Single-crystal growth from the melt suitable for substances with low melting point 195
Single crystal x-ray diffraction at high pressures 275
Snow, C. R., L. Driscoll, A compensated solenoid giving a uniform megnetic field over a large volume 49
Soil resistivity as related to underground corrosion and cathodic protection 71
Solenoid, compensated, giving a uniform magnetic field over a large volume 49
Some applications of the wave front shearing interferometer 245
Sondheimer-Wilson-Kohler formula in platinum resistance thermometry 283
Steady-state heat conduction in an exposed exterior column of rectangular cross section 145
Sterrett, K. F., D. H. Blackburn, A. B. Bestul, S. S. Chang, J. Horman, An adiabatic calorimeter for the range 10 to 360 °K 19

Page

Stress analysis of tape-wound magnet coils 287
Superimposed birefractory plates 103
Sze, W. C., Comparators for voltage transformer calibrations at NBS 257

T

Temperatures of thermocouple reference junctions in an ice bath 95
Ten-picofarad fused silica dielectric capacitor, improved 173
The National Bureau of Standards gas thermometer II. Measurement of capacitance to a grounded surface with a transformer ratio-arm bridge 13
Thermal-acoustic oscillations in low-temperature measurements, detection and damping 35
Thermocouples, temperature of, reference junctions in an ice bath 95
Thermometry, platinum resistance, the Sondheimer-Wilson-Kohler formula 283
Titanium (IV)—EDTA complex, polarographic analysis of, application to paint pigments 67
Transducer, rugged null-type pressure, of high reproducibility for accurate gas phase PVT measurement 27
Transitor screening procedure using leakage current measurements 319
Two picnometers of increased convenience and precision 1
Two-terminal dielectric measurements up to 6×10^8 Hz 165
Twyman interferometer, precision for evaluating primary aberrations of lenses 251

V

Vieth, D. L., H. Yakowitz, Exposure time relations for Kossel microdiffraction photographs 213
Voltage dependence of precision air capacitors 265
Voltage transformer calibration at NBS, comparators 257
Volume, common, to two intersecting cylinders 139

W

Wave front shearing interferometer, some applications 245
Waxler, R. H., L. H. Adams, Superimposed birefractory plates 103
Waxman, M., W. T. Chen, A rugged null-type transducer of high reproducibility for accurate gas phase PVT measurement 27
Weir, C., S. Block, G. Piermarini, Single crystal x-ray diffraction at high pressures 275
Wyckoff, H. O., P. J. Lamperti, NBS free-air chamber for measurement of 10 to 60 kV x-rays 39

X

X-ray diffraction, single crystal, at high pressures 275
X rays, NBS free-air chamber for measurement of 10 to 60 kV 39

Y

Yakowitz, H., D. L. Vieth, Exposure time relations for Kossel microdiffraction photographs 213

U. S. GOVERNMENT PRINTING OFFICE: 1965 O—784-657

SJR-C/JUNE 46129
UNIVERSITY MICROFILMS INC
SERIALS SECTION
313 NORTH FIRST ST
ANN ARBOR MICH

UNITED STATES
GOVERNMENT PRINTING OFFICE
DIVISION OF PUBLIC DOCUMENTS
WASHINGTON, D.C. 20402

OFFICIAL BUSINESS

POSTAGE AND FEES PAID
U.S. GOVERNMENT PRINTING OFFICE

JOURNAL OF RESEARCH of the National Bureau of Standards Vol. 69C, No. 4 October–December 1965
C. Engineering and Instrumentation

Contents

	Page
Some applications of the wave front shearing interferometer. James B. Saunders.	245
Precision method for evaluating primary aberrations of lenses with a Twyman interferometer. James B. Saunders.	251
Comparators for voltage transformer calibrations at NBS. Wilbur C. Sze.	257
Voltage dependence of precision air capacitors. J. Q. Shields.	265
Single crystal x-ray diffraction at high pressures. C. Weir, S. Block, and G. Piermarini.	275
The Sondheimer-Wilson-Kohler formula in platinum resistance thermometry. R. J. Corruccini.	283
Stress analysis of tape-wound magnet coils. Jesse Hord.	287
Centerline correction for precision roughness specimens. J. L. Chamberlin.	303
Electric currents and potentials resulting from the flow of charged liquid hydrocarbons through short pipes. M. R. Shafer, D. W. Baker, and K. R. Benson.	307
A transistor screening procedure using leakage current measurements. George T. Conrad and Donald C. Shook.	319
Publications of the National Bureau of Standards.	331
Index to volume 69C, January to December 1965.	341

Library of Congress Catalog Card Number: 62–3900

For sale by the Superintendent of Documents, U.S. Government Printing Office, Washington, D.C., 20402. Price 75 cents (single copy). Subscription price: $2.25 a year; 50 cents additional for foreign mailing.
UNITED STATES GOVERNMENT PRINTING OFFICE, WASHINGTON : 1965